Developing New Materials for Spintronic, Photovoltaic, and Optoelectronic Applications

by

Brandon Allen Buchanan

A dissertation submitted in partial fulfillment
of the requirements for the degree of
Doctor of Philosophy
(Materials Science and Engineering)
in the University of Michigan
2021

Doctoral Committee:

Professor Pierre Ferdinand Poudeu-Poudeu, Chair
Professor Bart Bartlett
Assistant Professor John Heron
Professor Ctirad Uher

Brandon Allen Buchanan

buchb@umich.edu

ORCID iD: 0000-0001-5737-3965

© Brandon Allen Buchanan 2021

Dedication

This dissertation is dedicated in loving memory of my late grandparents, William and Donna Buchanan, both of which helped instill in me the value of hard work. I hope this thesis would have made you both proud.

Acknowledgements

First, I would like to thank my advisor, Dr. Pierre Ferdinand Poudeu-Poudeu. When I joined in 2016, I was new to the whole field of Materials Science & Engineering (MSE). Dr. Poudeu graciously taught me about materials synthesis, the power that comes with understanding crystal structures, and structure-property relationships. Your insight and guidance have fostered my growth as a scientist, and I will forever be grateful for that. The experience that I have gained from these past five years will be invaluable in my future career.

Second, I would like to thank my committee members, Dr. John Heron, Dr. Bart Bartlett, and Dr. Ctirad Uher. Your scientific advice during my prelim, data meeting, and thesis has been crucial to me. I would like to extend a special thank you to Dr. Bartlett, as on short notice he was willing to join my prelim committee and attend my prelim oral presentation; thank you very much.

Next, I would like to thank my lab-mates, past and present, Dr. Ruiming Lu, Dr. Juan Lopez, Dr. Nick Moroz, Dr. Erica Chen, Dr. Alan Olvera, Yiqiao Huang, Yixuan Chen, Lamia Dawahre, Zhixiong Yin, Tyler Del Rose, Dr. Chinwe Ikpo, and Kayla Byrd. Your friendship, guidance, and collaboration have helped me get to where I am today. Yiqiao, thank you very much for measuring XPS on several compounds for me. Alan and Juan, thank you for taking me under your wing when I was a first-year graduate student; your mentorship in MSE and the lab was essential in preparing me for success these past five years.

Also, I would like to thank my collaborators Andrew Craig and Dr. Jennifer Aitken at Duquesne University, as well as Bradley Terry and Dr. Bartlett at the University of Michigan.

Thanks to your UV-Vis-NIR diffuse reflectance spectroscopy characterization, I was able to determine the optical bandgap of my various materials.

Then, I would like to thank the Van Vlack staff, Tim Chambers, Ying Qi, Keith McIntyre, Sahar Farjami, and Kevin Worth. Thanks to you all, equipment training, IT issues, and safety were all covered with great proficiency.

I would also like to thank the MSE office staff, Renee Hilgendorf, Patti Vogel, Shelley Fellers, Debbie Johnson, and Todd Richardson. Your department guidance has been greatly appreciated. I would like to extend a special thank you to Renee, any time I hit a tough time during the program, you were there to help me out; for that, I will be forever grateful.

In addition, I would like to thank my friends, Tyler Edgington, Ariba Javed, Max Powers, Steven Chavez, and the University of Michigan 2016 MSE cohort. You all have been there for me during the “highs” and “lows” of these past five years. This journey was not easy, but your friendship and support helped me push through. To my friends I made at Michigan, I will be forever grateful for the wonderful memories we have shared together.

Lastly, I would like my family, my mom Debbie, my dad Rich, and my sister Jordyn. Your love and support were truly what helped me make it to the finish line. Mom and Dad-thank you for instilling in me values of hard work and determination. Thank you for the sacrifices you have made for Jordyn and me to help us get where we are today. I know the road has not been easy. Jordyn-your drive to succeed is an inspiration to me every day.

Table of Contents

Dedication ii

Acknowledgements iii

List of Tables ix

List of Figures xiv

List of Appendices xxvi

Abstract xxvii

CHAPTER 1: Introduction 1

1.1 Moore's Law, Computing Performance, Spintronics, and Dilute Magnetic Semiconductors (DMSs) 1

1.2 Lifshitz Transition Materials 4

1.3 Climate Change, Clean Energy, and Photovoltaics 5

CHAPTER 2: Experimental 10

2.1 Synthesis 10

2.1.1 Powder Synthesis: 10

2.1.2 Hot-Pressed Pellet/Bar: 10

2.2 Characterization 11

2.2.1 Powder X-Ray Diffraction (PXRD) 11

2.2.2 Rietveld Refinement 12

2.2.3 Differential Scanning Calorimetry (DSC) 13

2.2.4 X-ray Photoelectron Spectroscopy (XPS) 13

2.2.5 Thermal Diffusivity/Heat Capacity 14

2.2.6 Electrical Conductivity/Seebeck Coefficient 14

2.2.7 Low-Temperature Direct-Current (DC) Magnetic Susceptibility 14

2.2.8 UV-Vis-NIR Diffuse Reflectance Spectroscopy 15

2.2.9 High-Temperature Powder X-Ray Diffraction (HT-XRD) 16

2.2.10 Optical Microscopy of $Cu_2Zn_{2x}Ti_{(3-2x)/2}Se_4$ (x = 1.5, 1, 0.5, 0) and $Cu_2Mn_3Se_4$ Single Crystals 17

2.2.11 Single-Crystal X-Ray Diffraction (SC-XRD) & Structure Determination 17

CHAPTER 3: $Mn_{1-x}Zn_xSb_2Se_4$ (x = 0, 0.01, 0.04, 0.05, 0.06, 0.08, 0.1, 0.15) Structural, Thermoelectric, and Magnetic Properties 20

3.1 Introduction: $Mn_{1-x}Zn_xSb_2Se_4$ (x = 0, 0.01, 0.04, 0.05, 0.06, 0.08, 0.1, 0.15) 20

3.2 Synthesis: $Mn_{1-x}Zn_xSb_2Se_4$ (x = 0, 0.01, 0.04, 0.05, 0.06, 0.08, 0.1, 0.15) 26

3.2.1 Powder Synthesis: 26

3.2.2 Hot-Pressed Pellet/Bar: 26

3.3 Results & Discussion: $Mn_{1-x}Zn_xSb_2Se_4$ (x = 0-0.15) 27

3.3.1 Structural Properties of $Mn_{1-x}Zn_xSb_2Se_4$ 27

3.3.2 Thermoelectric Properties of $Mn_{1-x}Zn_xSb_2Se_4$ 36

3.3.3 Magnetic Properties of $Mn_{1-x}Zn_xSb_2Se_4$ 44

3.4 Conclusion & Future Work: $Mn_{1-x}Zn_xSb_2Se_4$ (x = 0-0.15) 50

CHAPTER 4: $Sb_{2-x}Sn_xSe_3$ (x = 0, 0.01, 0.05, 0.1, 0.15, 0.2) Structural Properties and Optical Properties 51

4.1 Introduction: $Sb_{2-x}Sn_xSe_3$ (x = 0, 0.01, 0.05, 0.1, 0.15, 0.2) 51

4.2 Synthesis: $Sb_{2-x}Sn_xSe_3$ (x = 0, 0.01, 0.05, 0.1, 0.15, 0.2) 56

4.3 Results & Discussion: $Sb_{2-x}Sn_xSe_3$ (x = 0, 0.01, 0.05, 0.1, 0.15, 0.2) 57

4.3.1 Structural Properties of $Sb_{2-x}Sn_xSe_3$ 57

4.3.2 Optical Properties of $Sb_{2-x}Sn_xSe_3$ 65

4.4 Conclusion & Future Work: $Sb_{2-x}Sn_xSe_3$ (x = 0, 0.01, 0.05, 0.1, 0.15, 0.2) 69

CHAPTER 5: $Cu_2Zn_{2x}Ti_{(3-2x)/2}Se_4$ (x = 1.5, 1, 0.5, 0) and $Cu_2Mn_3Se_4$ 71

5.1 Introduction: $Cu_2Zn_{2x}Ti_{(3-2x)/2}Se_4$ (x = 1.5, 1, 0.5, 0) and $Cu_2Mn_3Se_4$ 71

5.2 Synthesis: $Cu_2Zn_{2x}Ti_{(3-2x)/2}Se_4$ (x = 1.5, 1, 0.5, 0) and $Cu_2Mn_3Se_4$ 84

5.2.1 Powder Synthesis: 84

5.2.2 Annealing Powder: 85

5.2.3 Hot-Pressed Pellet/Bar: 85

5.2.4 Single-Crystal Synthesis: High-T Annealing 85

5.2.5 Single-Crystal Synthesis: Melt & Slow-Cool 86

5.2.6 Single-Crystal Synthesis: Dual-Zone Furnace 86

5.3 $Cu_2Zn_3Se_4$ (x = 1.5) Single Crystal Synthesis ($Cu_2Zn_3Se_4$), Structural, Optical, and Thermoelectric Properties: 88

5.3.1 Results & Discussion: $Cu_2Zn_3Se_4$ (x = 1.5): 88

5.3.1.1 Single Crystal Synthesis ($Cu_2Zn_3Se_4$) (x = 1.5) 88

5.3.1.2 Structural Properties of $Cu_2Zn_3Se_4$ 89

5.3.1.3 Optical Properties of $Cu_2Zn_3Se_4$ 100

5.3.1.4 Thermoelectric Properties of $Cu_2Zn_3Se_4$ 102

5.3.2 Conclusion & Future Work: $Cu_2Zn_3Se_4$ (x = 1.5): 107

5.4 $Cu_2Zn_2Ti_{0.5}Se_4$ (x = 1) Single Crystal Synthesis ($Cu_{2.75}Zn_{0.625}TiSe_4$), Structural, and Optical Properties: 110

5.4.1 Results & Discussion: $Cu_2Zn_2Ti_{0.5}Se_4$ (x = 1): 110

5.4.1.1 Single Crystal Synthesis ($Cu_{2.75}Zn_{0.625}TiSe_4$) 110

5.4.1.2 Structural Properties of $Cu_2Zn_2Ti_{0.5}Se_4$ 111

5.4.1.3 Optical Properties of $Cu_2Zn_2Ti_{0.5}Se_4$ 119

5.4.2 Conclusion & Future Work: $Cu_2Zn_2Ti_{0.5}Se_4$ (x = 1): 120

5.5 $Cu_2ZnTiSe_4$ (x = 0.5) Single Crystal Synthesis ($Cu_2ZnTiSe_4$), Structural, and Optical Properties: 122

5.5.1 Results & Discussion: $Cu_2ZnTiSe_4$ (x = 0.5): 122

5.5.1.1 Single Crystal Synthesis ($Cu_2ZnTiSe_4$) (x = 0.5) 122

5.5.1.2 Structural Properties of $Cu_2ZnTiSe_4$ 123
5.5.1.3 Optical Properties of $Cu_2ZnTiSe_4$ 132
5.5.2 Conclusion & Future Work: $Cu_2ZnTiSe_4$ (x = 0.5): 134
5.6 $Cu_2Ti_{1.5}Se_4$ (x = 0) Single Crystal Synthesis ($Cu_3Ti_{1.25}Se_4$), Structural, and Optical Properties: 136
5.6.1 Results & Discussion: $Cu_2Ti_{1.5}Se_4$ (x = 0): 136
5.6.1.1 Single Crystal Synthesis ($Cu_3Ti_{1.25}Se_4$) 136
5.6.1.2 Structural Properties of $Cu_2Ti_{1.5}Se_4$ 138
5.6.1.3 Optical Properties of $Cu_2Ti_{1.5}Se_4$ 146
5.6.2 Conclusion & Future Work: $Cu_2Ti_{1.5}Se_4$ (x = 0): 148
5.7 $Cu_2Mn_3Se_4$ Single Crystal Synthesis ($Cu_2Mn_3Se_4$), Structural Properties, Optical Properties, and Predicted Magnetic Moment 150
5.7.1 Results & Discussion: $Cu_2Mn_3Se_4$: 150
5.7.1.1 Single Crystal Synthesis ($Cu_2Mn_3Se_4$) 150
5.7.1.2 Structural Properties of $Cu_2Mn_3Se_4$ 151
5.7.1.3 Optical Properties of $Cu_2Mn_3Se_4$ 161
5.7.1.4 Predicted Magnetic Moment of $Cu_2Mn_3Se_4$ 163
5.7.2 Conclusion & Future Work: $Cu_2Mn_3Se_4$: 165
CHAPTER 6: Conclusions and Future Work on $Cu_2Zn_{2x}Ti_{(3-2x)/2}Se_4$ (x = 1.5, 1, 0.5, 0) and $Cu_2Mn_3Se_4$ 168
APPENDICES 170
REFERENCES 216

List of Tables

Table 3.3.1: Extracted information from Rietveld refinement of the main phase. From refinement, lattice parameters were discovered, and the volume of the monoclinic unit cell was calculated using **Equation 3.3-1**. The best χ^2 fit for each composition was also listed. 31

Table 3.3.2: Electronic bandgap (E_g) and activation energy (E_a) at various zinc content (x). 38

Table 3.3.3: Table of corrected Lorenz # vs. temperature for x = 0.01-0.04. Due to the low σ of the samples, Fermi-corrected Lorenz # calculations were applied. For x = 0.01-0.04, the corrected L was found to be ~40% lower than the metallic value (2.44 x 10^{-8} W-Ω/K^2)..... 41

Table 3.3.4: Parameters extracted from magnetic susceptibility data, such as Néel temperature (T_N), effective magnetic moment (μ_{eff}), Curie constant (C), and Weiss constant (θ).[28] 47

Table 4.3.1: Lattice parameter and χ^2 values extracted from Rietveld refinement. Also noted was the lattice parameters of the Sb_2Se_3 Pnma (ICSD #30973[30]) phase, denoted by the asterisk..... 64

Table 4.3.2: Direct optical bandgap (E_g) and maximum absorbed wavelength (λ_{Max}) vs. Sn content (x). 68

Table 5.1.1: Optical Bandgap (E_g) and record efficiency for various solar absorber materials. . 71

Table 5.1.2: Occupational Safety and Health Administration (OSHA) permissible exposure limit (PEL) of various relevant elements for solar absorber materials. The PEL values were referenced from the Center for Disease Control and Prevention (CDC) database on the National Institute for Occupational Safety and Health (NIOSH). On the NIOSH database, elemental PEL values were not reported for the following: S, Ti, Zn, and Ga. In this case, the proper Sigma-Aldrich (SA) materials safety data sheet (MSDS) was referenced. Note: CAS stands for Chemical Abstracts Service. For the case of elements with a hyphen, this means that they are relatively safe and do not have specific OSHA PEL values reported. 75

Table 5.1.3: To estimate the relative safety of the absorber material, the PEL of each absorber element was summed together in the compound. CIGS was noted to have a low PEL, so each absorber compound was compared to CIGS. Also listed below are the thesis compounds 3.3-3.7 for comparison purposes. 76

Table 5.1.4: Generic M_ySe_4 formula for solar cell materials and dissertation compounds, where M is every metal and y are the total metal count in the compound. For the cases where single crystal growth formed a different stoichiometry than expected, the single crystal compound M_ySe_4 formula was also reported. 81

Table 5.1.5: Number of tetrahedral interstitial vacancies in each compound. 82

Table 5.1.6: Percent of tetrahedral vacancies in each compound. 83

Table 5.2.1: $Cu_2Zn_{2x}Ti_{(3-2x)/2}Se_4$ (x = 1.5, 1, 0.5, 0) and $Cu_2Mn_3Se_4$ synthesis methods. Refer to the proper sections for the procedures used. 84

Table 5.3.1: Selected crystallographic data for $Cu_2Zn_3Se_4$. 89

Table 5.3.2: $Cu_2Zn_3Se_4$ Small Cell atomic coordinates, equivalent isotropic displacement parameters $U_{eq.}$, and occupancies for all atoms. *Note: only U_{11} had values, so $U_{eq.} = U_{11}$ here. 90

Table 5.3.3: $Cu_2Zn_3Se_4$ Large Cell atomic coordinates, equivalent isotropic displacement parameters $U_{eq.}$, and occupancies for all atoms. 90

Table 5.3.4: $Cu_2Zn_3Se_4$ Small Cell selected inter-atomic bond distances (in Å). Small cell operators for generating equivalent atoms: (i) x, y+1/2, z+1/2; (ii) x+1/2, y, z+1/2; (iii) x+1/2, y+1/2, z; (iv) x, y-1/2, z-1/2; (v) x-1/2, y, z-1/2; (vi) x-1/2, y-1/2, z; (vii) -x, -y+1, -z+1; (viii) -x, -y+3/2, -z+3/2; (ix) -x+1, -y+3/2, -z+3/2; (x) -x+1/2, -y+1, -z+3/2; (xi) -x+1/2, -y+2, -z+3/2; (xii) -x+1/2, -y+3/2, -z+1; (xiii) -x+1/2, -y+3/2, -z+2. 94

Table 5.3.5: $Cu_2Zn_3Se_4$ Large Cell selected inter-atomic bond distances (in Å). Large cell operators for generating equivalent atoms: (i) -x, 1-y, 1-z; (ii) -x, y, z; (iii) -x, 1-y, z; (iv) x, y, 1-z; (v) -x, y, 1-z; (vi) x, 1-y, z; (vii) x, 1-y, 1-z; (viii) 1-x, y, z; (ix) 1-x, 1-y, z; (x) -0.5+z, -0.5+x, 1-y; (xi) -0.5+z, 1.5-x, 1-y; (xii) 0.5-x, 1-y, 1.5-z; (xiii) -1+x, y, z; (xiv) -1+x, 1-y, z; (xv) 1.5-y, -0.5+z, 1-x; (xvi) z, 0.5-x, 1.5-y; (xvii) 0.5+y, -0.5+z, x; (xviii) z, -0.5+x, 0.5+y; (xix) 1-z, 0.5-x, 1.5-y; (xx) 0.5-y, 1.5-z, 1-x; (xxi) x, y, 2-z; (xxii) 1-z, 1.5-x, 0.5+y; (xxiii) 0.5-y, 1.5-z, x; (xxiv) 0.5+y, 1-z, 0.5+x; (xxv) 1+x, y, z; (xxvi) 2-x, y, z; (xxvii) x, 0.5-y, 1.5-z; (xxviii) 1.5-x, 0.5-y, z; (xxix) 1.5-x, y, 1.5-z; (xxx) 0.5+x, -0.5+y, z; (xxxi) z, x, y; (xxxii) y, -0.5+z, 0.5+x; (xxxiii) -0.5+z, 0.5+x, y; (xxxiv) -0.5+y, z, 0.5+x; (xxxv) 0.5-y, z, 1.5-x; (xxxvi) -0.5+x, 1-y, 1.5-z; (xxxvii) -0.5+x, 0.5+y, z. 94

Table 5.4.1: Selected crystallographic data for $Cu_{2.75}Zn_{0.625}TiSe_4$. 111

Table 5.4.2: $Cu_{2.75}Zn_{0.625}TiSe_4$ atomic coordinates, equivalent isotropic displacement parameters $U_{eq.}$, and occupancies for all atoms. 112

Table 5.4.3: $Cu_{2.75}Zn_{0.625}TiSe_4$ selected inter-atomic bond distances (in Å). Operators for generating equivalent atoms: (i) y, z, x; (ii) z, x, y; (iii) -x, -y, z; (iv) -y, x, 0.5-z; (v) y, -x, 0.5-z; (vi) y, x, 0.5+z; (vii) x, -y, -z; (viii) -x, y, -z; (ix) y, -z, -x; (x) -z, -x, y; (xi) x, 0.5-y, 0.5-z; (xii) 0.5-x, 0.5-y, z; (xiii) 0.5-x, y, 0.5-z. 115

Table 5.5.1: Selected crystallographic data for $Cu_2ZnTiSe_4$. 123

Table 5.5.2: $Cu_2ZnTiSe_4$ Small Cell atomic coordinates, equivalent isotropic displacement parameters $U_{eq.}$, and occupancies for all atoms. 124

Table 5.5.3: $Cu_2ZnTiSe_4$ Large Cell atomic coordinates, equivalent isotropic displacement parameters $U_{eq.}$, and occupancies for all atoms. 124

Table 5.5.4: $Cu_2ZnTiSe_4$ Small Cell selected inter-atomic bond distances (in Å). Small cell operators for generating equivalent atoms: i) 0.5+x, 0.5+y, z; (ii) x, 0.5+y, 0.5+z; (iii) 0.5+x, y, 0.5+z; (iv) x, 0.5+y, -0.5+z; (v) 0.5+x, y, -0.5+z; (vi) -0.5+x, -0.5+y, z; (vii) -0.5+x, y, -0.5+z; (viii) x, -0.5+y, -0.5+z; (ix) x, y, -1+z; (x) -0.5+x, y, 0.5+z; (xi) x, -0.5+y, 0.5+z; (xii) x, y, 1+z. 128

Table 5.5.5: $Cu_2ZnTiSe_4$ Large Cell selected inter-atomic bond distances (in Å). Large cell operators for generating equivalent atoms: (i) 0.25-z, 0.25-x, 0.25-y; (ii) 0.25-x, 0.25-y, 0.25-z; (iii) x, 0.5+y, 0.5+z; (iv) 0.75-x, 0.25+y, 1.75+z; (v) -0.5-z, -1-x, 1.5+y; (vi) 1.25-x, 1.75-z, 1.75-y; (vii) 1.25-x, 1.75+y, 1.75+z; (viii) 0.75-y, -0.75+x, 0.75+z; (ix) 0.25-z, 1.75+y, 0.75+x; (x) 0, 0, 0; (xi) x, 1+y, z; (xii) 0, 0, 0; (xiii) y, z, x; (xiv) 0, 0, 0; (xv) x, 0.5+y, -0.5+z; (xvi) -0.5+z, 0.5+x, y; (xvii) 0, 0, 0; (xviii) 0, 0, 0; (xix) y, 0.5-x, 1.5-z; (xx) 0.25-y, 0.25-z, 1.25-x; (xxi) 0, 0, 0; (xxii) -0.75-y, 0.75-x, 0.75-z; (xxiii) 0.5+x, -z, 1.5-y; (xxiv) 0.25+z, 0.25+x, 0.25-y; (xxv) 0, 0, 0; (xxvi) 0.5+z, 1-y, 0.5-x; (xxvii) x, -1+y, z; (xxviii) -y, -0.5-x, -0.5+z; (xxix) x, -0.5+y, -0.5+z; (xxx) -0.5+z, -0.5+x, y; (xxxi) 0, 0, 0. 128

Table 5.6.1: Selected crystallographic data for $Cu_3Ti_{1.25}Se_4$. 138

Table 5.6.2: $Cu_3Ti_{1.25}Se_4$ atomic coordinates, equivalent isotropic displacement parameters $U_{eq.}$, and occupancies for all atoms. 139

Table 5.6.3: $Cu_3Ti_{1.25}Se_4$ selected inter-atomic bond distances (in Å). Operators for generating equivalent atoms: (i) 0.5-x, 0.5-y, z; (ii) 0.5-x, y, 0.5-z; (iii) x, 0.5-y, 0.5-z; (iv) z, x, y; (v) 0.5-z, 0.5-x, y; (vi) y, z, x; (vii) y, 0.5-z, 0.5-x; (viii) x, 0.5-y, -0.5-z; (ix) 0.5-x, y, -0.5-z; (x) 0.5+z, x, -0.5+y; (xi) -z, 0.5-x, -0.5+y; (xii) y, 0.5+z, -0.5+x; (xiii) y, -z, -x; (xiv) -x, y, -z; (xv) x, 1-y, -z; (xvi) -x, 1-y, z; (xvii) 1-x, 1-y, z; (xviii) 1-x, y, -z. 141

Table 5.7.1: Selected crystallographic data for $Cu_2Mn_3Se_4$..... 151

Table 5.7.2: $Cu_2Mn_3Se_4$ Small Cell atomic coordinates, equivalent isotropic displacement parameters $U_{eq.}$, and occupancies for all atoms. 152

Table 5.7.3: $Cu_2Mn_3Se_4$ Large Cell atomic coordinates, equivalent isotropic displacement parameters $U_{eq.}$, and occupancies for all atoms. 152

Table 5.7.4: $Cu_2Mn_3Se_4$ Small Cell selected inter-atomic bond distances (in Å). Small cell operators for generating equivalent atoms: (i) x, 0.5+y, 0.5+z; (ii) -0.5+x, 0.5+y, z; (iii) -0.5+x, y, 0.5+z; (iv) -x, 0.5-y, 0.5-z; (v) 0.5-x, 1-y, 0.5-z; (vi) 0.5-x, 0.5-y, -z; (vii) 0.5-x, 0.5-y, 1-z; (viii) 1-x, 0.5-y, 0.5-z; (ix) 0.5-x, -y, 0.5-z; (x) x, -0.5+y, -0.5+z; (xi) 0.5+x, -0.5+y, z; (xii) 1-x, -y, -z; (xiii) 0.5+x, y, -0.5+z. 156

Table 5.7.5: $Cu_2Mn_3Se_4$ Large Cell selected inter-atomic bond distances (in Å). Large cell operators for generating equivalent atoms: (i) 0, 0z, 0; (ii) -0.5+y, 0.5+z, -1+x; (iii) y, 1.5+z, 0.5+x; (iv) -1+x, y, z; (v) 1+y, 1-z, -x; (vi) z, -0.5+x, -0.5+y; (vii) y, 1-z, -x; (viii) 0, 0, 0; (ix) 1.25-y, 1.25+x, 0.25+z; (x) -0.5-y, -1-x, 0.5+z; (xi) x, 1.5+z, 0.5+y; (xii) 0, 0, 0; (xiii) 0, 0, 0;

(xiv) 0.25+x, 1.25-z, 0.25+y; (xv) 1.25+z, 0.25+y, 0.25-x; (xvi) y, 0.5+z, -0.5+x; (xvii) 0.5+z, x, -0.5+y; (xviii) 0.25-y, 1.25+x, 0.25+z; (xix) 0.25+z, 0.25+y, 0.25-x; (xx) 0.75+z, 0.25+x, 1.75-y; (xxi) 0, 0, 0; (xxii) 1.25+x, 1.25-z, 0.25+y; (xxiii) 1+x, y, z; (xxiv) 0, 0, 0; (xxv) 1+y, 1.5+z, 0.5+x; (xxvi) 0.25-z, 1.25-y, -0.75-x; (xxvii) 1-y, -0.5+z, -0.5-x. 156

Table 6.1.1: $Cu_2Zn_{2x}Ti_{(3-2x)/2}Se_4$ (x = 1.5, 1, 0.5, 0) E_g, λ_{Max}, and absorbed regions of the solar spectrum. 168

Table A.1: Extracted information from Rietveld refinement of the secondary phase, ZnSe. $\chi 2$ was noted before and after secondary phase refinement to depict the moderate improvement in the quality of fit upon secondary refinement. The lattice parameter of ZnSe for each composition was determined and compared to ICSD reference values. *ICSD Reference #77091[29] (ZnSe, F-43m). 172

Table A.2: XPS energy values, cross-referenced with the corresponding elemental energy windows. 172

Table A.3: Electrical conductivity of typical insulators, semiconductors, and metals. As a reference, $Mn_{1-x}Zn_xSb_2Se_4$ $\sigma \sim 10^{-1}$-10^2 S/m.[121] 175

Table C.1: $Cu_2Zn_3Se_4$ small cell anisotropic displacement parameters, in units of $Å^2$ x 10^{-4}... 187

Table C.2: $Cu_2Zn_3Se_4$ large cell anisotropic displacement parameters in units of $Å^2$ x 10^{-4}..... 187

Table C.3: $Cu_2Zn_3Se_4$ small cell selected inter-atomic bond angles (in °). Small cell operators for generating equivalent atoms: (i) x, y+1/2, z+1/2; (ii) x+1/2, y, z+1/2; (iii) x+1/2, y+1/2, z; (iv) x, y-1/2, z-1/2; (v) x-1/2, y, z-1/2; (vi) x-1/2, y-1/2, z; (vii) -x, -y+1, -z+1; (viii) -x, -y+3/2, -z+3/2; (ix) -x+1, -y+3/2, -z+3/2; (x) -x+1/2, -y+1, -z+3/2; (xi) -x+1/2, -y+2, -z+3/2; (xii) -x+1/2, -y+3/2, -z+1; (xiii) -x+1/2, -y+3/2, -z+2..... 188

Table C.4: $Cu_2Zn_3Se_4$ large cell selected inter-atomic bond angles (in °). Large cell operators for generating equivalent atoms: (i) -x, 1-y, 1-z; (ii) -x, y, z; (iii) -x, 1-y, z; (iv) x, y, 1-z; (v) -x, y, 1-z; (vi) x, 1-y, z; (vii) x, 1-y, 1-z; (viii) 1-x, y, z; (ix) 1-x, 1-y, z; (x) -0.5+z, -0.5+x, 1-y; (xi) -0.5+z, 1.5-x, 1-y; (xii) 0.5-x, 1-y, 1.5-z; (xiii) -1+x, y, z; (xiv) -1+x, 1-y, z; (xv) 1.5-y, -0.5+z, 1-x; (xvi) z, 0.5-x, 1.5-y; (xvii) 0.5+y, -0.5+z, x; (xviii) z, -0.5+x, 0.5+y; (xix) 1-z, 0.5-x, 1.5-y; (xx) 0.5-y, 1.5-z, 1-x; (xxi) x, y, 2-z; (xxii) 1-z, 1.5-x, 0.5+y; (xxiii) 0.5-y, 1.5-z, x; (xxiv) 0.5+y, 1-z, 0.5+x; (xxv) 1+x, y, z; (xxvi) 2-x, y, z; (xxvii) x, 0.5-y, 1.5-z; (xxviii) 1.5-x, 0.5-y, z; (xxix) 1.5-x, y, 1.5-z; (xxx) 0.5+x, -0.5+y, z; (xxxi) z, x, y; (xxxii) y, -0.5+z, 0.5+x; (xxxiii) -0.5+z, 0.5+x, y; (xxxiv) -0.5+y, z, 0.5+x; (xxxv) 0.5-y, z, 1.5-x; (xxxvi) -0.5+x, 1-y, 1.5-z; (xxxvii) -0.5+x, 0.5+y, z. 189

Table C.5: XPS energy values, cross-referenced with the corresponding elemental energy windows.[31] 191

Table D.1: $Cu_{2.75}Zn_{0.625}TiSe_4$ anisotropic displacement parameters, in units of $Å^2$ x 10^{-4}..... 194

Table D.2: $Cu_{2.75}Zn_{0.625}TiSe_4$ selected inter-atomic bond angles (in °). Operators for generating equivalent atoms: (i) y, z, x; (ii) z, x, y; (iii) -x, -y, z; (iv) -y, x, 0.5-z; (v) y, -x, 0.5-z; (vi) y, x,

0.5+z; (vii) x, -y, -z; (viii) -x, y, -z; (ix) y, -z, -x; (x) -z, -x, y; (xi) x, 0.5-y, 0.5-z; (xii) 0.5-x, 0.5-y, z; (xiii) 0.5-x, y, 0.5-z. 194

Table E.1: $Cu_2ZnTiSe_4$ small cell anisotropic displacement parameters, in units of $Å^2$ x 10^{-4}. 195

Table E.2: $Cu_2ZnTiSe_4$ large cell anisotropic displacement parameters, in units of $Å^2$ x 10^{-4}.. 195

Table E.3: $Cu_2ZnTiSe_4$ small cell selected inter-atomic bond angles (in °). Small cell operators for generating equivalent atoms: i) 0.5+x, 0.5+y, z; (ii) x, 0.5+y, 0.5+z; (iii) 0.5+x, y, 0.5+z; (iv) x, 0.5+y, -0.5+z; (v) 0.5+x, y, -0.5+z; (vi) -0.5+x, -0.5+y, z; (vii) -0.5+x, y, -0.5+z; (viii) x, -0.5+y, -0.5+z; (ix) x, y, -1+z; (x) -0.5+x, y, 0.5+z; (xi) x, -0.5+y, 0.5+z; (xii) x, y, 1+z..... 196

Table E.4: $Cu_2ZnTiSe_4$ large cell selected inter-atomic bond angles (in °). Large cell operators for generating equivalent atoms: (i) 0.25-z, 0.25-x, 0.25-y; (ii) 0.25-x, 0.25-y, 0.25-z; (iii) x, 0.5+y, 0.5+z; (iv) 0.75-x, 0.25+y, 1.75+z; (v) -0.5-z, -1-x, 1.5+y; (vi) 1.25-x, 1.75-z, 1.75-y; (vii) 1.25-x, 1.75+y, 1.75+z; (viii) 0.75-y, -0.75+x, 0.75+z; (ix) 0.25-z, 1.75+y, 0.75+x; (x) 0, 0, 0; (xi) x, 1+y, z; (xii) 0, 0, 0; (xiii) y, z, x; (xiv) 0, 0, 0; (xv) x, 0.5+y, -0.5+z; (xvi) -0.5+z, 0.5+x, y; (xvii) 0, 0, 0; (xviii) 0, 0, 0; (xix) y, 0.5-x, 1.5-z; (xx) 0.25-y, 0.25-z, 1.25-x; (xxi) 0, 0, 0; (xxii) -0.75-y, 0.75-x, 0.75-z; (xxiii) 0.5+x, -z, 1.5-y; (xxiv) 0.25+z, 0.25+x, 0.25-y; (xxv) 0, 0, 0; (xxvi) 0.5+z, 1-y, 0.5-x; (xxvii) x, -1+y, z; (xxviii) -y, -0.5-x, -0.5+z; (xxix) x, -0.5+y, -0.5+z; (xxx) -0.5+z, -0.5+x, y; (xxxi) 0, 0, 0. 197

Table F.1: $Cu_3Ti_{1.25}Se_4$ anisotropic displacement parameters, in units of $Å^2$ x 10^{-4}. 200

Table F.2: $Cu_3Ti_{1.25}Se_4$ selected inter-atomic bond angles (in °). Operators for generating equivalent atoms: (i) 0.5-x, 0.5-y, z; (ii) 0.5-x, y, 0.5-z; (iii) x, 0.5-y, 0.5-z; (iv) z, x, y; (v) 0.5-z, 0.5-x, y; (vi) y, z, x; (vii) y, 0.5-z, 0.5-x; (viii) x, 0.5-y, -0.5-z; (ix) 0.5-x, y, -0.5-z; (x) 0.5+z, x, -0.5+y; (xi) -z, 0.5-x, -0.5+y; (xii) y, 0.5+z, -0.5+x; (xiii) y, -z, -x; (xiv) -x, y, -z; (xv) x, 1-y, -z; (xvi) -x, 1-y, z; (xvii) 1-x, 1-y, z; (xviii) 1-x, y, -z. 200

Table G.1: $Cu_2Mn_3Se_4$ small cell anisotropic displacement parameters, in units of $Å^2$ x 10^{-4}.. 203

Table G.2: $Cu_2Mn_3Se_4$ large cell anisotropic displacement parameters, in units of $Å^2$ x 10^{-4}. . 203

Table G.3: $Cu_2Mn_3Se_4$ small cell selected inter-atomic bond angles (in °). Small cell operators for generating equivalent atoms: (i) x, 0.5+y, 0.5+z; (ii) -0.5+x, 0.5+y, z; (iii) -0.5+x, y, 0.5+z; (iv) -x, 0.5-y, 0.5-z; (v) 0.5-x, 1-y, 0.5-z; (vi) 0.5-x, 0.5-y, -z; (vii) 0.5-x, 0.5-y, 1-z; (viii) 1-x, 0.5-y, 0.5-z; (ix) 0.5-x, -y, 0.5-z; (x) x, -0.5+y, -0.5+z; (xi) 0.5+x, -0.5+y, z; (xii) 1-x, -y, -z; (xiii) 0.5+x, y, -0.5+z. 203

Table G.4: $Cu_2Mn_3Se_4$ large cell selected inter-atomic bond angles (in °). Large cell operators for generating equivalent atoms: (i) 0, 0z, 0; (ii) -0.5+y, 0.5+z, -1+x; (iii) y, 1.5+z, 0.5+x; (iv) -1+x, y, z; (v) 1+y, 1-z, -x; (vi) z, -0.5+x, -0.5+y; (vii) y, 1-z, -x; (viii) 0, 0, 0; (ix) 1.25-y, 1.25+x, 0.25+z; (x) -0.5-y, -1-x, 0.5+z; (xi) x, 1.5+z, 0.5+y; (xii) 0, 0, 0; (xiii) 0, 0, 0; (xiv) 0.25+x, 1.25-z, 0.25+y; (xv) 1.25+z, 0.25+y, 0.25-x; (xvi) y, 0.5+z, -0.5+x; (xvii) 0.5+z, x, -0.5+y; (xviii) 0.25-y, 1.25+x, 0.25+z; (xix) 0.25+z, 0.25+y, 0.25-x; (xx) 0.75+z, 0.25+x, 1.75-y; (xxi) 0, 0, 0; (xxii) 1.25+x, 1.25-z, 0.25+y; (xxiii) 1+x, y, z; (xxiv) 0, 0, 0; (xxv) 1+y, 1.5+z, 0.5+x; (xxvi) 0.25-z, 1.25-y, -0.75-x; (xxvii) 1-y, -0.5+z, -0.5-x. 204

List of Figures

Figure 1.1.1: Moore's Law, depicting the transistor count doubling roughly every year. Image was adapted from Moore's work titled Cramming more components onto integrated circuits.[2] ... 1

Figure 1.1.2: Sources of computing performance over the years. Notice that by 2020-2030, the # of transistors, thread performance, clock frequency, power, and core count are all predicted to plateau. Image was adapted from Shalf's article on The future of computing beyond Moore's Law.[4] 2

Figure 1.1.3: $Ga_{1-x}Mn_xAs$ III-V dilute magnetic semiconductor (DMS) crystal lattice. Image was adapted from Wang *et al*.[14] 4

Figure 1.3.1: a) Climate change model where the green line fixes greenhouse gas concentrations at the 2005 level; the dark red curve is when emissions are halved by 2050, i.e. the mitigation scenario.[21] **b)** Similar to the left model, but with the removal of aerosol cooling (invisible hand); this focuses the model on long-lasting greenhouse gases in the troposphere.[21] Figure was adapted from Schellnhuber.[21] 5

Figure 1.3.2: Illustration of a p-n junction solar cell and the photovoltaic effect. 6

Figure 1.3.3: Schematic of a photon with $E \geq Eg$ exciting an electron from valence band to conduction band (CB). Once the electron reaches the CB, it is a free electron, capable to flow through the external circuit. During the electron excitation, a hole is left behind in the valence band (VB)..... 7

Figure 1.3.4: Solar spectrum vs. wavelength. Image was adapted from Cleveland and Morris' Handbook of Energy.[27] 8

Figure 2.2.1: Left: Powder in an Inconel holder, mounted in the high-T XRD stage by Inconel clips. **Right:** High-T XRD stage mounted in place, with graphite dome over the sample. The black hose pictured has compressed air to regulate temperature and the silver hose is connected to the temperature controller. 16

Figure 3.1.1: $Fe_{0.87}Sn_{0.13}Sb_2Se_4$ crystal lattice, projected along the b-axis. Note the distinct magnetic and semiconducting sublattices. Image was adapted from Djieutedjeu *et al*.[39] 21

Figure 3.1.2: Predicting the Mn^{2+} [Ar]$3d^5$ theoretical magnetic moment in an octahedral Se^{2-} ligand geometry using Hund's rules and crystal-field theory. 22

Figure 3.1.3: $Fe_{1-x}Sn_xBi_2Se_4$ changes in the magnetic lattice with increasing Sn content. Note that for the case of b and c, Sn preferentially substitutes at the M1 and M2 sites, eventually replacing the Fe magnetic moment completely, rendering the M1 and M2 sites nonmagnetic. Image was adapted from Lopez *et al*.[32] 23

Figure 3.3.1: Powder X-ray diffraction of complete $Mn_{1-x}Zn_xSb_2Se_4$ series, compared to ICSD Reference #421940[28] ($MnSb_2Se_4$, C12/m1). Binary impurity phases of ZnSe (ICSD #77091[29], F-43m) and Sb_2Se_3 (ISCD #16680[52], Pbnm) are noted by the yellow and green asterisks, respectively. 28

Figure 3.3.2: Powder XRD Rietveld refinement fit for $Mn_{0.95}Zn_{0.05}Sb_2Se_4$. In the figure, the red curve is the experimental pattern, the black line is the fitted pattern, the green tick marks correspond to the peak positions, and the blue curve is the difference pattern between experimental and fitted patterns. The quality of fit was $\chi^2 = 0.824$. 29

Figure 3.3.3: Lattice parameters vs. zinc content. The inset of the plot highlights the overall downward trend in the c-axis with increasing zinc content. 30

Figure 3.3.4: Differential scanning calorimetry (DSC) vs. temperature for various compositions. A small Se melting peak was observed for all samples at ~488 K. T_m was found to be between 950-953 K, decreasing slightly from low to high zinc content. 33

Figure 3.3.5: XPS counts per second vs. binding energy for **(a)** Mn; **(b)** Zn; **(c)** Sb; **(d)** Se. 35

Figure 3.3.6: Temperature-dependent thermoelectric properties: **(a)** electrical conductivity (σ) with an inset zooming in from 300-450 K; **(b)** thermopower (S); **(c)** total thermal conductivity (κ_T); **(d)** figure of merit (zT). 36

Figure 3.3.7: (a) $Mn_{0.99}Zn_{0.01}Sb_2Se_4$ (x = 0.01) electrical conductivity Arrhenius plot. The figure was divided into the intrinsic region, saturation plateau, and extrinsic region depending on temperature; **(b)** Intrinsic region Arrhenius plot, utilized to extract electronic bandgap, E_g; **(c)** Extrinsic region Arrhenius plot, employed to obtain activation energy, E_a. 38

Figure 3.3.8: Electronic bandgap (E_g) and activation energy (E_a) at different Zn content, gathered by fitting temperature-dependent electrical conductivity data using the Arrhenius relationship. 39

Figure 3.3.9: Due to the low electrical conductivity of the samples, Fermi-corrected Lorenz # calculations were applied. For x = 0.01-0.04, the corrected L was found to be ~40% lower than the metallic value (2.44 x 10-^{8} W-Ω/K^2). Plot of corrected Lorenz # vs. temperature. 42

Figure 3.3.10: (a) Total thermal conductivity vs. temperature for all samples; **(b)** Electronic thermal conductivity (κ_e) and **(c)** Lattice thermal conductivity (κ_L) contributions, utilizing Wiedemann-Franz Law analysis. It was determined that κ_e contributed $\leq$ 0.19% to κ_T. 43

Figure 3.3.11: $Mn_{0.99}Zn_{0.01}Sb_2Se_4$ (x = 0.01) low-T magnetic susceptibility (χ) under **(a)** zero field-cooled and **(b)** field-cooled (FC) conditions; low-T inverse magnetic susceptibility (χ^{-1}) under **(c)** zero field-cooled and **(d)** field-cooled (FC) conditions. Also noted are important

magnetic parameters extracted using Curie-Weiss Law fitting from ~170-300 K and Langevin theory of paramagnetism calculations. Crystal field theory and Hund's rules was used to calculate the theoretical magnetic moment, $\mu_{theo.}$ 45

Figure 3.3.12: Effective magnetic moment and Weiss constant vs. zinc content..... 46

Figure 3.3.13: Proposed $Mn_{1-x}Zn_xSb_2Se_4$ magnetic lattice. For both images, each atomic site was coupled antiparallel to display the antiferromagnetic ordering nature of the compound. **Top:** x = 0, before any Zn is substituted; note that $\mu_{Net} = 0$ here. This case is an antiferromagnetic lattice. **Bottom:** Upon Zn substitution, the zinc preferentially substitutes first at the M1 and M2 sites. Zn^{2+} ([Ar]$3d^{10}$) has no unpaired e^- and thus does not contribute to magnetism. Since the M3 site has the most Mn^{2+} ([Ar]$3d^5$), a small net magnetic moment is observed in this case-i.e., $\mu_{Net} \neq 0$. The M1 and M2 substitution generates a ferrimagnetic lattice. This mechanism explains the increase in μ_{Net} with increasing Zn. 49

Figure 4.1.1: $FeSb_{2-x}Sn_xSe_4$ (x = 0.15) temperature-induced Lifshitz transition, going from p-type to n-type at low-T. Here, Sn^{2+} is substituting for Sb^{3+}, causing local excess negative charge. As such, some Sb^{3+} will oxidize to Sb^{5+} to charge-compensate, dumping electrons into the system. Image was adapted from Djieutedjeu *et al*.[38]..... 51

Figure 4.1.2: Sb_2Se_3 Pnma (ICSD #30973[30]) crystal lattice projected along the b-direction. Along the c-axis, 1-D ribbons of Se-Sb-Se are seen. Image was adapted from Mavlonov *et al*.[58] 52

Figure 4.1.3: Sb-Se square pyramidal polyhedron projected along the c-direction rotated. The $5s^2$ electron lone pair is also shown. [58] 53

Figure 4.1.4: SEM cross-sectional image of the Sb_2Se_3 nanorod array along the [001] direction, grown on a Mo substrate. The record Sb_2Se_3 cell efficiency of 9.2% was recorded using an absorber layer of over 1000 nm and a device architecture of ZnO:Al/ZnO/CdS/TiO_2/Sb_2Se_3 nanorod arrays/$MoSe_2$/Mo. Image was adapted from Li *et al*.[65] 54

Figure 4.1.5: Solar-driven water splitting photoelectrochemical cell. Image adapted from Li *et al*.[72]..... 55

Figure 4.3.1: $Sb_{2-x}Sn_xSe_3$ (x = 0-0.2) powder x-ray diffraction (PXRD). The plots were compared to the ICSD reference Sb_2Se_3 Pnma (#30973[30]), noted by the blue star..... 57

Figure 4.3.2: Differential scanning calorimetry (DSC) of the $Sb_{2-x}Sn_xSe_3$ series upon heating. 58

Figure 4.3.3: Melting point vs. tin content for the $Sb_{2-x}Sn_xSe_3$ series. With increasing tin content, the melting point (MP) was found to decrease from 887-857 K. The trend is roughly linear until x = 0.1-where the secondary phase starts forming..... 59

Figure 4.3.4: Differential scanning calorimetry (DSC) of the $Sb_{2-x}Sn_xSe_3$ series upon cooling. 60

Figure 4.3.5: Recrystallization temperature vs. tin content. For x = 0-0.1, the recrystallization temperature was seen to linearly increase from 777-791 K. For x = 0.1-0.2 (corresponding to secondary phase formation), the trend was more inconsistent. 61

Figure 4.3.6: Powder XRD Rietveld refinement fit for $Sb_{1.99}Sn_{0.01}Se_3$. In the figure, the red curve is the experimental pattern, the black line is the fitted pattern, the green tick marks correspond to the peak positions, and the blue curve is the difference pattern between experimental and fitted patterns. 62

Figure 4.3.7: Powder XRD Rietveld refinement fit for $Sb_{1.99}Sn_{0.01}Se_3$, zoomed in between 20-50°. 62

Figure 4.3.8: Lattice parameters vs. tin content, extracted from Rietveld refinement. The relevant Sb_2Se_3 Pnma (ICSD #30973[30]) phase lattice parameters (a, b, c) were also noted by the filled red circle, blue square, and green diamond, respectively. 63

Figure 4.3.9: (Left): UV-Vis-NIR diffuse reflectance Tauc plot analysis. The Kubelka-Munk function F(R) was used to transform the reflectance data to absorbance. Plot of F(R) vs. wavelength. **(Right):** Plot of $[F(R)*h\nu]^{1/r}$ vs. energy; r = ½ was chosen here to signify a direct, allowed transition (direct bandgap). To determine the direct optical bandgap (E_g) for each x value, an absorption edge tangent line was extrapolated to the x-axis; the intercept with the x-axis corresponds to E_g. 65

Figure 4.3.10: Direct optical bandgap vs. Sn content. For x = 0-0.1, E_g was seen to linearly decrease with increasing Sn. For x = 0.1-0.2 the trend becomes inconsistent-this correlates to the addition of the secondary phase. 68

Figure 5.1.1: Periodic table of the elements. Typical metals and anions for solar applications and those synthesized in this work were boxed in black and red, respectively. Image was adapted from PT.com. 72

Figure 5.1.2: Top: Elemental abundance for atomic numbers 1-48. **Bottom:** Elemental abundance for atomic numbers 49-93. The relevant elements for Si, CZTS, CIGS, CdTe, and the compounds used in this thesis were highlighted with a box around the element-green for a metal, and red for an anion. Images were adapted from Fleischer's work on the abundance of elements in the Earth's crust.[97] 73

Figure 5.1.3: Crustal abundance and price of various elements used in CZTS, CIGS, and CdTe. Relevant elements not depicted: Ti, Mn, and Si. According to the U.S. 2010 geological survey[98], these elements are priced at the following: Ti (sponge-porous, ~$10.7/kg); Mn, (50% ore, ~$0.00855/kg); Si (metal, ~$3.1/kg).[98] Bar graphs for Ti, Mn, and Si were manually added to the plot accordingly. Image was adapted from Das *et al*.[99] 74

Figure 5.1.4: a) $CuInSe_2$ chalcopyrite crystal structure. **b)** Kesterite $Cu_2ZnSn(S, Se)_4$ (CZTS) crystal structure. **c)** Stannite $Cu_2ZnSn(S, Se)_4$ (CZTS) crystal structure. Image was adapted from Das *et al*.[99] 77

Figure 5.1.5: a) Cu_4TiSe_4 crystal projection along [001], depicting the connectivity of the structure. **b)** $[Cu_4Se_4]^{4-}$ anion clusters, with Ti^{4+} ions sitting in the channels between the clusters. Image was adapted from Chen *et al.*[92] 79

Figure 5.1.6: β-Cu_2Se structure. It forms in an antifluorite-like M_2X lattice where M = Cu^{1+} and X = Se^{2-}. The Cu^{1+} are highly mobile in the lattice. Image was adapted from Sun *et al.*[105] 80

Figure 5.2.1: Dual-Zone furnace single-crystal method instructions. 87

Figure 5.2.2: Dual-zone furnace diagram. 87

Figure 5.3.1: Left: $Cu_2Zn_3Se_4$ powder after reaction and being ground. Photograph was taken using an Apple iPhone 11 Pro Max camera (12 MP). **Middle:** $Cu_2Zn_3Se_4$ single crystal taken using a Nikon brightfield optical microscope with DS-Ri2 camera. Recorded using the extended depth of focus (EDF) mode at 20x magnification. **Right:** $Cu_2Zn_3Se_4$ single crystal mounted on the tip of a glass fiber for single crystal XRD analysis. Image was recorded using a Leica S6E stereo microscope equipped with a Leica L2 light source at 4x zoom. Image was captured through the lenspiece with an Apple iPhone 11 Pro Max 2x telephoto optical zoom lens (12-megapixel), giving a total of ~8x magnification. 88

Figure 5.3.2: $Cu_2Zn_3Se_4$ Small Cell crystal projection along the a-direction. 91

Figure 5.3.3: $Cu_2Zn_3Se_4$ Large Cell crystal projection along the a-direction. The blue dotted lines were overlayed to depict the 3x3 supercell. Each square represents the small cell. 91

Figure 5.3.4: $Cu_2Zn_3Se_4$ Small Cell crystal projection along the a-direction, rotated, with all polyhedra. 92

Figure 5.3.5: $Cu_2Zn_3Se_4$ Large Cell crystal projection along the a-direction, rotated, with all polyhedra. 92

Figure 5.3.6: $Cu_2Zn_3Se_4$ Small Cell a-direction rotated, Cu/Zn chain with distances between metal ions noted. 93

Figure 5.3.7: $Cu_2Zn_3Se_4$ Large Cell a-direction, rotated Cu-Zn chain, with distances between metal ions noted. 93

Figure 5.3.8: PXRD of $Cu_2Zn_3Se_4$, plotted against the small cell and large cell patterns, as well as a potential minor binary phase of Cu_2Se C2/c (PDXL #04-018-3523[106]). 95

Figure 5.3.9: $Cu_2Zn_3Se_4$ DSC vs. temperature for both heating and cooling. The thermal transitions were also noted. 96

Figure 5.3.10: High-T PXRD of $Cu_2Zn_3Se_4$. First, background scans were done on just the graphite dome and Inconel holder to help identify the peaks later. Next, the powder was scanned at various temperatures and dwell times. 97

Figure 5.3.11: XPS counts per second vs. binding energy for **(a)** Cu; **(b)** Zn; **(c)** Se. Two scans were run on the same pellet portion to ensure the data collection was sufficient. 99

Figure 5.3.12: (Left): UV-Vis-NIR diffuse reflectance Tauc plot analysis. The Kubelka-Munk function F(R) was used to transform the reflectance data to absorbance. Plot of F(R) vs. wavelength. **(Right):** Plot of $[F(R)*h\nu]^{1/r}$ vs. energy; r = ½ was chosen here to signify a direct, allowed transition (direct bandgap). To determine the direct optical bandgap (E_g), an absorption edge tangent line was extrapolated to the x-axis; the intercept with the x-axis corresponds to E_g. 101

Figure 5.3.13: Temperature-dependent thermoelectric properties: **(a)** electrical conductivity (σ); **(b)** thermopower (S); **(c)** total thermal conductivity (κ_T); **(d)** figure of merit (zT). 102

Figure 5.3.14: (a) Electrical conductivity Arrhenius plot. The figure was divided into the high-T degenerate semiconductor/ metallic-like region (R1) and the low-T extrinsic semiconductor region (R2). **(b)** Low-T extrinsic region Arrhenius plot, employed to obtain the activation energy, E_a by fitting the ln(σ) vs. 1/T region with a linear trendline and extracting the slope. E_a was found to be 36.58 meV. 104

Figure 5.3.15: (a) Total thermal conductivity vs. temperature **(b)** Electronic thermal conductivity (κ_e) and **(c)** Lattice thermal conductivity (κ_L) contributions, utilizing Wiedemann-Franz Law analysis. It was determined that κ_e contributed ~2-9% to κ_T. 105

Figure 5.4.1: Left: $Cu_2Zn_2Ti_{0.5}Se_4$ powder after reaction and being ground. Photograph was taken using an Apple iPhone 11 Pro Max camera (12 MP). **Right:** $Cu_{2.75}Zn_{0.625}TiSe_4$ single crystal mounted on the tip of a glass fiber for single crystal XRD analysis. Image was recorded using a Leica S6E stereo microscope equipped with a Leica L2 light source at 4x zoom. Image was captured through the lenspiece with an Apple iPhone 11 Pro Max 2x telephoto optical zoom lens (12-megapixel), giving a total of ~8x magnification. 110

Figure 5.4.2: $Cu_{2.75}Zn_{0.625}TiSe_4$ crystal structure. 112

Figure 5.4.3: $Cu_{2.75}Zn_{0.625}TiSe_4$ crystal structure with tetrahedral polyhedra drawn. 113

Figure 5.4.4: $Cu_{2.75}Zn_{0.625}TiSe_4$ Ti coordination connectivity. 114

Figure 5.4.5: $Cu_{2.75}Zn_{0.625}TiSe_4$ Zn coordination connectivity. 114

Figure 5.4.6: PXRD of $Cu_2Zn_2Ti_{0.5}Se_4$, plotted against the $Cu_{2.75}Zn_{0.625}TiSe_4$ single crystal pattern. 116

Figure 5.4.7: $Cu_2Zn_2Ti_{0.5}Se_4$ DSC vs. temperature for both heating and cooling. The thermal transitions were also noted. 117

Figure 5.4.8: High-T PXRD of $Cu_2Zn_2Ti_{0.5}Se_4$. First, background scans were done on just the graphite dome and Inconel holder to help identify the peaks later. Next, the powder was scanned at various temperatures and dwell times. 118

Figure 5.4.9: (Left): UV-Vis-NIR diffuse reflectance Tauc plot analysis. The Kubelka-Munk function F(R) was used to transform the reflectance data to absorbance. Plot of F(R) vs. wavelength. **(Right):** Plot of $[F(R)*h\nu]^{1/r}$ vs. energy; r = ½ was chosen here to signify a direct, allowed transition (direct bandgap). To determine the direct optical bandgap (E_g), an absorption edge tangent line was extrapolated to the x-axis; the intercept with the x-axis corresponds to E_g. 119

Figure 5.5.1: Left: $Cu_2ZnTiSe_4$ powder after reaction and being ground. Photograph was taken using an Apple iPhone 11 Pro Max camera (12 MP). **Right:** $Cu_2ZnTiSe_4$ single crystal mounted on the tip of a glass fiber for single crystal XRD analysis. Image was recorded using a Leica S6E stereo microscope equipped with a Leica L2 light source at 4x zoom. Image was captured through the lenspiece with an Apple iPhone 11 Pro Max 2x telephoto optical zoom lens (12-megapixel), giving a total of ~8x magnification. 122

Figure 5.5.2: $Cu_2ZnTiSe_4$ Small Cell crystal projection along the a-direction. 125

Figure 5.5.3: $Cu_2ZnTiSe_4$ Large Cell crystal projection along the a-direction. The blue dotted lines were overlayed to depict the 2x2 supercell. Each square represents the small cell. 125

Figure 5.5.4: $Cu_2ZnTiSe_4$ Small Cell crystal projection along the a-direction, rotated, with all polyhedra. 126

Figure 5.5.5: $Cu_2ZnTiSe_4$ Large Cell crystal projection along the a-direction, rotated, with all polyhedra. 126

Figure 5.5.6: $Cu_2ZnTiSe_4$ small cell [011] direction rotated, Cu/Zn-Cu/Zn chain. 127

Figure 5.5.7: $Cu_2ZnTiSe_4$ large cell [011] direction rotated, Ti-Cu/Zn-Ti chain. 127

Figure 5.5.8: PXRD of $Cu_2ZnTiSe_4$, plotted against the small cell and large cell patterns, as well as a potential binary phase of $TiSe_2$ P-3m1 (PDXL #00-030-1383[111]). The two blue asterisks were unidentified peaks. 129

Figure 5.5.9: $Cu_2ZnTiSe_4$ DSC vs. temperature for both heating and cooling. The thermal transitions were also noted. 130

Figure 5.5.10: (Left): UV-Vis-NIR diffuse reflectance Tauc plot analysis. The Kubelka-Munk function F(R) was used to transform the reflectance data to absorbance. Plot of F(R) vs. wavelength. **(Right):** Plot of $[F(R)*h\nu]^{1/r}$ vs. energy; r = ½ was chosen here to signify a direct, allowed transition (direct bandgap). To determine the direct optical bandgap (E_g), an absorption edge tangent line was extrapolated to the x-axis; the intercept with the x-axis corresponds to E_g. 133

Figure 5.6.1: Left: $Cu_2Ti_{1.5}Se_4$ powder after reaction and being ground. Photograph was taken using an Apple iPhone 11 Pro Max camera (12 MP). **Right:** $Cu_3Ti_{1.25}Se_4$ single crystal mounted on the tip of a glass fiber for single crystal XRD analysis. Image was recorded using a Leica S6E stereo microscope equipped with a Leica L2 light source at 4x zoom. Image was captured

through the lenspiece with an Apple iPhone 11 Pro Max 2x telephoto optical zoom lens (12-megapixel), giving a total of ~8x magnification. 136

Figure 5.6.2: $Cu_3Ti_{1.25}Se_4$ crystal structure, with polyhedra drawn. 139

Figure 5.6.3: $Cu_3Ti_{1.25}Se_4$ Ti substructure. 140

Figure 5.6.4: $Cu_3Ti_{1.25}Se_4$ Cu substructure. 141

Figure 5.6.5: PXRD of $Cu_2Ti_{1.5}Se_4$, plotted against the $Cu_3Ti_{1.25}Se_4$ single crystal pattern, as well as a potential binary $TiSe_2$ P-3m1 phase (PDXL #00-030-1383[111]). 142

Figure 5.6.6: $Cu_2Ti_{1.5}Se_4$ DSC vs. temperature for both heating and cooling. The thermal transitions were also noted. 143

Figure 5.6.7: High-T PXRD of $Cu_2Ti_{1.5}Se_4$. First, background scans were done on just the graphite dome and Inconel holder to help identify the peaks later. Next, the powder was scanned at various temperatures and dwell times. 144

Figure 5.6.8: (Left): UV-Vis-NIR diffuse reflectance Tauc plot analysis. The Kubelka-Munk function F(R) was used to transform the reflectance data to absorbance. Plot of F(R) vs. wavelength. **(Right):** Plot of $[F(R)*h\nu]^{1/r}$ vs. energy; r = ½ was chosen here to signify a direct, allowed transition (direct bandgap). To determine the direct optical bandgap (E_g), an absorption edge tangent line was extrapolated to the x-axis; the intercept with the x-axis corresponds to E_g. 147

Figure 5.7.1: Left: $Cu_2Mn_3Se_4$ powder after reaction and being ground. Photograph was taken using an Apple iPhone 11 Pro Max camera (12 MP). **Right:** $Cu_2Mn_3Se_4$ single crystal mounted on the tip of a glass fiber for single crystal XRD analysis. Image was recorded using a Leica S6E stereo microscope equipped with a Leica L2 light source at 4x zoom. Image was captured through the lenspiece with an Apple iPhone 11 Pro Max 2x telephoto optical zoom lens (12-megapixel), giving a total of ~8x magnification. 150

Figure 5.7.2: $Cu_2Mn_3Se_4$ Small Cell crystal projection along the a-direction. 153

Figure 5.7.3: $Cu_2Mn_3Se_4$ Large Cell crystal projection along the a-direction. The blue dotted lines were overlayed to depict the 2x2 supercell. Each square represents the small cell. 153

Figure 5.7.4: $Cu_2Mn_3Se_4$ Small Cell crystal projection along the a-direction, rotated, with all polyhedra. 154

Figure 5.7.5: $Cu_2Mn_3Se_4$ Large Cell crystal projection along the a-direction, rotated, with all polyhedra. 154

Figure 5.7.6: $Cu_2Mn_3Se_4$ Small Cell a-direction rotated, Mn-Mn chain with distances between metal ions noted. 155

Figure 5.7.7: $Cu_2Mn_3Se_4$ Large Cell a-direction, rotated Mn-Mn chain, with distances between metal ions noted. 155

Figure 5.7.8: $Cu_2Mn_3Se_4$ Small Cell single Cu/Mn tetrahedron. Note that all bond angles are what is expected: 109.5°. Additionally, all Cu1/Mn1-Se bond distances are regular. 157

Figure 5.7.9: $Cu_2Mn_3Se_4$ Large Cell single Mn tetrahedron. Note that some bond angles are smaller than 109.5°, while other bond angles are larger than 109.5°. Also, all Mn5-Se1 bond distances are shorter at 2.410 Å, while the Mn5-Se2 bond distances are longer at 2.572 Å. 157

Figure 5.7.10: PXRD of $Cu_2Mn_3Se_4$, plotted against the small cell and large cell patterns, as well as a potential binary phases of MnSe Fm-3m (PDXL #04-004-5377[113]) and Cu_3Se_2 P-421m (PDXL #04-003-6622[114]). 158

Figure 5.7.11: $Cu_2Mn_3Se_4$ DSC vs. temperature for both heating and cooling. The thermal transitions were also noted. 159

Figure 5.7.12: (Left): UV-Vis-NIR diffuse reflectance Tauc plot analysis. The Kubelka-Munk function F(R) was used to transform the reflectance data to absorbance. Plot of F(R) vs. wavelength. **(Right):** Plot of $[F(R)*h\nu]^{1/r}$ vs. energy; r = ½ was chosen here to signify a direct, allowed transition (direct bandgap). To determine the direct optical bandgap (E_g), an absorption edge tangent line was extrapolated to the x-axis; the intercept with the x-axis corresponds to E_g. 162

Figure 5.7.13: Predicting the Mn^{2+} $[Ar]3d^5$ theoretical magnetic moment in a tetrahedral Se^{2-} ligand geometry using Hund's rules and crystal-field theory. 164

Figure 5.7.14: Spectrochemical series of ligands, listed from weaker to stronger ligands. A weak-field ligand would lead to a high-spin configuration, while a strong-field ligand would lead to a low-spin configuration. Based on work originally done by Tsuchida.[117] 164

Figure A.1: $MnSb_2Se_4$ XRD peak analysis using Jade software. The Starred peaks were chosen to match the theoretical (hkl) values to the experimental 2θ values. Using Bragg's law and the monoclinic interplanar spacing equation, the lattice parameters a, b, c, and β were calculated. 171

Figure A.2: Rietveld refinement procedure of the main phase using the FullProf software. 171

Figure A.3: (a) $Mn_{0.97}Zn_{0.03}Sb_2Se_4$ (x = 0.03) electrical conductivity Arrhenius plot. The figure was divided into the intrinsic region, saturation plateau, and extrinsic region depending on temperature; **(b)** Intrinsic region Arrhenius plot, utilized to extract electronic bandgap, E_g; **(c)** Extrinsic region Arrhenius plot, employed to obtain activation energy, E_a. 173

Figure A.4: (a) $Mn_{0.96}Zn_{0.04}Sb_2Se_4$ (x = 0.04) electrical conductivity Arrhenius plot. The figure was divided into the intrinsic region, saturation plateau, and extrinsic region depending on temperature; **(b)** Intrinsic region Arrhenius plot, utilized to extract electronic bandgap, E_g; **(c)** Extrinsic region Arrhenius plot, employed to obtain activation energy, E_a. 174

Figure A.5: Fermi-corrected Lorenz # file folder, displaying the relevant files. 175

Figure A.6: (Left): Screenshot of the data_test file that loads in Seebeck coefficient data to the Fermi-corrected Lorenz # Mathematica script. **(Right):** Screenshot of the result file that is generated once the Mathematica script is ran. 176

Figure A.7: Fermi-corrected Lorenz # Mathematica script, written by Hang Chi of the Uher group. It inputs Seebeck coefficient data and calculates accurate values for L. 177

Figure A.8: The bottom portion of the Fermi-corrected Lorenz # Mathematica script, written by Hang Chi of the Uher group. 178

Figure A.9: (a, b) Temperature-dependent magnetic susceptibility in zero field-cooled (ZFC) and field-cooled (FC) configurations, respectively; **(c, d)** Temperature-dependent inverse magnetic susceptibility in ZFC and FC configurations. 179

Figure B.1: (Top): $Sb_{2-x}Sn_xSe_3$ compound series ingots after the solid-state reaction. The ingots were dark grey and lustrous in appearance. No apparent color changes were seen. With increasing Sn content. **(Bottom):** After grinding the reacted ingots into powder-dark grey in appearance. 180

Figure B.2: Sb-Sn-Se pseudo-binary phase diagram (ASM #952732[82]). This diagram was gathered from a vertical section of the Sb-Sn-Se ternary phase diagram. For x = 0-0.2, this corresponded to 0-4 at% Sn. The proper window on the diagram was highlighted with a box in yellow. We see that as Sn increases, we go further into the 2-phase region on the phase diagram between the Sb_2Se_3 Pnma and $SnSb_2Se_4$ Pnnm phases. So, this is consistent with the heating DSC observation of a growing secondary peak from x = 0.1-0.2. 181

Figure B.3: Powder x-ray diffraction comparing $Sb_{1.8}Sn_{0.2}Se_3$ to both the Sb_2Se_3 Pnma (ICSD #30973[30]) and $SnSb_2Se_4$ Pnnm (ICSD #49723[122]) phases. At this zoom level, it is difficult to decipher if the $SnSb_2Se_4$ Pnnm phase is in fact present. See **Figure B.4** 182

Figure B.4: Powder x-ray diffraction comparing $Sb_{1.8}Sn_{0.2}Se_3$ to both the Sb_2Se_3 Pnma (ICSD #30973[30]) and $SnSb_2Se_4$ Pnnm (ICSD #49723[122]) phases, zoomed-in from 20-60° to show the peaks more clearly. Upon close inspection, there are minor $SnSb_2Se_4$ Pnnm peaks present in the $Sb_{1.8}Sn_{0.2}Se_3$ in-between the Sb_2Se_3 Pnma peaks at various 2θ values. 183

Figure B.5: Sb_2Se_3 (x = 0) lattice parameter analysis using PDXL software. The experimental data was compared to the Sb_2Se_3 Pnma (ICSD #30973[30]) phase with lattice parameters: a = 11.7938 Å; b = 3.9858 Å; c = 11.6478 Å; α = β = γ = 90°. Three sets of (hkl) values were correlated to the proper experimental 2θ values. Bragg's Law and the orthorhombic interplanar spacing equation were applied to manually extract more accurate lattice parameters. Corrected lattice parameters from manual peak analysis: a = 11.8126 Å; b = 3.98339 Å; c = 11.6672 Å; α = β = γ = 90°. 184

Figure B.6: FullProf Rietveld refinement procedure implemented to gather the lattice parameters a, b, c for the $Sb_{2-x}Sn_xSe_3$ compound series. 184

Figure B.7: Instructions on how to convert reflectance data into absorbance using the Kubelka-Munk function F(R). By plotting $[F(R)*h\nu]^{1/r}$ vs. energy, we can extract the proper optical

transition. For the case of r = ½, this corresponds to a direct allowed transition, i.e., a direct optical bandgap (E_g). E_g is determined by extrapolating the absorption edge to the baseline; the intersection of the two tangent lines corresponds to E_g. In the case where there is not a clear baseline to extrapolate to, the intersection of the absorption edge tangent line with the x-axis corresponds to E_g. Note: this slide originated from course material in MSE 510: Materials Chemistry, instructed by Dr. McCrory at the University of Michigan. 185

Figure B.8: Kubelka-Munk function F(R) vs. energy. Drawn on the plot is a vertical line at 1.4 eV, noting the onset of the absorption edge. 186

Figure C.1: Cu-Se binary phase diagram from ASM alloy phase diagram database (#101112[123]). The relevant $Cu_2Zn_3Se_4$ DSC peaks were noted with orange horizontal lines. The binary Cu_2Se RT C2/c phase was noted with an orange vertical line. 190

Figure C.2: Cu_2Se powder XRD, compared to the binary Cu_2Se C2/c phase. **(Right):** Heating DSC of Cu_2Se powder with the peaks noted. 190

Figure C.3: $Cu_2Zn_3Se_4$ σ vs. 1/T plot. At high-T, we see the relationship become linear. 192

Figure C.4: Power Factor ($PF = \sigma S^2$) vs. temperature. With increasing T, PF also increased. Values ranged from 0.63-1.53 μW/cm*K. 193

Figure E.1: Ti-Se binary phase diagram from ASM alloy phase diagram database (#903522[124]). The relevant $Cu_2ZnTiSe_4$ DSC peaks were noted with orange horizontal lines. The binary $TiSe_2$ RT P-3m1 phase was also noted. Note: this phase diagram displays a Ti At% range from 36-52 At% Ti. For the $TiSe_2$ RT P-3m1 phase, this corresponds to 33 At% Ti. So, this phase diagram does not display the optimal Ti At% range. Interestingly, this was the only Ti-Se binary phase diagram on the ASM database. 198

Figure E.2: (Left): $TiSe_2$ powder XRD, compared to the binary $TiSe_2$ phase. **(Right):** Heating DSC of $TiSe_2$ powder with the peaks noted. This data was used for comparison purposes with the $Cu_2ZnTiSe_4$ DSC peaks. 199

Figure F.1: Ti-Se binary phase diagram from ASM alloy phase diagram database (#903522[124]). The relevant $Cu_2Ti_{1.5}Se_4$ DSC peaks were noted with orange horizontal lines. The binary $TiSe_2$ RT P-3m1 phase was also noted. Note: this phase diagram displays a Ti At% range from 36-52 At% Ti. For the $TiSe_2$ RT P-3m1 phase, this corresponds to 33 At% Ti. So, this phase diagram does not display the optimal Ti At% range. Interestingly, this was the only Ti-Se binary phase diagram on the ASM database. 201

Figure F.2: $TiSe_2$ powder XRD, compared to the binary $TiSe_2$ phase. **(Right):** Heating DSC of $TiSe_2$ powder with the peaks noted. This data was used for comparison purposes with the $Cu_2Ti_{1.5}Se_4$ DSC peaks. 202

Figure G.1: Mn-Se binary phase diagram from ASM alloy phase diagram database (#901613[125]). The relevant $Cu_2Mn_3Se_4$ DSC peak was noted with an orange horizontal line. The binary MnSe Fm-3m phase was noted with an orange vertical line. 205

Figure G.2: Cu-Se binary phase diagram from ASM alloy phase diagram database (#101112[123]). The relevant DSC peak was noted with an orange horizontal line. The binary Cu_3Se_2 RT P-421m phase was noted with an orange vertical line..... 206

List of Appendices

APPENDIX A: Mn1-xZnxSb2Se4 (x = 0, 0.01, 0.04, 0.05, 0.06, 0.08, 0.1, 0.15) 171

APPENDIX B: Sb2-xSnxSe3 (x = 0, 0.01, 0.05, 0.1, 0.15, 0.2) 180

APPENDIX C: Cu2Zn3Se4 (x = 1.5) 187

APPENDIX D: Cu2Zn2Ti0.5Se4 (x = 1) 194

APPENDIX E: Cu2ZnTiSe4 (x = 0.5) 195

APPENDIX F: Cu2Ti1.5Se4 (x = 0) 200

APPENDIX G: Cu2Mn3Se4 203

APPENDIX H: Magnetic Property Equations 207

APPENDIX I: Thermoelectric Equations 209

APPENDIX J: Structural Equations 213

APPENDIX K: Optical Equations 215

Abstract

In 1965, Gordon Moore predicted that the number of components on an integrated circuit (IC) would double every year for the foreseeable future, later revised to doubling every two years. Moore's Law has ushered in a technological revolution, leading to ubiquitous products such as laptops, tablets, and smartphones. However, Moore's Law has recently begun to slow down. As such, it is crucial to search for solutions to this problem and spin-electronic (spintronic) materials are a promising candidate, taking advantage of the charge and spin of the electron to process and store information. A class of $M_{1-x}M'_xPn_2Se_4$ (M = Fe, Mn; M' = Sn, Cu, Zn; Pn = Sb, Bi) materials show great potential for spintronics, as the lattice provides for separate and precise electronic and magnetic tunability. Here, $Mn_{1-x}Zn_xSb_2Se_4$ (x = 0-0.15) was synthesized, a p-type antiferromagnetic semiconductor. Increasing the Zn content was found to enhance the antiferromagnetic coupling (θ) and effective magnetic moment (μ_{eff}). Throughout the composition range, μ_{eff} was larger than $\mu_{Theoretical}$, so a substitution mechanism of Zn replacing Mn at the M1 and M2 sites was proposed, generating a ferrimagnetic lattice.

Research on $FeSb_{2-x}Sn_xSe_4$ has revealed that a p-type to n-type transition at low-temperature (Lifshitz transition) can be induced by doping Sb^{3+} with Sn^{2+}. In the literature, a Lifshitz transition has been observed to generate interesting properties such as colossal magnetoresistance and superconductivity. With $FeSb_{2-x}Sn_xSe_4$ as the model system, inducing a Lifshitz transition in p-type Sb_2Se_3 by Sn doping ($Sb_{2-x}Sn_xSe_3$, x = 0-0.2) could be intriguing. Sb_2Se_3 and Sb_2Se_3: Sn have shown promise in near-infrared (NIR) photodetectors, thermoelectrics,

optoelectronics, and photovoltaics. In this work, Ultraviolet (UV)-visible (Vis)-NIR spectroscopy on $Sb_{2-x}Sn_xSe_3$ revealed an absorption edge at 1.4 eV, with a decreasing optical bandgap from 1.17 eV to 1.07 eV for increasing Sn. The tunable bandgap of the material around ~1.1 eV makes it an ideal candidate as a photovoltaic absorber layer, as it can absorb wavelengths in the UV, Vis, and NIR. With increasing Sn content, the amount of low-energy band tailing also increased. This could be evidence of impurity sub-bands. In the future, photoluminescence and low-T electrical transport would help elucidate further information on the doping effects and if a Lifshitz transition is induced upon large enough Sn.

Rising greenhouse gas levels is linked to an increase in global temperature and an increase in extreme weather events. As such, it is essential to curb fossil fuel consumption and turn to clean, renewable energy sources such as wind, geothermal, and solar. Within solar, it is vital to choose cheap, abundant, and non-toxic elements. In this work, the face-centered cubic Fm-3m Cu_8Se_4 structure with 8/8 tetrahedral sites filled was used as the model lattice, and $Cu_2Zn_{2x}Ti_{(3-2x)/2}Se_4$ (x = 1.5, 1, 0.5, 0) and $Cu_2Mn_3Se_4$ were synthesized. Single crystals of all five compounds were grown and unique 2x2x2 or 3x3x3 supercell structures were revealed. Lowering the x value was found to increase the level of tetrahedral vacancies and increased the bandgap from 2.24 eV-2.75 eV. $Cu_2Zn_3Se_4$ was revealed to be a promising UV or Vis (violet → green) photodetector material, exhibiting p-type conduction and a large electrical/thermal conductivity. $Cu_2Mn_3Se_4$ holds promise both as an optical material, as well as the potential of exhibiting antiferromagnetic order; a bulk single-crystal synthesis route could be implemented to explore coupled magneto-optic effects.

CHAPTER 1: Introduction

1.1 Moore's Law, Computing Performance, Spintronics, and Dilute Magnetic Semiconductors (DMSs)

In 1965, Gordon Moore predicted that the number of components on an integrated circuit (IC) will double every year for the foreseeable future.[1] **Figure 1.1.1** depicts the original Moore's law.

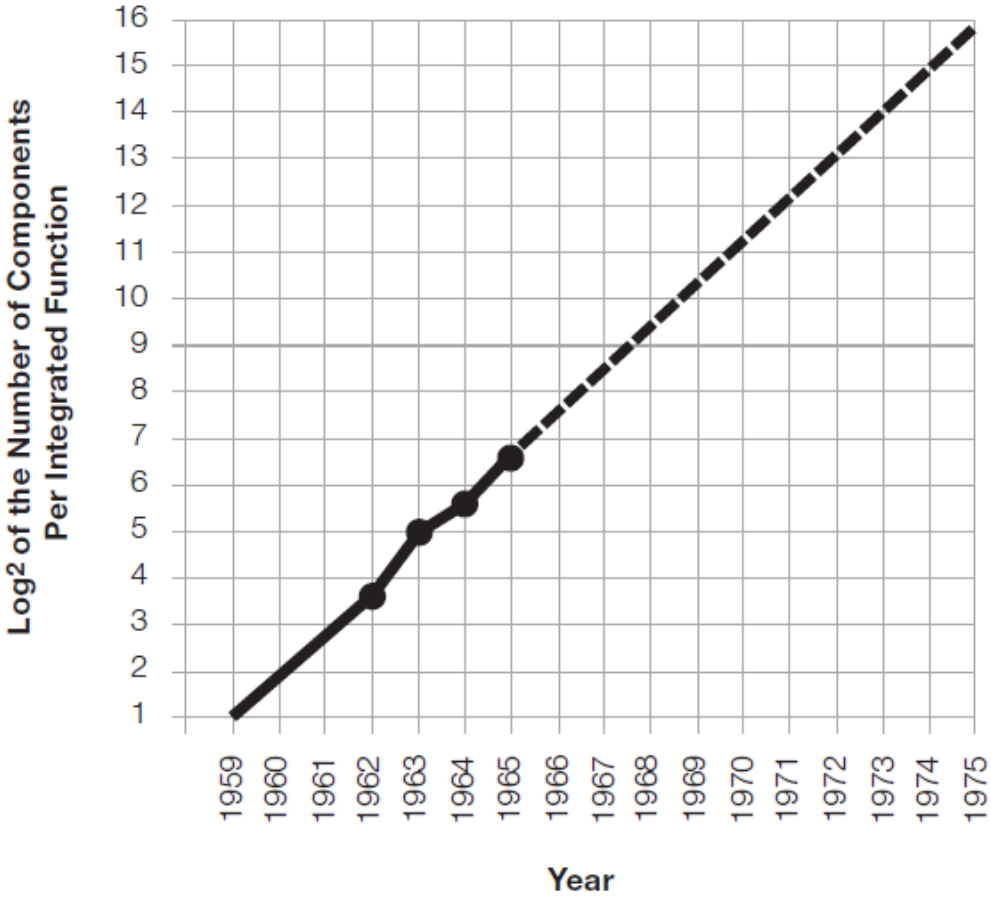

Figure 1.1.1: Moore's Law, depicting the transistor count doubling roughly every year. Image was adapted from Moore's work titled Cramming more components onto integrated circuits.[2]

In 1975, Moore revised his predictions to doubling every two years. Over the past several decades, the steady march of Moore's Law has ushered in a technological revolution. In practice, chip manufacturers manage to fit more components onto an integrated circuit by decreasing the process node size-the distance between transistors. However, as device architectures have shrunk into the <20 nm regime, integrated circuits have become increasingly difficult to manufacture. By the early 2020's, engineers predict that transistors will reach a 2-3 nm limit, where features are just 10 silicon atoms across. At this scale, electron behavior will be governed by quantum uncertainties and transistors will become unstable.[3] The 2016 International Technology Roadmap for Semiconductors (ITRS) meeting was the first global assembly where scientists discussed what comes next after Moore's Law, as computing performance improvements have recently slowed down. **Figure 1.1.2** depicts sources of computing performance over the years. In 2020-2030, all main means of performance boost are predicted to plateau.[4]

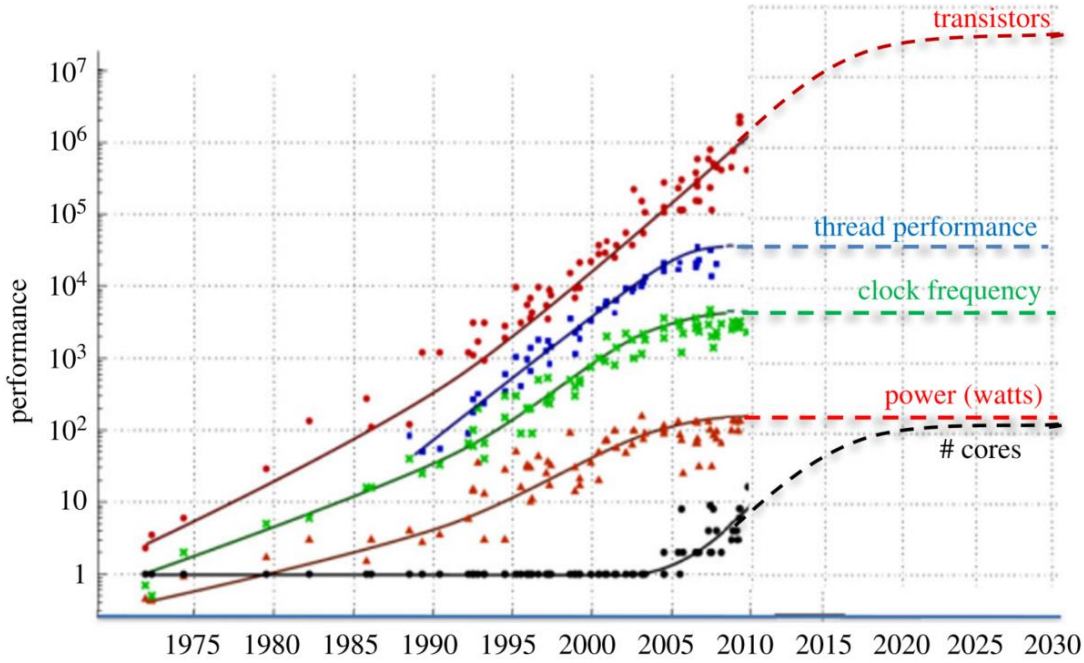

Figure 1.1.2: Sources of computing performance over the years. Notice that by 2020-2030, the # of transistors, thread performance, clock frequency, power, and core count are all predicted to plateau. Image was adapted from Shalf's article on The future of computing beyond Moore's Law.[4]

Possible solutions to the encroaching fundamental limits are techniques like quantum computing, neuromorphic computing, and millivolt switch devices.[3] Millivolt switch devices would produce less heat, while being as fast as silicon devices.[3] Spin electronics (spintronics) is positioned as a great candidate for millivolt switch devices, taking advantage of both the charge and spin of the electron to process and store information. A significant contribution to the field of spintronics was the discovery of giant magnetoresistance (GMR), found in 1988 by Baibich *et al*.[5] The GMR effect was found in a (001) Fe/ (001) Cr magnetic superlattice, where upon application of a 2 Tesla magnetic field, the resistance was lowered by a factor of 2. GMR-based devices take advantage of the high/low resistance states, encoding binary information accordingly.[5] Other milestones for spintronics were the discovery of spin-transfer torque, the spin valve head, magnetic tunnel junctions, and magnetoresistive random access memory (MRAM). [6-9] In 2007, a proposed spin-MOSFET was studied, probing the use of spintronic materials for active three-terminal semiconductor devices. The spin-MOSFET-based device showed promise, as well as the ability to integrate with conventional Si circuit architectures.[10] Traditional spintronic devices are based on ferromagnetic (FM) materials, but recently the viability of antiferromagnetic (AFM) materials for spintronics has been analyzed. Although AFM materials possess no net magnetic moment, since the relativistic anisotropic magnetoresistance (AMR) is sensitive to the microscopic magnetic moment vector, AFM-based spintronic devices are still feasible.[11]

Two classes of materials, dilute magnetic semiconductors (DMS) and magnetic semiconductors (MS), are well-suited for spintronic applications. Dilute magnetic semiconductors such as $Ga_{1-x}Mn_xAs$ have gathered interest recently due to exhibiting a fairly high-T_c of ~110 K[12], as well as compatibility with existing III-V technologies.[13] **Figure 1.1.3** depicts the $Ga_{1-x}Mn_xAs$ III-V (DMS) crystal lattice.

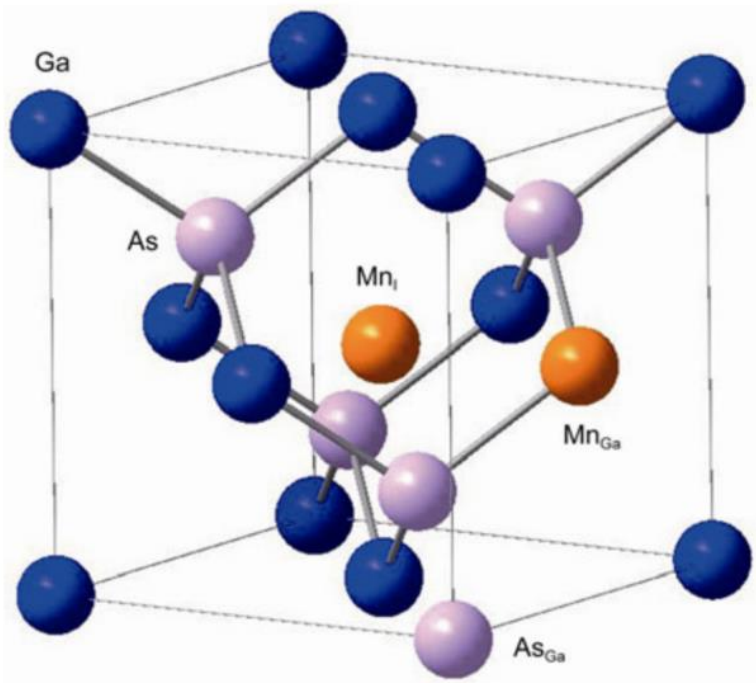

Figure 1.1.3: $Ga_{1-x}Mn_xAs$ III-V dilute magnetic semiconductor (DMS) crystal lattice. Image was adapted from Wang *et al*.[14]

In addition, DMS can exhibit complex magnetic behavior that can be tuned based on the level of magnetic substitution. In the case of $Zn_{1-x}Mn_xSe$, for $y < 0.3$, it exhibits paramagnetic behavior of uncorrelated Mn spins; for $0.3 < x < 0.6$, AFM spin-glass structure is observed; for $x > 0.6$, AFM behavior is seen.[13] However, one downfall of the DMS substitution mechanism is the fact that the magnetic atom is directly substituting for a semiconducting atom within the structure. For DMS, one cannot decouple the changing electronic and magnetic properties that occur with this type of substitution.

1.2 Lifshitz Transition Materials

In 1960, Lifshitz discovered that the Fermi surface of metals can be deformed at high pressures, a phenomenon which was later coined the Lifshitz transition.[15] A rapid transition in the Fermi surface topology has been observed to generate interesting properties such as colossal

magnetoresistance and superconductivity.[16] Parameters such as strain, doping, pressure, and temperature have been seen to induce a Lifshitz transition.[16] In particular, temperature-induced Lifshitz transitions have been observed in materials such as $HfTe_5$, WTe_2, $TaIrTe_4$, and $InTe_{1-\delta}$.[17-20]

1.3 Climate Change, Clean Energy, and Photovoltaics

Climate change is a worldwide catastrophe, being linked to an increase in global temperature, sea level rise, ocean warming, an increase in glacial ice melt, and an increase in extreme weather events. [21-24] Recently, in 2015, 200 countries around the world came together to sign the Paris Climate agreement. One of the major goals of the agreement was to keep the global temperature rise below 2 °C, with a concerted effort to limit the rise to 1.5 °C.[25] Scientific models have assessed that the additional 0.5 °C of temperature rise would have drastic consequences on the Earth's climate and ecosystem.[25] In fact, this rise could cause certain regions in the globe to move into a new climate regime, and cause extreme coral bleaching.[25] Schellnhuber's[21] predictive models on global warming are alarming. **Figure 1.3.1** makes it clear that without a united global effort to curb greenhouse gas emissions, the warming effects will continue to rise dramatically.

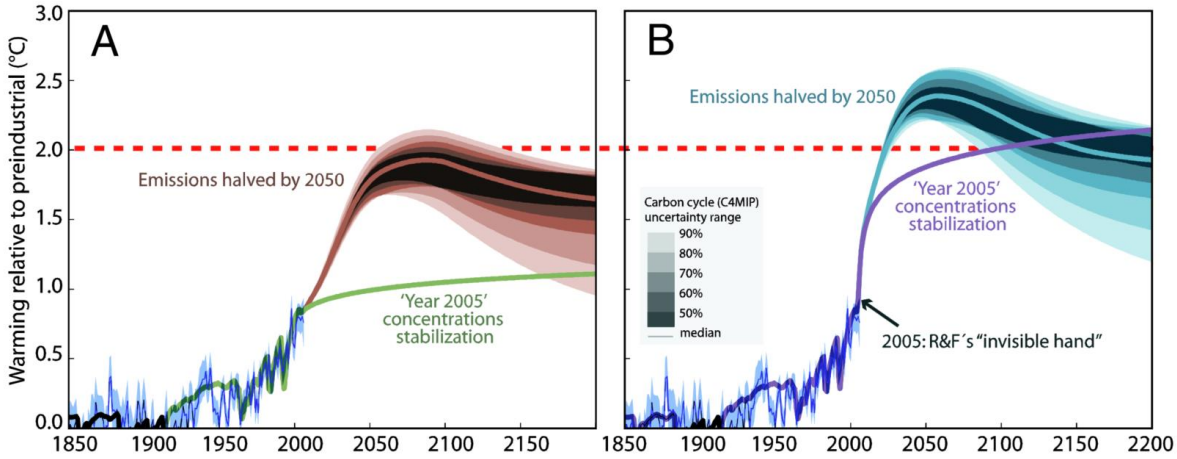

Figure 1.3.1: a) Climate change model where the green line fixes greenhouse gas concentrations at the 2005 level; the dark red curve is when emissions are halved by 2050, i.e. the mitigation

scenario.[21] **b)** Similar to the left model, but with the removal of aerosol cooling (invisible hand); this focuses the model on long-lasting greenhouse gases in the troposphere.[21] Figure was adapted from Schellnhuber.[21]

Interestingly, aerosols have shown to have a global cooling effect, but they exist in the atmosphere for a shorter period than CO_2.[26] As such, once the aerosols decompose global temperatures will spike. [26]

To curb greenhouse gas emissions, the energy sector needs to further utilize clean and renewable energy sources such as wind, geothermal, hydroelectric, and solar power. In this work, the focus is on solar, with the goal of developing new materials for photovoltaic applications. The major operating principle for solar cells is a phenomenon called the photovoltaic effect, as illustrated in **Figure 1.3.2** and **Figure 1.3.3**.

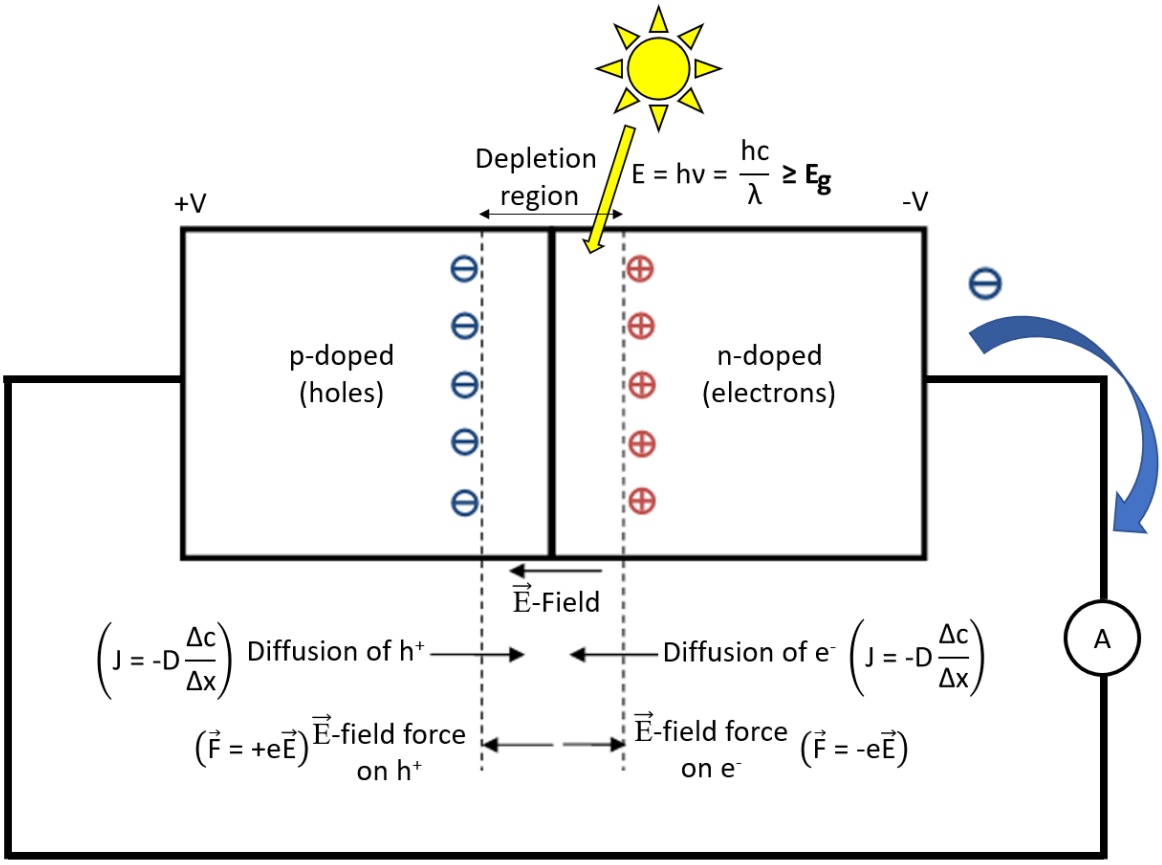

Figure 1.3.2: Illustration of a p-n junction solar cell and the photovoltaic effect.

In a solar cell, a p-doped material is joined by an n-doped material. Due to the concentration gradient of holes (h^+) and electrons (e^-), holes will flow towards the n-type side, while electrons will flow towards the p-type side, under the principle of Fick's 1st Law. Charges will build up and create a depletion region between the charge buildup. Positive holes on the n-side and negative electrons on the p-side will generate an electric field pointing from positive to negative charge, i.e., n-side to p-side. **Figure 1.3.3** depicts that when a photon of sunlight with energy $E \geq E_g$ strikes the depletion region, it generates an electron-hole pair, exciting the electron from valence band (VB) to conduction band (CB), leaving behind a hole in the valence band.

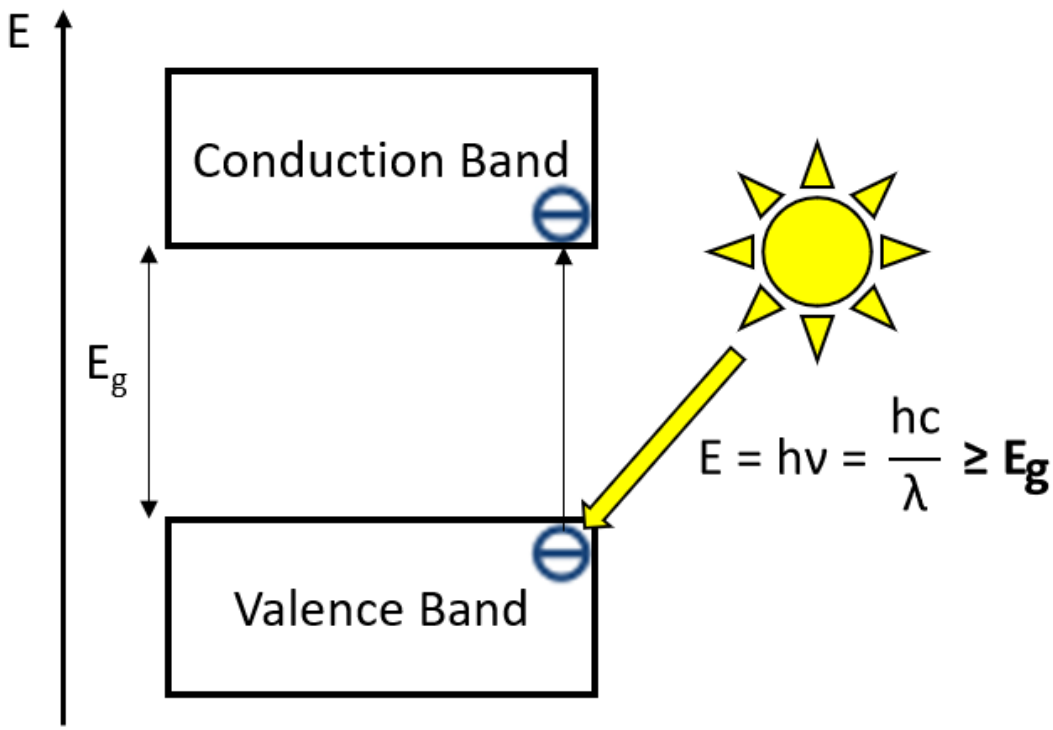

Figure 1.3.3: Schematic of a photon with $E \geq E_g$ exciting an electron from valence band to conduction band (CB). Once the electron reaches the CB, it is a free electron, capable to flow through the external circuit. During the electron excitation, a hole is left behind in the valence band (VB).

Due to the electric field pointing from n-side to p-side in the depletion region of the p-n junction, the excited electron will flow towards the n-side and the hole will be driven towards the p-side.

Eventually, electrons build up on the far-right portion of the n-side and holes build up on the far-left portion of the p-side. This charge build-up generates a potential difference in the solar cell, called the photovoltaic effect. Upon connecting the p-n junction together using a wire, electrons will flow in the circuit towards the p-side. If an ammeter (A) is placed in the circuit, a current will be measured.

To efficiently harness sunlight and convert it to electricity, one must understand the wavelengths of light the sun emits. **Figure 1.3.4** depicts the solar spectrum vs. wavelength.

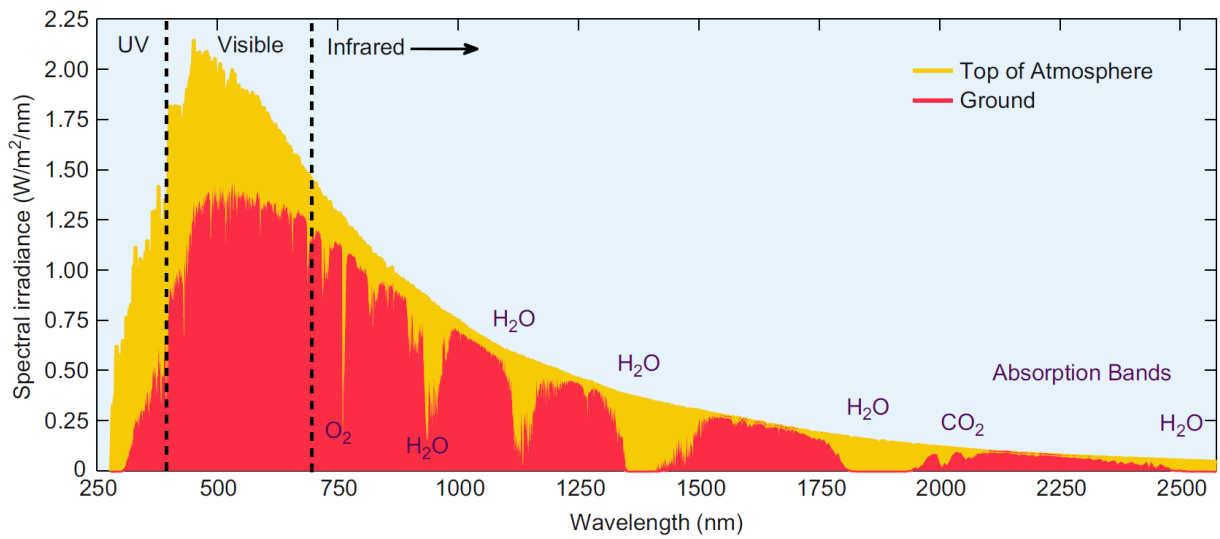

Figure 1.3.4: Solar spectrum vs. wavelength. Image was adapted from Cleveland and Morris' Handbook of Energy.[27]

We see that the sun emits in the ultraviolet (~250-400 nm), visible (~400-700 nm), and infrared (~700-2600 nm), centering at a peak irradiance around 500-550 nm, in the visible portion of the spectrum. Converting these wavelength values to energies (in eV) would be useful since solar cell materials are reported in terms of bandgap. To convert from wavelength to energy, we use the following equation:

$$E \text{ (in eV)} = \frac{hc}{\lambda e} \qquad \textbf{1.3-1,}$$

where E is energy, h is Planck's constant, c is the speed of light, λ is wavelength, and e is the electronic charge. Utilizing **Equation 1.3-1**, the sun emits in UV energies of 3.10-4.96 eV, visible energies of 1.77-3.10 eV, and infrared energies of 0.48-1.77 eV. Additionally, the centered peak irradiance is around 2.25-2.48 eV. Recall from **Figure 1.3.3**, only photons with energy $E \geq E_g$ will be absorbed, so in the case of $E_g = 1$ eV, this corresponds to a maximum absorbed wavelength of ~1240 nm, in the Near-IR portion of the spectrum. In this case, the 1240-nm-2600 nm portion of the IR region cannot be absorbed.

CHAPTER 2: Experimental

2.1 Synthesis

2.1.1 Powder Synthesis:

Polycrystalline powders were generated from a solid-state reaction of elements. Stoichiometric amounts of each element were weighed in an argon glovebox and ground thoroughly with a mortar and pestle for 15 minutes. The resultant powder was placed in quartz tubes, evacuated to a pressure of ~10^{-3}-10^{-5} Torr, and rapidly flame-sealed while keeping the sample cool with liquid nitrogen. The sealed tubes were placed in mullite ceramic tubes, and both ends were capped with fiberglass to keep the temperature uniform during the reaction. The mullite tubes were placed into a programmable furnace, reacting the samples using a two-step reaction profile. In the first step, the sample was dwelled at 300 °C to react Se slowly with the other elements due to its low melting temperature. The second step at a higher temperature gave the system enough thermal energy to form the desired phase. Following the reaction, the ingot was ground into a fine powder. In this form, various powder measurements were performed.

2.1.2 Hot-Pressed Pellet/Bar:

For thermal diffusivity/heat capacity and electrical conductivity/Seebeck coefficient measurements, the powder was hot-pressed into densified pellets. Approximately 1.5 g of sample was weighed out to get a ~3-mm thick pellet, poured into a 10-mm graphite die, and hot-pressed between graphite anvils under a pressure of 98.6 MPa under evacuated conditions (~508 Torr)

using an Astro Industries hot press. A graphite spacer was placed between samples to allow for two pellets to be pressed simultaneously. The pressing temperature profile followed a heat, dwell, and cool process; specific temperature profiles are found in the specific compound chapters. The pellet was polished to a mirror finish using 400/600/800/1000 grit SiC paper. To confirm that the pellets were properly densified, the mass was measured with an analytical balance and the volume was measured using a He gas Quantachrome ULTRAPYC 1200e pycnometer (machine accuracy of < 0.3%). Then, the experimental density was calculated and compared to the theoretical density; all pellets showed >96% densification. The pellet for electrical conductivity/Seebeck coefficient analysis was cut into a rectangular bar with the approximate dimensions of 3 mm x 3 mm x 10 mm using an Isomet 1000 precision diamond saw and polished using the above SiC paper grit series.

2.2 Characterization

2.2.1 Powder X-Ray Diffraction (PXRD)

Phase purity was probed using a Rigaku Smartlab X-ray diffractometer equipped with a monochromatic 2.2 kW Cu-Kα (λ = 1.54059 Å) X-ray source (40 kV, 44 mA). For $Mn_{1-x}Zn_xSe_4$, the 2θ scan range was 10-80°, with a step size of 0.01°. For the $Sb_{2-x}Sn_xSe_3$, $Cu_2Zn_{2x}Ti_{(3-2x)/2}Se_4$ (x = 1.5, 1, 0.5, 0) and $Cu_2Mn_3Se_4$ systems, the 2θ scan range was 3-110°, with a step size of 0.05°. The scans were done in Bragg-Brentano geometry using a D/teX Ultra 250 high-speed detector. Cu-Kβ peaks were eliminated using a Cu-Kβ filter, a knife-edge was implemented to reduce low-angle scattering, and a beamstop was employed to eliminate direct beams from striking the detector.

2.2.2 Rietveld Refinement

$Mn_{1-x}Zn_xSb_2Se_4$ refinement: Please refer to **Figure A.1**, **Figure A.2**, **Equation J-1**, **Equation J-2, and Equation J-3** for information about the refinement process. To extract lattice parameters of the $Mn_{1-x}Zn_xSb_2Se_4$ and ZnSe phases, FullProf was implemented to carry out Rietveld refinement. The $MnSb_2Se_4$ crystallographic information file (ICSD Ref. #421940[28]) was used as the starting PCR file for refinement. However, due to a collective peak shift to lower angle (higher lattice parameter) compared to the reference pattern, it was not possible to accurately refine lattice parameters in this fashion since the refinement would not converge. Rather, a more accurate determination of experimental lattice parameters was required for the refinement to converge properly. Lattice parameters were manually calculated for all compositions by rearranging Bragg's Law for $1/d^2$ and equating this to the monoclinic interplanar spacing (d) equation. By inputting the wavelength of the X-ray source and 4 sets of Miller indices from space group #12, a system of 4 equations and 4 unknowns (a, b, c, β) was generated.

The Miller indices employed were as follows: (002), (200), $(\bar{3}12)$, and $(\bar{3}13)$. The manually calculated lattice parameters were inserted into FullProf and refinement was carried out, proceeding in the following order: background (coefficients), profile (scale, lattice parameters, FWHM parameters), and x/z atomic coordinates of non-special positions (Mn1, Sb2, Mn2, Sb1, Se1). Successful refinement was first performed on $Mn_{0.94}Zn_{0.06}Sb_2Se_4$, and this PCR file became the input file for all other refinement on additional compositions. For each composition, the lattice parameters were updated with the manually calculated values, and refinement proceeded as previously described. For x = 0.04-0.15, the refined PCR files were updated with the secondary phase (ZnSe ICSD Ref. #77091[29]), and ZnSe lattice parameter was refined using the same steps as before.

$Sb_{2-x}Sn_xSe_3$ Refinement: Please refer to **Figure B.5**, **Figure B.6**, **Equation J-9, and Equation J-10** for information on the process used for refinement. As in the case of $Mn_{1-x}Zn_xSb_2Se_4$, manual lattice parameters were gathered for Sb_2Se_3, in this case using PDXL software to index the peaks. Sb_2Se_3 Pnma (ICSD #30973[30]) was used as the phase of comparison. Since this structure is orthorhombic, 3 sets of experimental 2θ and (hkl) values were chosen and lattice parameters were calculated using the referenced equations. The starting values were then input into FullProf, and the refinement procedure was carried out as listed in **Figure B.6**.

2.2.3 Differential Scanning Calorimetry (DSC)

Approximately 20-30 mg of sample was placed into a round quartz crucible and sealed under a vacuum of ~10^{-3}-10^{-5} Torr. Differential scanning calorimetry was performed using a NETZSCH DSC 404 F1 Pegasus instrument. Thermal events were probed under flowing nitrogen gas. The samples underwent one heating/cooling cycle to check for melting point and recrystallization temperature values. The DSC data was processed using NETZSCH Proteus Thermal Analysis software. Due to broad melting peaks, the melting point was determined by locating the minimum of the peak, as opposed to the onset method. Refer to each compounds' DSC curve in **Chapters 3-5** for the respective temperature scan ranges used.

2.2.4 X-ray Photoelectron Spectroscopy (XPS)

Portions of a pellet from each composition were characterized with a Kratos Axis Ultra XPS (mono Al source; Al-Kα =1486.6eV) to confirm the oxidation states of Mn, Zn, Sb, Cu, and Se in the compound. Proper narrow scan ranges were determined using the Handbook of X-Ray Photoelectron Spectroscopy.[31] In order to eliminate any possible oxide on the surface, samples were again polished to a mirror finish using the SiC grit series listed above. Newly polished

samples were placed in an argon glovebox and sealed in a plastic bag to avoid oxidation during transit to the instrument.

2.2.5 Thermal Diffusivity/Heat Capacity

Thermal Diffusivity (D) and Heat capacity (C_p) measurements were performed using a Linseis LFA 1000. The accuracy in D and C_p was ± 5%. Pellets were cleaned with methanol and both sides were coated with graphite spray. Measurements were taken from 297-623 K ($Mn_{1-x}Zn_xSb_2Se_4$) or 298-912 K ($Cu_2Zn_3Se_4$) under a vacuum of ~10^{-3} Torr and compared to a Pyroceram 9606 reference. For $Cu_2Zn_3Se_4$, C_p was calculated via the Dulong-Petit law:

$$C_p = \frac{N3R}{FM} \qquad \textbf{2.2-1,}$$

Where N = number of atoms, R is the ideal gas constant, and FM is the formula mass.

2.2.6 Electrical Conductivity/Seebeck Coefficient

Electrical conductivity (σ)/Seebeck coefficient (S) was measured with a ULVAC-RIKO ZEM-3 using the standard 4-point probe method. The accuracy in σ and S was ± 4%. The temperature was scanned from 323-623 K (for $Mn_{1-x}Zn_xSb_2Se_4$) or 300-905 K (for $Cu_2Zn_3Se_4$) under a He atmosphere of ~600 Torr.

2.2.7 Low-Temperature Direct-Current (DC) Magnetic Susceptibility

Low-T DC magnetic susceptibility (χ) measurements were taken using a Quantum Design MPMS-XL SQUID magnetometer. Approximately 40 mg of powder was placed into a gel capsule, and the measurements were taken under a direct-current (DC) magnetic field of 100 Oe, with a temperature scan range of 2-300 K. Both zero field-cooled (ZFC) and field-cooled (FC) data was

taken. The ZFC and FC methods were described in Lopez *et al*.'s work on $Fe_{1-x}Sn_xBi_2Se_4$.[32] Samples were cooled to 2 K without a magnetic field; then, the field was turned on and χ was measured upon heating back to room temperature (ZFC). [32] For Field-cooled data, the field was left on during cooling back to 2 K, then χ was measured upon heating back to room temperature.[32]

2.2.8 UV-Vis-NIR Diffuse Reflectance Spectroscopy

$Sb_{2-x}Sn_xSe_3$ and $Cu_2Zn_{2x}Ti_{(3-2x)/2}Se_4$ (x = 1.5, 1, 0.5, 0) Systems: Optical diffuse reflectance data over the UV, visible and near-IR regions were gathered for each compound in the $Sb_{2-x}Sn_xSe_3$ series with a Varian Cary 5000 spectrometer. The UV-Vis wavelength accuracy was ± 0.1 nm; the NIR wavelength accuracy was ± 0.4 nm. The photometric accuracy in absorbance for UV-Vis was ± 0.0003. $BaSO_4$ (Fisher Scientific, 99.92%) was used as the reflectance standard (100%). Samples were ground in a mortar and pestle and placed into the top of the sample cup that was preloaded with the $BaSO_4$. The sample cup was inserted into the Harrick Praying Mantis diffuse reflectance accessory. Using a scan rate of 600 nm/min, percent reflectance scans were collected over the range of 2500 to 200 nm. Later, the Kubelka-Munk equation[33] was used to transform percent reflectance data to absorption, which was then plotted as a function of energy in electron volts, eV.

$Cu_2Mn_3Se_4$ System: Optical diffuse reflectance data over the UV, visible, and near-IR regions were gathered for $Cu_2Mn_3Se_4$ with an Agilent Cary 5000 spectrophotometer equipped with a PbS detector and a thin film diffuse reflectance accessory with integration sphere. The UV-Vis wavelength accuracy was ± 0.1 nm; the NIR wavelength accuracy was ± 0.4 nm. The photometric accuracy in absorbance for UV-Vis was ± 0.0003. $BaSO_4$ was used as the reflectance standard. Using a scan rate of 600 nm/min, percent reflectance scans were collected over a wavelength range of 1500-200 nm. Later, the Kubelka-Munk equation[33] was used to transform percent reflectance data to absorption, which was then plotted as a function of energy in electron volts, eV. The

framework to collect and analyze the data was partly based on Milosevic and Berets' Review of FT-IR Diffuse Reflection Sampling Considerations.[34]

2.2.9 High-Temperature Powder X-Ray Diffraction (HT-XRD)

Phase purity at elevated temperature was probed using a Rigaku Smartlab X-ray diffractometer equipped with a domed hot stage-1100 (DHS-1100). The X-ray source was a monochromated 2.2 kW Cu-Kα (λ = 1.54059 Å) with a voltage of 40 kV and a current of 44 mA. The 2θ scan range was 3-110°, with a step size of 0.05°. The scans were done in Bragg-Brentano geometry using a D/teX Ultra 250 high-speed detector. Cu-Kβ peaks were eliminated using a Cu-Kβ filter. **Figure 2.2.1 (Left):** Powder sample was loaded into an Inconel (Ni-Cr-Fe superalloy) holder, which was mounted on the high-T stage using Inconel metal clips.

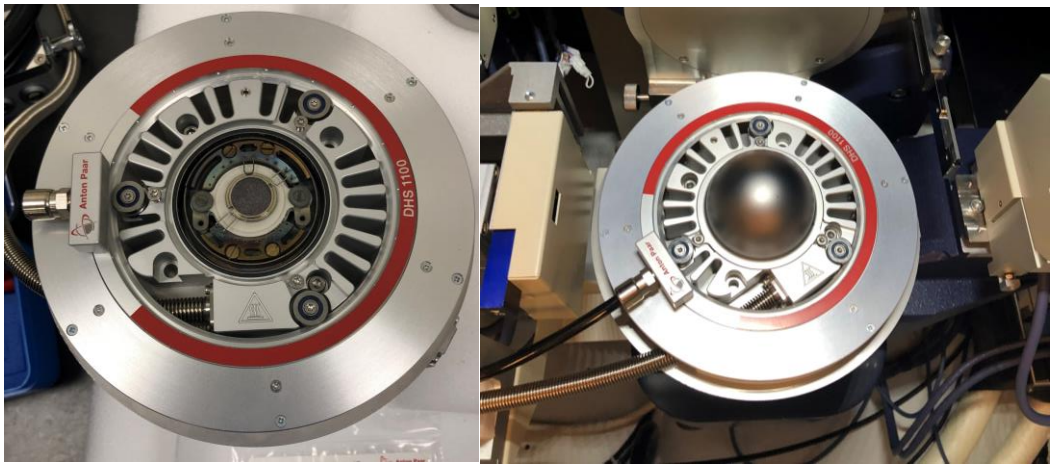

Figure 2.2.1: Left: Powder in an Inconel holder, mounted in the high-T XRD stage by Inconel clips. **Right:** High-T XRD stage mounted in place, with graphite dome over the sample. The black hose pictured has compressed air to regulate temperature and the silver hose is connected to the temperature controller.

A graphite dome was placed over the sample and screwed in place. **Figure 2.2.1 (Right):** The stage was then mounted in the diffractometer, with a metal hose that connected to the temperature controller. A compressed air line (black hose) was connected to regulate the stage temperature for T > 200 C. A rotary vacuum pump was used to keep the sample under a slight vacuum of ~0.6 atm

(456 Torr). Once the hot stage was connected, the measurement was operated using the SmartLab Guidance software with temperature package. The scan temperatures were chosen based on each compounds' DSC heating curve.

2.2.10 Optical Microscopy of $Cu_2Zn_{2x}Ti_{(3-2x)/2}Se_4$ (x = 1.5, 1, 0.5, 0) and $Cu_2Mn_3Se_4$ Single Crystals

$Cu_2Zn_3Se_4$ single crystal Figure 5.3.1 (Middle Image): This was recorded with a Nikon Eclipse LV100ND upright brightfield optical microscope with DS-R12 cameras, equipped with the Nikon Imaging Software (NIS) Elements suite. Recorded using the extended depth of focus (EDF) mode at 20x magnification. EDF created an all-in-focus image from a series of z-axis images.

All other $Cu_2Zn_{2x}Ti_{(3-2x)/2}Se_4$ (x = 1.5, 1, 0.5, 0) and $Cu_2Mn_3Se_4$ Single Crystals: The rest of the single crystal optical micrographs were taken with a Leica S6E stereo microscope equipped with a Leica L2 light source at 4x zoom. Images were captured through the lenspiece with an Apple iPhone 11 Pro Max 2x telephoto optical zoom lens (12-megapixel), giving a total of ~8x magnification.

2.2.11 Single-Crystal X-Ray Diffraction (SC-XRD) & Structure Determination

Short or long glass fibers were mounted into hollow metal stubs with wax. Devcon 2-stage epoxy resin was mixed, and promising crystals were isolated in a Petri dish. A minute amount of the epoxy was added to the tip of the glass fiber, and the crystal was gathered. Several single crystals of the $Cu_2Zn_{2x}Ti_{(3-2x)/2}Se_4$ (x = 1.5, 1, 0.5, 0) and $Cu_2Mn_3Se_4$ suitable for X-ray single-crystal structure determination (approximate dimensions of $0.02 \times 0.04 \times 0.09$ mm^3) were selected from the sample mass and used for X-ray diffraction study at 300 K. Intensity data were collected using graphite-monochromated Mo_Kα radiation (λ = 0.71073 Å) on a STOE IPDS-2T

diffractometer operated at 50 kV and 40 mA. The diffraction data for various compounds was indexed in the cubic crystal system with varying space group depending on the order of the superlattice (see **Table 5.3.1**, **Table 5.4.1**, **Table 5.5.1**, **Table 5.6.1**, and **Table 5.7.1** for details). The structure solution was obtained using the direct methods, and the structure refinement was performed using least squares techniques in the SHELTXL package.[35, 36]

The structure solution revealed all heavy metal positions and all selenium positions. The refinement of the initial model showed larger atomic displacement parameters for some of the metal positions when compared to Se atoms, which suggests the presence of structural vacancies and/or some intermixing heavy and lighter metal atoms at these positions. Therefore, we considered mixed occupancy between Cu and various metals (Zn, Mn, Ti) at all metal positions in the subsequent refinement cycles and assumed full occupancy of all sites. This model significantly improved the structure agreement parameters, but the composition of the crystal contains a large excess of positive atoms. Therefore, we then consider the presence of vacancies at various positions while maintaining mixed occupancy. The refinement improved the charge balance of the composition of the crystal. The final refinement step, which included anisotropy parameters for all atoms and extinction correction, yielded the final structure refinement agreement factors (see tables referenced above).

A summary of the crystallographic parameters for the structure refinement of $Cu_2Zn_{2x}Ti_{(3-2x)/2}Se_4$ (x = 1.5, 1, 0.5, 0) and $Cu_2Mn_3Se_4$ phases at 300 K is gathered in the above referenced tables. The final distribution of metal atoms at all metal positions is reported in **Table 5.3.2** (Small Cell), **Table 5.3.3** (Large Cell), **Table 5.4.2**, **Table 5.5.2** (Small Cell), **Table 5.5.3** (Large Cell), **Table 5.6.2**, **Table 5.7.2** (Small Cell), and **Table 5.7.3** (Large Cell) for the $Cu_2Zn_{2x}Ti_{(3-2x)/2}Se_4$ (x = 1.5, 1, 0.5, 0) and $Cu_2Mn_3Se_4$ phases, along with the atomic coordinates and isotropic

displacement parameters for all atoms in the crystal structure. Selected interatomic bond distances between metal atoms and selenium atoms forming the coordination environment are given in **Table 5.3.4** (Small Cell), **Table 5.3.5** (Large Cell), **Table 5.4.3**, **Table 5.5.4** (Small Cell), **Table 5.5.5** (Large Cell), **Table 5.6.3**, **Table 5.7.4** (Small Cell), and **Table 5.7.5** (Large Cell). The crystal structure of $Cu_2Zn_{2x}Ti_{(3-2x)/2}Se_4$ (x = 1.5, 1, 0.5, 0) and $Cu_2Mn_3Se_4$ phases and the distorted coordination polyhedron formed by selenium atoms around various atoms **Figure 5.3.4** (Small Cell), **Figure 5.3.5** (Large Cell), **Figure 5.4.3**, **Figure 5.5.4** (Small Cell), **Figure 5.5.5** (Large Cell), **Figure 5.6.2**, **Figure 5.7.4** (Small Cell), and **Figure 5.7.5** (Large Cell) were created using the software Diamond and CrystalMaker.[37]

CHAPTER 3: $Mn_{1-x}Zn_xSb_2Se_4$ (x = 0, 0.01, 0.04, 0.05, 0.06, 0.08, 0.1, 0.15) Structural, Thermoelectric, and Magnetic Properties

3.1 Introduction: $Mn_{1-x}Zn_xSb_2Se_4$ (x = 0, 0.01, 0.04, 0.05, 0.06, 0.08, 0.1, 0.15)

An exciting new class of magnetic semiconductors given by the parent structure $M_{1-x}M'_xPn_2Se_4$ (M = Fe, Mn; M' = Sn, Cu, Zn; Pn = Sb, Bi) have garnered much research attention recently since the system has been shown to exhibit separate and precise magnetic/electronic tunability.[28, 32, 38-45] The compound series crystallizes isostructurally in the low-symmetry monoclinic space group C2/m (#12). The structure allows decoupling at the atomic-scale of the magnetic and semiconducting sublattices. [28, 32, 38-45] This gives the ability to separately tune the electronic and magnetic properties of the system. **Figure 3.1.1** depicts an example $M_{1-x}M'_xPn_2Se_4$ lattice-$Fe_{0.87}Sn_{0.13}Sb_2Se_4$ in this case. The separate magnetic and semiconducting sublattices are noted.

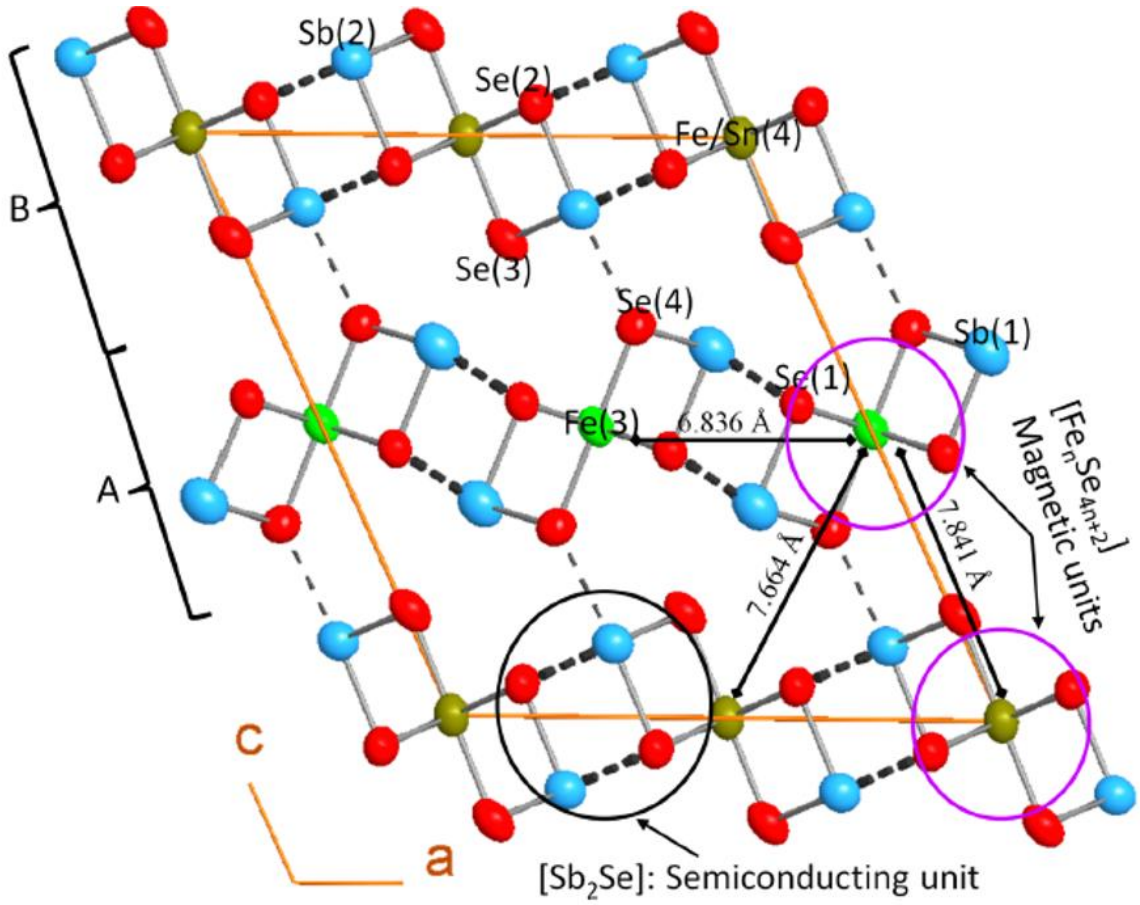

Figure 3.1.1: $Fe_{0.87}Sn_{0.13}Sb_2Se_4$ crystal lattice, projected along the b-axis. Note the distinct magnetic and semiconducting sublattices. Image was adapted from Djieutedjeu *et al*.[39]

The magnetic behavior can be selected by using Fe/Mn (FM or AFM) and the carrier type can be chosen with Sb/Bi (p-type or n-type). In the case of $FeBi_2Se_4$, an n-type ferromagnetic semiconductor, a T_c of ~450 K was observed.[44]

The magnetic moment of $MnSb_2Se_4$ can be predicted via Hund's rules and crystal-field theory. **Appendix H** lists more details on this. In $MnSb_2Se_4$, the Mn^{2+} [Ar]$3d^5$ ion is surrounded in an octahedral ligand geometry arrangement of Se^{2-}.[28] An octahedral ligand geometry splits the degenerate 3d orbitals into a triplet level and a higher energy doublet level. Selenium is known as a weak-field ligand, so the five 3d electrons will fill high-spin. **Figure 3.1.2** depicts a schematic for this.

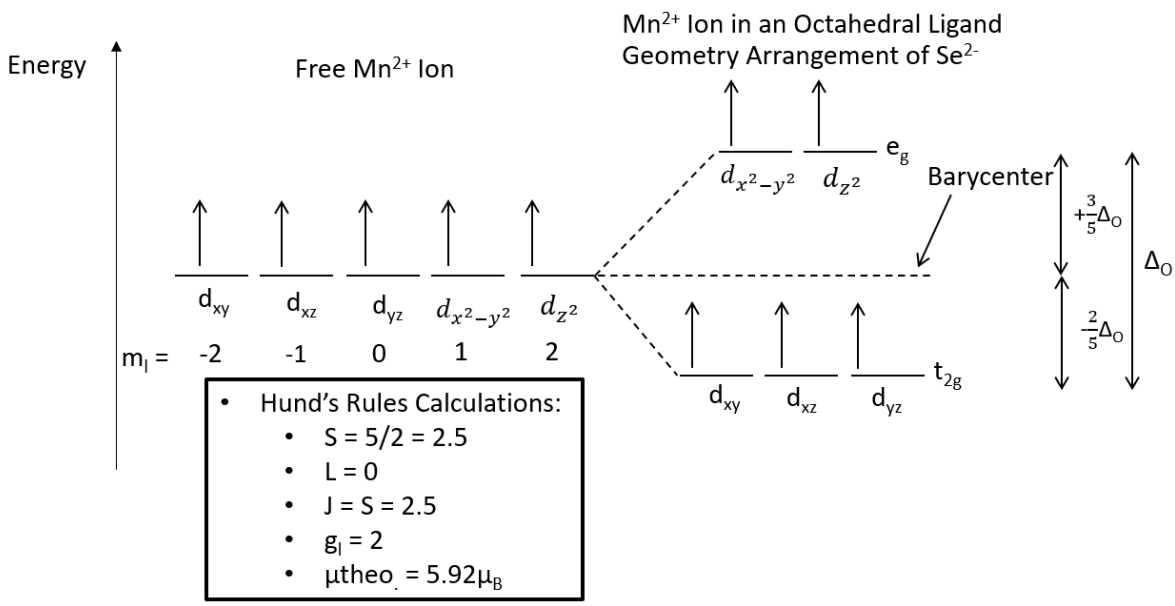

Figure 3.1.2: Predicting the Mn^{2+} [Ar]$3d^5$ theoretical magnetic moment in an octahedral Se^{2-} ligand geometry using Hund's rules and crystal-field theory.

Now, Hund's rules can be applied, and the theoretical magnetic moment can be calculated. In this arrangement, $\mu_{theo.} = 5.92\mu_B$. The $MnSb_2Se_4$ experimental magnetic moment was found to be $5.82\mu_B$, quite close to the predicted moment.[28] A similar type of magnetic moment analysis can also be applied to other magnetic materials as well.

Interestingly, for the case of $Fe_{1-x}Sn_xBi_2Se_4$, changes in the magnetic properties were observed with increasing Sn content.[32] In fact, increasing x was found to fundamentally change the magnetic lattice.[32] **Figure 3.1.3** shows the changes in the magnetic lattice at specific Sn content values. For the case of structure B and C, the Sn was found to substitute at the M1 and M2 sites, eventually replacing all Fe^{2+} magnetic moment from those sites.[32] At this point, the M1 and M2 sites become nonmagnetic.[32]

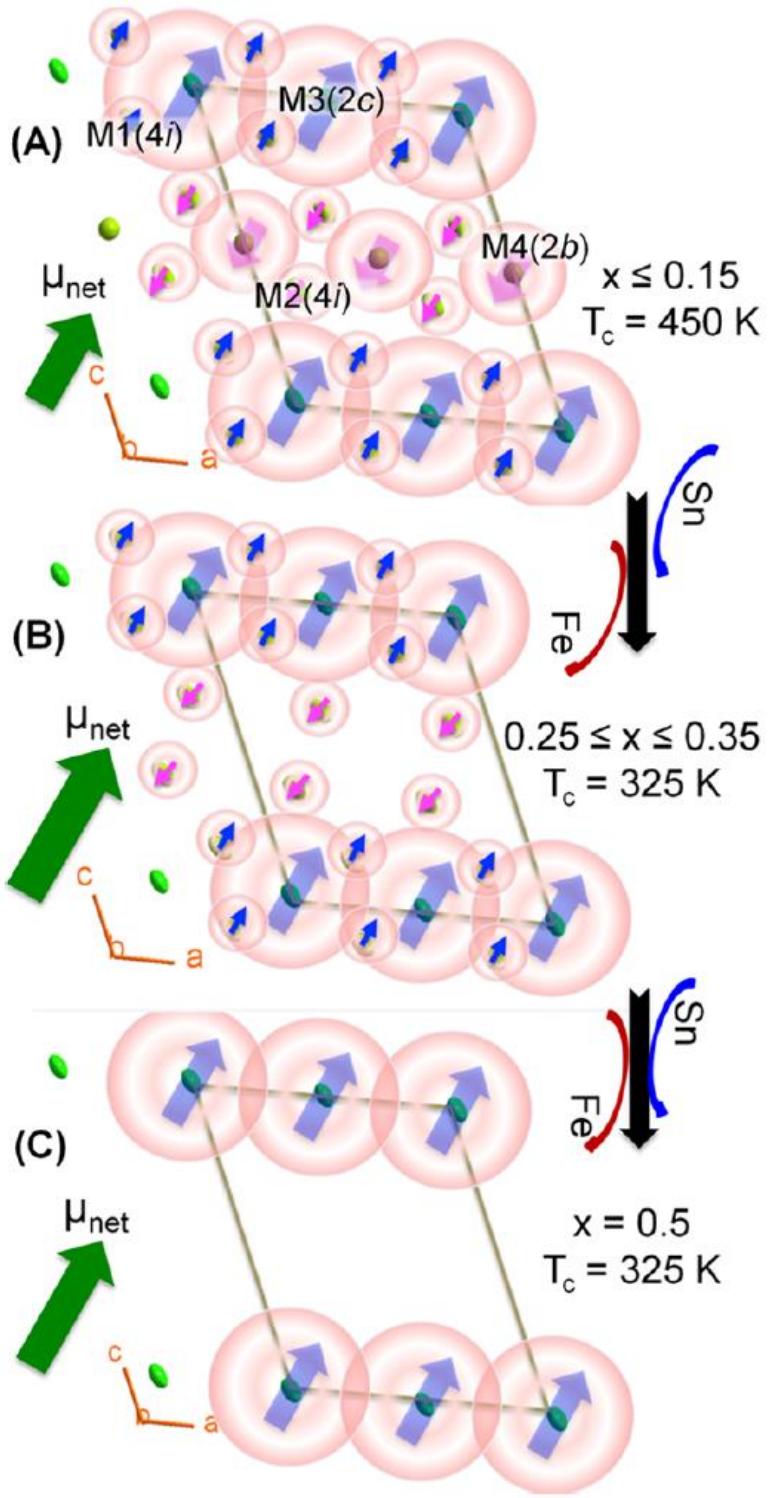

Figure 3.1.3: $Fe_{1-x}Sn_xBi_2Se_4$ changes in the magnetic lattice with increasing Sn content. Note that for the case of b and c, Sn preferentially substitutes at the M1 and M2 sites, eventually replacing the Fe magnetic moment completely, rendering the M1 and M2 sites nonmagnetic. Image was adapted from Lopez *et al*.[32]

$MnBi_2Se_4$ has recently received much attention in the topological insulator (TI) community. In the bulk, the material exhibits AFM ordering with T_N ~ 14 K; however, an atomically thin heterostructure of $MnBi_2Se_4$ and Bi_2Se_3 simultaneously exhibits ferromagnetic and topologically insulating behavior.[46] $MnBi_2Se_4/Bi_2Se_3$-based magnetic topological insulator (MTI) heterostructures display unique properties such as massive Dirac cones and axion insulator states.[46-49] Axion insulators are hopeful contenders for spintronics and quantum computing applications.[48]

In addition, $M_{1-x}M'_xPn_2Se_4$ has shown promise as a thermoelectric material as well. The thermoelectric figure of merit (zT) is defined as $zT = \sigma S^2T/\kappa_T$, where σ is electrical conductivity, S is Seebeck coefficient, T is temperature, and κ_T is total thermal conductivity. The total thermal conductivity is defined as $\kappa_T = \kappa_L + \kappa_e$, where κ_L and κ_e are the lattice and electronic thermal conductivities, respectively. Due to the low crystal symmetry, $M_{1-x}M'_xPn_2Se_4$ exhibits an ultra-low lattice thermal conductivity, a criterion that is critical for achieving a high figure of merit. In the case of $FeSb_{2-x}In_xSe_4$, for x = 0.25 at room temperature, κ_T = 0.27 W/mK; for x = 0.125 at 650 K, zT = 0.13 was observed. Wiedemann-Franz Law analysis determined that κ_L was the dominant contribution to κ_T.[42] Additionally, the thermoelectric properties of $MnSb_2Se_4$ were shown to be enhanced through Cu resonant doping. For x = 0.25 ($Mn_{0.75}Cu_{0.25}Sb_2Se_4$) at T = 773 K, zT = 0.64 was achieved, a 100% increase in zT compared to x = 0.[50] Further, by adding a 2 mol% secondary phase of $Mn_{0.8}Cu_{0.2}Sb_2Se_4$ to $Bi_{0.48}Sb_{1.52}Te_3$, a ~40% improvement in zT was observed. The $Mn_{0.8}Cu_{0.2}Sb_2Se_4$ nanoparticles served as phonon scattering centers, yielding a zT of 1.43 at 375 K.[51]

In this work, $Mn_{1-x}Zn_xSb_2Se_4$ (x = 0-0.15) was synthesized via a solid-state reaction. Structural, thermoelectric, and magnetic properties were probed to analyze its viability for

spintronic and thermoelectric applications. Powder X-ray diffraction was utilized to probe phase purity and Rietveld refinement was implemented to extract lattice parameters. Differential scanning calorimetry tested phase stability and thermal events, and X-ray photoelectron spectroscopy confirmed expected oxidation states of all elements. Temperature-dependent electrical conductivity (σ) and Seebeck coefficient (S) were measured, and S indicated a p-type semiconductor. The temperature-dependent electrical conductivity data was fit using an Arrhenius plot to calculate activation energy (E_a) and electronic bandgap (E_g). Heat capacity (C_p) and thermal diffusivity (D) were probed to extract the total thermal conductivity.

The Wiedemann-Franz Law was used to calculate κ_e; by subtracting the electronic thermal conductivity from κ_T, κ_L was found. Using this analysis, the relative contributions of the electronic and lattice thermal conductivity to κ_T was determined. Afterwards, the thermoelectric figure of merit, zT, was computed. Finally, temperature-dependent magnetic susceptibility was recorded and fit using the Curie-Weiss Law in the paramagnetic region. The Weiss constant was negative, indicating an antiferromagnetic coupling. The Langevin theory of paramagnetism was applied to calculate the effective magnetic moment for each composition. The theoretical magnetic moment was predicted using Hund's rules. Throughout the series, the effective magnetic moment calculated from the fitted data was consistently larger than the magnetic moment predicted by the spin and orbital angular momentum contributions only. So, an additional contribution must be adding to the magnetic moment in the lattice. A substitution mechanism of Mn with Zn at the M1 and M2 sites must be the cause, similar to what was observed in Lopez *et al.*'s work on $Fe_{1-x}Sn_xBi_2Se_4$.[32] This would explain the observed enhancement in the magnetic moment, as the lattice would convert from antiferromagnetic to ferrimagnetic-exhibiting a small permanent moment.

3.2 Synthesis: $Mn_{1-x}Zn_xSb_2Se_4$ (x = 0, 0.01, 0.04, 0.05, 0.06, 0.08, 0.1, 0.15)

3.2.1 Powder Synthesis:

Polycrystalline powders of $Mn_{1-x}Zn_xSb_2Se_4$ (x = 0, 0.01, 0.03, 0.04, 0.05, 0.06, 0.08, 0.1, 0.15) were generated from a solid-state reaction of elements. Stoichiometric amounts of Mn (99.3%, Alfa Aesar), Zn (100%, J.T. Baker Chemical), Sb (99.5%, Alfa Aesar), and Se (99.5%, Sigma Aldrich) were weighed in an argon glovebox and ground thoroughly with a mortar and pestle, vacuum flame-sealed in quartz tubes, and placed in a programmable furnace as described in **Section 2.1.1**. The reaction profile was as follows: heat to 573 K over 12 hours; dwell at 573 K for 48 hours; heat to 753 K over 4 hours; dwell at 753 K for 72 hours; cool to 298 K over 4 hours. Following the reaction, the lustrous dark-grey ingot was ground into a fine powder. In this form, powder X-ray diffraction (PXRD), differential scanning calorimetry (DSC), and low-temperature direct current (DC) magnetic susceptibility measurements were performed.

3.2.2 Hot-Pressed Pellet/Bar:

Hot pressing was carried out in a similar fashion as described in **Section 2.1.2**. The pressing temperature profile was as follows: heated to 623 K over 2 hours; dwelled at 623 K for 1 hour; cooled to 298 K over 2 hours. The pellet was pressed at a pressure of 98.6 MPa. The pellet was polished to a mirror finish using 400/600/800/1000 grit SiC paper. Proper densification was confirmed using a pycnometer (machine accuracy of < 0.3%). For electrical conductivity/Seebeck coefficient analysis, the pellet was cut into a rectangular bar with the approximate dimensions of 3 mm x 3 mm x 10 mm using an Isomet 1000 precision diamond saw and polished using the above SiC paper grit series.

3.3 Results & Discussion: $Mn_{1-x}Zn_xSb_2Se_4$ (x = 0-0.15)

3.3.1 Structural Properties of $Mn_{1-x}Zn_xSb_2Se_4$

Powder X-ray diffraction (PXRD)/Rietveld Refinement: To probe the phase purity of $Mn_{1-x}Zn_xSb_2Se_4$, powder X-ray diffraction was utilized. **Figure 3.3.1** depicts the PXRD of the composition series, plotted against a reference pattern. From x = 0.01-0.03, a single phase was formed; for x = 0.04-0.15, an extra ZnSe peak was detected. Additionally, in the case of x = 0.15, a small Sb_2Se_3 shoulder was found. Throughout the composition series, the patterns were shifted to lower 2θ (larger lattice parameter) relative to the reference, indicating successful zinc incorporation into the lattice. However, even x = 0 lattice parameters were found to be larger than the $MnSb_2Se_4$ reference (ICSD Ref. #421940[28]). To extract lattice parameters of the ternary and binary phases, Rietveld refinement using FullProf was implemented. **Section 2.2.2** describes the refinement procedure in more detail. **Figure A.1** shows manual peak analysis to extract accurate lattice parameters for refinement. **Figure A.2** describes the steps used in refinement. The best refinement fit (χ^2 = 0.824) was found for x = 0.05, seen in **Figure 3.3.2**.

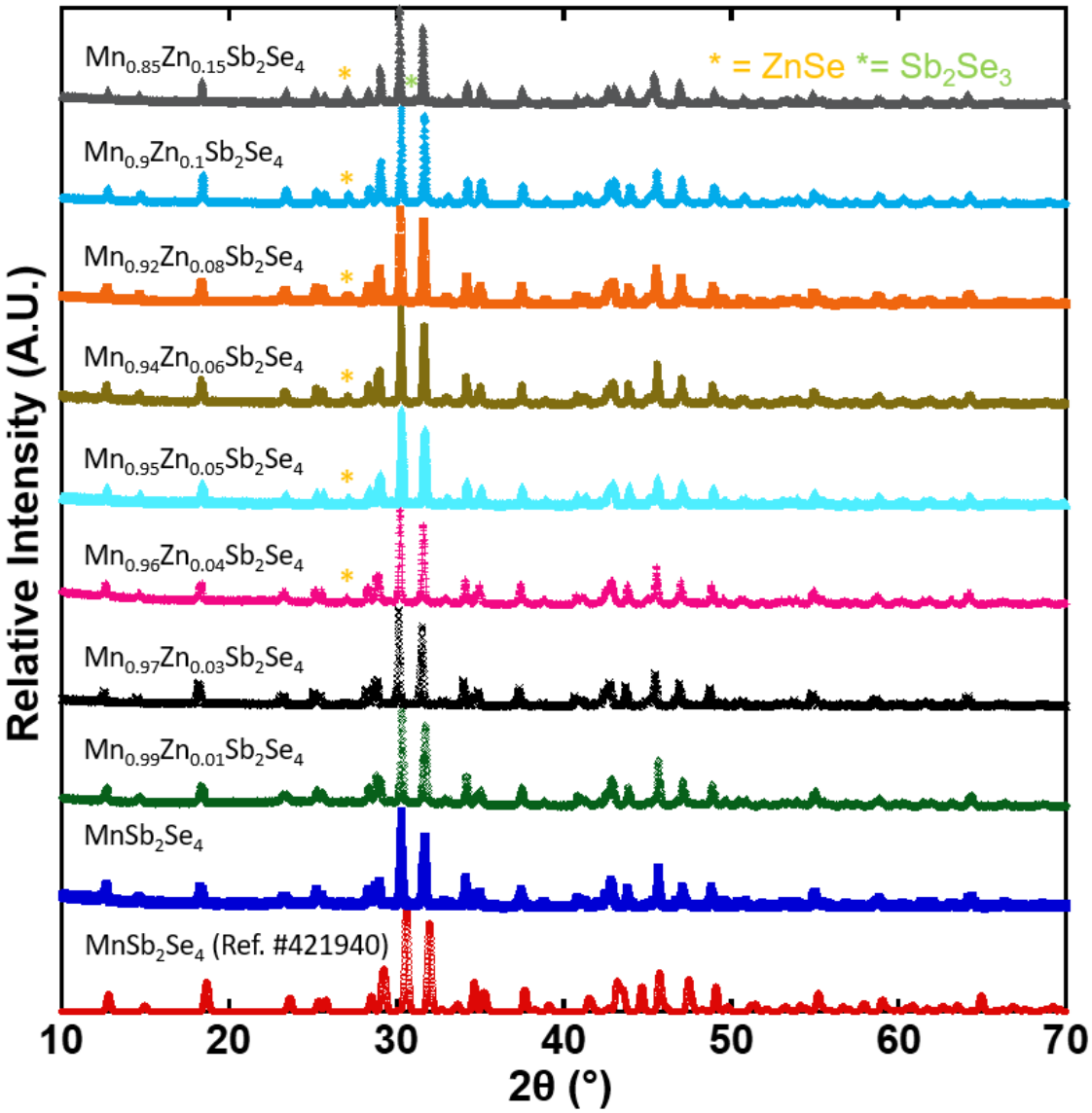

Figure 3.3.1: Powder X-ray diffraction of complete $Mn_{1-x}Zn_xSb_2Se_4$ series, compared to ICSD Reference #421940[28] ($MnSb_2Se_4$, C12/m1). Binary impurity phases of ZnSe (ICSD #77091[29], F-43m) and Sb_2Se_3 (ISCD #16680[52], Pbnm) are noted by the yellow and green asterisks, respectively.

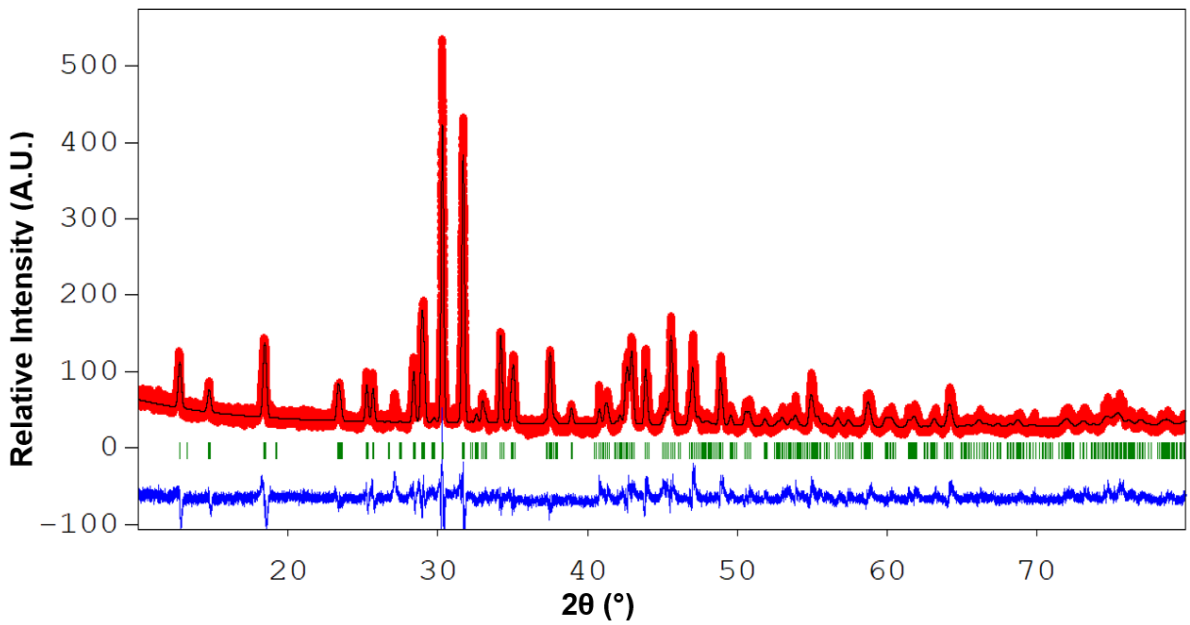

Figure 3.3.2: Powder XRD Rietveld refinement fit for $Mn_{0.95}Zn_{0.05}Sb_2Se_4$. In the figure, the red curve is the experimental pattern, the black line is the fitted pattern, the green tick marks correspond to the peak positions, and the blue curve is the difference pattern between experimental and fitted patterns. The quality of fit was $\chi^2 = 0.824$.

Figure 3.3.3 depicts the extracted lattice parameters for $Mn_{1-x}Zn_xSb_2Se_4$. The a/b axes were relatively constant, while a slight decrease in c axis and β angle with increasing zinc content was observed. The c-axis decreased by 1.1% (Δc/c) and the β angle reduced by 0.4% (Δβ/β) for x = 0.15 relative to x = 0. The decrease in the c-axis with increasing zinc content is consistent with substituting high-spin Mn^{2+} $\left(CN = 6;\ R_{Mn^{2+}} = 0.83\ Å\right)$ with Zn^{2+} $\left(CN = 6;\ R_{Zn^{2+}} = 0.74\ Å\right)$, an ionic radius reduction of ~11% (ΔR/R). The inset of **Figure 3.3.3** highlights the shortening of the c-axis with increasing zinc content. Numerical values of the lattice parameters, volume of the monoclinic cell (V_{cell}), and best quality of fit for each composition are listed in **Table 3.3.1**. The equation for V_{Cell} is as follows:

$$V_{Cell} = abc \times \sin\beta. \qquad \textbf{3.3-1.}$$

V_{cell} was found to fluctuate around ~740 Å^3 aside from x = 0.08, which exhibited a cell volume of 775 Å^3; this is because the a-axis was elongated by ~4.3% (Δa/a) relative to x = 0.

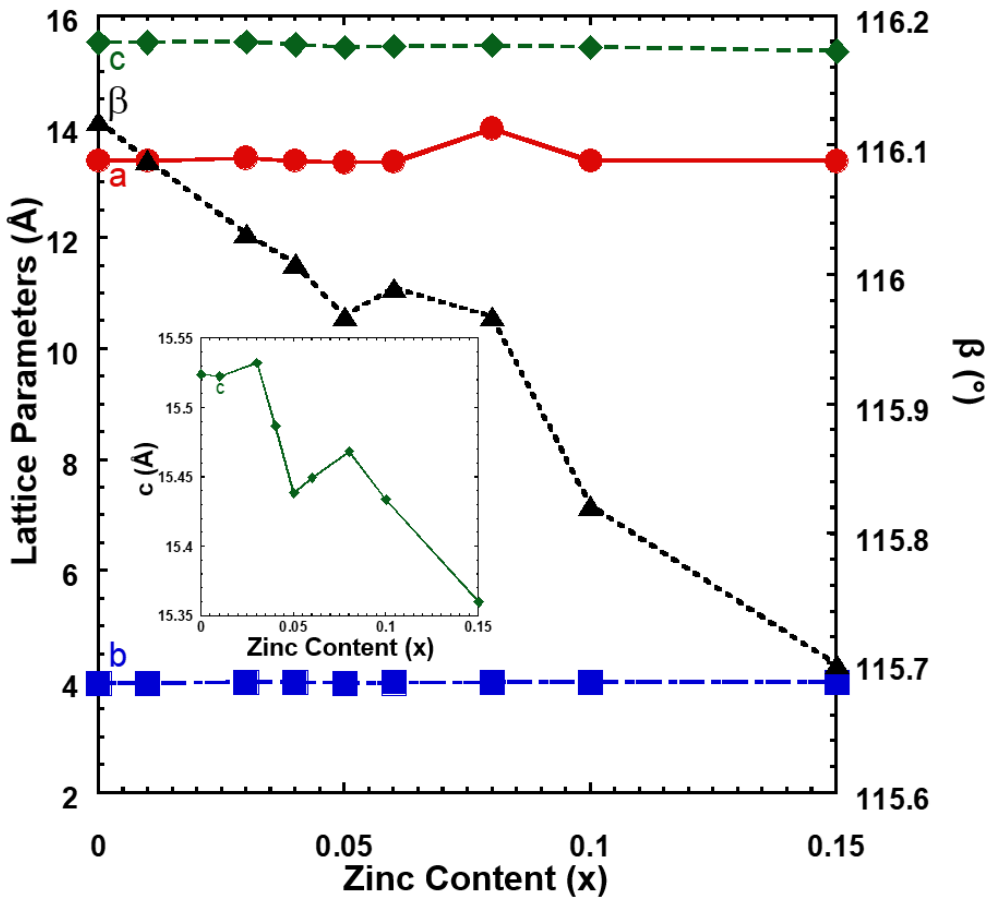

Figure 3.3.3: Lattice parameters vs. zinc content. The inset of the plot highlights the overall downward trend in the c-axis with increasing zinc content.

Table 3.3.1: Extracted information from Rietveld refinement of the main phase. From refinement, lattice parameters were discovered, and the volume of the monoclinic unit cell was calculated using **Equation 3.3-1**. The best χ^2 fit for each composition was also listed.

Zn Content (x)	a (Å)	b (Å)	c (Å)	β (°)	V_{cell} (Å^3)	Best χ^2 Fit
0*	13.076	3.9651	15.236	115.07	715.53	N/A
0	13.394	3.9744	15.524	116.12	741.99	1.34
0.01	13.396	3.9797	15.523	116.09	743.24	2.28
0.03	13.437	3.9956	15.533	116.03	749.36	18.7
0.04	13.398	3.9863	15.487	116.01	743.36	8.34
0.05	13.357	3.9789	15.439	115.97	737.67	0.824
0.06	13.369	3.982	15.45	115.99	739.31	4.12
0.08	13.97	3.9893	15.469	115.97	775.04	14.9
0.1	13.389	3.9906	15.434	115.82	742.31	21.1
0.15	13.383	3.9964	15.36	115.7	740.25	13.5

For x = 0.04-0.15, additional Rietveld refinement was performed on the secondary ZnSe phase to refine its lattice parameter and improve the quality of fit. **Table A.1** portrays the information revealed from Rietveld refinement of the secondary phase. A slight improvement in χ^2 was for x = 0.04-0.15, and the lattice parameter increased between ~0.05-0.6% relative to ZnSe (ICSD Ref. #77091[29]). The slight increase in lattice parameter indicated that a possible $Zn_{1-y}Mn_ySe$ solid solution was forming, as the rise in the a-axis is consistent with replacing Zn^{2+} $\left(\mathrm{CN} = 4;\ \mathrm{R}_{\mathrm{Zn}^{2+}} = 0.6\ \text{Å}\right)$ with high-spin Mn^{2+} $\left(\mathrm{CN} = 4;\ \mathrm{R}_{\mathrm{Mn}^{2+}} = 0.66\ \text{Å}\right)$, a rise in the ionic radius by 10% (ΔR/R). To determine the Mn content (y) substituting in $Zn_{1-y}Mn_ySe$, a Vegard's Law equation was established:

$$a_{Zn_{1-y}Mn_ySe} = ya_{MnSe} + (1 - y)a_{ZnSe} \qquad \textbf{3.3-2.}$$

The $Zn_{1-y}Mn_ySe$ lattice parameter was determined previously using secondary refinement, while a_{MnSe} and a_{ZnSe} were referenced using ICSD Ref. #'s 24252[53] and 77091[29], respectively. The equation was rearranged for y:

$$y = \frac{a_{Zn_{1-y}Mn_ySe} - a_{ZnSe}}{a_{MnSe} - a_{ZnSe}} \quad \textbf{3.3-3,}$$

and it was discovered that between y = 0.0175-0.238 Mn was substituting at the Zn site in $Zn_{1-y}Mn_ySe$ for x = 0.04-0.15. During refinement, quantitative phase coefficient analysis (ATZ) was applied to calculate the weight percent of each phase present for x = 0.04-0.15; it was determined that between 0.5-1.5 wt% $Zn_{1-y}Mn_ySe$ was present in addition to the ternary phase for the mixed phase compositions. FullProf determined the weight percent of each phase by the equation:

$$ATZ = \frac{ZM_w f^2}{t} \quad \textbf{3.3-4,}$$

where Z is the number of formula units per cell, M_w is the molecular weight, f is the site multiplicity, and t is the Brindley coefficient for microabsorption. Since only a minor amount of $Zn_{1-y}Mn_ySe$ impurity phase is present for x = 0.04-0.15, major effects on the physical properties are not expected.

Differential Scanning Calorimetry (DSC): To probe the phase purity and effects of Zn incorporation on melting point, differential scanning calorimetry was implemented. **Figure 3.3.4** depicts the DSC curve of each sample composition, respectively.

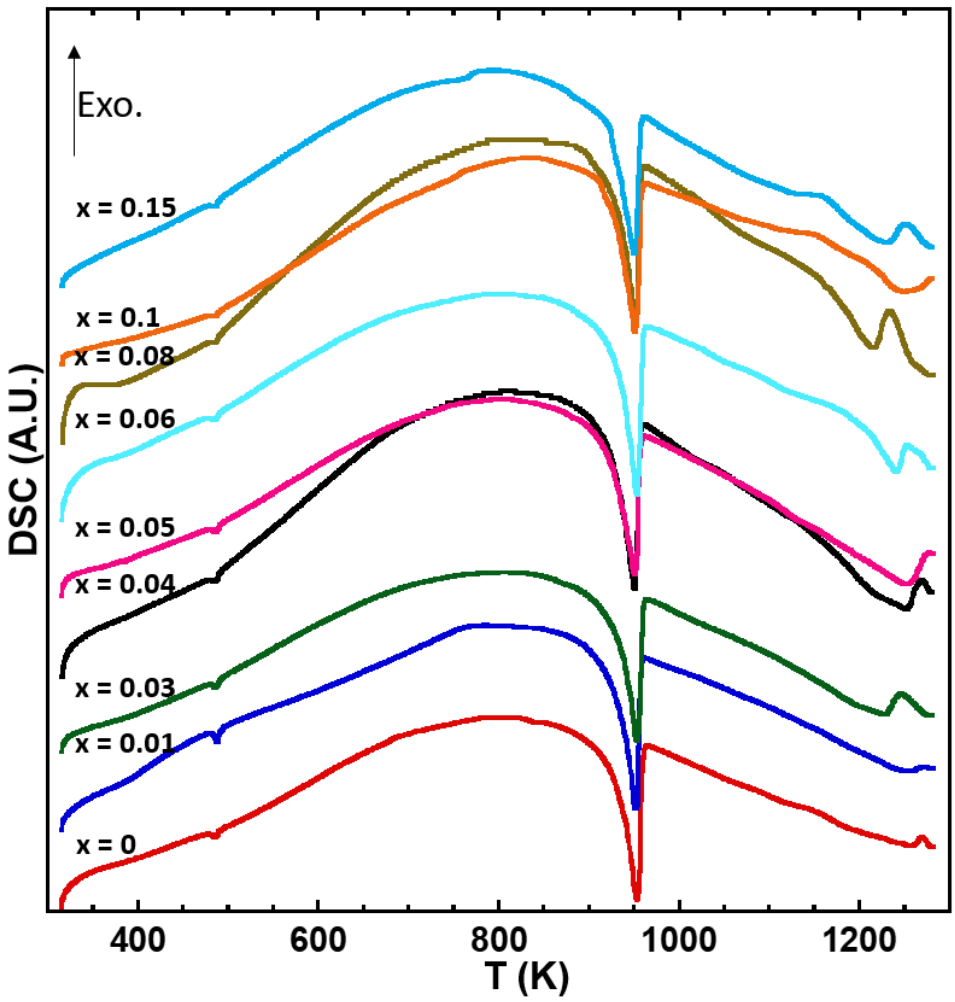

Figure 3.3.4: Differential scanning calorimetry (DSC) vs. temperature for various compositions. A small Se melting peak was observed for all samples at ~488 K. T_m was found to be between 950-953 K, decreasing slightly from low to high zinc content.

All samples exhibited a small endothermic Se melting peak at ~488 K, followed by an endothermic $Mn_{1-x}Zn_xSb_2Se_4$ melting peak ranging from ~950-953 K. With increasing Zn content, the melting point is shown to gradually decrease. After first melting, the ternary phase was found to decompose. Curiously, x = 0 exhibited a melting point of 953.3 K, ~160 K higher than previously reported melting point values of $MnSb_2Se_4$ (T_m = 790 K).[28]

X-ray photoelectron spectroscopy (XPS): X-ray photoelectron spectroscopy was used to verify the elemental oxidation states in $Mn_{1-x}Zn_xSb_2Se_4$. **Figure 3.3.5a-d** reveals the XPS core scan results for Mn, Zn, Sb, and Se, respectively; the relevant chemical states of each plot were also noted. The Mn and Zn graphs showed noticeably weaker signal and stronger noise when compared to the Sb and Se plots, but this can be explained based on stoichiometry. Recall that the $Mn_{1-x}Zn_xSb_2Se_4$ (x = 0-0.15) compound has between 12.1-14.3 at% Mn, 0-2.1 at% Zn, 28.6 at% Sb and 57.1 at% Se. Due to the small amounts of Mn and Zn relative to Sb and Se, it was difficult to precisely determine the peak locations for some Mn and Zn compositions. Mn $2p_{3/2}$ exhibited a binding energy (BE) of 641.4 eV, aligning well with MnSe reference values.[54] Zn $2p_{3/2}$ had a BE of 1024.7 eV, corresponding to ZnSe reference values.[55] Sb $3d_{5/2}$ had a BE of 529.6 eV, matching reported Sb_2Se_3 values.[56] Se $3d_{3/2}$ and $3d_{5/2}$ had binding energies of 54.7 eV and 54.2 eV, respectively, consistent with SnSe reference energies.[31] **Table A.2** contains the extracted XPS energy values, as well as the corresponding elemental energy windows for reference. It was determined that all elements were in their expected oxidation states: Mn^{2+}, Zn^{2+}, Sb^{3+}, and Se^{2-}.

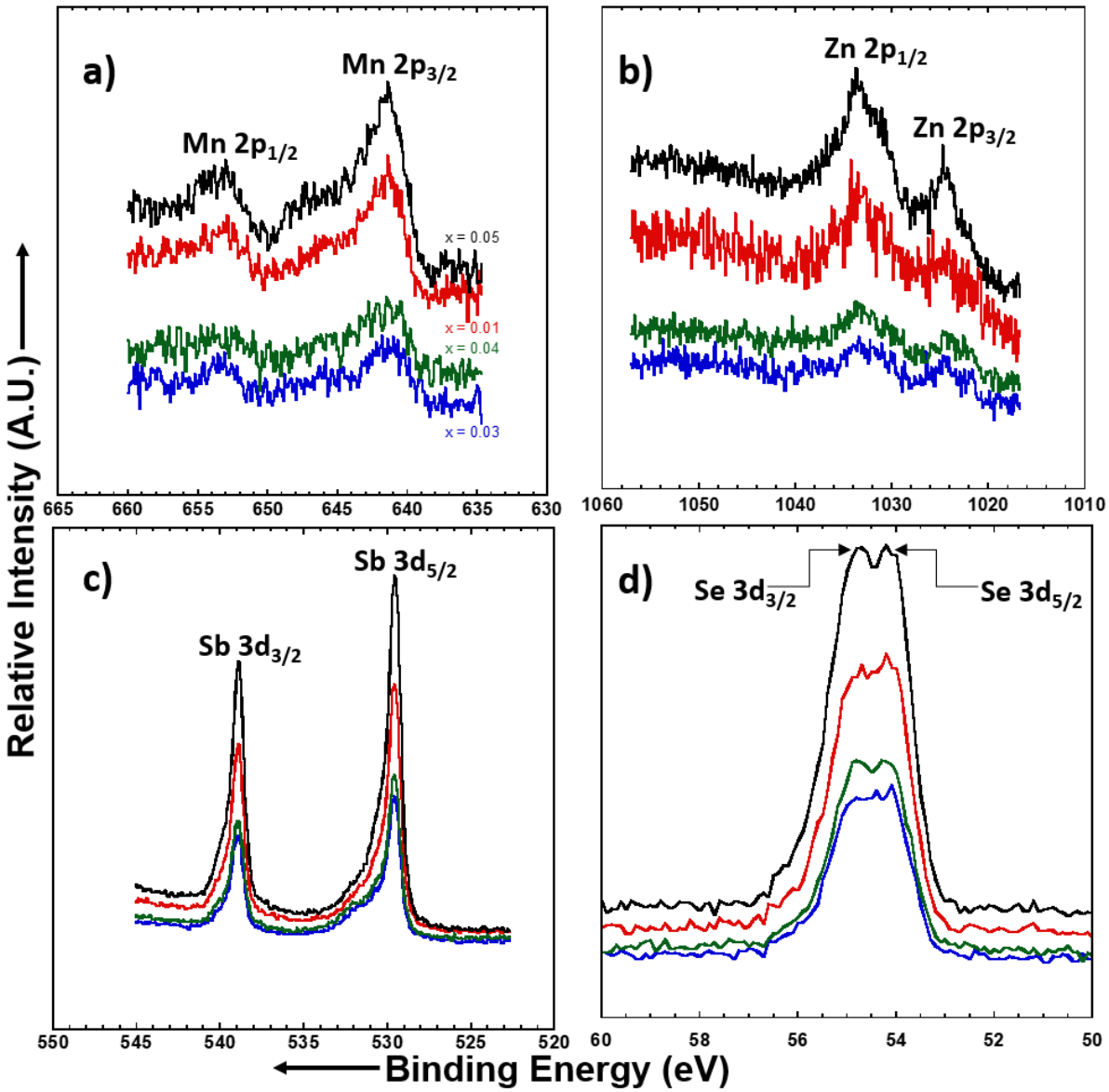

Figure 3.3.5: XPS counts per second vs. binding energy for **(a)** Mn; **(b)** Zn; **(c)** Sb; **(d)** Se.

3.3.2 Thermoelectric Properties of $Mn_{1-x}Zn_xSb_2Se_4$

Temperature-dependent electrical conductivity (σ) and Seebeck coefficient (S) were measured to analyze the effects of Zn substitution on the thermoelectric properties. Raw heating and cooling σ/S data were fit using 6th-order and 3rd-order polynomials with respect to temperature, respectively, with polynomial coefficients taken to 16 decimal places. **Figure 3.3.6a** presents the fitted σ data, exhibiting exponential behavior with temperature-typical of a semiconductor.

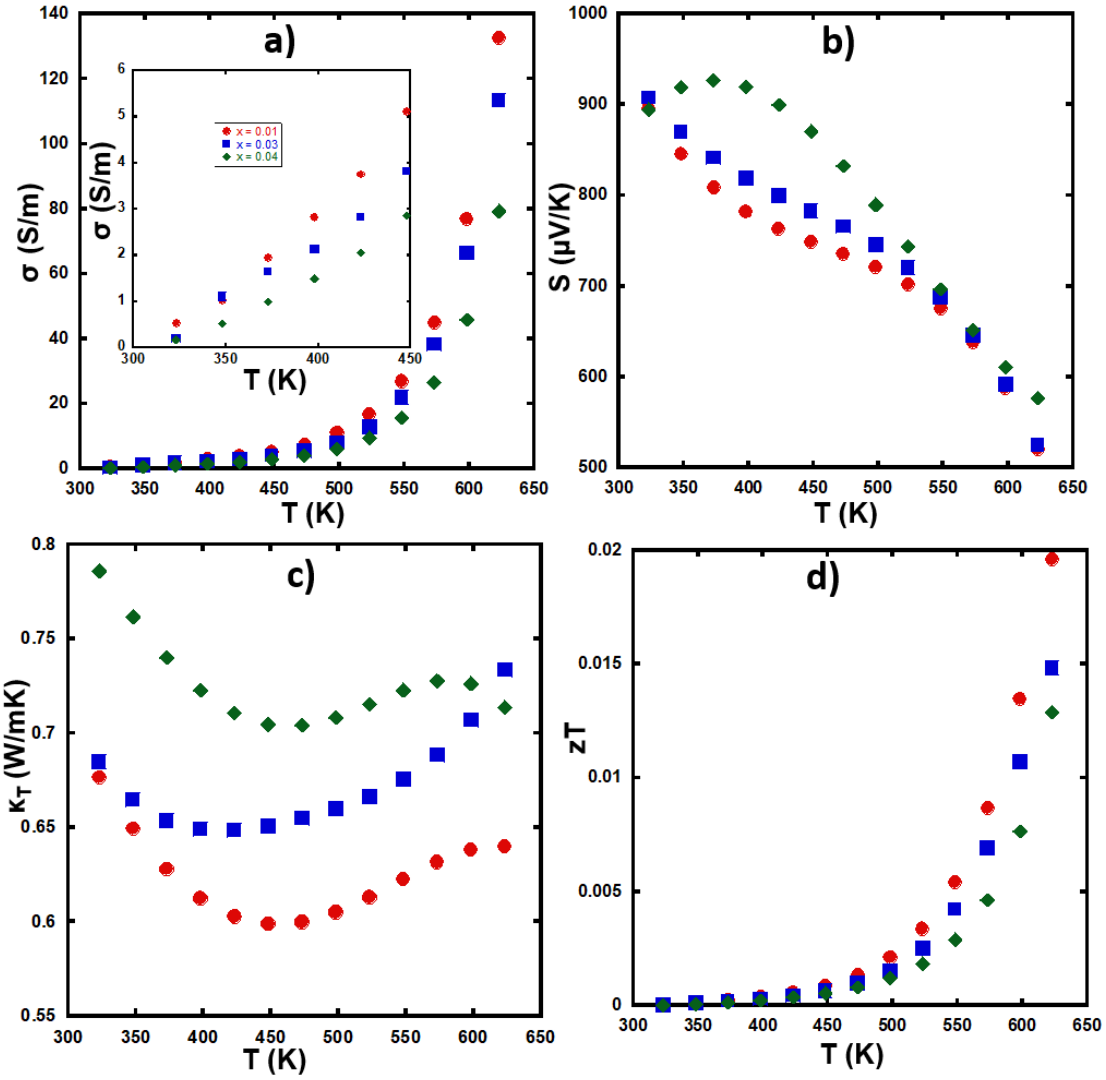

Figure 3.3.6: Temperature-dependent thermoelectric properties: **(a)** electrical conductivity (σ) with an inset zooming in from 300-450 K; **(b)** thermopower (S); **(c)** total thermal conductivity (κ_T); **(d)** figure of merit (zT).

The inset in **Figure 3.3.6a** zooms in from T = 300-450 K to highlight the trend in electrical conductivity with Zn content. A slight decrease in σ with increasing zinc content is observed. At 323.15 K, the electrical conductivity of x = 0.01 is 0.53 S/m; at 623.15 K, σ = 132.53 S/m. Since an exponential relationship between σ and T was observed, ln(σ) vs. 1/T Arrhenius plots were utilized to uncover the activation energy (E_a) and electronic bandgap (E_g) of each composition. For each Arrhenius plot, the curve was separated into three regions: low-T, medium-T, and high-T. The low-T region corresponds to the extrinsic section of the plot; activation energy was extracted from fitting this section. The medium-T region corresponds to the saturation plateau. Finally, the high-T region corresponds to the intrinsic region of the plot; electronic bandgap was gathered from fitting this region. **Figure 3.3.7a** shows the $Mn_{0.99}Zn_{0.01}Sb_2Se_4$ ln(σ) vs. 1/T Arrhenius plot; **Figure 3.3.7b** portrays the intrinsic region fitting for x = 0.01; **Figure 3.3.7c** depicts the extrinsic region fitting for x = 0.01. **Figure A.3** and **Figure A.4** presents the same Arrhenius fitting for x = 0.03 and x = 0.04, respectively. For x = 0.01, 0.03, and 0.04, E_a was determined to be 0.252 eV, 0.290 eV, and 0.291 eV, respectively; E_g was determined to be 1.16 eV, 1.23 eV, and 1.20 eV.

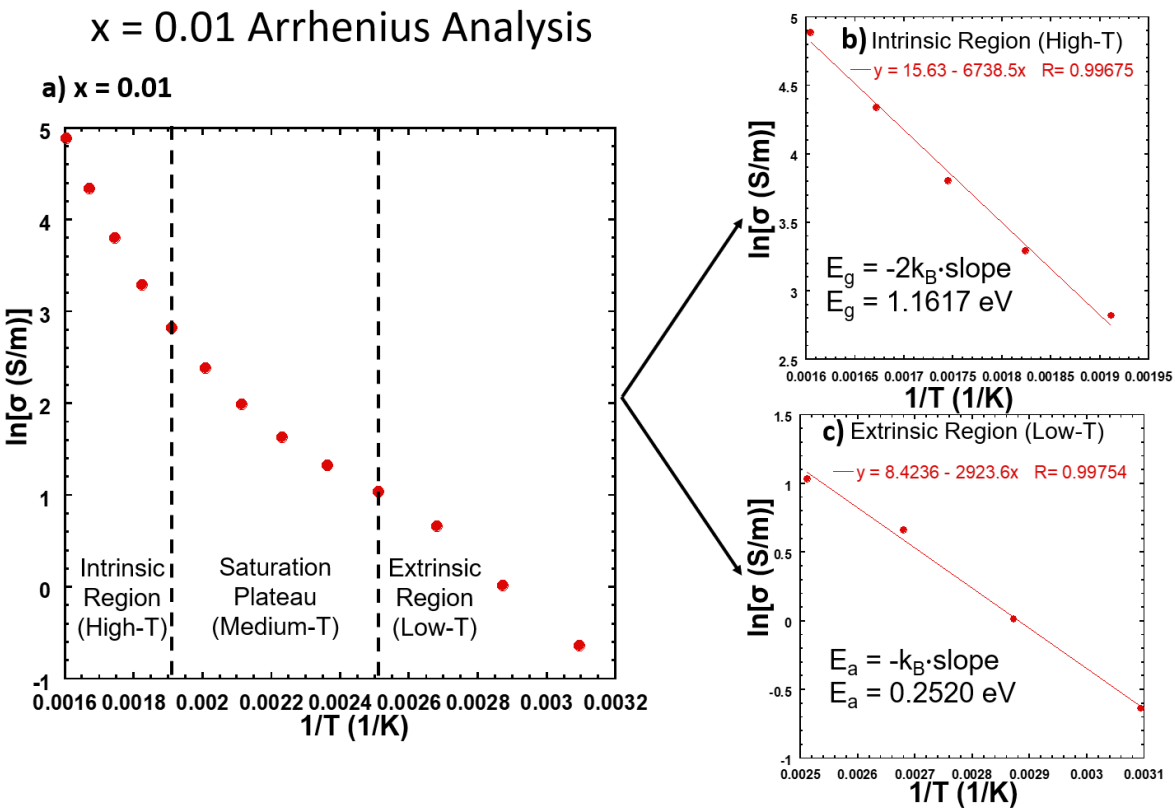

Figure 3.3.7: (a) $Mn_{0.99}Zn_{0.01}Sb_2Se_4$ (x = 0.01) electrical conductivity Arrhenius plot. The figure was divided into the intrinsic region, saturation plateau, and extrinsic region depending on temperature; **(b)** Intrinsic region Arrhenius plot, utilized to extract electronic bandgap, E_g; **(c)** Extrinsic region Arrhenius plot, employed to obtain activation energy, E_a.

Table 3.3.2 and **Figure 3.3.8** portrays numerical and graphical representations of E_a and E_g vs. Zn content, respectively. The fact that E_a is increasing with increasing Zn content is consistent with the decrease in conductivity.

Table 3.3.2: Electronic bandgap (E_g) and activation energy (E_a) at various zinc content (x).

x Value	E_g (eV)	E_a (eV)
0.01	1.16	0.252
0.03	1.23	0.290
0.04	1.20	0.291

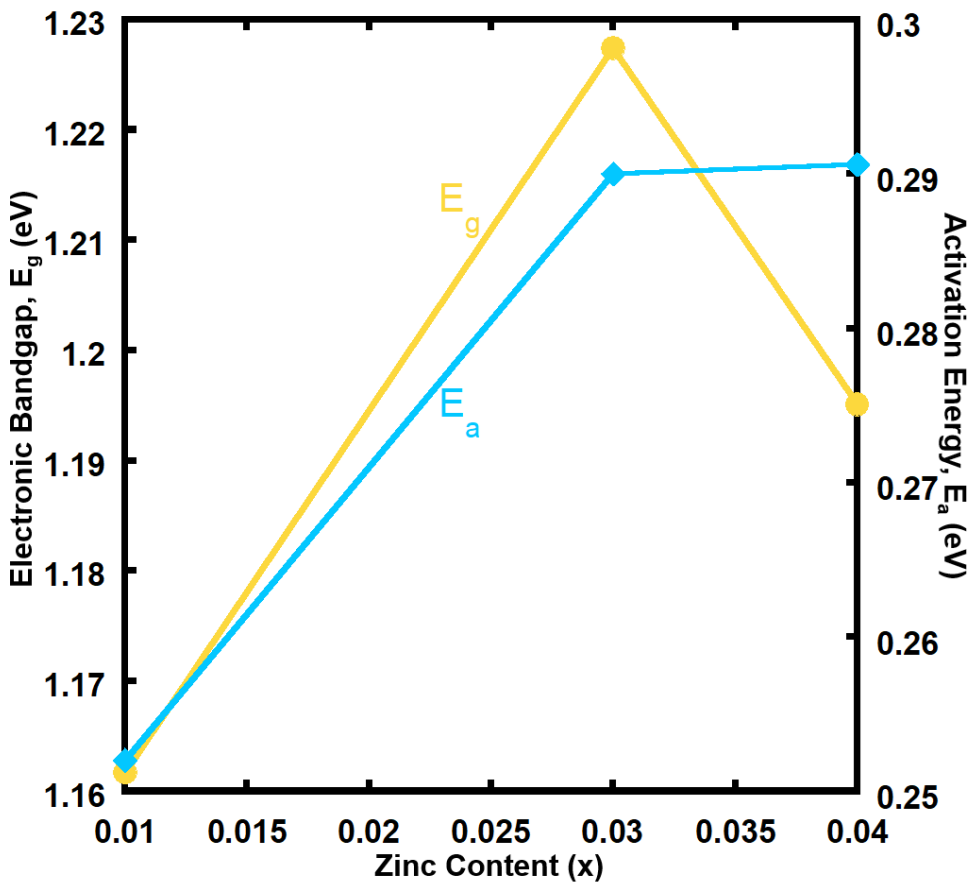

Figure 3.3.8: Electronic bandgap (E_g) and activation energy (E_a) at different Zn content, gathered by fitting temperature-dependent electrical conductivity data using the Arrhenius relationship.

Figure 3.3.6b portrays the fitted thermopower data; throughout the temperature range, S is positive, indicating a p-type material. Seebeck coefficient is seen to decrease slightly from x = 0.04 to 0.01, with S_{max} = +926.97 μV/K at 373.15 K for x = 0.04. Assuming a single parabolic band, thermopower is given by $S = \left(8\pi^{8/3}{k_B}^2/3^{5/3}h^2\right)m^* p^{-2/3}T$, where k_B is Boltzmann's constant, h is Planck's constant, m* is effective mass, p is hole concentration, and T is temperature. Interestingly, Seebeck coefficient is seen to decrease with increasing temperature for all samples, but the model states that S should increase linearly with temperature; this implies that either m* or p is causing the overall downward trend. Effective mass is inversely proportional to band structure curvature, so if this is causing the decrease in S, the curvature of the band structure must

steepen upon further zinc substitution. However, Mn^{2+} ([Ar]$3d^5$) and Zn^{2+} ([Ar]$3d^{10}$) both possess 3d valence electron distributions, so no major changes in the band structure are expected. By deduction, the hole concentration is increasing with temperature, causing the thermopower to decrease accordingly since $S \alpha p^{-2/3}$. In **Figure 3.3.6a-b**, opposite trends in σ and S with zinc content are observed. This is consistent with the rise in E_a as Zn content increases, as if E_a grows, σ and p decreases, while S increases accordingly.

To calculate the thermoelectric figure of merit ($zT = \sigma S^2T/\kappa_T$) for this system, the total thermal conductivity (κ_T) first needed to be probed. To accomplish this, laser flash analysis (LFA) was utilized to measure heat capacity (C_p) and thermal diffusivity (D), and the total thermal conductivity was calculated using the equation $\kappa_T = \rho C_p D$, where ρ is the density of the pressed pellet. Raw κ_T data was fit using a 4th-order temperature polynomial with respect to temperature, with polynomial coefficients taken to 16 decimal places. **Figure 3.3.6c** illustrates the temperature-dependent total thermal conductivity. With increasing zinc content, κ_T is seen to increase as well. This trend can be correlated to the shortening of the c-axis with increasing Zn; as the c-axis decreases, bond strength increases, making κ_T increase as a result. The minimum total thermal conductivity value of 0.599 W/mK was observed for x = 0.01 at T = 448.15 K. **Figure 3.3.6d** illustrates the temperature-dependent figure of merit (zT) for x = 0.01-0.04; zT followed the same trend as electrical conductivity, with x = 0.01 possessing the highest figure of merit ($zT_{max} = 0.02$ at 623.15 K).

To determine the electronic thermal conductivity (κ_e) contribution to the total thermal conductivity (κ_L), the Wiedemann-Franz Law ($\kappa_e = \sigma LT$) was implemented, where L = 2.44 x 10^{-8} $W\Omega/K^2$-the Lorenz number (metallic value). However, the electrical conductivity of $Mn_{1-x}Zn_xSb_2Se_4$ was relatively low (~10^{-1}-10^{-2} S/m), much smaller than typical σ values of metals-

shown in **Table A.3**. As such, one must correct the L values using Fermi-corrections, applying the same analysis as in Lu *et al*.[57] Please refer to **Appendix I** for equations on the Fermi-corrected Lorenz #. **Figure A.5**, **Figure A.6**, **Figure A.7**, and **Figure A.8** contain the relevant files, data and results files, and Mathematica script, respectively. The script was written by Hang Chi of the Uher group. Refer to **Table 3.3.3** and **Figure 3.3.9** for the Fermi-corrected Lorenz # values gathered. In general, L was found to be ~40% lower than the metallic value. L was found to be dependent on T, increasing slightly with increasing T.

Table 3.3.3: Table of corrected Lorenz # vs. temperature for x = 0.01-0.04. Due to the low σ of the samples, Fermi-corrected Lorenz # calculations were applied. For x = 0.01-0.04, the corrected L was found to be ~40% lower than the metallic value (2.44 x 10^{-8} W-Ω/K^2).

T (K)	x = 0.01 Fermi-Corrected L (W-Ohm/K^2)	x = 0.03 Fermi-Corrected L (W-Ohm/K^2)	x = 0.04 Fermi-Corrected L (W-Ohm/K^2)
323.15	1.48521E-08	1.48521E-08	1.48521E-08
348.15	1.48525E-08	1.48523E-08	1.48520E-08
373.15	1.48529E-08	1.48525E-08	1.48520E-08
398.15	1.48533E-08	1.48527E-08	1.48520E-08
423.15	1.48537E-08	1.48530E-08	1.48521E-08
448.15	1.48540E-08	1.48533E-08	1.48523E-08
473.15	1.48544E-08	1.48536E-08	1.48526E-08
498.15	1.48549E-08	1.48541E-08	1.48532E-08
523.15	1.48557E-08	1.48549E-08	1.48542E-08
548.15	1.48572E-08	1.48564E-08	1.48559E-08
573.15	1.48601E-08	1.48594E-08	1.48588E-08
598.15	1.48668E-08	1.48660E-08	1.48632E-08
623.15	1.48846E-08	1.48829E-08	1.48688E-08

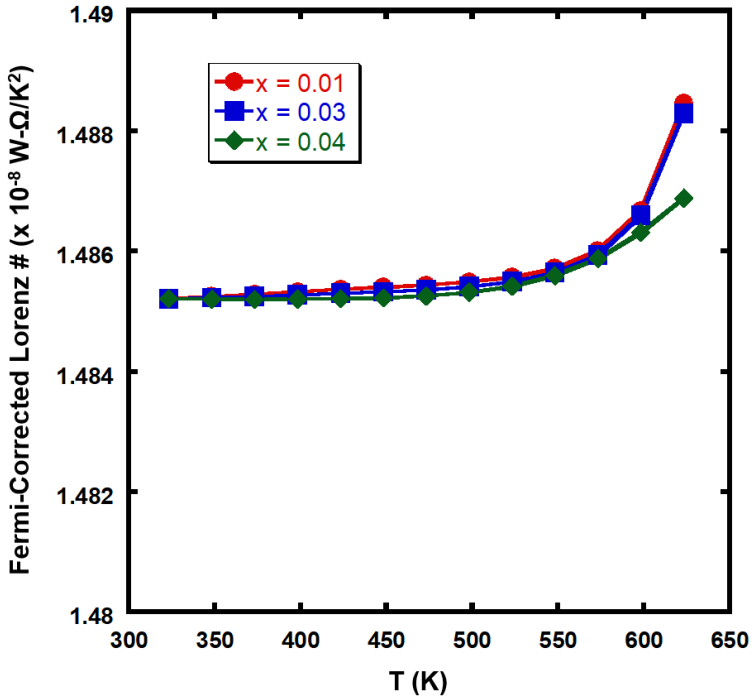

Figure 3.3.9: Due to the low electrical conductivity of the samples, Fermi-corrected Lorenz # calculations were applied. For x = 0.01-0.04, the corrected L was found to be ~40% lower than the metallic value (2.44 x 10^{-8} W-Ω/K^2). Plot of corrected Lorenz # vs. temperature.

To decouple the electronic (κ_e) and lattice thermal conductivity (κ_L) contributions to κ_T, the equation $\kappa_T = \kappa_L + \kappa_e$ was solved for κ_L. **Figure 3.3.10a** presents the total thermal conductivity for x = 0-0.04. κ_T was observed to increase with increasing x value, correlating well with the shortening of the c-axis upon increasing Zn content. Refer to **Figure 3.3.10b-c** for the results of the electronic and lattice thermal conductivity, respectively. It was determined that κ_e contributed $\leq$ 0.19% to κ_T; this minor amount is consistent with the fact that σ is small and L ~ 10^{-8}. So, κ_L contributed $\geq$ 99.81% to κ_T; this is attributed to the low symmetry of the monoclinic crystal lattice (C2/m).

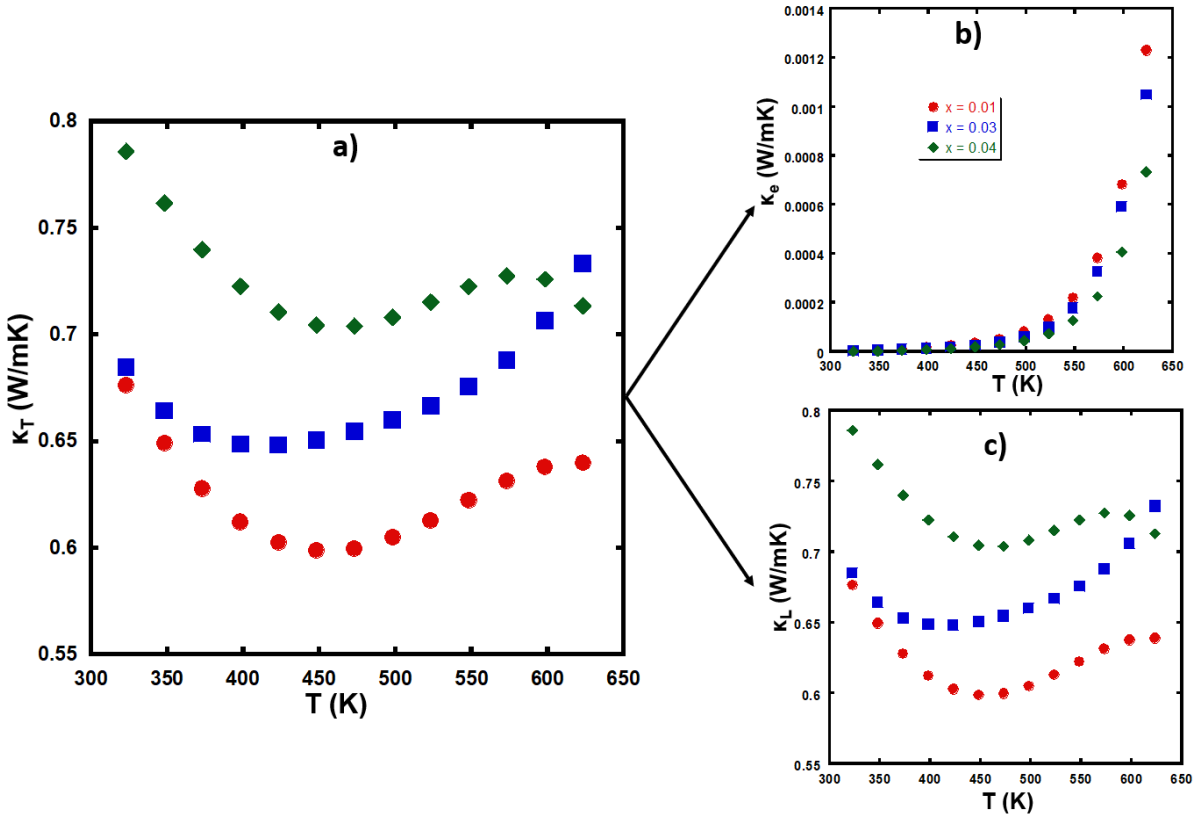

Figure 3.3.10: (a) Total thermal conductivity vs. temperature for all samples; **(b)** Electronic thermal conductivity (κ_e) and **(c)** Lattice thermal conductivity (κ_L) contributions, utilizing Wiedemann-Franz Law analysis. It was determined that κ_e contributed $\leq$ 0.19% to κ_T.

3.3.3 Magnetic Properties of $Mn_{1-x}Zn_xSb_2Se_4$

To characterize the magnetic behavior of $Mn_{1-x}Zn_xSb_2Se_4$, temperature-dependent magnetic susceptibility (χ) was performed from 2-300 K, under zero field-cooled (ZFC) and field-cooled (FC) conditions. **Figure A.9a-b** depicts the χ vs. T behavior of x = 0-0.15 in ZFC and FC configurations; typical antiferromagnetic (AFM) behavior was observed. The Néel temperature (T_N) ranged from 16.5-21.5 K, where the reported T_N values were averaged between the ZFC and FC curves for each x value. Since **Figure A.9** was crowded due to the multitude of compositions, x = 0.01 was selected as a representation of the ZFC and FC χ vs. T data for **Figure 3.3.11a-b**.

To extract the effective magnetic moment (μ_{eff}) of each composition, the susceptibility data was fit using the Curie-Weiss Law, $\chi = C/(T - \theta)$, where C is the Curie constant and θ is the Weiss constant. By expressing χ as inverse magnetic susceptibility (χ^{-1}), a linear relationship with temperature is revealed. **Figure 3.3.11c-d** portrays the ZFC and FC χ^{-1} vs. T data for x = 0.01; **Figure A.9c-d** presents the ZFC and FC χ^{-1} vs. T data for all compositions. From fitting a linear trendline to the inverse susceptibility data, both C and θ were calculated; to ensure a good quality of fit, the trendline was implemented for the most linear segment of the χ^{-1} vs. T plots-from ~170-300 K. The Curie constant was found to range between 5.29-9.22 emu·K/Oe·mol, while θ spanned from -63.8 K to -140.5 K. The Weiss constant is a measure of the magnetic coupling in the system; a negative θ corresponds to antiferromagnetic ordering, consistent with the observed AFM behavior in the magnetic susceptibility. With the Curie constant determined, the Langevin theory of paramagnetism was applied to calculate the effective magnetic moment for each composition; C is related to μ_{eff} by the expression $\mu_{eff} = \sqrt{3Ck_B/N_A}$, where k_B is Boltzmann's constant and N_A is Avogadro's number. The effective magnetic moment was found to range between 6.5-8.59μ_B.

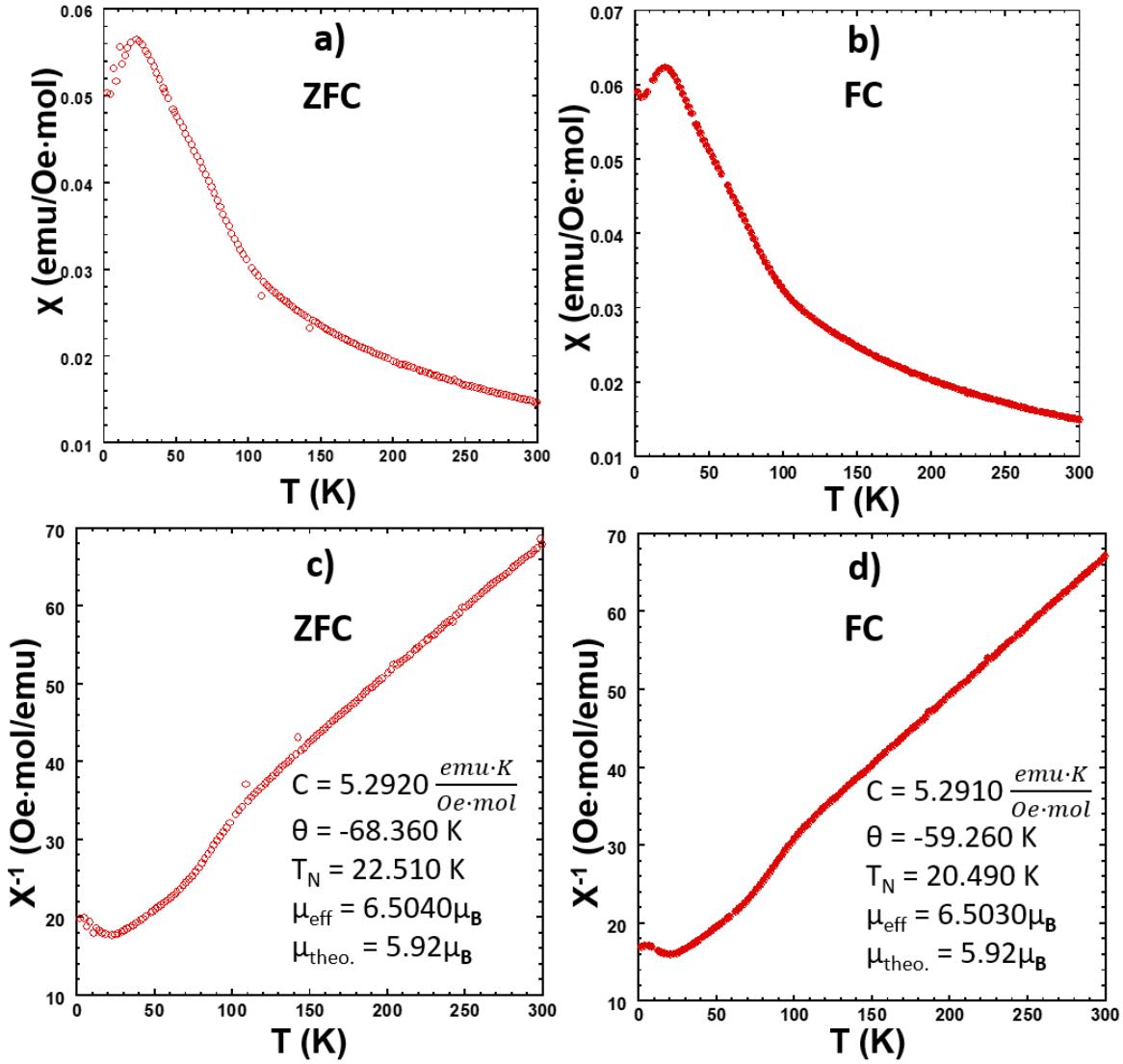

Figure 3.3.11: $Mn_{0.99}Zn_{0.01}Sb_2Se_4$ (x = 0.01) low-T magnetic susceptibility (χ) under **(a)** zero field-cooled and **(b)** field-cooled (FC) conditions; low-T inverse magnetic susceptibility (χ^{-1}) under **(c)** zero field-cooled and **(d)** field-cooled (FC) conditions. Also noted are important magnetic parameters extracted using Curie-Weiss Law fitting from ~170-300 K and Langevin theory of paramagnetism calculations. Crystal field theory and Hund's rules was used to calculate the theoretical magnetic moment, $\mu_{theo.}$

Figure 3.3.12 portrays the effective magnetic moment (μ_{eff}) and Weiss constant (θ). The effective magnetic moment increased from x = 0.01-0.05, followed by a decrease afterward. The Weiss constant became more negative from x = 0.01-0.04, showing an increase in the relative AFM strength; after x = 0.04.

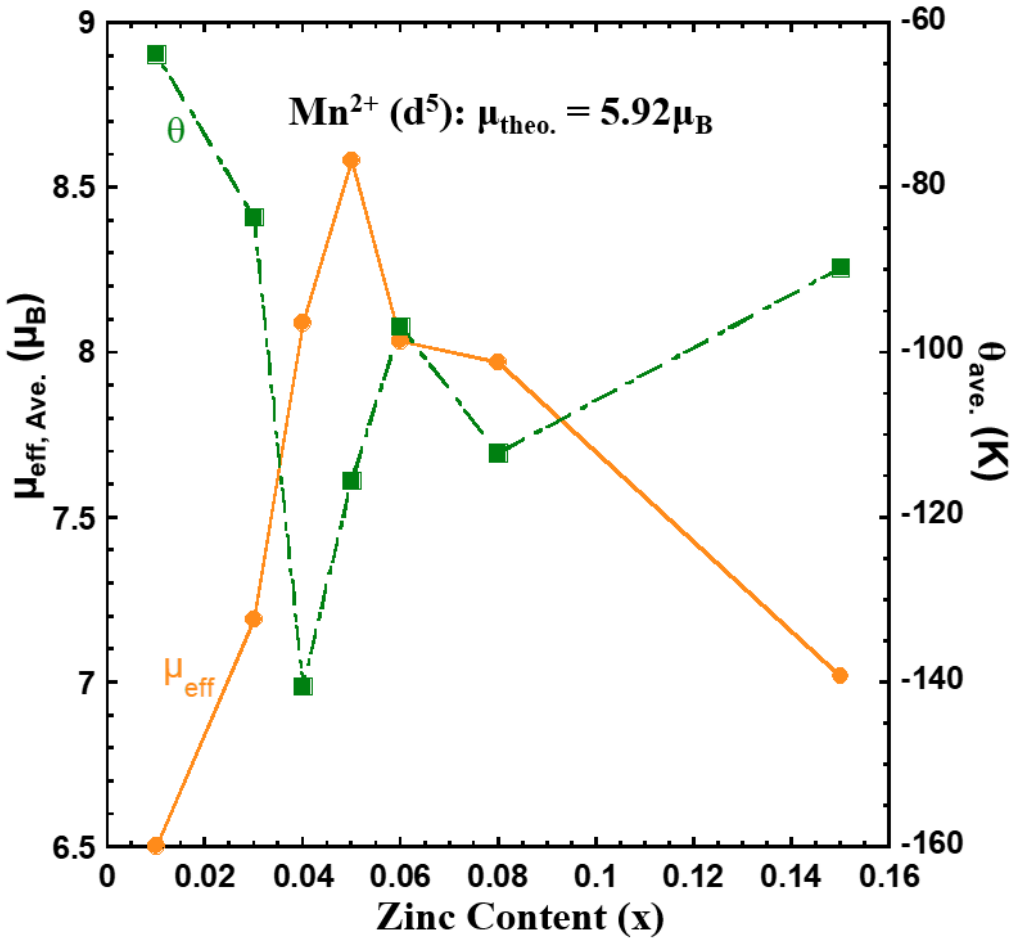

Figure 3.3.12: Effective magnetic moment and Weiss constant vs. zinc content.

Table 3.3.4 contains the parameters extracted from the magnetic susceptibility data analysis. T_N was seen to decrease from x = 0.01 to 0.03, increase to a maximum at x = 0.05, and decline upon further zinc addition. To predict the theoretical magnetic moment (μ_{theo}) of the compound, the equation $\mu_{theo} = g_l\sqrt{J(J+1)}\mu_B$ was applied, where g_l is the Landé g-factor and J is the total angular momentum. Recall that the oxidation states and electron configurations of the elements involved are Mn^{2+} ([Ar]$3d^5$), Zn^{2+} ([Ar]$3d^{10}$), Sb^{3+} ([Kr]$4d^{10}5s^2$), and Se^{2-} ([Ar]$3d^{10}4s^24p^6$). Due to its electron configuration, Mn^{2+} possesses unpaired electrons to generate a magnetic moment. Also recall that Mn^{2+} is octahedrally coordinated to Se^{2-}, a weak-field ligand, so electrons will tend to fill high-spin. Hund's rules were applied to determine g_l and J. To compute these parameters,

one must first calculate the spin angular momentum (S) and orbital angular momentum (L) based on crystal field theory. For high-spin Mn^{2+} ([Ar]$3d^5$) in octahedral coordination, S = 5/2, L = 0, g_l = 2, J = 5/2, and $\mu_{theo.} = 5.92\mu_B$.

Table 3.3.4: Parameters extracted from magnetic susceptibility data, such as Néel temperature (T_N), effective magnetic moment (μ_{eff}), Curie constant (C), and Weiss constant (θ).[28]

Zn Content (x)	$T_{N, Ave.}$ (K)	$\mu_{eff, Ave.}$ (μ_B)	$C_{Ave.}$ (emu·K/Oe·mol)	$\theta_{Ave.}$ (K)
0*	20	5.82	5.48	-74
0.01	21.505	6.5035	5.2915	-63.81
0.03	19.523	7.191	6.47	-83.585
0.04	21.505	8.09	8.14	-140.45
0.05	21.5	8.583	9.2227	-115.52
0.06	19.51	8.035	8.0815	-96.78
0.08	19.725	7.9705	7.9472	-112.19
0.15	16.5	7.019	6.3647	-89.697

Surprisingly, μ_{eff} was much higher than predicted from Hund's rules throughout the composition series. As such, some other phenomenon must be enhancing the magnetic moment. It is possible that $Zn_{1-y}Mn_ySe$ is taking part in increasing the observed magnetic moment-for y < 0.3, $Zn_{1-y}Mn_ySe$ exhibits paramagnetic behavior of uncorrelated Mn spins; for 0.3 < y < 0.6, AFM spin-glass structure is observed; for y > 0.6, it has AFM behavior.[13] However, Vegard's Law calculations estimated y = 0.0175-0.238-within the paramagnetic regime for $Zn_{1-y}Mn_ySe$. High-spin Mn^{2+} ([Ar]$3d^5$) in tetrahedral coordination predicts a theoretical moment of $5.92\mu_B$, the same value as predicted for Mn^{2+} in $Mn_{1-x}Zn_xSb_2Se_4$. So, any $Zn_{1-y}Mn_ySe$ impurity phase should not enhance the magnetic moment of the system. So, an additional contribution must be adding to the magnetic moment in the lattice. A substitution mechanism of Mn with Zn at the M1 and M2 sites must be the cause, similar to what was observed in Lopez *et al.*'s work on $Fe_{1-x}Sn_xBi_2Se_4$.[32] This would explain the observed enhancement in the magnetic moment-as the magnetic lattice would

convert from antiferromagnetic to ferrimagnetic, having a small permanent moment. **Figure 3.3.13** depicts the proposed $Mn_{1-x}Zn_xSb_2Se_4$ magnetic lattice. The top figure depicts the magnetic lattice in the case of $x = 0$, where the antiferromagnetic lattice has no net magnetic moment. The bottom figure shows the magnetic lattice for $x \neq 0$, where Zn substitutes for Mn at the M1 and M2 sites. Since Zn is a nonmagnetic atom, it converts the AFM lattice to a ferrimagnetic lattice with a small net moment.

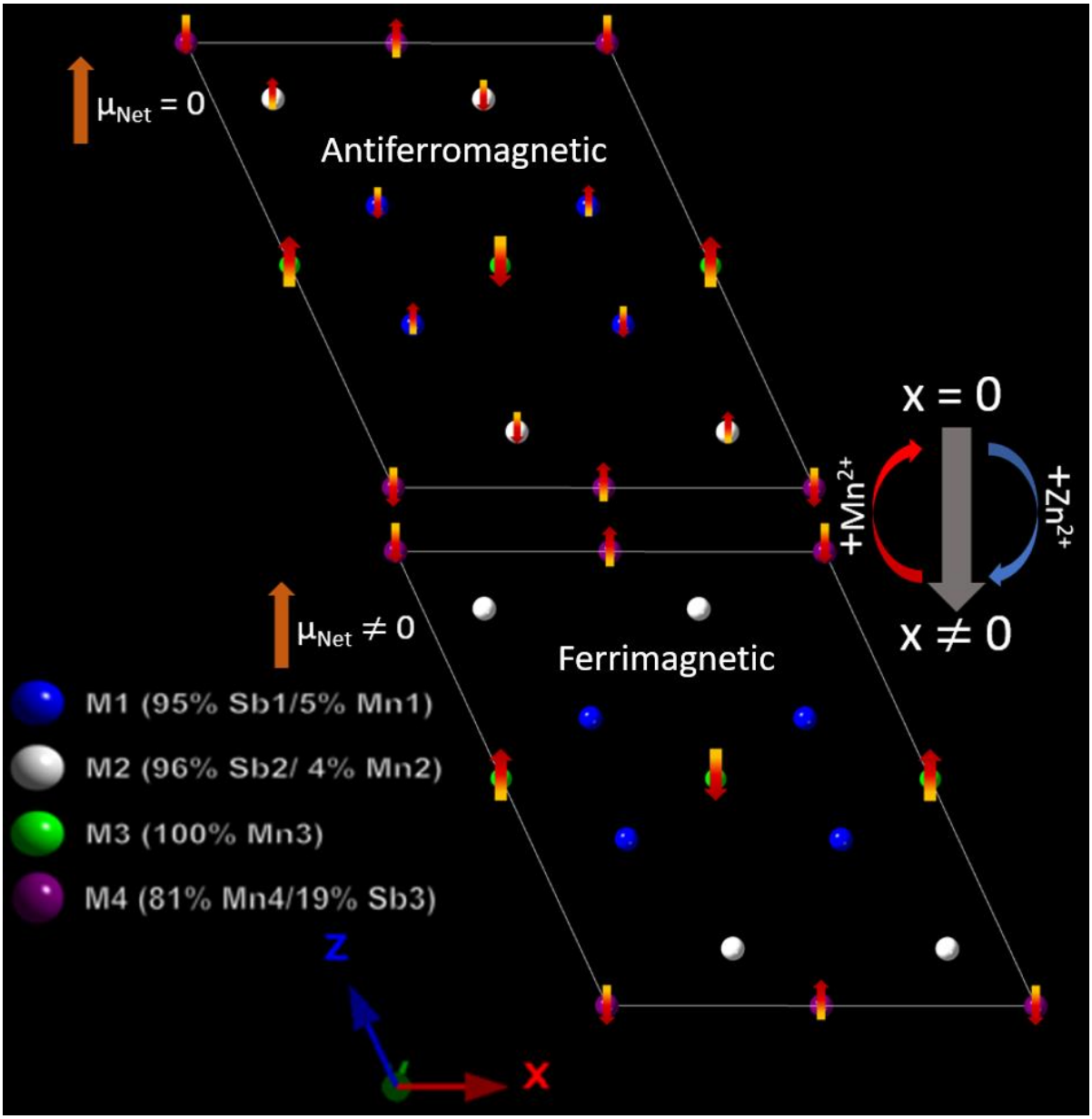

Figure 3.3.13: Proposed $Mn_{1-x}Zn_xSb_2Se_4$ magnetic lattice. For both images, each atomic site was coupled antiparallel to display the antiferromagnetic ordering nature of the compound. **Top:** x = 0, before any Zn is substituted; note that $\mu_{Net} = 0$ here. This case is an antiferromagnetic lattice. **Bottom:** Upon Zn substitution, the zinc preferentially substitutes first at the M1 and M2 sites. Zn^{2+} ([Ar]$3d^{10}$) has no unpaired e^- and thus does not contribute to magnetism. Since the M3 site has the most Mn^{2+} ([Ar]$3d^5$), a small net magnetic moment is observed in this case-i.e., $\mu_{Net} \neq 0$. The M1 and M2 substitution generates a ferrimagnetic lattice. This mechanism explains the increase in μ_{Net} with increasing Zn.

3.4 Conclusion & Future Work: $Mn_{1-x}Zn_xSb_2Se_4$ (x = 0-0.15)

In this work, $Mn_{1-x}Zn_xSb_2Se_4$ (x = 0-0.15), a p-type AFM semiconductor, was successfully synthesized. For x = 0.04-0.15, a minor secondary ZnSe phase was observed. PXRD, XPS, and DSC probed the phase purity, oxidation states of elements, and phase stability of the material. Rietveld refinement on the main phase noted a slight decrease in the c-axis and β angle with increasing zinc content, signifying successful Zn substitution in the lattice. Refinement on the secondary ZnSe phase indicated Mn incorporation in the lattice, creating a $Zn_{1-y}Mn_ySe$ solid solution; Vegard's Law determined that y = 0.0175-0.238. Quantitative phase coefficient analysis (ATZ) estimated that for x = 0.04-0.15, between 0.5-1.5 wt% $Zn_{1-y}Mn_ySe$ was present in addition to $Mn_{1-x}Zn_xSb_2Se_4$. Thermoelectric properties were probed to determine the figure of merit (zT) of each composition, with $(zT)_{max}$ = 0.02 occurring at 623.15 K for x = 0.01. Thermoelectric performance could be improved by hole doping at the Sb site, enhancing σ and zT as a result. Fitting the temperature-dependent magnetic susceptibility data with the Curie-Weiss Law found that $\mu_{eff} > \mu_{theo}$ throughout the composition series, so a Mn replacement with Zn at the M1 and M2 sites mechanism was proposed. With this mechanism, the magnetic lattice goes from antiferromagnetic to ferrimagnetic-exhibiting a small nonzero magnetic moment. While the commercial viability of $Mn_{1-x}Zn_xSb_2Se_4$ could be optimized further, it adds to the expanding library of ternary magnetic semiconductor compounds in the literature.

CHAPTER 4: $Sb_{2-x}Sn_xSe_3$ (x = 0, 0.01, 0.05, 0.1, 0.15, 0.2) Structural Properties and Optical Properties

4.1 Introduction: $Sb_{2-x}Sn_xSe_3$ (x = 0, 0.01, 0.05, 0.1, 0.15, 0.2)

Recently, in 2019, Djieutedjeu *et al*. found that charge disproportionation was able to cause a temperature-induced Lifshitz transition in $FeSb_{2-x}Sn_xSe_4$, as seen in **Figure 4.1.1**.[38]

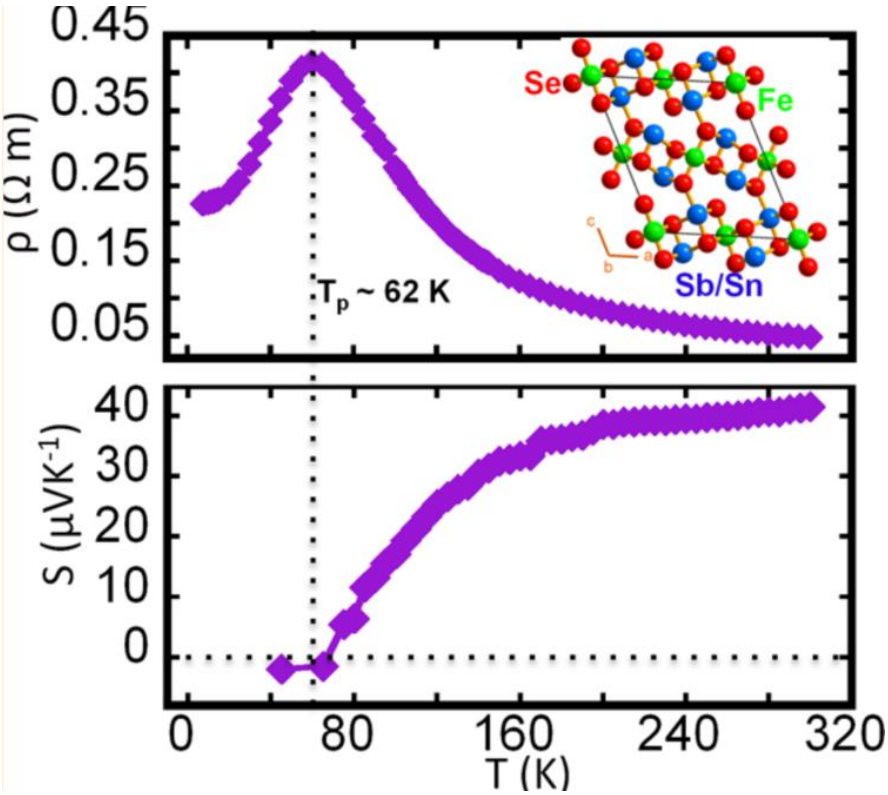

Figure 4.1.1: $FeSb_{2-x}Sn_xSe_4$ (x = 0.15) temperature-induced Lifshitz transition, going from p-type to n-type at low-T. Here, Sn^{2+} is substituting for Sb^{3+}, causing local excess negative charge. As such, some Sb^{3+} will oxidize to Sb^{5+} to charge-compensate, dumping electrons into the system. Image was adapted from Djieutedjeu *et al*.[38]

In $FeSb_{2-x}Sn_xSe_4$, Sb^{3+} is being substituted by Sn^{2+}, causing local excess negative charge. As such, some Sb^{3+} will oxidize to Sb^{5+} to charge-compensate, dumping electrons into the system. In **Figure 4.1.1**, we can see the Seebeck coefficient switching from p-type to n-type at low temperature, a signature hallmark of the Lifshitz transition.

The $FeSb_{2-x}Sn_xSe_4$ chemical system was the ideal inspiration for the $Sb_{2-x}Sn_xSe_3$ project, as here, Sn^{2+} is substituting for Sb^{3+}. As such, it may be possible to generate a temperature-induced Lifshitz transition in this material as well. Sb_2Se_3 is already a well-studied material, crystallizing in the orthorhombic space group Pnma (ICSD #30973[30]), with lattice parameters a = 11.7938 Å, b = 3.9858 Å, c = 11.6478 Å; $\alpha = \beta = \gamma = 90°$.[30] **Figure 4.1.2** depicts the Sb_2Se_3 Pnma crystal structure along the b-axis.

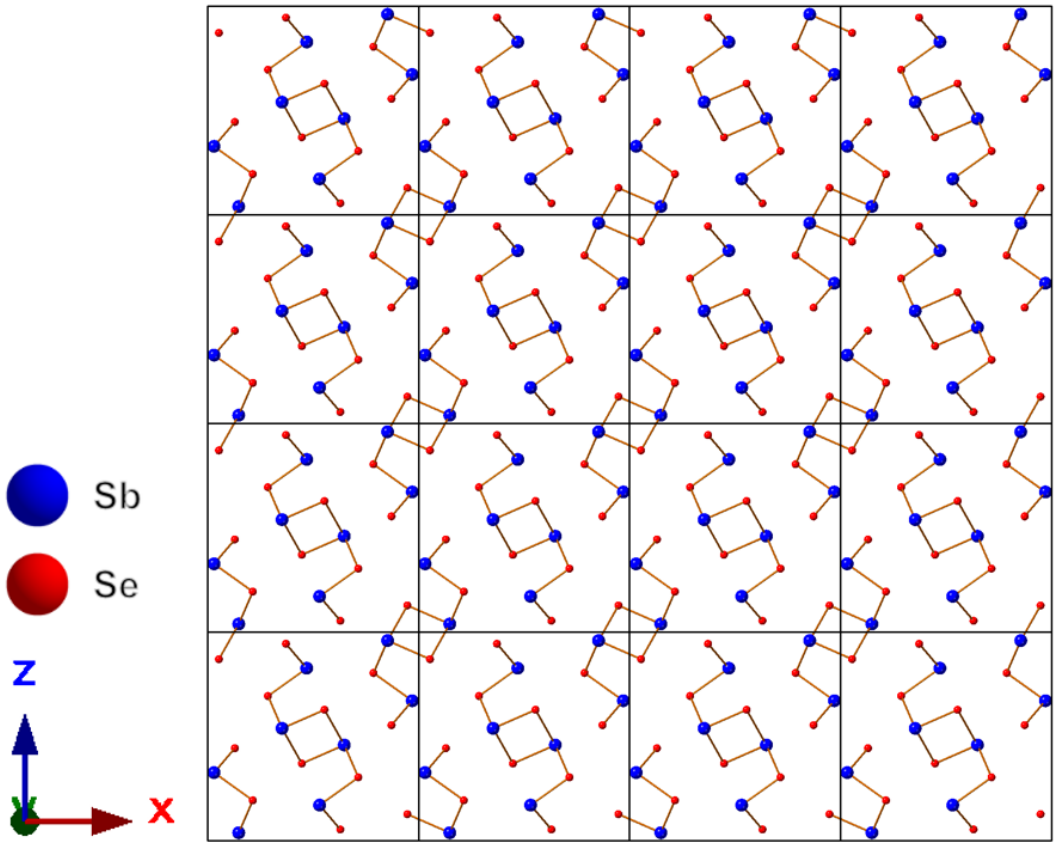

Figure 4.1.2: Sb_2Se_3 Pnma (ICSD #30973[30]) crystal lattice projected along the b-direction. Along the c-axis, 1-D ribbons of Se-Sb-Se are seen. Image was adapted from Mavlonov *et al*.[58]

Along the c-axis, 1-D ribbons of Se-Sb-Se are visible. The electron configuration of Sb^{3+} is $[Kr]4d^{10}5s^2$, so there is a stereochemically active $5s^2$ electron lone pair. This lone pair causes the Sb-Se to connect in a square pyramidal coordination, aiding in the formation of the 1-D ribbon structure seen above. **Figure 4.1.3** depicts the Sb-Se polyhedron.

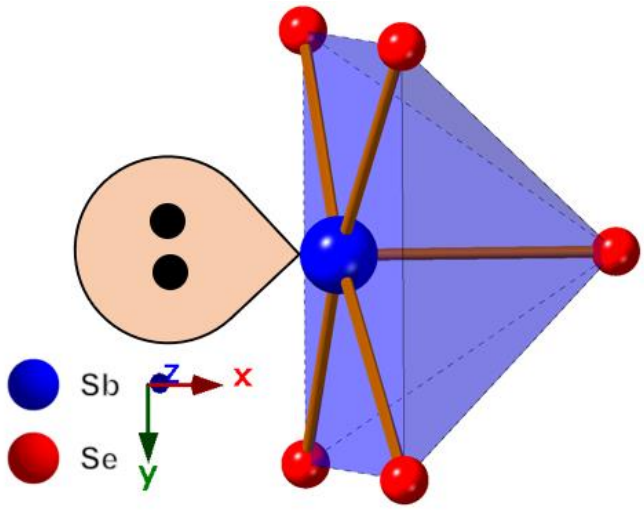

Figure 4.1.3: Sb-Se square pyramidal polyhedron projected along the c-direction rotated. The $5s^2$ electron lone pair is also shown. [58]

Due to the anisotropic nature of Sb_2Se_3, nanostructured growth has been studied extensively. Sb_2Se_3 and Sb_2Se_3: Sn-based nanowires, nanorods, nanotubes, and microrods have found potential applications in near-IR photodetectors, thermoelectrics, optoelectronics, and photovoltaics.[59-65] In fact, a Sb_2Se_3 nanorod array solar cell was recently discovered to have a 9.2% efficiency.[65] **Figure 4.1.4** depicts an SEM cross-section image of the array.[65]

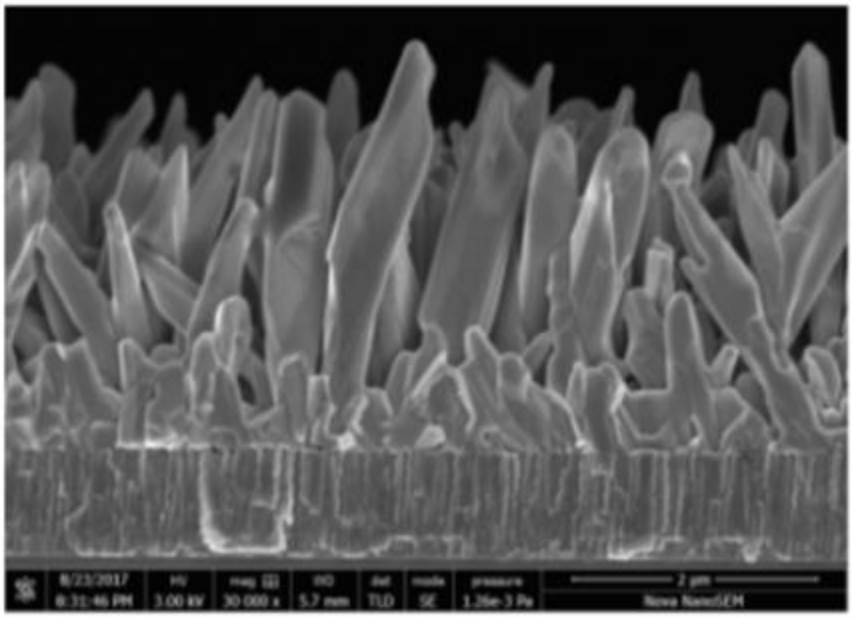

Figure 4.1.4: SEM cross-sectional image of the Sb_2Se_3 nanorod array along the [001] direction, grown on a Mo substrate. The record Sb_2Se_3 cell efficiency of 9.2% was recorded using an absorber layer of over 1000 nm and a device architecture of ZnO:Al/ZnO/CdS/TiO_2/Sb_2Se_3 nanorod arrays/$MoSe_2$/Mo. Image was adapted from Li *et al*.[65]

Due to a nearly ideal optical bandgap of ~1.1 eV and high absorption coefficient, Sb_2Se_3 is positioned as a promising material for photovoltaics and has seen widespread research.[58, 65-72] Interestingly, Sb_2Se_3 has even seen promise in solar water splitting, serving as the photocathode; shown in **Figure 4.1.5**.[72]

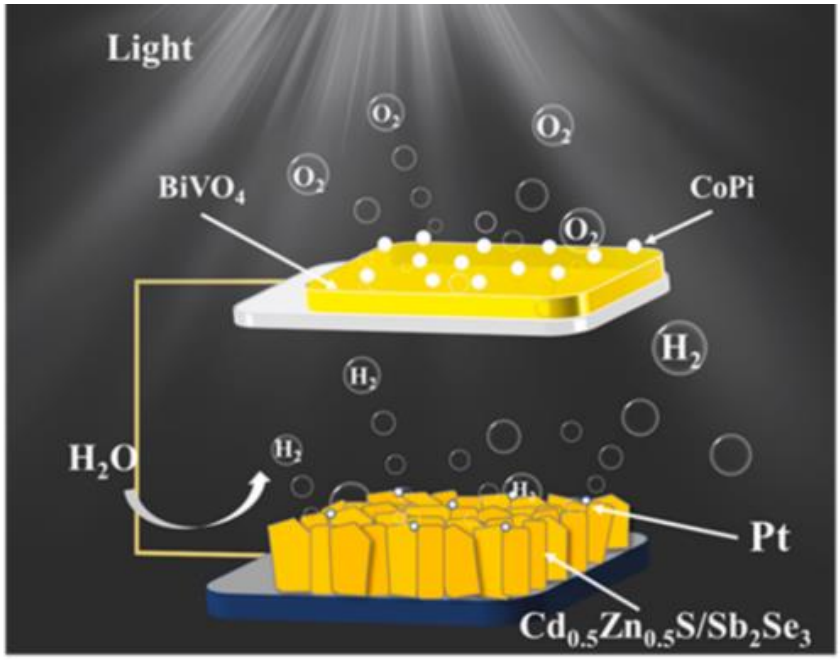

Figure 4.1.5: Solar-driven water splitting photoelectrochemical cell. Image adapted from Li *et al*.[72]

Additionally, Sb_2Se_3 is a topological insulator, and exhibits superconductivity at low temperatures.[73, 74] Amorphous Sb_2Se_3 and Sb_2Se_3: Sn films have been probed for potential photonics and holographic recording applications.[75-80] Chen *et al*. also found that the optical bandgap of Sb_2Se_3 can be tuned by doping Sb with Sn, decreasing from 1.17 eV to 1.1 eV.[81] Due to the wealth of applications within Sb_2Se_3 and Sb_2Se_3: Sn, as well as the potential to generate a temperature-induced Lifshitz transition, $Sb_{2-x}Sn_xSe_3$ was an ideal chemical system to explore further.

4.2 Synthesis: $Sb_{2-x}Sn_xSe_3$ (x = 0, 0.01, 0.05, 0.1, 0.15, 0.2)

Polycrystalline powders of $Sb_{2-x}Sn_xSe_3$ (x = 0, 0.01, 0.05, 0.1, 0.15, 0.2) were generated from a solid-state reaction of elements. Stoichiometric amounts of Sb (99.5%, Alfa Aesar), Sn (99.8%, Cerac Specialty Inorganics), and Se (99.5%, Sigma Aldrich) were weighed in an argon glovebox and ground thoroughly with a mortar and pestle, vacuum flame-sealed in quartz tubes, and placed in a programmable furnace as described in **Section 2.1.1**. The reaction profile was as follows: heat to 300 C over 12 hours, dwell at 300 C over 24 hours, heat to 550 C over 6 hours, dwell at 550 C for 48 hours, cool to 25 C over 6 hours. The resultant ingots were ground into powder and PXRD, DSC, and UV-Vis-NIR diffuse reflectance spectroscopy measurements were performed.

4.3 Results & Discussion: $Sb_{2-x}Sn_xSe_3$ (x = 0, 0.01, 0.05, 0.1, 0.15, 0.2)

4.3.1 Structural Properties of $Sb_{2-x}Sn_xSe_3$

In this work, proper stoichiometric amounts of Sb, Sn, and Se were reacted and $Sb_{2-x}Sn_xSe_3$ grey, lustrous ingots resulted, as seen in **Figure B.1**. The ingots were ground into fine grey powder, also seen in the figure. In order to probe the phase purity of the system, powder X-ray diffraction was used. **Figure 4.3.1** depicts the PXRD of the composition series, plotted against a reference pattern.

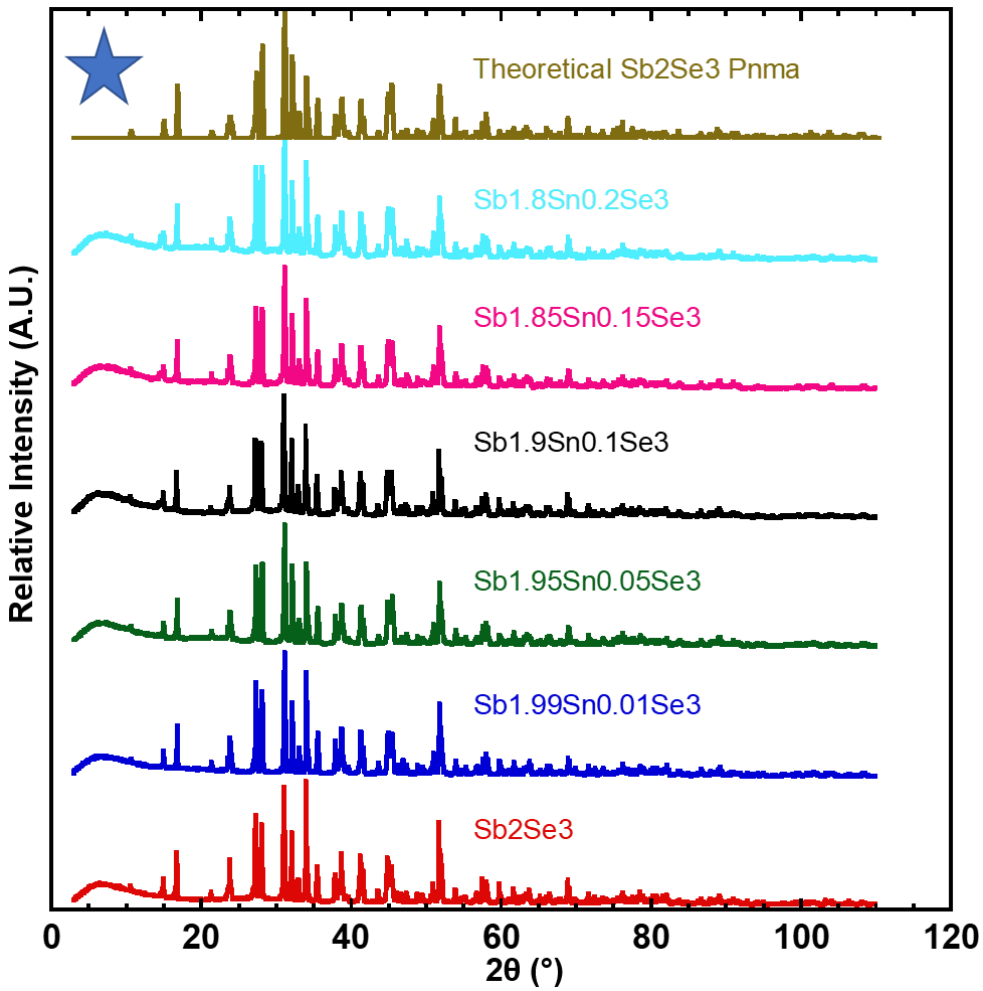

Figure 4.3.1: $Sb_{2-x}Sn_xSe_3$ (x = 0-0.2) powder x-ray diffraction (PXRD). The plots were compared to the ICSD reference Sb_2Se_3 Pnma (#30973[30]), noted by the blue star.

Throughout the x = 0-0.2 substitution range, the samples crystallized isostructurally with the ICSD reference Sb_2Se_3 Pnma (#30973[30]) phase. Additionally, the thermal stability and melting point of each composition was probed using Differential Scanning Calorimetry (DSC). **Figure 4.3.2** depicts the heating DSC curve. With increasing tin content, the melting point (MP) was found to decrease from 887 K to 857 K (**Figure 4.3.3**). The trend is roughly linear until x = 0.1, where a secondary phase starts forming.

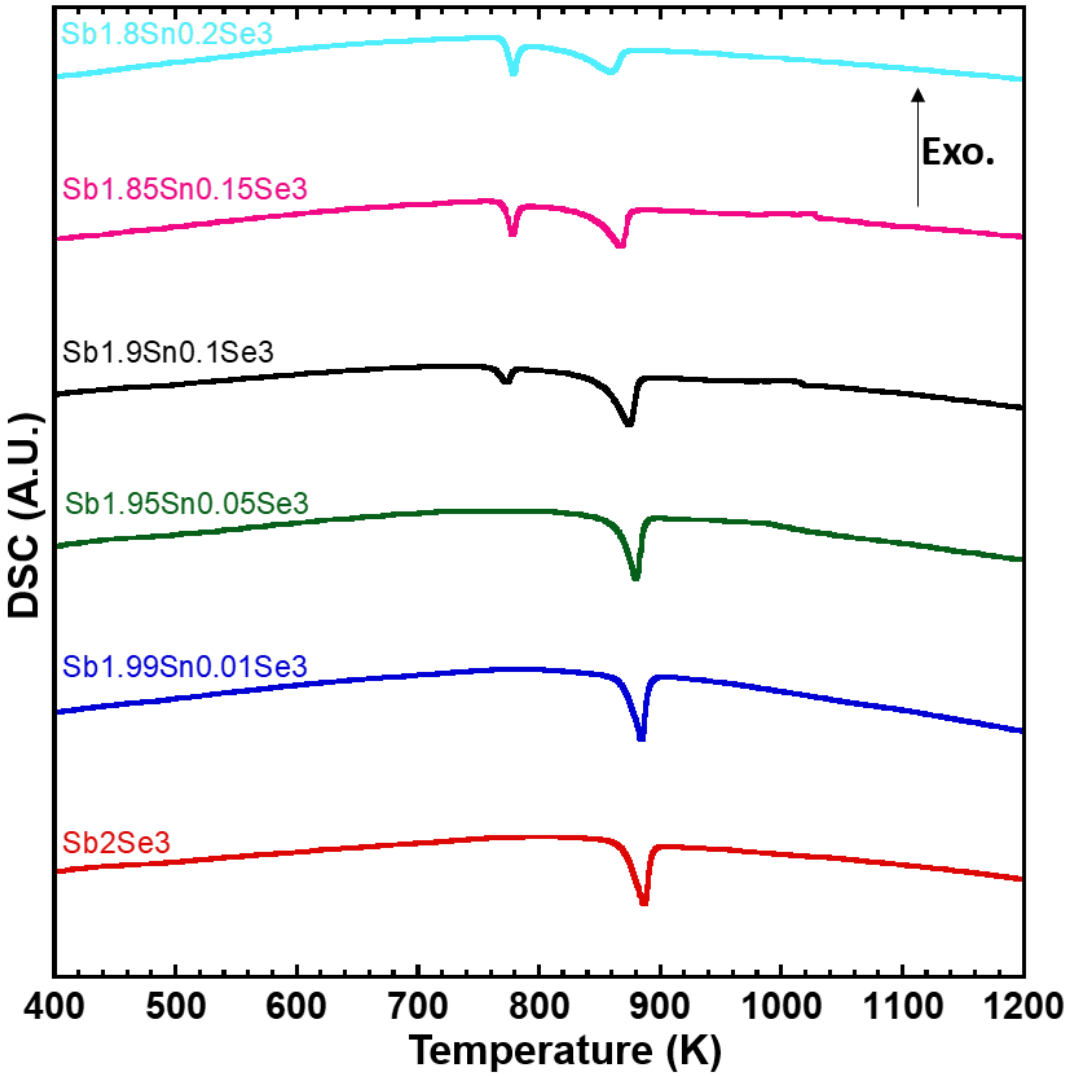

Figure 4.3.2: Differential scanning calorimetry (DSC) of the $Sb_{2-x}Sn_xSe_3$ series upon heating.

For the case of x = 0.1-0.2, a growing secondary phase was observed. According to the Sb-Sn-Se pseudo-binary phase diagram (ASM #952732[82]) displayed in **Figure B.2**, the secondary phase corresponds to a $SnSb_2Se_4$ Pnnm phase (experimental MP = 778 K).

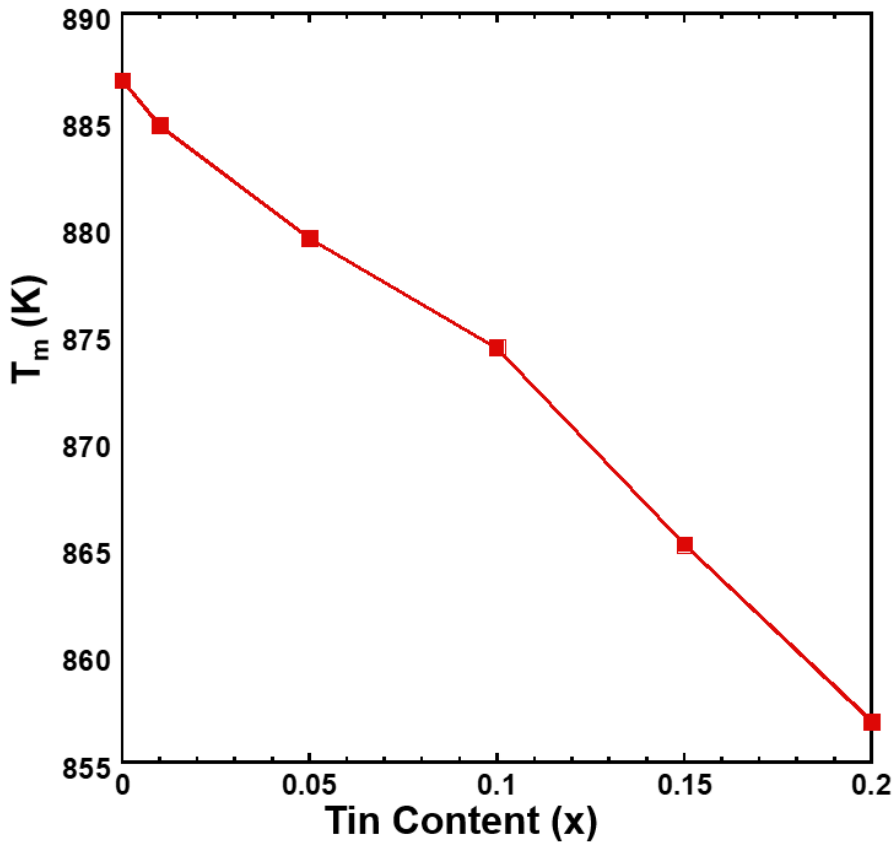

Figure 4.3.3: Melting point vs. tin content for the $Sb_{2-x}Sn_xSe_3$ series. With increasing tin content, the melting point (MP) was found to decrease from 887-857 K. The trend is roughly linear until x = 0.1-where the secondary phase starts forming.

Interestingly, plotting PXRD of the $SnSb_2Se_4$ Pnnm phase against the $Sb_{2-x}Sn_xSe_3$ series (**Figure B.3**) did not reveal drastic evidence of the additional phase. Upon zooming in between 20-60° (**Figure B.4**), minor evidence of the phase can be seen as various satellite peaks. Thus, the $SnSb_2Se_4$ Pnnm phase must be small, but present for x = 0.1-0.2.

In order to verify the thermal stability of the samples, DSC upon cooling was also recorded (**Figure 4.3.4**). In the case of x = 0 and x = 0.01, a single recrystallization peak was

observed. However, for x = 0.05-0.2, multiple peaks upon cooling were noticed. So, the samples for x = 0 and x = 0.01 had reversible transitions. Still, the main recrystallization peak for each x value was recorded and plotted in **Figure 4.3.5**.

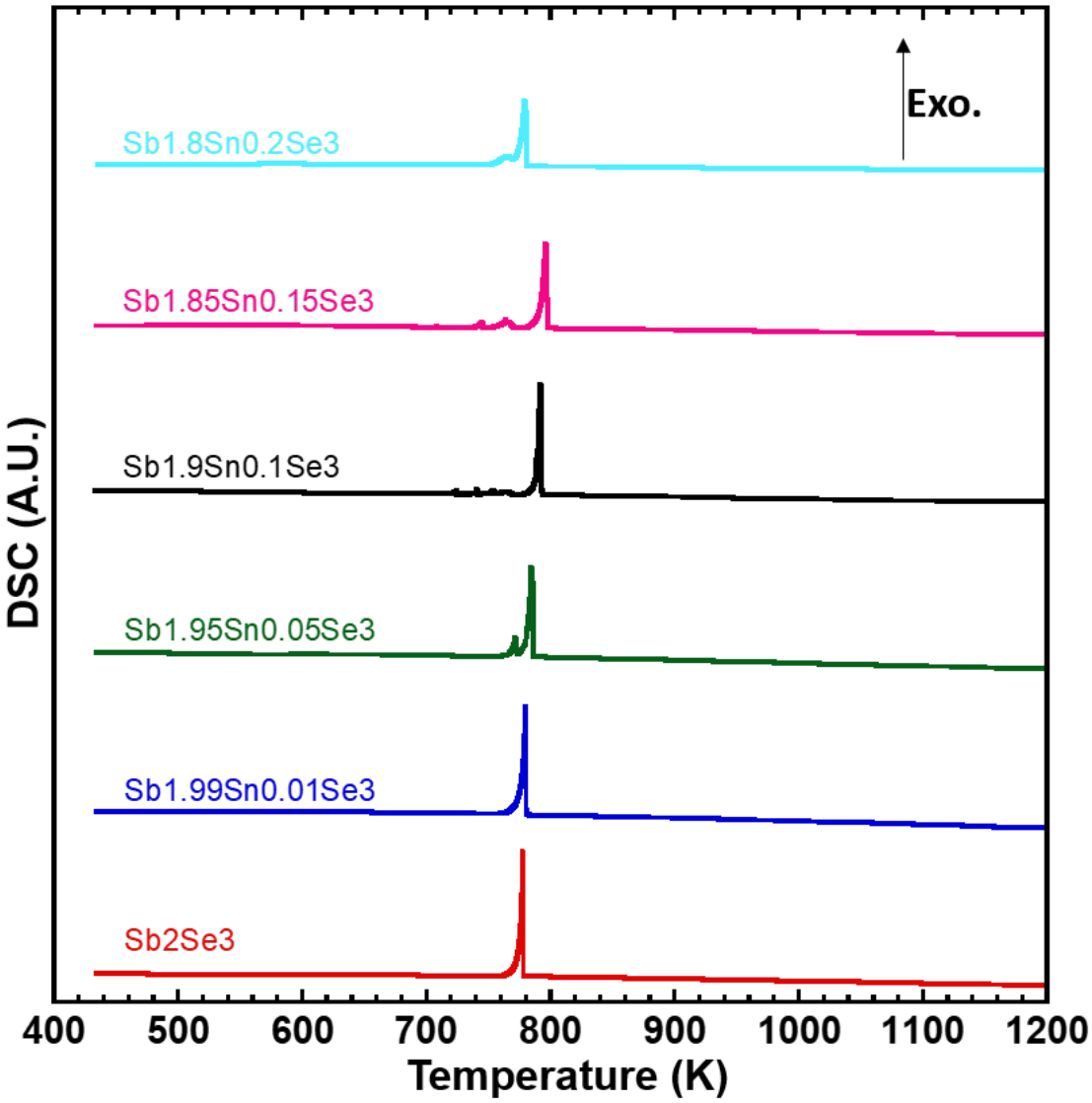

Figure 4.3.4: Differential scanning calorimetry (DSC) of the $Sb_{2-x}Sn_xSe_3$ series upon cooling. For x = 0-0.1, the recrystallization temperature was seen to increase from 777 K to 791 K. For x = 0.1-0.2 (corresponding to secondary phase formation), the trend was more irregular. For x = 0 and x = 0.01, only a single recrystallization peak was observed, signifying a reversible transition. In the case of x = 0.05-0.2, multiple peaks are seen, evidence of thermal instability.

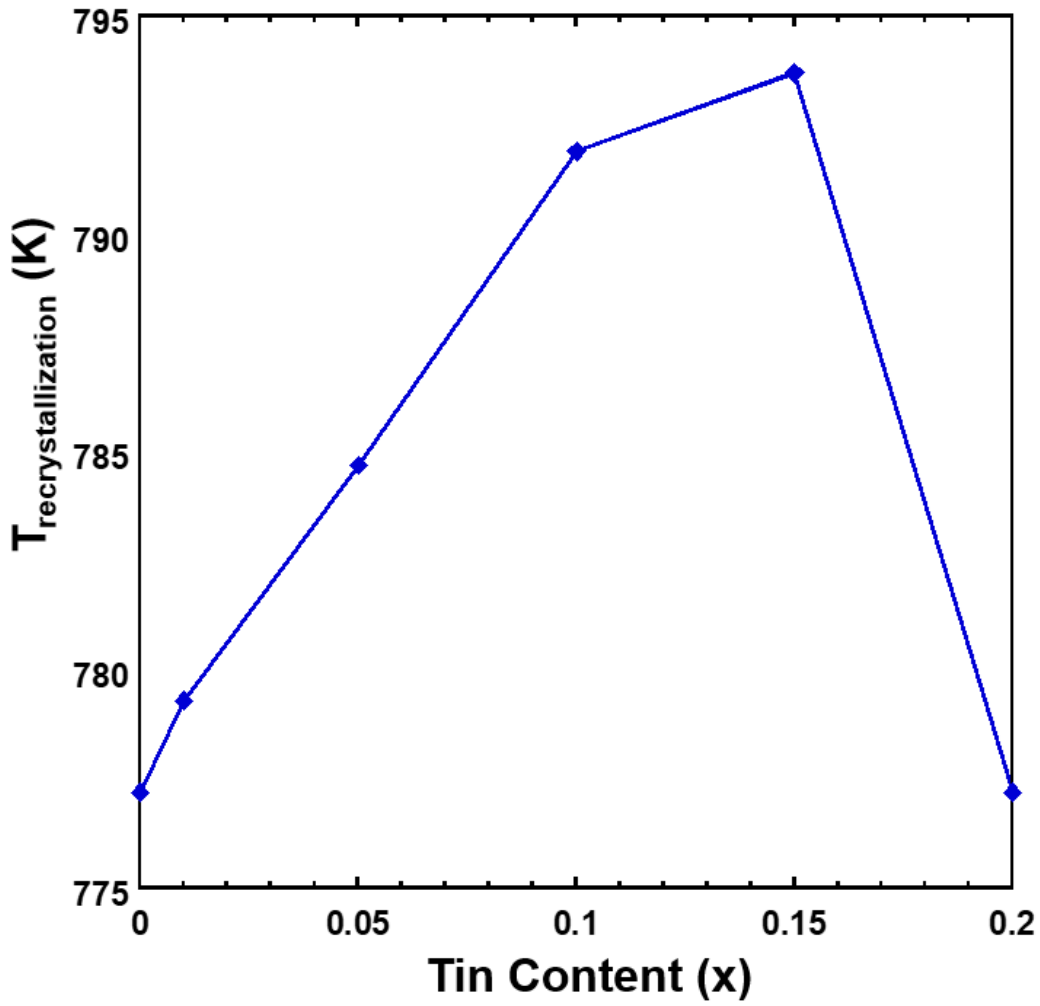

Figure 4.3.5: Recrystallization temperature vs. tin content. For x = 0-0.1, the recrystallization temperature was seen to linearly increase from 777-791 K. For x = 0.1-0.2 (corresponding to secondary phase formation), the trend was more inconsistent.

In order to probe the lattice parameters of the $Sb_{2-x}Sn_xSe_3$ series, Rietveld refinement using FullProf was utilized, as described in **Section 2.2.2**. Before the refinement was carried out, accurate starting values of lattice parameter were manually calculated. Recall that the Sb_2Se_3 Pnma phase is orthorhombic, so a, b, c parameters were gathered using 3 sets of experimental 2θ and (hkl) values (**Figure B.5**).Rigaku integrated X-ray powder diffraction software (PDXL) was implemented to identify the (hkl) values and a, b, and c were calculated. **Figure B.6** describes the

refinement procedure steps taken. An example refinement fit for x = 0.01 ($Sb_{1.99}Sn_{0.01}Se_3$) is seen in **Figure 4.3.6**. The ICSD phase Sb_2Se_3 Pnma (#30973[30]) was used as the CIF file. The quality of fit was χ^2 = 58.4. Due to the orthorhombic nature of the structure (lattice parameters a = 11.7938 Å; b = 3.9858 Å; c = 11.6478 Å; α = β = γ = 90°), preferred orientation was observed on several peaks, noted with the relevant (hkl) values.

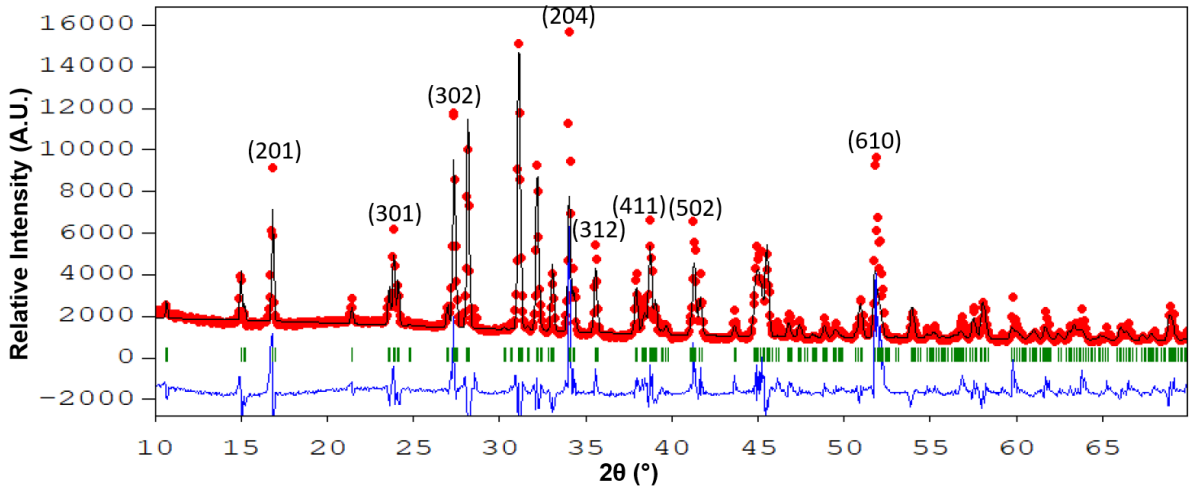

Figure 4.3.6: Powder XRD Rietveld refinement fit for $Sb_{1.99}Sn_{0.01}Se_3$. In the figure, the red curve is the experimental pattern, the black line is the fitted pattern, the green tick marks correspond to the peak positions, and the blue curve is the difference pattern between experimental and fitted patterns.

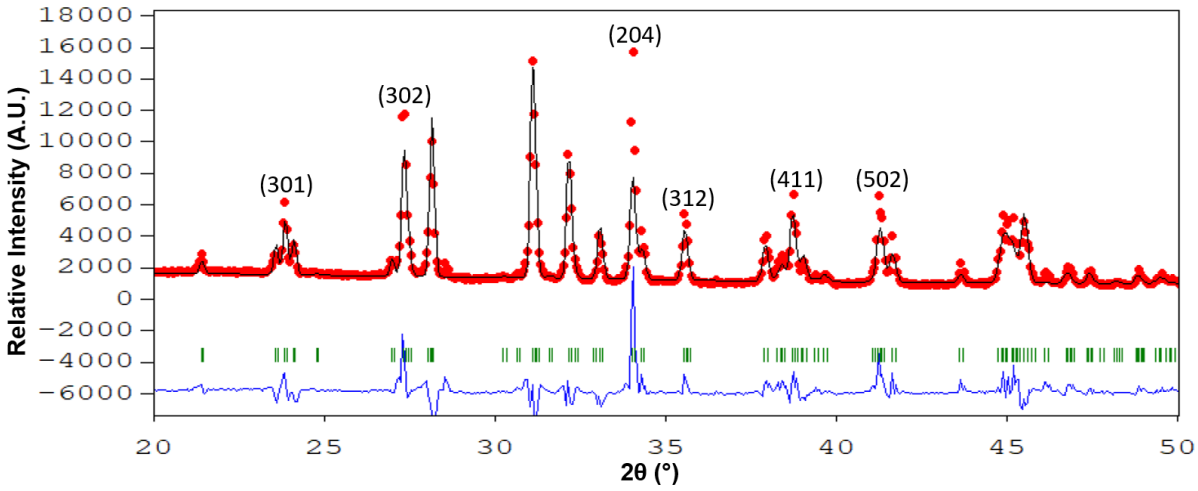

Figure 4.3.7: Powder XRD Rietveld refinement fit for $Sb_{1.99}Sn_{0.01}Se_3$, zoomed in between 20-50°.

Figure 4.3.7 shows a zoomed-in version of the x = 0.01 refinement plot, from 20-50°. Used to highlight the good alignment of the peak positions with the experimental data. So, the lattice parameters gathered will be accurate.

The same refinement procedure was applied for x = 0-0.2, and the lattice parameters were gathered-displayed in **Figure 4.3.8** and **Table 4.3.1**. Both the a-axis and c-axis stayed relatively constant with increasing Sn; overall, the b-axis was seen to increase with increasing Sn. According to the Shannon radii, for CN = 6, R_{Sb3+} = 0.76 Å, while R_{Sn2+} = 1.18 Å; so, Sn^{2+} is ~55% larger than Sb^{3+} ($\Delta R/R$).[83] As such, the increase in the b-axis with rising Sn content is consistent. Recall that the Sb_2Se_3 Pnma (#30973[30]) lattice parameters were: a = 11.7938 Å; b = 3.9858 Å; c = 11.6478 Å; $\alpha = \beta = \gamma = 90°$. Since the b-axis is the shortest axis, the Sn substitution had the most dramatic effect on this crystal direction.

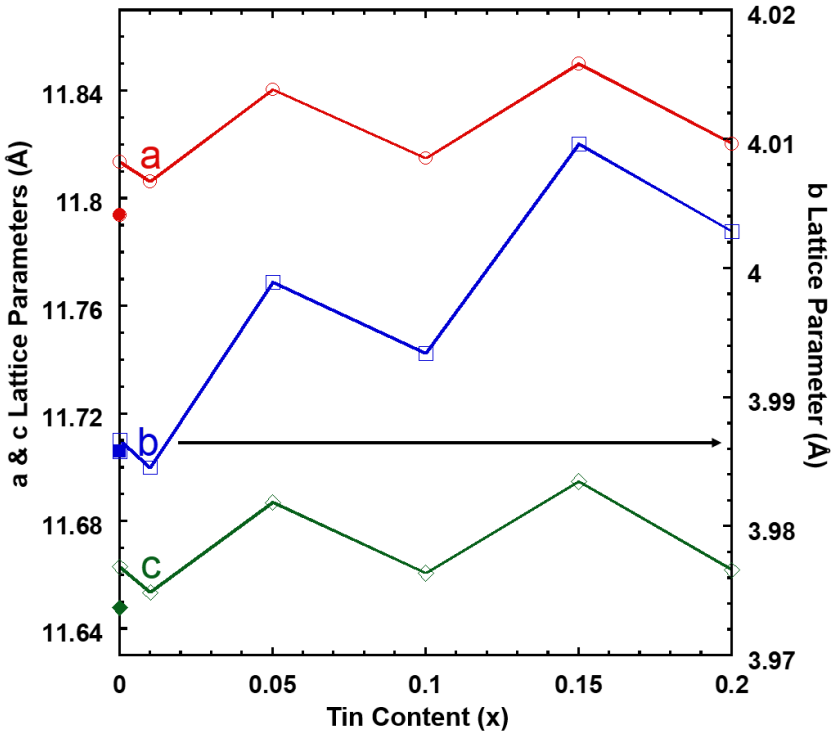

Figure 4.3.8: Lattice parameters vs. tin content, extracted from Rietveld refinement. The relevant Sb_2Se_3 Pnma (ICSD #30973[30]) phase lattice parameters (a, b, c) were also noted by the filled red circle, blue square, and green diamond, respectively.

Table 4.3.1: Lattice parameter and χ^2 values extracted from Rietveld refinement. Also noted was the lattice parameters of the Sb_2Se_3 Pnma (ICSD #30973[30]) phase, denoted by the asterisk.

x Value (Sn Content)	$Sb_{2-x}Sn_xSe_3$ Composition	χ^2 Value	a (Å)	b (Å)	c (Å)
0*	Sb_2Se_3*	N/A	11.7938	3.9858	11.6478
0	Sb_2Se_3	69.1	11.81361	3.98669	11.66308
0.01	$Sb_{1.99}Sn_{0.01}Se_3$	58.4	11.80614	3.98455	11.65348
0.05	$Sb_{1.95}Sn_{0.05}Se_3$	119	11.84047	3.99894	11.68689
0.1	$Sb_{1.9}Sn_{0.1}Se_3$	67.5	11.81487	3.99342	11.66068
0.15	$Sb_{1.85}Sn_{0.15}Se_3$	112	11.85019	4.00964	11.69478
0.2	$Sb_{1.8}Sn_{0.2}Se_3$	73.4	11.82041	4.00287	11.66180

4.3.2 Optical Properties of $Sb_{2-x}Sn_xSe_3$

Diffuse reflectance UV-Vis-NIR spectroscopy was performed on each of the six samples in the $Sb_{2-x}Sn_xSe_3$ series. Later, the Kubelka-Munk equation F(R)[33] was used to transform percent reflectance data to absorption, which was then plotted as a function of energy in electron volts, eV. **Figure B.7** shows the method for extracting the optical bandgap. Bulk Sb_2Se_3 is known to have an optical bandgap of ~1.1 eV.[84] The bandgap of the sample of Sb_2Se_3 prepared in this work, ~1.168 eV, was in good agreement with this value. **Figure B.8** depicts analysis of the spectrum obtained for this sample; an onset of the absorption edge at ~1.4 eV is observed. This onset is consistent for all samples of the formula $Sb_{2-x}Sn_xSe_3$, as can be seen when all spectra are displayed in one plot (**Figure 4.3.9**).

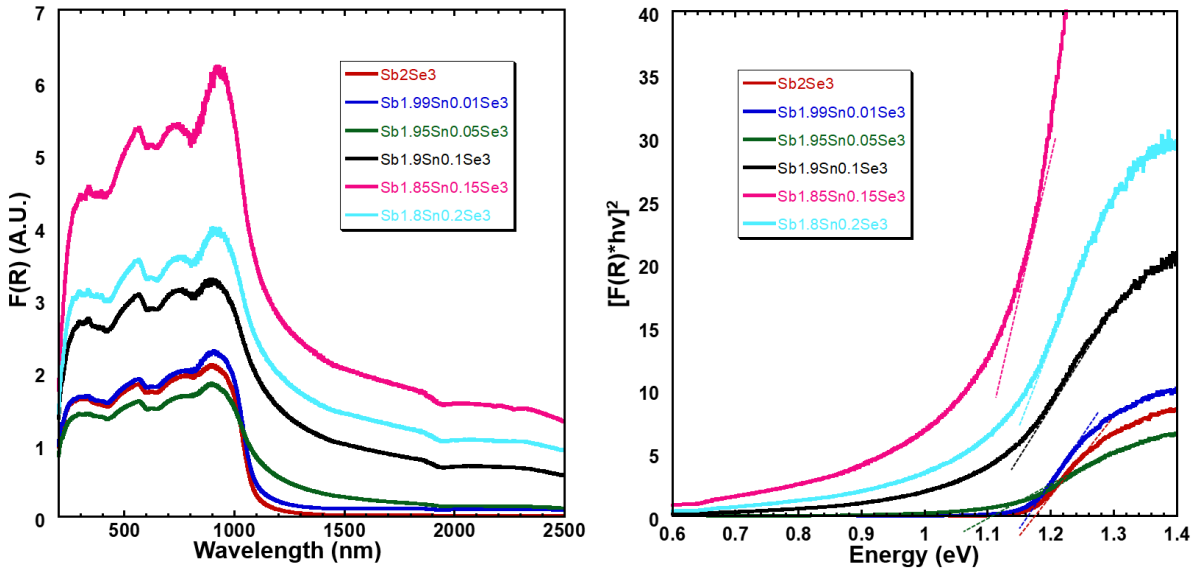

Figure 4.3.9: (Left): UV-Vis-NIR diffuse reflectance Tauc plot analysis. The Kubelka-Munk function F(R) was used to transform the reflectance data to absorbance. Plot of F(R) vs. wavelength. **(Right):** Plot of $[F(R)*hv]^{1/r}$ vs. energy; r = ½ was chosen here to signify a direct, allowed transition (direct bandgap). To determine the direct optical bandgap (E_g) for each x value, an absorption edge tangent line was extrapolated to the x-axis; the intercept with the x-axis corresponds to E_g.

The undoped sample of Sb_2Se_3 had a sharp, well-defined absorption edge. As the amount of Sn increased, the absorption edges appeared more gradual. As such, bandgap values could not

be as easily assessed for these samples, as there was not a clear baseline to which the absorption edge can be extrapolated. As such, to be consistent for all samples, the optical bandgap (E_g) was identified by extrapolating the absorption edge to the energy axis; the x-intercept was recorded as E_g. When the value of x increased from 0.01 to 0.05, in the formula $Sb_{2-x}Sn_xSe_3$, a significant amount of band tailing could be seen on the low energy side of the absorption edge. The band tailing could be evidence of the presence of impurity sub-bands within the band gap. Kumar *et al*'s[41] work on $(Sb_2Se_3)_{100-x}Sn_x$ (x = 0, 1, 3, 5, 7 at%) amorphous films and Chen *et al*.'s [42] work on $(Sb_{1-x}Sn_x)_2Se_3$ (x = 0, 0.03, 0.05, 0.07, 0.1) had similar findings-increasing Sn content raised the level of low-energy band tailing.[78, 81]

Values of the optical bandgap for each x value were recorded, and a plot of this is shown in **Figure 4.3.10**. Interestingly, with increasing Sn, the bandgap was found to decrease linearly up until x = 0.1, corresponding to when the secondary $SnSb_2Se_4$ Pnnm phase started forming. For x = 0 to x = 0.1, E_g decreased from 1.17 eV to 1.09 eV. Interestingly, the secondary phase formation at x = 0.1 led to a rise in E_g to 1.11 eV for x = 0.15, followed by a decrease in E_g to 1.07 eV for x = 0.2. Specific values of E_g are recorded in **Table 4.3.2**. Also found in this table is the maximum absorbed wavelength (λ_{Max}) at each x value. For x = 0, the value was ~1062 nm, and for x = 0.2, λ_{Max} was ~1156 nm. Recalling the solar spectrum figure (**Figure 1.3.4**), We see that throughout the x = 0-0.2 range, the $Sb_{2-x}Sn_xSe_3$ series can absorb wavelengths in the UV, visible, and near-IR (NIR) region. With more Sn content, the compound can absorb further into the NIR portion of the solar spectrum. The tunable bandgap of the material around ~1.1 eV makes it an ideal candidate as a photovoltaic absorber layer. In fact, luminescence analysis done by Miller *et al*. found that the ideal bandgap ranges between 1-1.5 eV.[85]

To be complete in the optical analysis, effects of the $SnSb_2Se_4$ Pnnm secondary phase must be considered as well for x = 0.1-0.2. Upon searching through the literature, optical bandgap measurements on this compound do not seem to have been recorded. As such, an equation reaction involving SnSe Pnma and Sb_2Se_3 Pnma phases was implemented to estimate E_g:

$$\mathrm{SnSe(Pnma)} + \mathrm{Sb_2Se_3(Pnma)} \longrightarrow \mathrm{SnSb_2Se_4(Pnnm)} \qquad \textbf{4.3-1.}$$

Now, since both SnSe and Sb_2Se_3 crystallize in the same space group, the $SnSb_2Se_4$ E_g can be estimated via a linear interpolation equation:

$$\mathrm{E_g(SnSb_2Se_4, Pnnm)} = \frac{1}{2}\mathrm{E_g(Sb_2Se_3, Pnma)} + \frac{1}{2}\mathrm{E_g(SnSe, Pnma)}, \qquad \textbf{4.3-2,}$$

where $E_g(Sb_2Se_3, \mathrm{Pnma})$ = 1.1 eV-bulk, direct bandgap, and $E_g(\mathrm{SnSe, Pnma})$ = 0.61 eV-bulk, direct bandgap.[65, 86] Now, based on **Equation 4.3-2,** $E_g(SnSb_2Se_4, \mathrm{Pnnm})$ = 0.86 eV; since this value is lower than the 1.17-1.07 eV range found for the $Sb_{2-x}Sn_xSe_3$ series, the secondary phase is not likely the cause of the decreasing bandgap for higher Sn values.

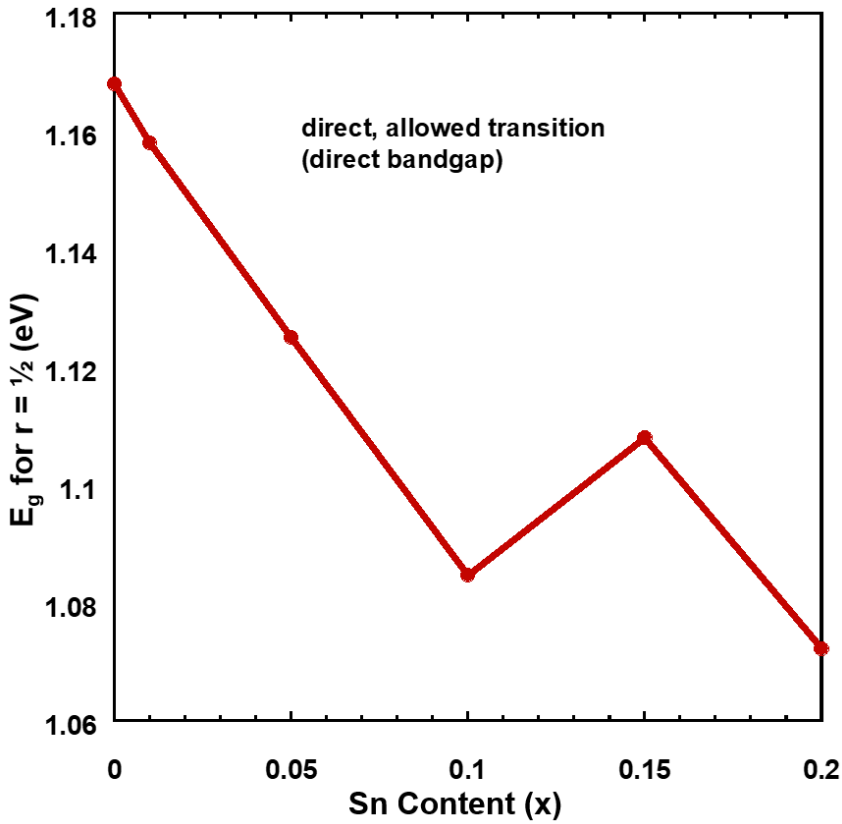

Figure 4.3.10: Direct optical bandgap vs. Sn content. For x = 0-0.1, E_g was seen to linearly decrease with increasing Sn. For x = 0.1-0.2 the trend becomes inconsistent-this correlates to the addition of the secondary phase.

Table 4.3.2: Direct optical bandgap (E_g) and maximum absorbed wavelength (λ_{Max}) vs. Sn content (x).

x Value	E_g for r = 1/2 (eV)	λ_{Max} (nm)
0	1.17	~1062
0.01	1.16	~1071
0.05	1.13	~1102
0.1	1.09	~1143
0.15	1.11	~1119
0.2	1.07	~1156

4.4 Conclusion & Future Work: $Sb_{2-x}Sn_xSe_3$ (x = 0, 0.01, 0.05, 0.1, 0.15, 0.2)

In this work, $Sb_{2-x}Sn_xSe_3$ (x = 0, 0.01, 0.05, 0.1, 0.15, 0.2) powders were synthesized and found to crystallize in the orthorhombic Sb_2Se_3 Pnma phase. DSC revealed that x = 0-0.1 was single phase, with a growing $SnSb_2Se_4$ Pnnm secondary phase for x = 0.1-0.2. The $Sb_{2-x}Sn_xSe_3$ melting point decreased linearly with increasing Sn content, from 887-857 K. Similarly, the $Sb_{2-x}Sn_xSe_3$ recrystallization temperature was found to increase somewhat linearly from 777-791 K for x = 0-0.1; once the $SnSb_2Se_4$ secondary phase formed, the trend was more inconsistent. The cooling DSC curves revealed that for x = 0-0.01, the melting was reversible; for x = 0.05-0.2, multiple cooling peaks were observed, showing evidence of thermal instability. Rietveld refinement was implemented to extract the lattice parameters for the $Sb_{2-x}Sn_xSe_3$ series, and it was found that both the a-axis and b-axis were relatively constant with increasing Sn. The a-axis and c-axis fluctuated around ~11.8251 Å and ~11.6718 Å. On the other hand, the b-axis showed a general rise with increasing Sn, from b = 3.9867-4.0096 Å. According to the Shannon radii, for CN = 6, R_{Sb3+} = 0.76 Å, while R_{Sn2+} = 1.18 Å; so, Sn^{2+} is ~55% larger than Sb^{3+} ($\Delta R/R$). As such, the increase in the b-axis with rising Sn content is consistent. Since the b-axis is the shortest axis, the Sn substitution had the most dramatic effect on this crystal direction.

Diffuse reflectance UV-Vis-NIR spectroscopy was implemented to analyze the optical properties of the samples, and the Kubelka-Munk function and Tauc plot analysis was applied to gather the direct optical bandgap, E_g. All $Sb_{2-x}Sn_xSe_3$ samples had an onset of the absorption edge at ~1.4 eV. The undoped Sb_2Se_3 sample had a well-defined absorption edge, while as the amount of Sn increased, the absorption edges appeared more gradual. Increasing the Sn content raised the level of low-energy band tailing. The band tailing could be evidence of the presence of impurity sub-bands within the band gap. With increasing x value, E_g was found to decrease linearly from

1.17 eV for x = 0 to 1.09 eV for x = 0.1. Intriguingly, the secondary phase formation at x = 0.1 led to a rise in E_g to 1.11 eV for x = 0.15, followed by a decrease in E_g to 1.07 eV for x = 0.2. In terms of the maximum absorbed wavelength λ_{Max}: for x = 0, λ_{Max} = 1062 nm; for x = 0.2, λ_{Max} = 1156 nm. So, throughout the x = 0-0.2 range, the $Sb_{2-x}Sn_xSe_3$ series can absorb wavelengths in the UV, visible, and near-IR (NIR) region. With more Sn content, the compound can absorb further into the NIR portion of the solar spectrum. The tunable bandgap of the material around ~1.1 eV makes it an ideal candidate as a photovoltaic absorber layer.

For the x = 0.1-0.2 compositions, the optical bandgap of $SnSb_2Se_4$ Pnnm secondary phase was also considered. A reported literature value for E_g of $SnSb_2Se_4$ Pnnm was not known, so the bandgap was estimated via a linear interpolation equation based on a reaction of SnSe (Pnma) and Sb_2Se_3 (Pnma). It was found that the E_g of $SnSb_2Se_4$ Pnnm was 0.86 eV; since the value was lower than the 1.17-1.07 eV range, it likely did not cause the decreasing bandgap for higher Sn values.

In the future for the $Sb_{2-x}Sn_xSe_3$ series (where Sb^{3+} and Sn^{2+}), it is suggested to analyze the samples using photoluminescence or another spectroscopy technique that could reveal the impurity states causing the low-energy band tailing at increased Sn content. Since we are doping Sb^{3+} with Sn^{2+}, there may be both donor and acceptor states found in some Sn content. Undoped Sb_2Se_3 is a known p-type material, and adding Sn^{2+} would cause a charge imbalance, eventually dumping electrons into the system. At high enough Sn content, a p-type to n-type transition at low-T could be generated-a Lifshitz transition. As such, for the composition series, low-T Seebeck coefficient and low-T Hall effect measurements would be ideal to shed light on this idea. As a reminder, for x = 0-0.1 the sample is single phase, so focusing on this composition range for both photoluminescence and low-T electrical transport measurements would be wise.

CHAPTER 5: $Cu_2Zn_{2x}Ti_{(3-2x)/2}Se_4$ (x = 1.5, 1, 0.5, 0) and $Cu_2Mn_3Se_4$

5.1 Introduction: $Cu_2Zn_{2x}Ti_{(3-2x)/2}Se_4$ (x = 1.5, 1, 0.5, 0) and $Cu_2Mn_3Se_4$

In terms of photovoltaic materials currently in the literature, Si, $CuInSe_2$ (CIS), $CuIn_xGa_{1-x}Se_2$ (CIGS), $Cu_2ZnSn(S, Se)_4$ (CZTS), and CdTe are well-studied.[87-91] Interestingly, in 2018 Chen *et al*.[92] recently discovered Cu_4TiSe_4, a promising p-type material with a large optical absorption coefficient and direct bandgap of 1.34 eV.[92] **Table 5.1.1** lists the optical bandgap and record efficiency for several absorber materials. Additionally, the type of bandgap of each material was also listed. Direct bandgap transitions much more efficiently convert a photon of light to electricity when compared to indirect transitions. This is due to the fact that indirect bandgap materials have to rely on phonon-assisted Umklapp processes to carry out the electron excitation from valence to conduction band.[93] Based on the bandgap, the maximum wavelength of light the material can absorb was calculated.

Table 5.1.1: Optical Bandgap (E_g) and record efficiency for various solar absorber materials.

Solar Absorber	Direct or Indirect Bandgap?	E_g (eV)	λ_{Max} (nm)	Record Efficiency
Si	Indirect[94]	1.11[93]	1117	26.3%[87]
$CuInSe_2$ (CIS)	Direct[95]	1[95]	1240	13.5%[88]
$CuIn_xGa_{1-x}Se_2$ (CIGS)	Direct[96]	1.05-1.6[89]	775-1181	23.4%[89]
$Cu_2ZnSn(S, Se)_4$ (CZTS)	Direct[94]	1.0-1.5[94]	827-1240	12.6%[90]
CdTe	Indirect[93]	1.44[93]	861	22.1%[91]
Cu_4TiSe_4	Direct[92]	1.34[92]	925	-

In this work, the following copper-metal-selenides were synthesized: $Cu_2Zn_3Se_4$, $Cu_2Zn_2Ti_{0.5}Se_4$, $Cu_2ZnTiSe_4$, $Cu_2Ti_{1.5}Se_4$, and $Cu_2Mn_3Se_4$. To help visualize the typical elements utilized for solar applications, as well as those used in this work-please refer to **Figure 5.1.1** for a periodic table. In the diagram, the elements utilized were boxed-black for the metals, and red for the anions.

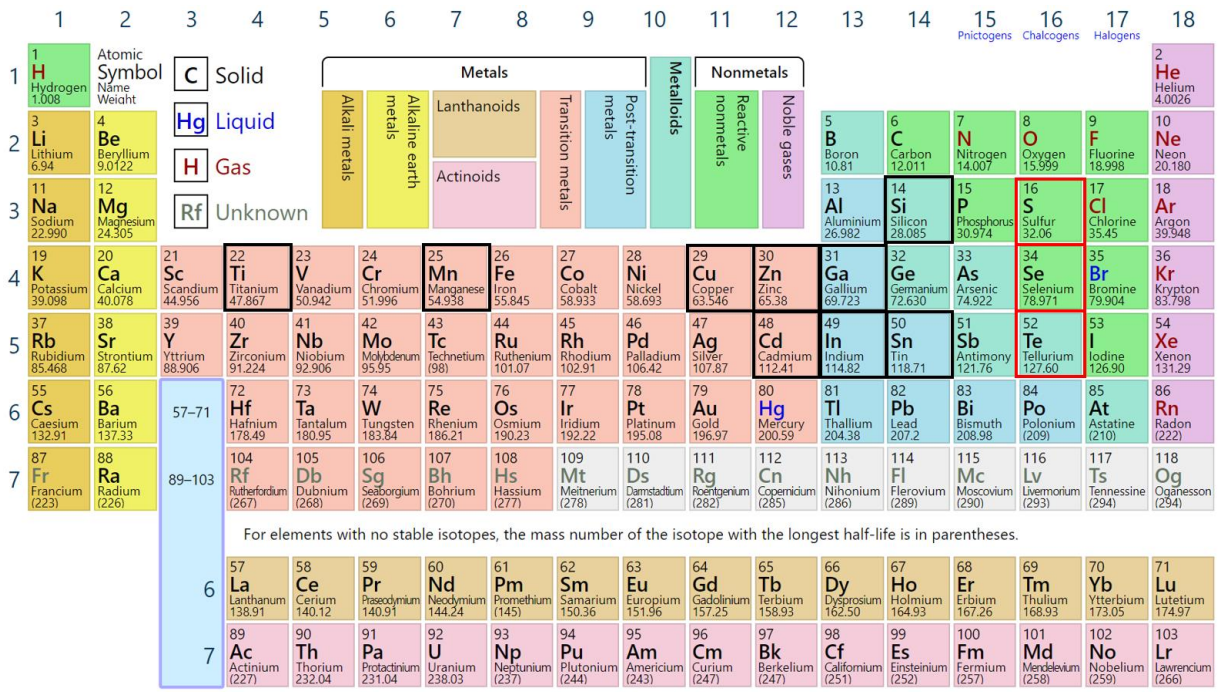

Figure 5.1.1: Periodic table of the elements. Typical metals and anions for solar applications and those synthesized in this work were boxed in black and red, respectively. Image was adapted from PT.com.

Now, it is crucial to analyze the elemental abundance of the solar absorber materials in question-as this will partially dictate the commercial viability of the compound. In terms of the elements involved in the absorbers as well as in this work, there are the following: Cu, Zn, Sn, Ti, Se, Mn, Si, In, Ga, S, Cd, and Te. **Figure 5.1.2** depicts the abundance of the elements listed-metals boxed in green, and anions boxed in red. In this figure, we can see that Si is extremely abundant, so it makes sense that most commercially made solar cells are based on silicon. Fortunately for the case of CZTS, Cu_4TiSe_4, and the Cu-M-Se elements in this work, the

elemental abundance is relatively high as well. However, for the case of CIS, CIGS, and CdTe, we see that In, Cd, and Te are somewhat scarce by comparison.

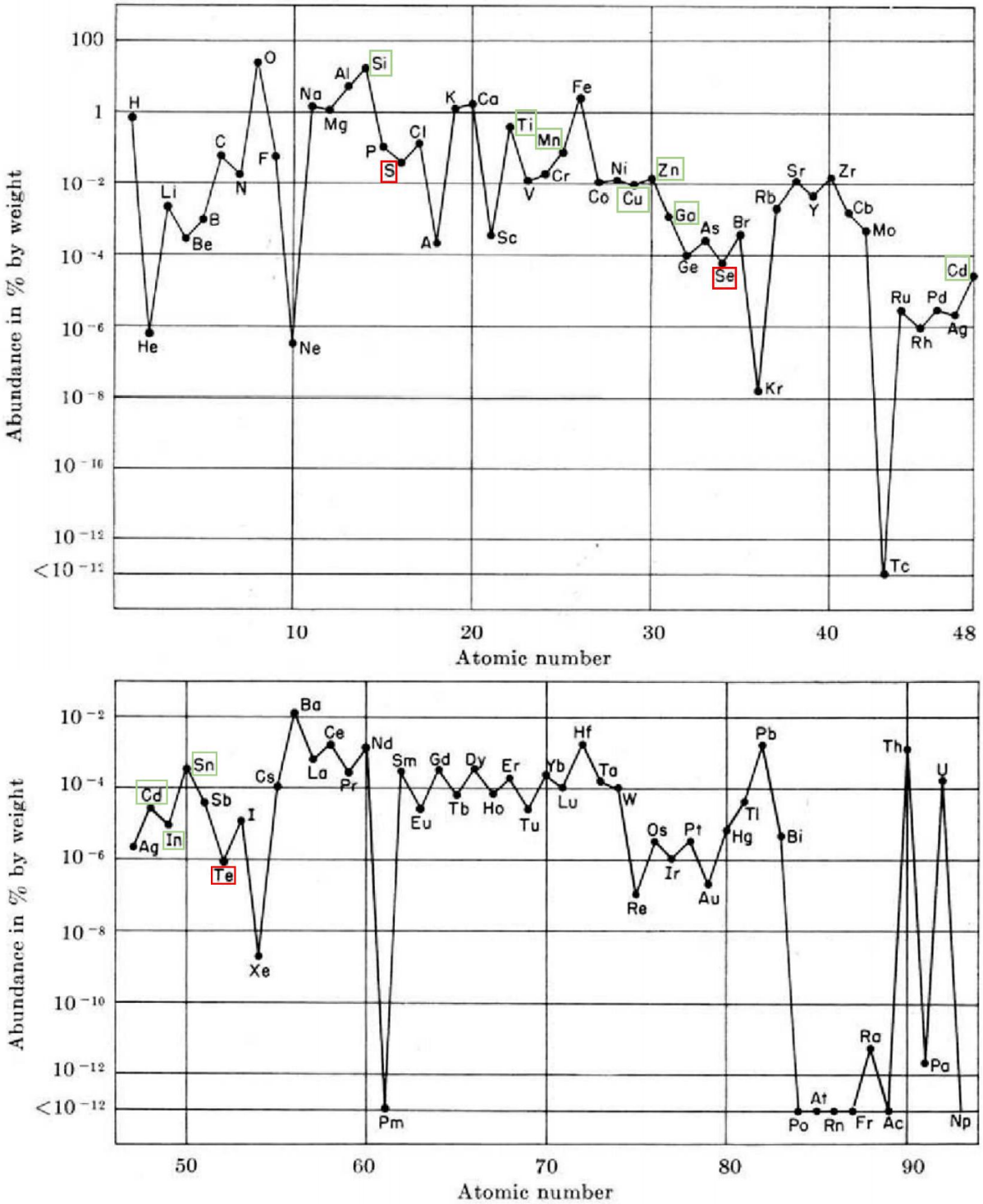

Figure 5.1.2: Top: Elemental abundance for atomic numbers 1-48. **Bottom:** Elemental abundance for atomic numbers 49-93. The relevant elements for Si, CZTS, CIGS, CdTe, and the compounds used in this thesis were highlighted with a box around the element-green for a metal, and red for

an anion. Images were adapted from Fleischer's work on the abundance of elements in the Earth's crust.[97]

In addition to the elemental abundance, the price in USD/kg is also an important quantity, as this will estimate the raw materials cost to form the solar absorber. The y-axis on the right side of **Figure 5.1.3** lists the cost of the elements in question by the black/grey bar graphs.

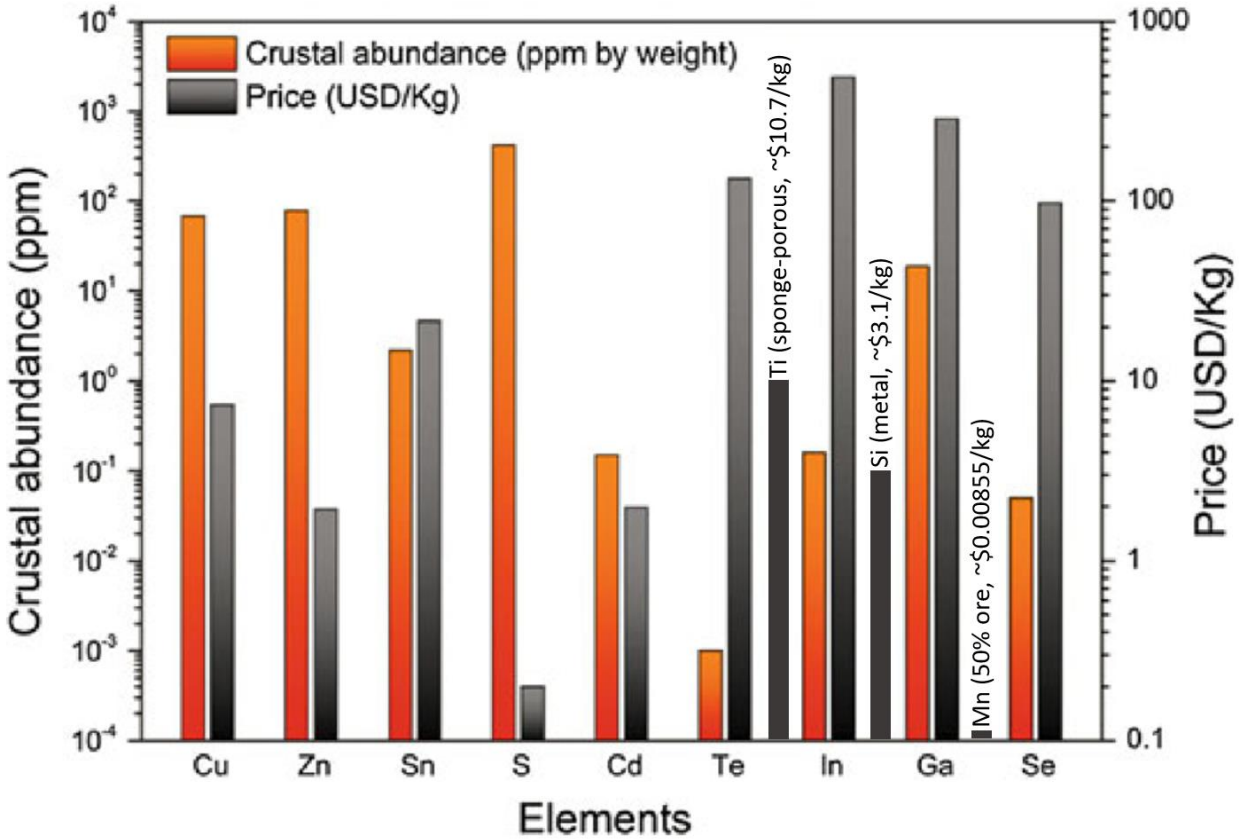

Figure 5.1.3: Crustal abundance and price of various elements used in CZTS, CIGS, and CdTe. Relevant elements not depicted: Ti, Mn, and Si. According to the U.S. 2010 geological survey[98], these elements are priced at the following: Ti (sponge-porous, ~$10.7/kg); Mn, (50% ore, ~$0.00855/kg); Si (metal, ~$3.1/kg).[98] Bar graphs for Ti, Mn, and Si were manually added to the plot accordingly. Image was adapted from Das *et al*.[99]

In terms of cheapest to most expensive elements, the list is as follows: Mn, S, Zn & Cd, Si, Cu, Ti, Sn, Se, Te, Ga, and In. Since the costliest elements are Te, Ga, and In, CIS, CIGS, and CdTe would be expensive to synthesize.

An additional consideration one must consider is the toxicity of each element involved. The Occupational Safety and Health Administration (OSHA) permissible exposure limit (PEL) is one way the relative toxicity of the elements can be considered. A material with a lower PEL value is less safe for humans. To gather this data, the PEL values were referenced from the Center for Disease Control and Prevention (CDC) database on the National Institute for Occupational Safety and Health (NIOSH). On the NIOSH database, elemental PEL values were not reported for the following: S, Ti, Zn, and Ga. In this case, the proper Sigma-Aldrich (SA) materials safety data sheet (MSDS) was referenced. **Table 5.1.2** lists the PEL of the twelve elements in consideration.

Table 5.1.2: Occupational Safety and Health Administration (OSHA) permissible exposure limit (PEL) of various relevant elements for solar absorber materials. The PEL values were referenced from the Center for Disease Control and Prevention (CDC) database on the National Institute for Occupational Safety and Health (NIOSH). On the NIOSH database, elemental PEL values were not reported for the following: S, Ti, Zn, and Ga. In this case, the proper Sigma-Aldrich (SA) materials safety data sheet (MSDS) was referenced. Note: CAS stands for Chemical Abstracts Service. For the case of elements with a hyphen, this means that they are relatively safe and do not have specific OSHA PEL values reported.

Element	Atomic #	OSHA PEL (mg/m^3)	Source: NIOSH or SA-MSDS?
Si	14	15	NIOSH CAS #7440-21-3
S	16	-	SA-MSDS #414980
Ti	22	-	SA-MSDS #366994
Mn	25	5	NIOSH CAS #7439-96-5
Cu	29	1	NIOSH CAS #7440-50-8
Zn	30	10	SA-MSDS #96454
Ga	31	-	SA-MSDS #263265
Se	34	0.2	NIOSH CAS #7782-49-2
Cd	48	0.005	NIOSH CAS #7440-43-9
In	49	0.1	NIOSH CAS #7440-74-6
Sn	50	2	NIOSH CAS #7440-31-5
Te	52	0.1	NIOSH CAS #13494-80-9

With the elemental PEL values in mind, it may be wise to analyze the overall PEL limit of the complete solar compound. In **Table 5.1.3**, this was carried out by summing the individual PEL

values of each element in the compound. This should provide at least a reasonable estimate for the relative toxicity of the photovoltaic material in question. CIGS was found to have a low PEL, so it was used as a standard of comparison for the rest of the solar materials.

Table 5.1.3: To estimate the relative safety of the absorber material, the PEL of each absorber element was summed together in the compound. CIGS was noted to have a low PEL, so each absorber compound was compared to CIGS. Also listed below are the thesis compounds 3.3-3.7 for comparison purposes.

Thesis Compound #	Solar Absorber	Solar Absorber PEL Sum (mg/m^3)	PEL Relative to CIGS
-	Si	15	12.5x safer
-	$CuInSe_2$ (CIS)	1.3	1.1x safer
-	$CuIn_xGa_{1-x}Se_2$ (CIGS)	1.2	-
-	$Cu_2ZnSn(S, Se)_4$ (CZTS)	13.2	11x safer
-	CdTe	0.105	11.4x more toxic
-	Cu_4TiSe_4[92]	1.2	equal
3.3	$Cu_2Zn_3Se_4$	11.2	9.3x safer
3.4	$Cu_2Zn_2Ti_{0.5}Se_4$	11.2	9.3x safer
3.5	$Cu_2ZnTiSe_4$	11.2	9.3x safer
3.6	$Cu_2Ti_{1.5}Se_4$	1.2	equal
3.7	$Cu_2Mn_3Se_4$	6.2	5.2x safer

Relative to CIGS, most compounds were found to be less toxic except for CdTe. Due to the extremely low PEL values for both Cd and Te, it was found to be quite toxic. Si, CZTS, and most of the thesis Cu-M-Se compounds had much higher PEL values.

So, to recap, although CIS, CIGS, and CdTe have relatively high cell efficiencies and close to ideal band gap values, The elements are relatively scarce, expensive, and toxic. On a positive note, Si, CZTS, and the Cu-M-Se systems have relatively favorable properties overall.

To gain further insight on the Cu-based solar materials (CIS, CIGS, CZTS, Cu_4TiSe_4) in particular, one must turn to the crystal structure of each compound. **Figure 5.1.4a** depicts the CIS

chalcopyrite crystal structure.[99] CIS crystallizes in the tetragonal space group I$\bar{4}$2d (#122), with lattice parameters a = b = 5.7810 Å, c = 11.6422 Å (~2*a); α = β = γ = 90°.[99, 100] In CIS, both Cu and In are tetrahedrally coordinated to S/Se; when projected along the b-axis, the elements alternate along the c-axis as Cu-In-Cu, Se-Se, Cu-In-Cu, Se-Se, In-Cu-Se, Se-Se, In-Cu-Se, Se-Se, and Cu-In-Se.[99]

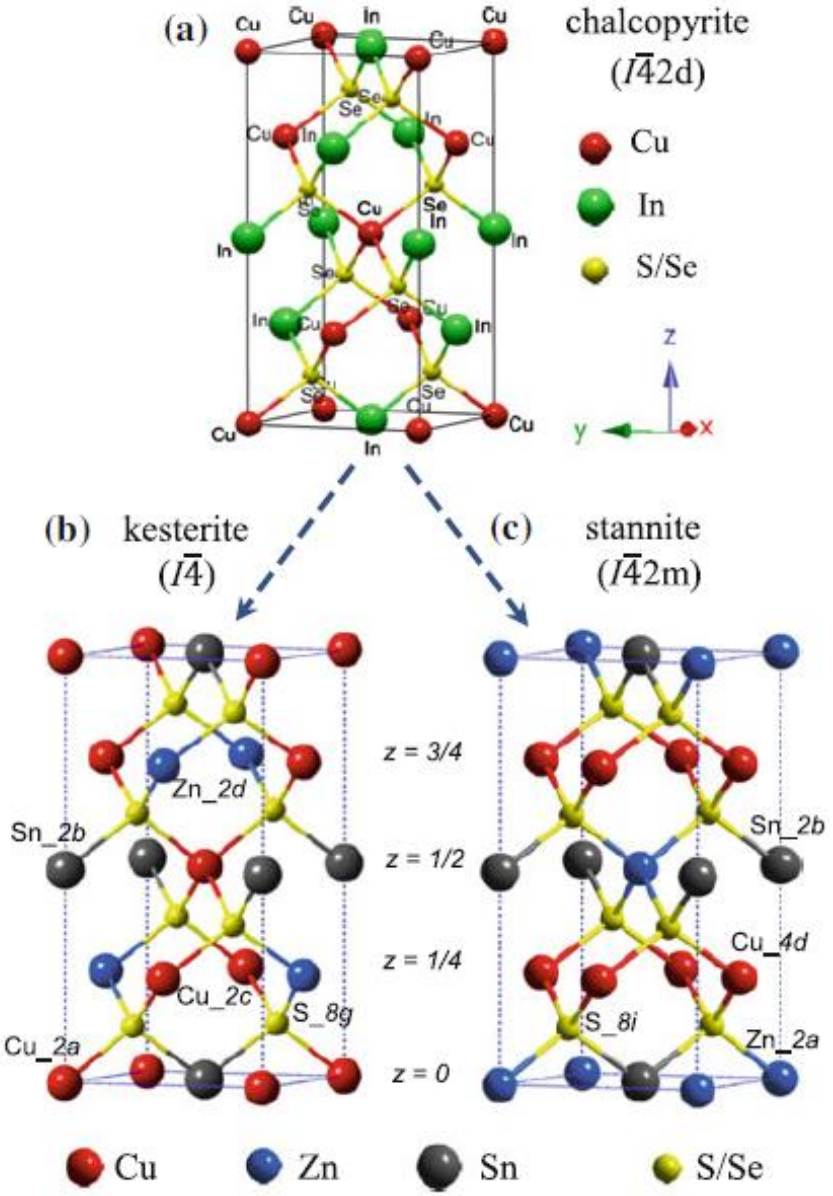

Figure 5.1.4: a) $CuInSe_2$ chalcopyrite crystal structure. **b)** Kesterite $Cu_2ZnSn(S, Se)_4$ (CZTS) crystal structure. **c)** Stannite $Cu_2ZnSn(S, Se)_4$ (CZTS) crystal structure. Image was adapted from Das *et al*.[99]

$CuIn_{1-x}Ga_xSe_2$ (CIGS) forms isostructurally with CIS, with the exact lattice parameters varying with the x value in question.

Interestingly, CZTS forms in a similar fashion to CIS, where half of the In atoms are replaced by Zn, and the other half are replaced by Sn. **Figure 5.1.4b** and **Figure 5.1.4c** illustrate this point.[99] Surprisingly, CZTS forms two distinct forms: Kesterite (**Figure 5.1.4b**) and Stannite (**Figure 5.1.4c**). Kesterite CZTS forms in the tetragonal space group tetragonal space group $I\bar{4}$ (#82), with lattice parameters a = b = 5.693 Å, c = 11.342 Å (~2*a); α = β = γ = 90°.[101] Stannite CZTS forms in the tetragonal space group tetragonal space group $I\bar{4}2m$ (#121), with lattice parameters a = b = 5.6954 Å, c = 11.3475 Å (~2*a); α = β = γ = 90°.[102] As we can see from **Figure 5.1.4b** and **Figure 5.1.4c**, the two structures are quite similar. Both structures have cations that sit at tetrahedral sites, but when along the c-axis, a very slight difference in the stacking arrangement of Cu and Zn is observed.[99] For purposes of consistency, for the remainder of this dissertation, CZTS will be referred to as kesterite.

Cu_4TiSe_4 crystallizes in the cubic space group $F\bar{4}3c$ (#219), with lattice parameters a = b = c = 11.2936 Å; α = β = γ = 90°.[92] **Figure 5.1.5** depicts the Cu_4TiSe_4 structure. In the structure, Ti^{4+} ions sit in channels between $[Cu_4Se_4]^{4-}$ anion clusters.[92]

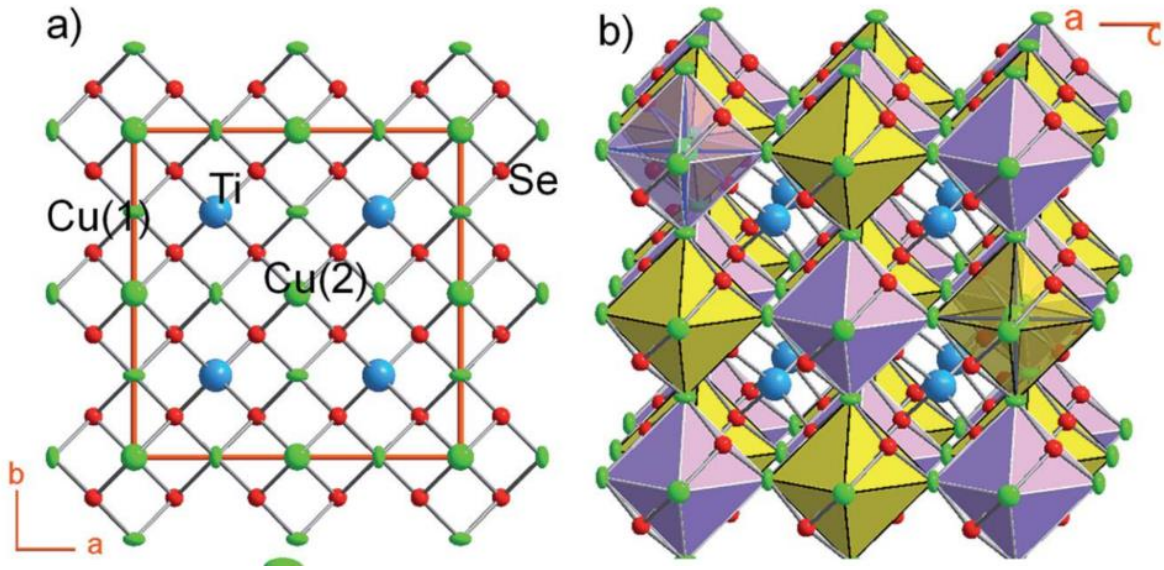

Figure 5.1.5: a) Cu_4TiSe_4 crystal projection along [001], depicting the connectivity of the structure. **b)** $[Cu_4Se_4]^{4-}$ anion clusters, with Ti^{4+} ions sitting in the channels between the clusters. Image was adapted from Chen *et al*.[92]

In this work, we took a systematic topochemical approach to engineering the structure and vacancies of Cu-metal-selenides. A parent formula of $\left(Cu^{1+}\right)_2\left(Zn^{2+}\right)_{2x}\left(Ti^{4+}\right)_{\frac{3-2x}{2}}\left(Se^{2-}\right)_4$ (x = 1.5, 1, 0.5, 0) or $Cu_2Mn_3Se_4$ was synthesized, with the high-temperature β-phase of Cu_2Se (i.e., Cu_8Se_4) as the model structure. β-Cu_2Se crystallizes in the cubic space group $Fm\bar{3}m$ (#225), with lattice parameters a = b = c = 5.694 Å; α = β = γ = 90°.[103] In the lattice, the Cu^{1+} ions are superionic, having high mobility to move throughout the structure.[104] **Figure 5.1.6** depicts the β-Cu_2Se structure. It forms in an antifluorite-like M_2X lattice where M = Cu^{1+} and X = Se^{2-}.[105] In the crystal, Se^{3-} forms an fcc lattice, with the Cu^{1+} cations filling the 8/8 tetrahedral interstitial sites.[105] For Cu^{1+}, CN = 4-corresponding to a tetrahedral coordination geometry.

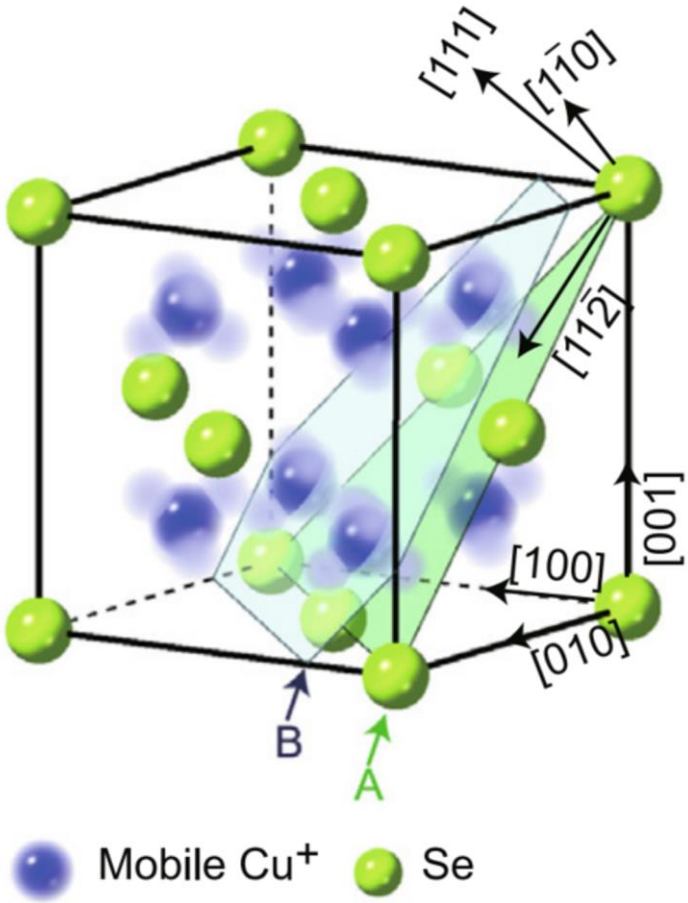

Figure 5.1.6: β-Cu_2Se structure. It forms in an antifluorite-like M_2X lattice where M = Cu^{1+} and X = Se^{2-}. The Cu^{1+} are highly mobile in the lattice. Image was adapted from Sun *et al*.[105]

By writing Cu_2Se as Cu_8Se_4, we can see the interstitial vacancy count. More generally, we can say M_ySe_4, where M is every metal and y are the total metal count in the compound. Now, we can write the various absorber materials and dissertation compounds in this M_ySe_4 form to analyze the amount of interstitial tetrahedral vacancies. **Table 5.1.4** depicts these results below. We see that aside for Cu_2Se, all other compounds in the list exhibit at least some level of interstitial tetrahedral vacancies.

Table 5.1.4: Generic M_ySe_4 formula for solar cell materials and dissertation compounds, where M is every metal and y are the total metal count in the compound. For the cases where single crystal growth formed a different stoichiometry than expected, the single crystal compound M_ySe_4 formula was also reported.

x Value	Compound	M_ySe_4 of Compound	Single Crystal Compound	M_ySe_4 of Single Crystal Compound	Any change in M_ySe_4 between compound and single crystal?
-	Cu_8Se_4	M_8Se_4	-	-	-
-	Cu_4TiSe_4	M_5Se_4	-	-	-
-	$Cu_2ZnSnSe_4$	M_4Se_4	-	-	-
-	$Cu_2In_2Se_4$	M_4Se_4	-	-	-
-	$Cu_2In_{2-2x}Ga_{2x}Se_4$	M_4Se_4	-	-	-
-	$Cu_2Mn_3Se_4$	M_5Se_4	$Cu_2Mn_3Se_4$	M_5Se_4	No
x = 1.5	$Cu_2Zn_3Se_4$	M_5Se_4	$Cu_2Zn_3Se_4$	M_5Se_4	No
x = 1	$Cu_2Zn_2Ti_{0.5}Se_4$	$M_{4.5}Se_4$	$Cu_{2.75}Zn_{0.625}TiSe_4$	$M_{4.375}Se_4$	M ↓ by 0.125
x = 0.5	$Cu_2ZnTiSe_4$	M_4Se_4	$Cu_2ZnTiSe_4$	M_4Se_4	No
x = 0	$Cu_2Ti_{1.5}Se_4$	$M_{3.5}Se_4$	$Cu_3Ti_{1.25}Se_4$	$M_{4.25}Se_4$	M ↑ by 0.75

For $Cu_2Mn_3Se_4$, there were 3/8 tetrahedral vacancies. For the parent formula $\left(Cu^{1+}\right)_2\left(Zn^{2+}\right)_{2x}\left(Ti^{4+}\right)_{\frac{3-2x}{2}}\left(Se^{2-}\right)_4$ (x = 1.5, 1, 0.5, 0), decreasing the x value increased the number of tetrahedral vacancies from 3/8, to 3.5/8, 4/8, and 4.5/8. **Table 5.1.5** and **Table 5.1.6** depict the number of vacancies and percent of vacancies for each compound, respectively. By engineering the total metal count and number of vacancies of each compound, changes in the crystal structure and materials properties are to be expected.

Table 5.1.5: Number of tetrahedral interstitial vacancies in each compound.

x Value	Compound	# of Tetrahedral Interstitial Vacancies in Compound $\frac{8-y}{8}$	Single Crystal Compound	# of Tetrahedral Interstitial Vacancies in Single-Crystal Compound $\frac{8-y}{8}$	Any change in the # of Tetrahedral Interstitial Vacancies between the compound and single crystal?
-	Cu_8Se_4	$\frac{0}{8}$	-	-	-
-	Cu_4TiSe_4	$\frac{3}{8}$	-	-	-
-	$Cu_2ZnSnSe_4$	$\frac{4}{8}$	-	-	-
-	$Cu_2In_2Se_4$	$\frac{4}{8}$	-	-	-
-	$Cu_2In_{2-2x}Ga_{2x}Se_4$	$\frac{4}{8}$	-	-	-
-	$Cu_2Mn_3Se_4$	$\frac{3}{8}$	$Cu_2Mn_3Se_4$	$\frac{3}{8}$	No
x = 1.5	$Cu_2Zn_3Se_4$	$\frac{3}{8}$	$Cu_2Zn_3Se_4$	$\frac{3}{8}$	No
x = 1	$Cu_2Zn_2Ti_{0.5}Se_4$	$\frac{3.5}{8}$	$Cu_{2.75}Zn_{0.625}TiSe_4$	$\frac{3.625}{8}$	$\uparrow \frac{0.125}{8}$
x = 0.5	$Cu_2ZnTiSe_4$	$\frac{4}{8}$	$Cu_2ZnTiSe_4$	$\frac{4}{8}$	No
x = 0	$Cu_2Ti_{1.5}Se_4$	$\frac{4.5}{8}$	$Cu_3Ti_{1.25}Se_4$	$\frac{3.75}{8}$	$\downarrow \frac{0.75}{8}$

Table 5.1.6: Percent of tetrahedral vacancies in each compound.

x Value	Compound	% Tetrahedral Interstitial Vacancies in Compound $\frac{8 - y}{8} * 100$	Single Crystal Compound	% Tetrahedral Interstitial Vacancies in Single-Crystal Compound $\frac{8 - y}{8} * 100$	Any change in the % Tetrahedral Interstitial Vacancies between the compound and single crystal?
-	Cu_8Se_4	0%	-	-	-
-	Cu_4TiSe_4	37.5%	-	-	-
-	$Cu_2ZnSnSe_4$	50%	-	-	-
-	$Cu_2In_2Se_4$	50%	-	-	-
-	$Cu_2In_{2-2x}Ga_{2x}Se_4$	50%	-	-	-
-	$Cu_2Mn_3Se_4$	37.5%	$Cu_2Mn_3Se_4$	37.5%	No
x = 1.5	$Cu_2Zn_3Se_4$	37.5%	$Cu_2Zn_3Se_4$	37.5%	No
x = 1	$Cu_2Zn_2Ti_{0.5}Se_4$	43.75%	$Cu_{2.75}Zn_{0.625}TiSe_4$	45.31%	↑ 1.56%
x = 0.5	$Cu_2ZnTiSe_4$	50%	$Cu_2ZnTiSe_4$	50%	No
x = 0	$Cu_2Ti_{1.5}Se_4$	56.25%	$Cu_3Ti_{1.25}Se_4$	46.88%	↓ 9.38%

5.2 Synthesis: $Cu_2Zn_{2x}Ti_{(3-2x)/2}Se_4$ (x = 1.5, 1, 0.5, 0) and $Cu_2Mn_3Se_4$

Table 5.2.1: $Cu_2Zn_{2x}Ti_{(3-2x)/2}Se_4$ (x = 1.5, 1, 0.5, 0) and $Cu_2Mn_3Se_4$ synthesis methods. Refer to the proper sections for the procedures used.

Compound	Powder Synthesis	Annealed Powder Synthesis	Hot Pressed Pellet/ Bar Synthesis	Single Crystal (SC) Method	SC Synthesis Temperature(s) Used
$Cu_2Zn_3Se_4$	Section 5.2.1	Section 5.2.2	Section 5.2.3	High-T Annealing (Section 5.2.4)	1080 °C
$Cu_2Zn_2Ti_{0.5}Se_4$	Section 5.2.1	-	-	Melt & Slow Cool (Section 5.2.5)	900 °C, then slow cool to 750 °C
$Cu_2ZnTiSe_4$	Section 5.2.1	-	-	Melt & Slow Cool (Section 5.2.5)	900 °C, then slow cool to 750 °C
$Cu_2Ti_{1.5}Se_4$	Section 5.2.1	-	Section 5.2.3	Dual-Zone Furnace (Section 5.2.6)	T_{Hot} = 720 °C; T_{Cold} = 520 °C
$Cu_2Mn_3Se_4$	Section 5.2.1	-	-	Dual Zone Furnace (Section 5.2.6)	T_{Hot} = 450 °C; T_{Cold} = 250 °C

5.2.1 Powder Synthesis:

Polycrystalline powder of were generated from a solid-state reaction of elements. Stoichiometric amounts of the proper elements: Cu (99.5%, Alfa Aesar), Zn (99.99%, J.T. Baker Chemical), Ti (99.5%, Alfa Aesar), Mn (99.3%, Alfa Aesar), or Se (99.5%, Sigma Aldrich) were weighed in an argon glovebox and ground thoroughly with a mortar and pestle, vacuum flame-sealed in quartz tubes, and placed in a programmable furnace as described in **Section 2.1.1**. The reaction profile was as follows: heat to 300 °C in 12 hours, hold at 300 °C for 24 hours, heat to 700 °C in 6 hours, hold at 700 °C for 72 hours, cool to 50 °C in 6 hours, and cool to 25 °C in 1

hour. The resultant ingot was ground into powder and PXRD, DSC, and UV-Vis-NIR diffuse reflectance spectroscopy measurements were performed.

5.2.2 Annealing Powder:

Ground powder was loaded into a quartz tube and flame-sealed at ~10 cm. When annealing was applied, the following conditions were used: heat to 1000 °C over 6 hours, dwell at 1000 °C for 3 weeks, cool to 25 °C over 24 hours.

5.2.3 Hot-Pressed Pellet/Bar:

Hot pressing was carried out in a similar fashion as described in **Section 2.1.2**. In this case, the temperature program was as follows: heat to 300 °C over 2 hours, dwell at 300 °C for 4 hours, cool to 25 °C over 2 hours. The pellet was pressed at a pressure of 98.6 MPa. The pellet was polished to a mirror finish using 600/P1200/800 grit SiC paper. Proper densification was confirmed using the pycnometer (machine accuracy of < 0.3%). For electrical conductivity/Seebeck coefficient analysis, the pellet was cut into a rectangular bar with the approximate dimensions of 3 mm x 3 mm x 10 mm using an Isomet 1000 precision diamond saw and polished using the above SiC paper grit series.

5.2.4 Single-Crystal Synthesis: High-T Annealing

Due to a high melting point of ~1150 C, high-T annealing was utilized. Approximately 200 mg of sample was placed into a quartz tube and sealed at a length of 7 cm. The following reaction profile was used: heat to 1080 °C over 12 hours, dwell at 1080 °C for 5 days, cool to 25 °C over 12 hours.

5.2.5 Single-Crystal Synthesis: Melt & Slow-Cool

Having a melting point around 800 °C, a melt & slow cool crystal growth procedure was used. Approximately 200 mg of sample was placed into a quartz tube and sealed at a length of 7 cm. The following reaction profile was used: heat to 900 °C over 24 hours, slow cool to 750 °C over 5 days, cool to 25 °C over 12 hours.

5.2.6 Single-Crystal Synthesis: Dual-Zone Furnace

A dual-zone furnace method was used in this case. **Figure 5.2.1** depicts the melting point of the sample, and the chosen hot temperature and cold temperature. A temperature gradient of 200 °C was used. **Figure 5.2.2** gives a schematic of the dual-zone furnace. A tube length of 23 cm was utilized, with 200 mg powder. The sample end of the tube was placed at T

Compound	MP (°C)	T_{Hot} (°C)	T_{Cold} (°C)
$Cu_2Ti_{1.5}Se_4$	~814.0	720	520
$Cu_2Mn_3Se_4$	~550.2	450	250

Hot Thermocouple Reaction Profile:

- Heat to T_{Hot} over 12 hours
- Dwell at T_{Hot} for 24 hours
- Dwell at T_{Hot} for 12 hours
- Dwell at T_{Hot} for 11 days (264 hours)
- Cool to 25 °C over 72 hours
- Total time: 384 hours, i.e., 16 days

Cold Thermocouple Reaction Profile:

- Heat to T_{Hot} over 12 hours
- Dwell at T_{Hot} for 24 hours
- Cool to T_{Cold} over 12 hours
- Dwell at T_{Cold} for 11 days (264 hours)
- Cool to 25 °C over 72 hours
- Total time: 384 hours, i.e., 16 days

Figure 5.2.1: Dual-Zone furnace single-crystal method instructions.

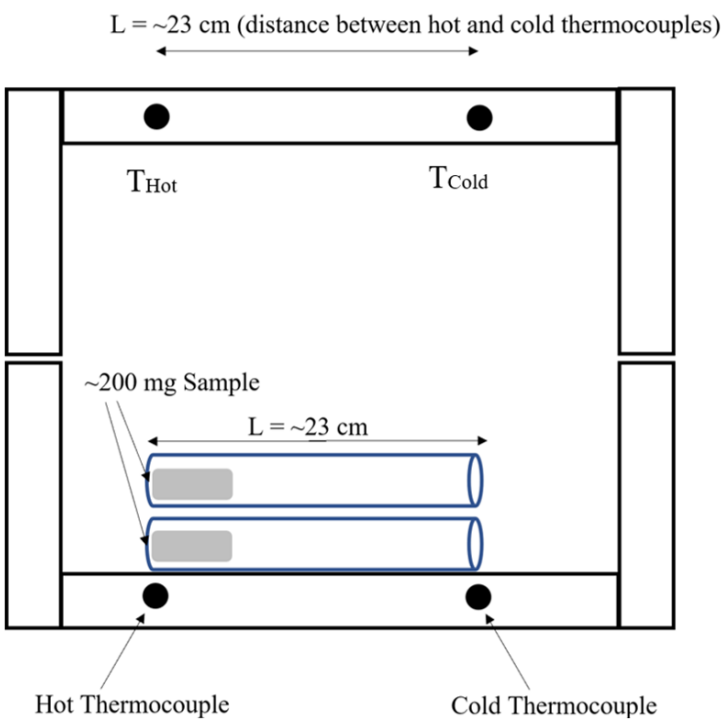

Figure 5.2.2: Dual-zone furnace diagram.

5.3 $Cu_2Zn_3Se_4$ (x = 1.5) Single Crystal Synthesis ($Cu_2Zn_3Se_4$), Structural, Optical, and Thermoelectric Properties:

5.3.1 Results & Discussion: $Cu_2Zn_3Se_4$ (x = 1.5):

5.3.1.1 Single Crystal Synthesis ($Cu_2Zn_3Se_4$) (x = 1.5)

$Cu_2Zn_3Se_4$ single crystals were grown via a high-T annealing method at 1080 °C. Refer to **Section 5.2** for more details. **Figure 5.3.1** depicts the reacted powder on the left. The powder appeared dark/army green in color. The center image is an extended depth of focus (EDF) optical micrograph. The crystal is amber yellow in appearance and faceted. Also noted is the scale bar, with the crystal size being ~200 μm, i.e., 0.2 mm. The right image is another single crystal mounted on a glass fiber for single-crystal XRD analysis. Again, the crystal appeared amber yellow in color.

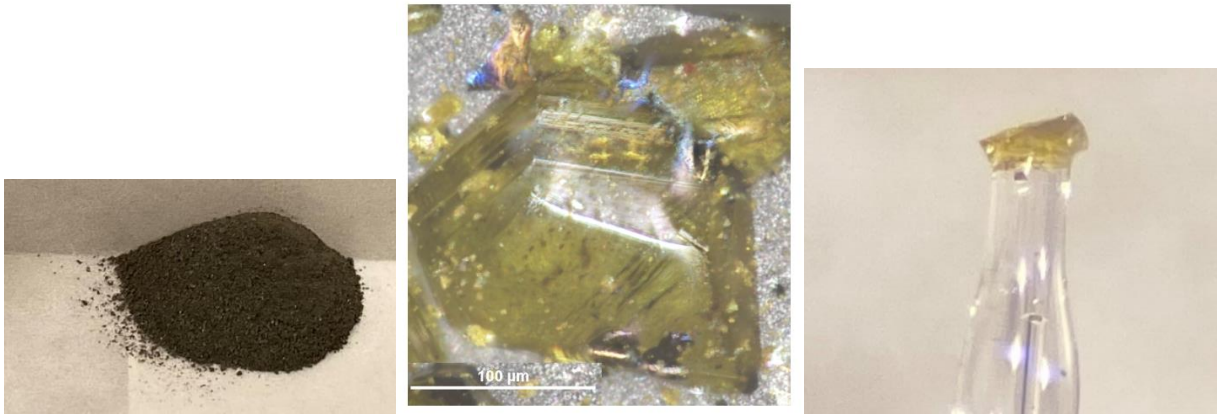

Figure 5.3.1: Left: $Cu_2Zn_3Se_4$ powder after reaction and being ground. Photograph was taken using an Apple iPhone 11 Pro Max camera (12 MP). **Middle:** $Cu_2Zn_3Se_4$ single crystal taken using a Nikon brightfield optical microscope with DS-Ri2 camera. Recorded using the extended depth of focus (EDF) mode at 20x magnification. **Right:** $Cu_2Zn_3Se_4$ single crystal mounted on the tip of a glass fiber for single crystal XRD analysis. Image was recorded using a Leica S6E stereo microscope equipped with a Leica L2 light source at 4x zoom. Image was captured through the lenspiece with an Apple iPhone 11 Pro Max 2x telephoto optical zoom lens (12-megapixel), giving a total of ~8x magnification.

5.3.1.2 Structural Properties of $Cu_2Zn_3Se_4$

$Cu_2Zn_3Se_4$ single crystals were grown and the crystal structure was solved using single-crystal XRD and structure refinement. During refinement, two lattices were discovered, a small cell (SC) and a 3x3x3 supercell version of the SC (labeled large cell, LC). Selected crystal data is listed in **Table 5.3.1**. Both the SC and LC versions of $Cu_2Zn_3Se_4$ crystallized in the cubic

Table 5.3.1: Selected crystallographic data for $Cu_2Zn_3Se_4$.

Cell Type	**Small Cell**	**Large Cell**
Formula	$Cu_2Zn_3Se_4$	$Cu_2Zn_3Se_4$
Crystal system	Cubic	Cubic
Space group	$Fm\bar{3}m$ (#225)	$Fm\bar{3}m$ (#225)
a = b = c (Å)	5.6721(7)	17.014(2)
$\alpha = \beta = \gamma$ (°)	90	90
V (Å^3)	182.49(4)	4925.15(100)
Formula Mass (g/mol)	639.03	639.03
ρ (g/cm^3)	5.81451	5.81686
Z	1	27
Temperature (K)	300	300
R_{All}	0.0174	0.0922
R_{int}	0.0865	0.0491
$R_1(F_o > 4\sigma(F_o))$	0.0174	0.0735
wR_2 (all)	0.0317	0.0913
GooF	1.307	1.332

Fm-3m (#225) space group with lattice parameters of a = 5.6721 Å and a =17.014 Å, respectively. **Table 5.3.2** and **Table 5.3.3** lists the atomic coordinates, equivalent isotropic displacement parameters, and site occupancies for the SC and LC, respectively. For the SC case, Zn1 and Cu1 share the same Wyckoff position 8c, corresponding to the tetrahedral sites in the lattice. Also note the large amount of vacancies at each position. There is disorder of Cu and Zn atoms in all

tetrahedral sites: site ocupancy = 5/8, vacancy = 3/8. The 3x3x3 supercell was found to resolve the ordering of the Cu and Zn atoms in all tetrahedral sites. Notice that the overall site occupancy

Table 5.3.2: $Cu_2Zn_3Se_4$ Small Cell atomic coordinates, equivalent isotropic displacement parameters $U_{eq.}$, and occupancies for all atoms. *Note: only U_{11} had values, so $U_{eq.} = U_{11}$ here.

$Cu_2Zn_3Se_4$-small cell							
Atom	**Wyck.**	**S.O.F.**	**Vac.**	**x**	**y**	**z**	***$U_{eq.}$ (Å^2 x 10^{-4})**
Se1	4a	1	-	0	0.5	0.5	349.4(7)
Zn1	8c	0.38	62%	0.25	0.75	0.75	420.7(9)
Cu1	8c	0.25	75%	0.25	0.75	0.75	420.7(9)

Table 5.3.3: $Cu_2Zn_3Se_4$ Large Cell atomic coordinates, equivalent isotropic displacement parameters $U_{eq.}$, and occupancies for all atoms.

$Cu_2Zn_3Se_4$-large cell							
Atom	**Wyck.**	**S.O.F.**	**Vac.**	**x**	**y**	**z**	**$U_{eq.}$ (Å^2 x 10^{-4})**
Se1	4a	1	-	0	0.5	0.5	352.1(4)
Se2	48h	1	-	0.16667(3)	0.5	0.66667(3)	287.7(2)
Se3	24e	1	-	0	0.5	0.83338(6)	321.4(2)
Se4	32f	1	-	0.83334(2)	0.33334(2)	0.83334(2)	256.4(2)
Zn1	32f	0.63	37%	0.08246(5)	0.58246(5)	0.91754(5)	371.8(4)
Zn2	96k	0.63	37%	0.91661(4)	0.41661(4)	0.74917(7)	423(3)
Cu1	8c	0.61	39%	0.75	0.25	0.75	273.2(5)
Cu2	32f	0.61	39%	0.08407(4)	0.58407(4)	0.58407(4)	218.6(3)
Cu3	48g	0.61	39%	0.25	0.58336	0.75	272(3)

increased and the vacancies in each site decreased for the LC case. **Figure 5.3.2** and **Figure 5.3.3** and depict the crystal projection along the a-axis for the SC and LC, respectively. Notice the mixed Cu/Zn site for the SC case. For the LC projection, the cell was divided into a 3x3x3 grid to help visualize the small cell repeat unit. Notice that in this case, Cu and Zn have separate atomic positions.

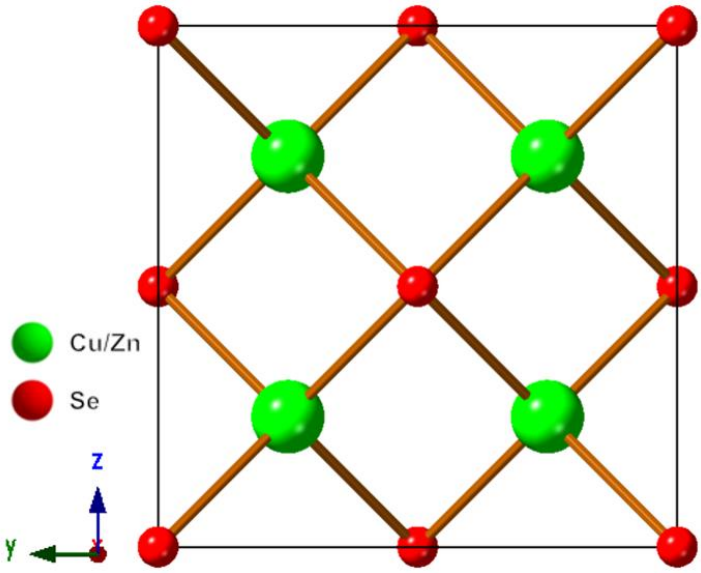

Figure 5.3.2: $Cu_2Zn_3Se_4$ Small Cell crystal projection along the a-direction.

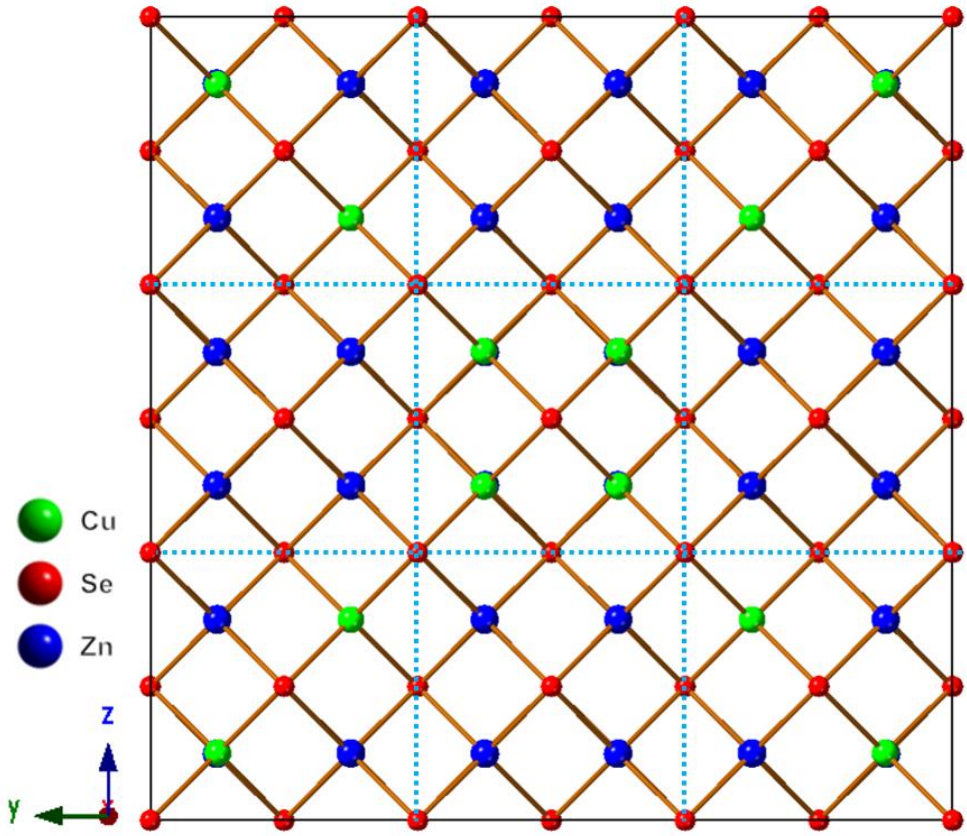

Figure 5.3.3: $Cu_2Zn_3Se_4$ Large Cell crystal projection along the a-direction. The blue dotted lines were overlayed to depict the 3x3 supercell. Each square represents the small cell.

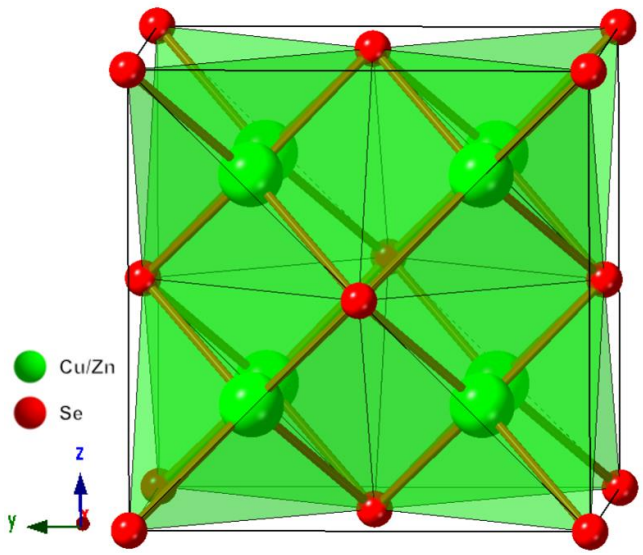

Figure 5.3.4: $Cu_2Zn_3Se_4$ Small Cell crystal projection along the a-direction, rotated, with all polyhedra.

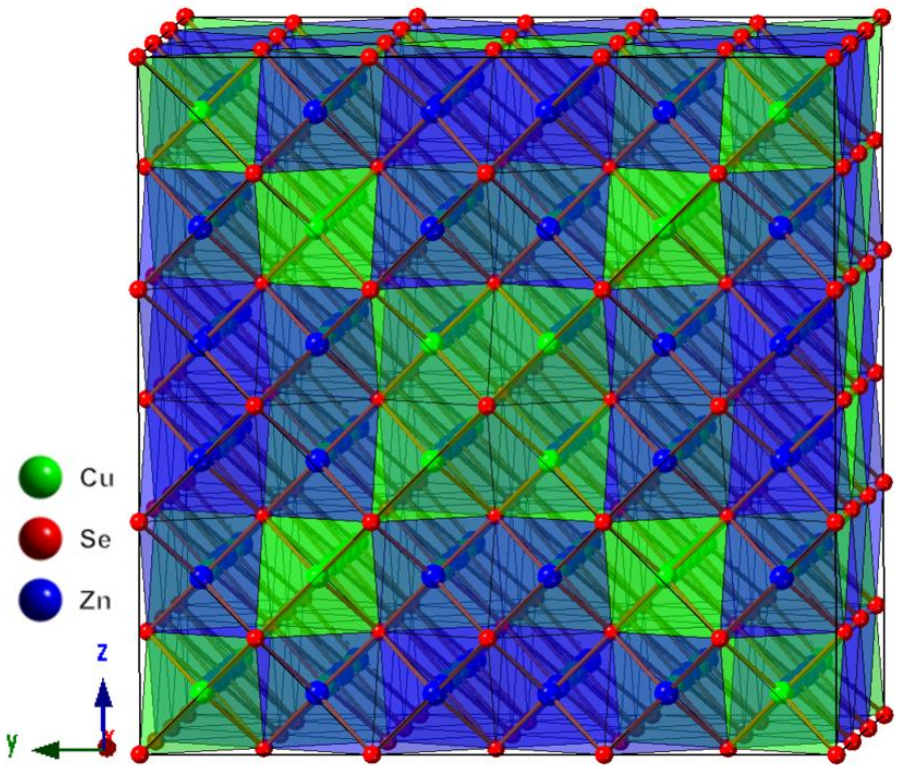

Figure 5.3.5: $Cu_2Zn_3Se_4$ Large Cell crystal projection along the a-direction, rotated, with all polyhedra.

$Cu_2Zn_3Se_4$ polyhedral projections along the a-direction rotated are found for SC and LC in **Figure 5.3.4** and **Figure 5.3.5**, respectively. For all cases, the Cu^{1+} and Zn^{2+} were in tetrahedral coordination, forming MSe_4 tetrahedra. In **Figure 5.3.6**, a small cell Cu/Zn-Cu/Zn chain is depicted to illustrate typical distances between metal ions, which is 2.836 Å. For LC metal chains, **Figure 5.3.7** illustrates metal-metal distances as well, being typically < 3 Å.

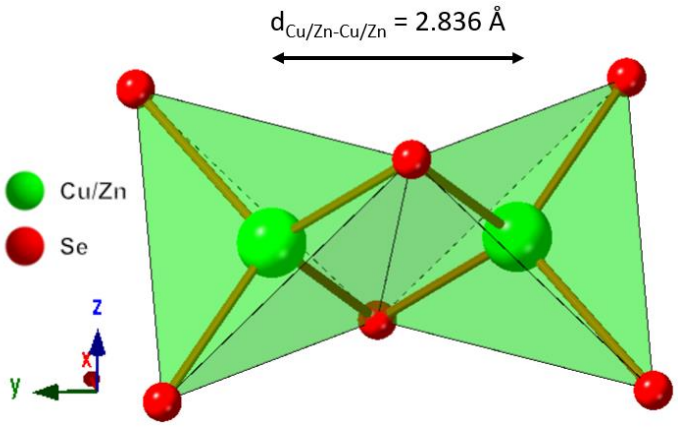

Figure 5.3.6: $Cu_2Zn_3Se_4$ Small Cell a-direction rotated, Cu/Zn chain with distances between metal ions noted.

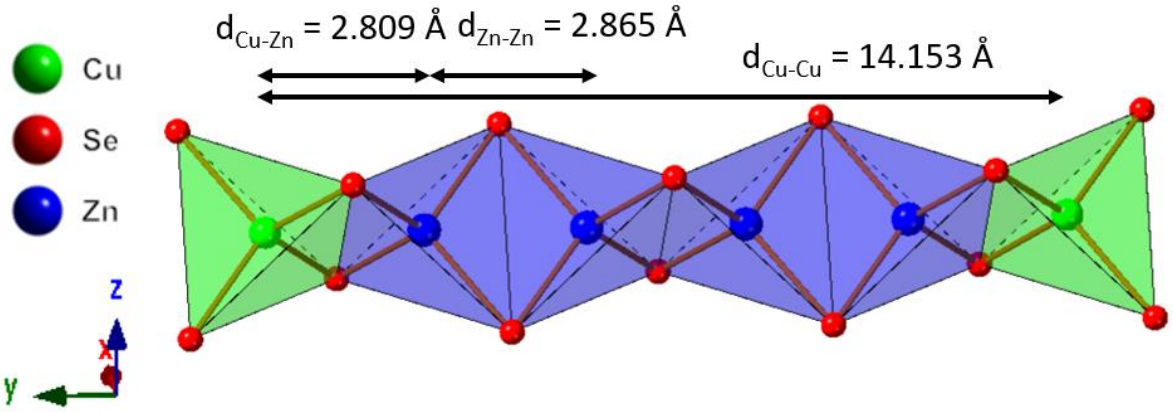

Figure 5.3.7: $Cu_2Zn_3Se_4$ Large Cell a-direction, rotated Cu-Zn chain, with distances between metal ions noted.

Bond distances between M-Se is shown for SC and LC in **Table 5.3.4** and **Table 5.3.5**, respectively. In the SC case, the M-Se distances are uniformly 2.4561 Å.

Table 5.3.4: $Cu_2Zn_3Se_4$ Small Cell selected inter-atomic bond distances (in Å). Small cell operators for generating equivalent atoms: (i) x, y+1/2, z+1/2; (ii) x+1/2, y, z+1/2; (iii) x+1/2, y+1/2, z; (iv) x, y-1/2, z-1/2; (v) x-1/2, y, z-1/2; (vi) x-1/2, y-1/2, z; (vii) -x, -y+1, -z+1; (viii) -x, -y+3/2, -z+3/2; (ix) -x+1, -y+3/2, -z+3/2; (x) -x+1/2, -y+1, -z+3/2; (xi) -x+1/2, -y+2, -z+3/2; (xii) -x+1/2, -y+3/2, -z+1; (xiii) -x+1/2, -y+3/2, -z+2.

$Cu_2Zn_3Se_4$-small cell	
Atoms 1,2	**d 1,2 [Å]**
Zn1/Cu1—Se1^{i}	2.4561(3)
Zn1/Cu1—Se1^{ii}	2.4561(3)
Zn1/Cu1—Se1^{iii}	2.4561(3)

Table 5.3.5: $Cu_2Zn_3Se_4$ Large Cell selected inter-atomic bond distances (in Å). Large cell operators for generating equivalent atoms: (i) -x, 1-y, 1-z; (ii) -x, y, z; (iii) -x, 1-y, z; (iv) x, y, 1-z; (v) -x, y, 1-z; (vi) x, 1-y, z; (vii) x, 1-y, 1-z; (viii) 1-x, y, z; (ix) 1-x, 1-y, z; (x) -0.5+z, -0.5+x, 1-y; (xi) -0.5+z, 1.5-x, 1-y; (xii) 0.5-x, 1-y, 1.5-z; (xiii) -1+x, y, z; (xiv) -1+x, 1-y, z; (xv) 1.5-y, -0.5+z, 1-x; (xvi) z, 0.5-x, 1.5-y; (xvii) 0.5+y, -0.5+z, x; (xviii) z, -0.5+x, 0.5+y; (xix) 1-z, 0.5-x, 1.5-y; (xx) 0.5-y, 1.5-z, 1-x; (xxi) x, y, 2-z; (xxii) 1-z, 1.5-x, 0.5+y; (xxiii) 0.5-y, 1.5-z, x; (xxiv) 0.5+y, 1-z, 0.5+x; (xxv) 1+x, y, z; (xxvi) 2-x, y, z; (xxvii) x, 0.5-y, 1.5-z; (xxviii) 1.5-x, 0.5-y, z; (xxix) 1.5-x, y, 1.5-z; (xxx) 0.5+x, -0.5+y, z; (xxxi) z, x, y; (xxxii) y, -0.5+z, 0.5+x; (xxxiii) -0.5+z, 0.5+x, y; (xxxiv) -0.5+y, z, 0.5+x; (xxxv) 0.5-y, z, 1.5-x; (xxxvi) -0.5+x, 1-y, 1.5-z; (xxxvii) -0.5+x, 0.5+y, z.

$Cu_2Zn_3Se_4$-large cell	
Atoms 1,2	**d 1,2 [Å]**
Zn1—Se3^{xix}	2.4469(8)
Zn1—Se3^{xx}	2.4468(8)
Zn1—Se4^{ix}	2.4811(16)
Zn2—Se2^{ix}	2.4476(7)
Zn2—Se2^{xxiv}	2.4476(7)
Zn2—Se3^{xxv}	2.4655(11)
Cu1—Se4^{xxvii}	2.4560(7)
Cu1—Se4^{xxviii}	2.4560(7)
Cu1—Se4^{xxix}	2.4560(7)
Cu2—Se2^{xxxiii}	2.4486(7)
Cu2—Se2^{xxxiv}	2.4486(7)
Cu3—Se4^{xxxvi}	2.4556(7)
Cu3—Se4^{ix}	2.4556(7)
Cu3—Se2^{xii}	2.4560(7)

For LC, the M-Se bond distances are not uniform, showing evidence of distorted tetrahedra. In general, bond distances ranged from ~2.44-2.5 Å. **Table C.1** and **Table C.2** display the SC and LC anisotropic displacement parameters of each structure. **Table C.3** and **Table C.4** list the interatomic Se-M-Se bond angles for SC and LC. The $Cu_2Zn_3Se_4$ small cell had uniform tetrahedral bond angles of 109.5°. The large cell had some Se-M-Se bond angles that were ideal, others more narrow than expected, and some wider than 109.5°.

In this work, polycrystalline powders of $Cu_2Zn_3Se_4$ were synthesized via solid-state synthesis. PXRD of the sample was recorded to analyze the phase purity, shown in **Figure 5.3.8**.

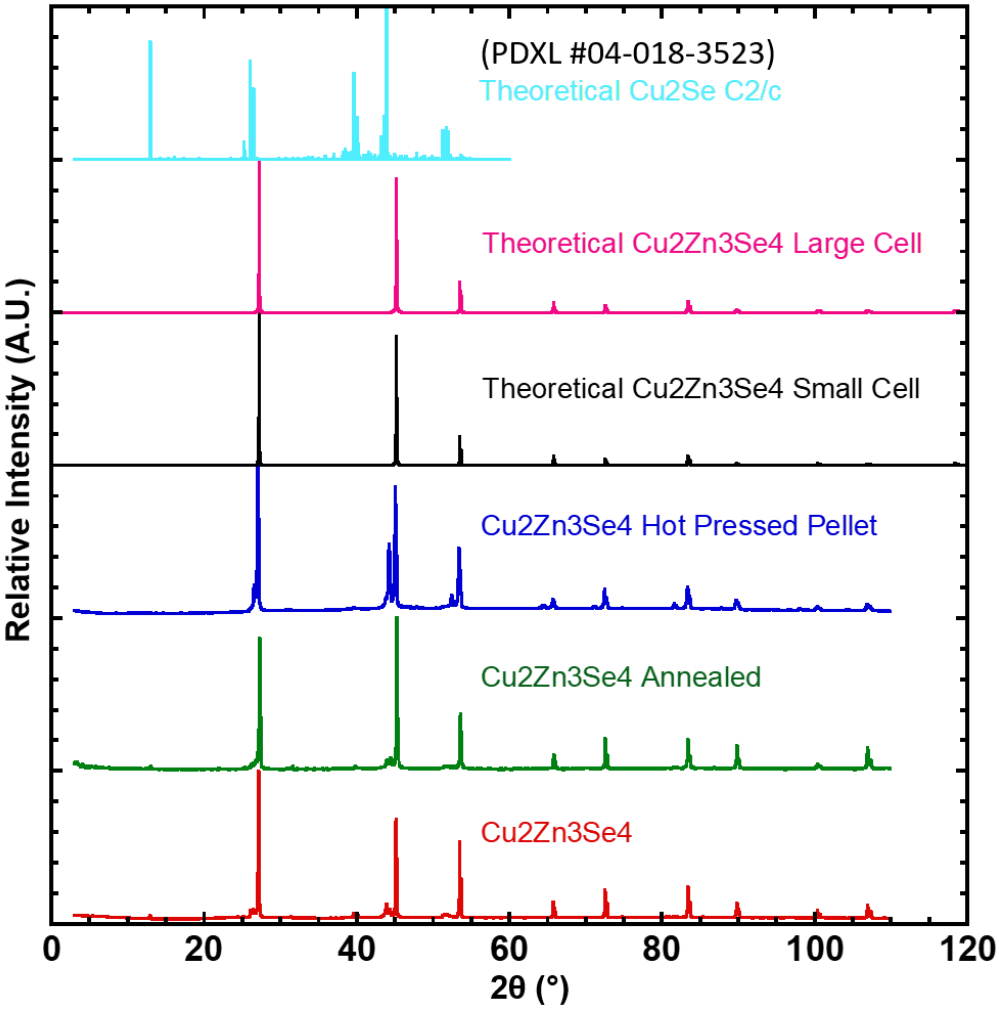

Figure 5.3.8: PXRD of $Cu_2Zn_3Se_4$, plotted against the small cell and large cell patterns, as well as a potential minor binary phase of Cu_2Se C2/c (PDXL #04-018-3523[106]).

The reacted, annealed, and hot-pressed pellet of $Cu_2Zn_3Se_4$ was plotted against the SC and LC patterns, as well as a potential minor binary phase of Cu_2Se C2/c (PDXL #04-018-3523[106]). The major peaks were indexed to the SC/LC $Cu_2Zn_3Se_4$ pattern, with PDXL phase analysis identifying a minor Cu_2Se monoclinic binary phase present. To verify the thermal stability of the compound, DSC was also performed, as can be seen in **Figure 5.3.9**. Thermal events were noted on the plot.

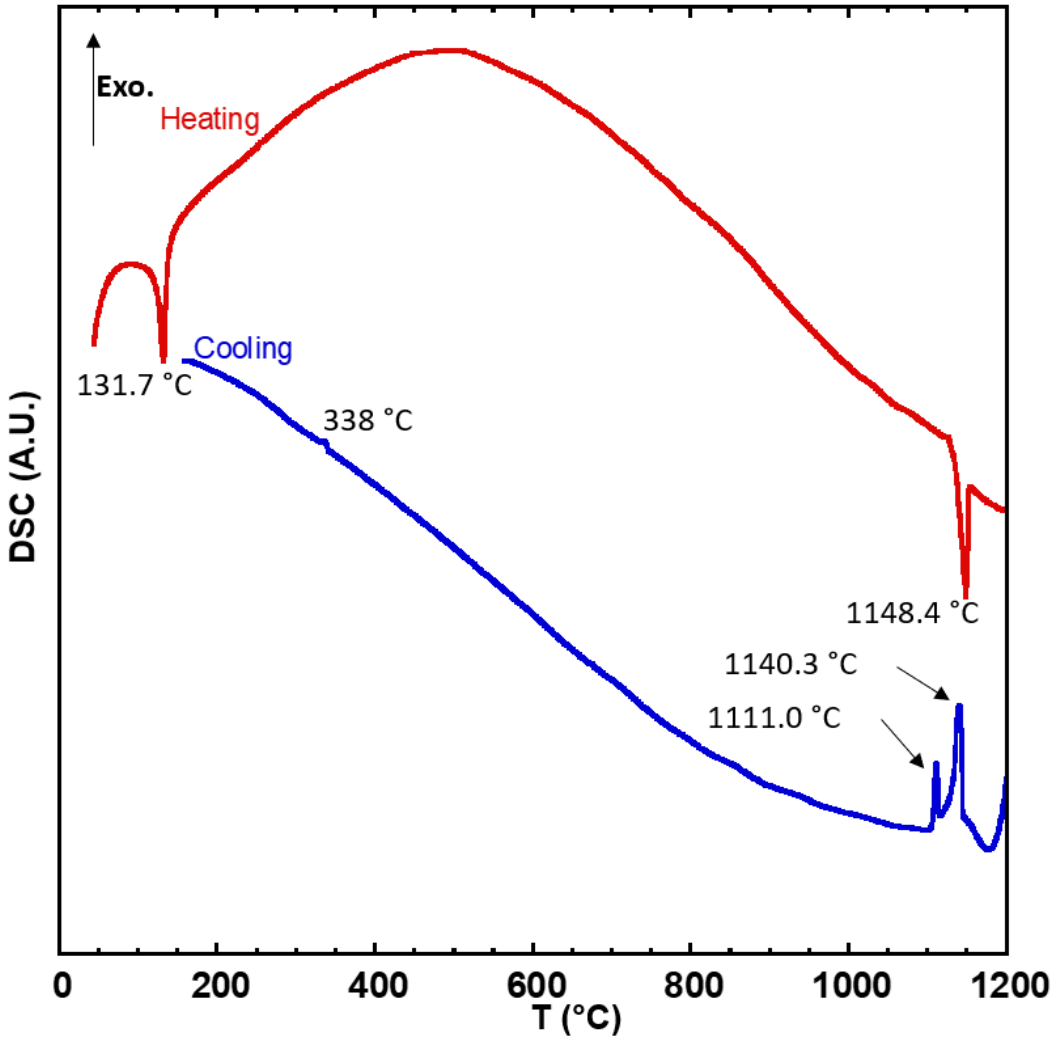

Figure 5.3.9: $Cu_2Zn_3Se_4$ DSC vs. temperature for both heating and cooling. The thermal transitions were also noted.

A low-T phase transition was noted at 131.7 °C, with the melting point occurring at 1148.4 °C. Upon cooling, multiple transitions were observed, so the sample is not thermally stable after melting. To further probe the sample after the phase transition, high-T PXRD was utilized, as shown in **Figure 5.3.10**. In the experiment, the powder was loaded onto an inconel holder and covered with a graphite dome, as depicted in **Figure 2.2.1**. Before adding the sample powder, background scans were first recorded of the holder and dome.

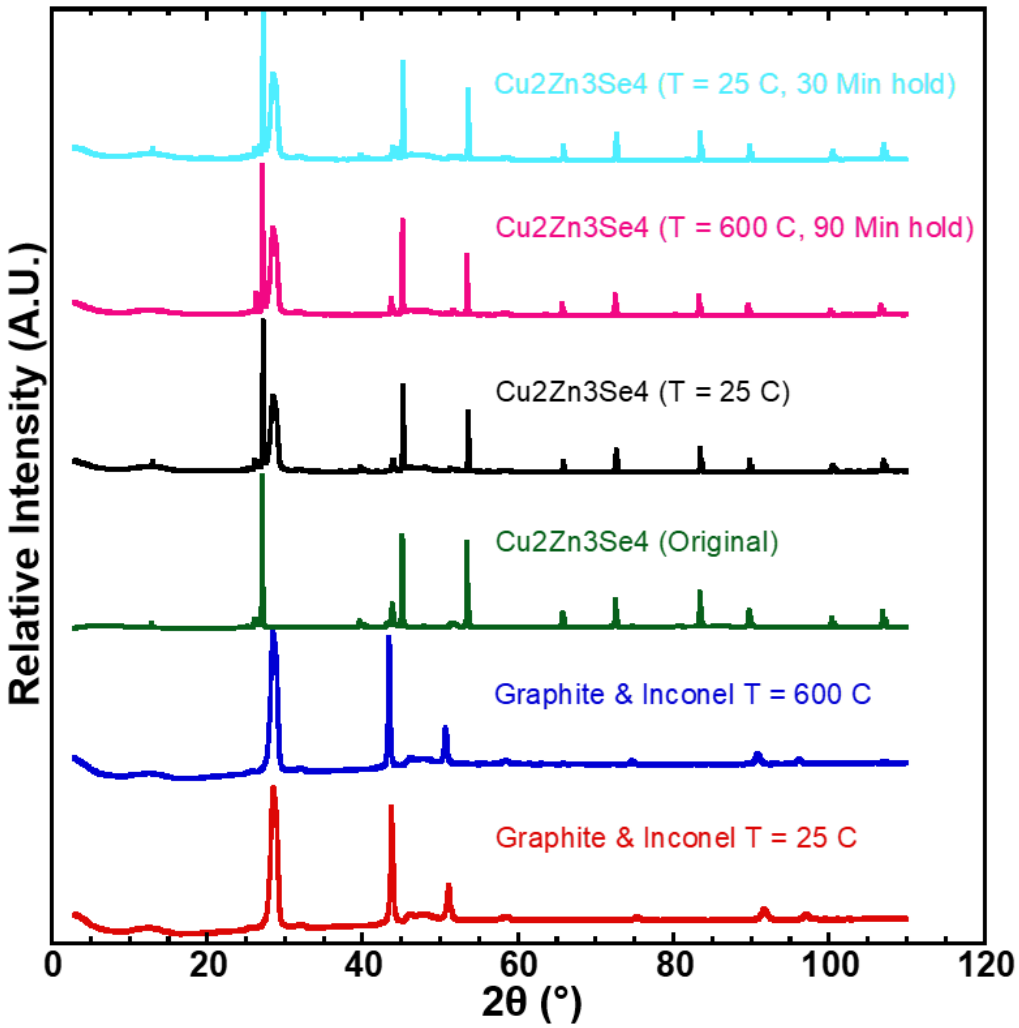

Figure 5.3.10: High-T PXRD of $Cu_2Zn_3Se_4$. First, background scans were done on just the graphite dome and Inconel holder to help identify the peaks later. Next, the powder was scanned at various temperatures and dwell times.

Next, the powder was added, and PXRD scans were taken at room temperature, 600 °C, then RT again. At 12.92°, a peak does indeed disappear at high-T and appear again upon cooling back to RT. This is further confirmation that the DSC peak at 131.7 °C is indeed a phase transition.

Now, to analyze the $Cu_2Zn_3Se_4$ phase purity further, a Cu-Se binary phase diagram from ASM was referenced, as seen in **Figure C.1**. Also, for a reference, experimental Cu_2Se powder XRD and DSC plots are shown in **Figure C.2**. On the phase diagram, the heating DSC transition temperatures were noted on the y-axis, and the potential binary Cu_2Se monoclinic phase was noted on the x-axis. We see that the temperatures correspond closely to the Cu_2Se phase transitions, but this is consistent with the fact that the original design of the $Cu_2Zn_3Se_4$ compound was modeled after the Cu_2Se system. Re-writing $Cu_2Zn_3Se_4$ as M_5Se_4 and Cu_2Se as M_8Se_4, we have very similar chemical make-up, with more vacancies in the lattice present in the ternary compound. Further, Cu^{1+} and Zn^{2+} are isoelectronic, with both ions having an electron configuration of $[Ar]3d^{10}$. As such, the PXRD and DSC results are what was to be expected. The $Cu_2Zn_3Se_4$ chemical system should behave quite similar to Cu_2Se.

Finally, the oxidation states in $Cu_2Zn_3Se_4$ (Cu^{1+}, Zn^{2+}, Se^{2-}) were verified via XPS. **Figure 5.3.11** shows the results. Reference values were obtained via the handbook of XPS, and listed in **Table C.5**.[31] Cu^{1+}, Zn^{2+}, and Se^{2-} were found to be within the proper energy windows, so the oxidation states of each of the elements were indeed confirmed.

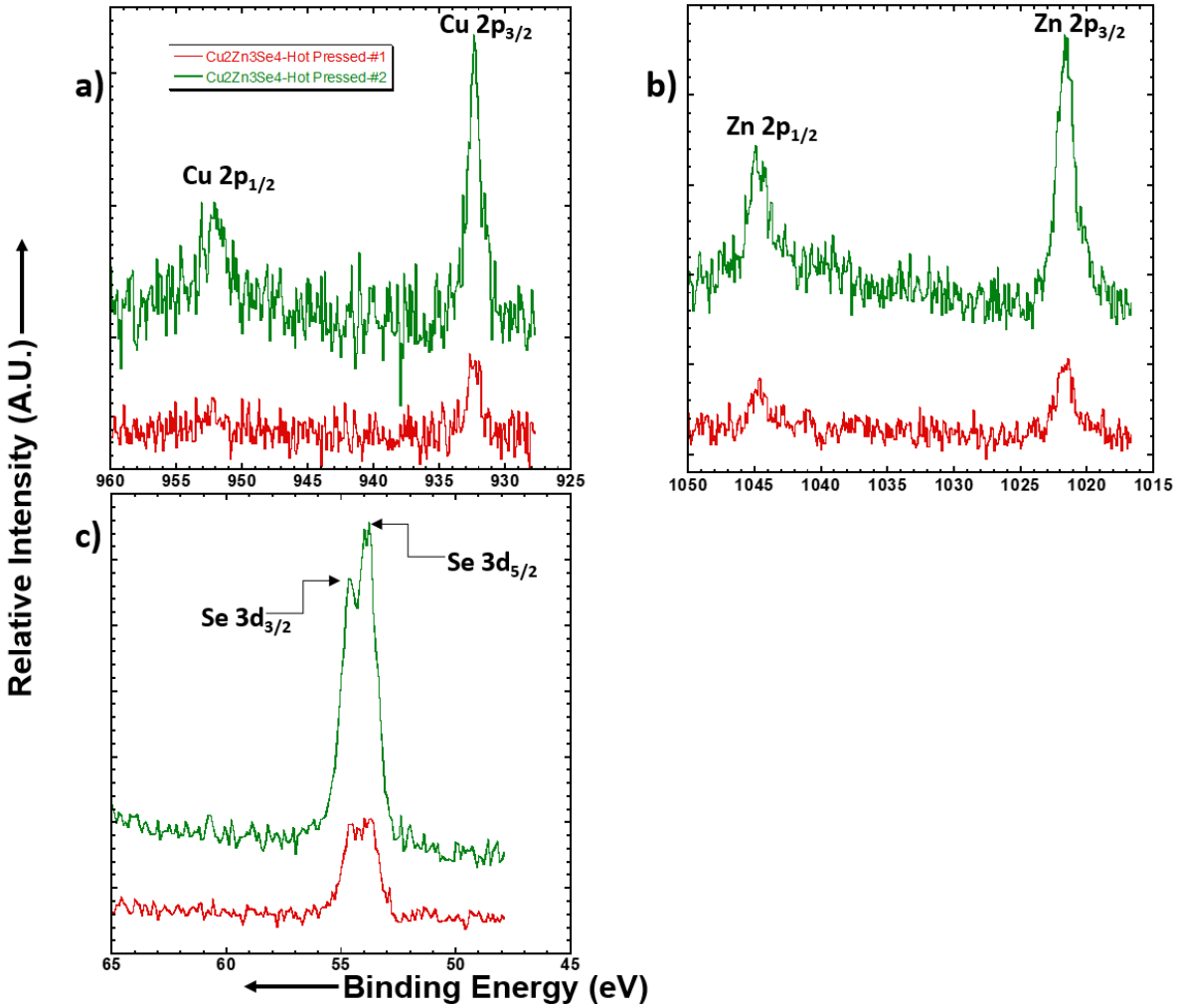

Figure 5.3.11: XPS counts per second vs. binding energy for **(a)** Cu; **(b)** Zn; **(c)** Se. Two scans were run on the same pellet portion to ensure the data collection was sufficient.

5.3.1.3 Optical Properties of $Cu_2Zn_3Se_4$

Diffuse reflectance UV-Vis-NIR spectroscopy was performed on $Cu_2Zn_3Se_4$. Later, the Kubelka-Munk equation F(R)[33] was used to transform percent reflectance data to absorption, which was then plotted as a function of energy in electron volts, eV. The left image in **Figure 5.3.12** depicts F(R) vs. wavelength. On the right, we see a plot of $[F(R)*h\nu]^{1/r}$ vs. energy, where r = ½ corresponds to a direct bandgap E_g. To determine E_g, an absorption edge tangent line was extrapolated to the x-axis; the intercept with the x-axis corresponded to E_g. The direct bandgap was found to be 2.24 eV, corresponding to a maximum absorbed wavelength (λ_{Max}) of ~554 nm. As such, $Cu_2Zn_3Se_4$ can absorb in the UV and a portion of the visible spectrum (violet, blue, cyan, and green). However, lower energy visible colors (yellow, orange, and red) will not be absorbed, as well as the whole NIR/IR portion of the solar spectrum. See **Figure 1.3.4** to reference the solar spectrum.

Now, in order to be complete in the optical analysis, one must consider the potential minor Cu_2Se monoclinic secondary phase. According to Choi *et al*., the low-T α-Cu_2Se monoclinic phase has a bulk indirect bandgap between 1-1.3 eV.[107] For reference, the high-T β-Cu_2Se cubic Fm-3m phase essentially has no bandgap, being semi-metallic.[107] Since the $Cu_2Zn_3Se_4$ bandgap was found to be 2.24 eV, and because the secondary Cu_2Se phase is very minor with a much lower bandgap, the second phase should not be factoring into the recorded $Cu_2Zn_3Se_4$ E_g value.

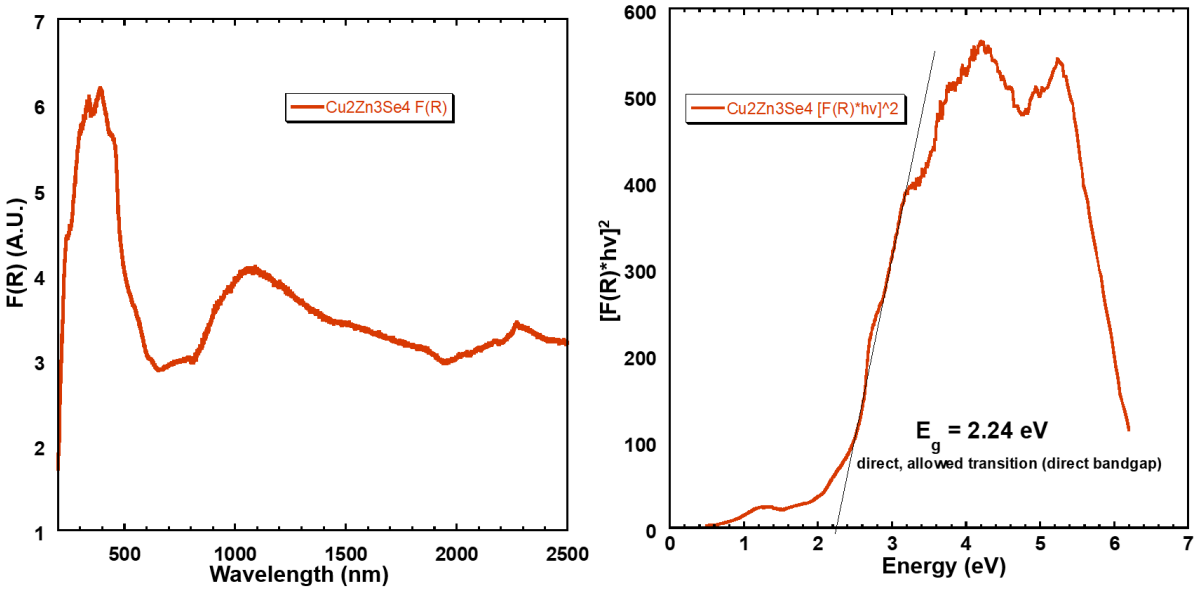

Figure 5.3.12: (Left): UV-Vis-NIR diffuse reflectance Tauc plot analysis. The Kubelka-Munk function F(R) was used to transform the reflectance data to absorbance. Plot of F(R) vs. wavelength. **(Right):** Plot of $[F(R)*hv]^{1/r}$ vs. energy; r = ½ was chosen here to signify a direct, allowed transition (direct bandgap). To determine the direct optical bandgap (E_g), an absorption edge tangent line was extrapolated to the x-axis; the intercept with the x-axis corresponds to E_g.

5.3.1.4 Thermoelectric Properties of $Cu_2Zn_3Se_4$

Temperature-dependent electrical conductivity (σ) and Seebeck coefficient (S) were measured. Raw heating and cooling σ/S data were fit using 4th-order and 3rd-order polynomials with respect to temperature, respectively, with polynomial coefficients taken to 16 decimal places. **Figure 5.3.13a** presents the fitted σ data. Between T = 300-425 K, typical semiconductor behavior with increasing T was observed. However, due to the high electrical conductivity, at high enough

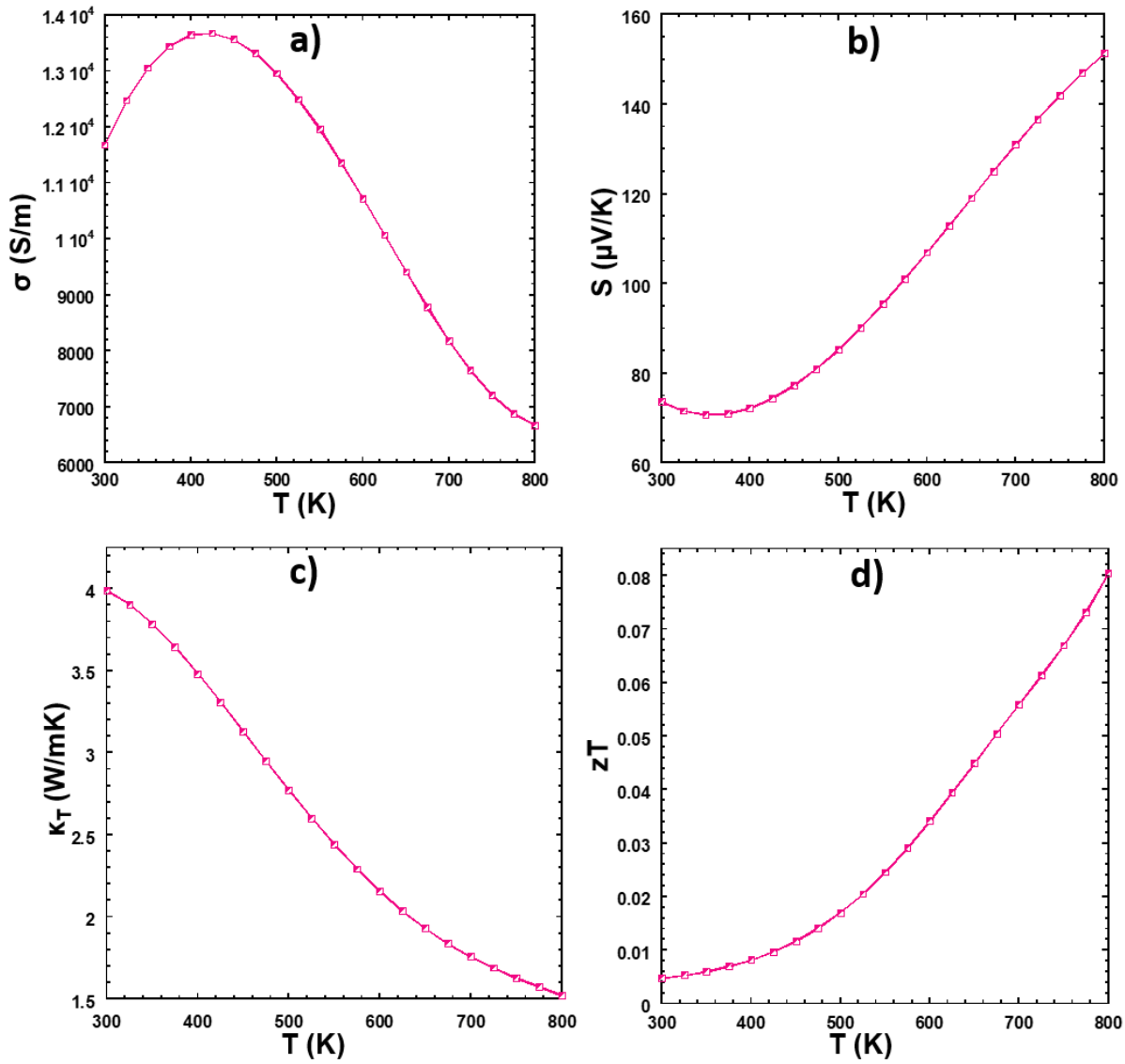

Figure 5.3.13: Temperature-dependent thermoelectric properties: **(a)** electrical conductivity (σ); **(b)** thermopower (S); **(c)** total thermal conductivity (κ_T); **(d)** figure of merit (zT).

temperature, enough p-type hole carriers were thermally excited to behave in a metallic-like fashion (degenerate semiconductor). For T = 425-800 K, σ was seen to decrease with increasing T, following a metallic Wiedemann-Franz Law-like behavior of $\sigma = \kappa_e / LT$, i.e., $\sigma \propto \frac{1}{T}$. **Figure C.3** depicts a plot of σ vs. 1/T-at high-T, a linear relationship with 1/T is indeed observed. The values for σ ranged from 6672.3 S/m at T = 800 K to 13682 S/m at T = 425 K; at T = 300 K, σ = 11681 S/m.

The temperature-dependent Seebeck coefficient is seen in **Figure 5.3.13b**. Between 300-350 K, S was found to slightly decrease from +73.7 μV/K to +70.7 μV/K. For T = 350-800 K, S increased from +70.7 μV/K to +151.3 μV/K. Throughout the temperature range, S was positive, indicating a p-type material. According to the Mott equation, the Seebeck coefficient of a degenerate semiconductor is given by:

$$S = -\frac{\pi^2 k_B^2}{6eE_F} T \propto T \qquad \textbf{5.3-1,}$$

Where k_B is the Boltzman constant, e is the electronic charge, and E_F is the Fermi energy.[108] So, the roughly linear increase in S with rising T after the transition temperature is consistent with what theory predicts.

Next, **Figure C.4** depicts the temperature-dependent power factor ($PF = \sigma S^2$). PF ranged from 0.634 μV/cm*K for T = 300 K to 1.53 μV/cm*K for T = 800 K. Throughout the temperature range, PF was seen to increase with increasing T. In order to analyze the electrical conductivity further, Arrhenius analysis was carried out in **Figure 5.3.14**. In **Figure 5.3.14a**, the figure was divided into the high-T degenerate semiconductor/ metallic-like region (R1) and the low-T extrinsic semiconductor region (R2). **Figure 5.3.14b** shows the low-T extrinsic region Arrhenius plot, used to obtain the activation energy, E_a by fitting the ln(σ) vs. 1/T region with a linear trendline and extracting the slope. E_a was found to be 36.6 meV. Interestingly, the E_a value of 36.6

meV was quite consistent with the Cu vacancy defect level reported for $CuInSe_2$ ($Cu_2In_2Se_4$) by Zhang, Wei, and Zunger.[109] In their work on $CuInSe_2$ ($Cu_2In_2Se_4$), these Cu vacancies caused p-type self-doping.[109] It is likely that a similar Cu vacancy p-type doping mechanism is involved for $Cu_2Zn_3Se_4$. For σ vs. T, the increasing behavior from T = 300 K-425 K was caused by the carrier population of the Cu vacancy acceptor level. Similarly, the carrier population caused a slight dip in S vs. T from T = 300 K-350 K.

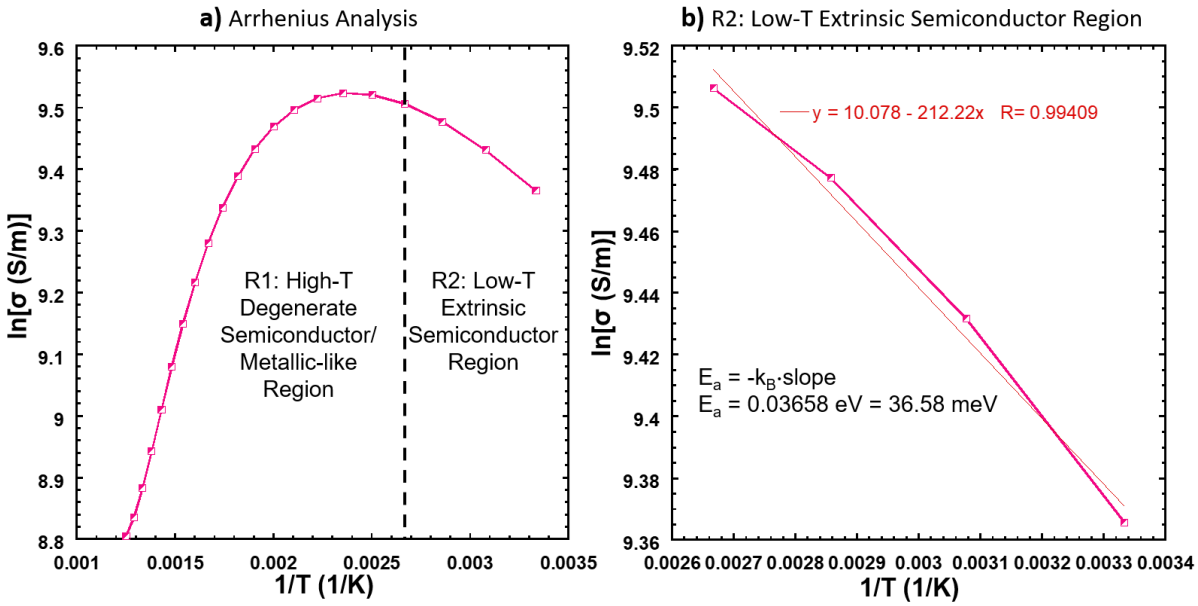

Figure 5.3.14: (a) Electrical conductivity Arrhenius plot. The figure was divided into the high-T degenerate semiconductor/ metallic-like region (R1) and the low-T extrinsic semiconductor region (R2). **(b)** Low-T extrinsic region Arrhenius plot, employed to obtain the activation energy, E_a by fitting the ln(σ) vs. 1/T region with a linear trendline and extracting the slope. E_a was found to be 36.6 meV.

Additionally, the temperature-dependent total thermal conductivity was recorded in **Figure 5.3.13c**. To gather κ_T, The equation $\kappa_T = \rho C_p D$ was used, where ρ is pellet density, C_p is heat capacity, and D is thermal diffusivity. The Dulong-Petit Law was used to calculate C_p, given by **Equation 2.2-1**. The temperature-dependent thermal diffusivity was measured during the laser flash analysis (LFA) measurement, with the raw data being fit by a 4th-order polynomial, with

coefficients taken to 16 decimal places. With increasing T, κ_T was found to decrease from ~4 W/mK at 300 K, to ~1.52 W/mK at 800 K.

Wiedemann-Franz Law analysis was applied to κ_T to decouple the κ_e and κ_L contributions, as shown in **Figure 5.3.15**. It was found that κ_e contributed between ~2-9% to κ_T, while κ_L

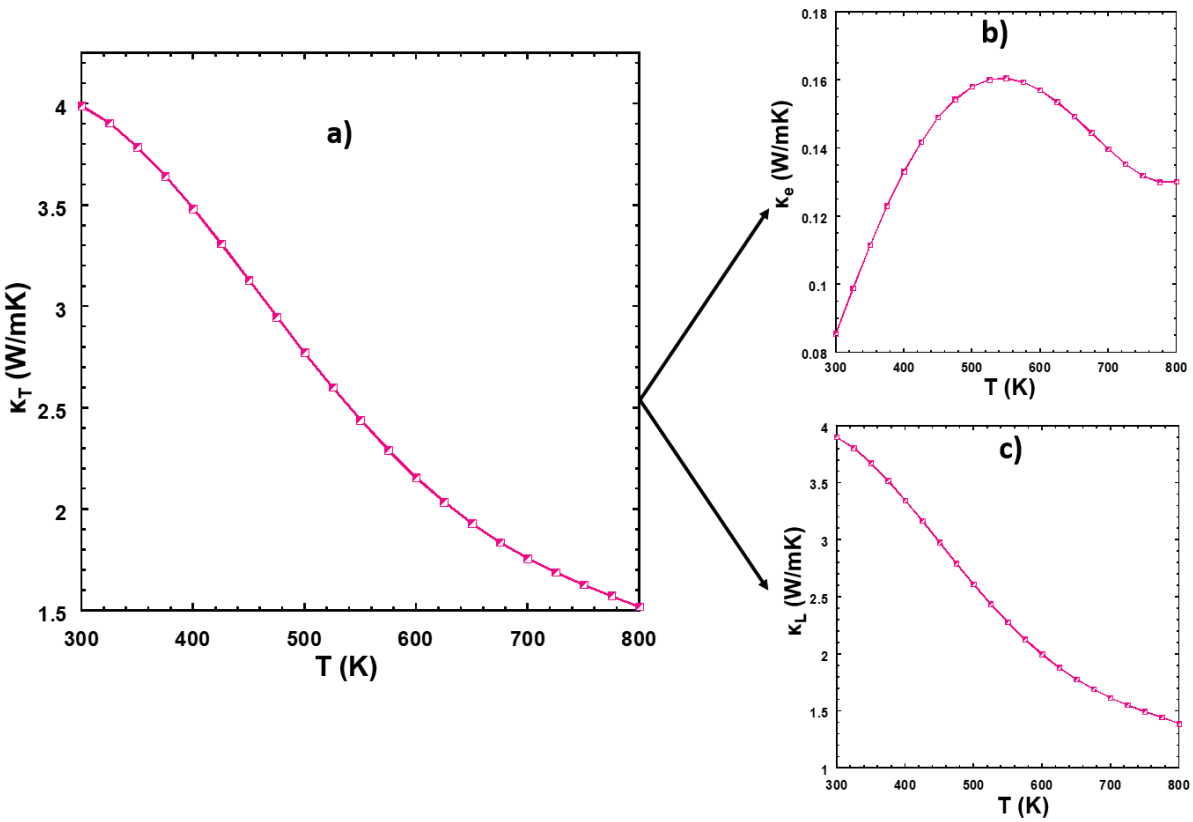

Figure 5.3.15: (a) Total thermal conductivity vs. temperature **(b)** Electronic thermal conductivity (κ_e) and **(c)** Lattice thermal conductivity (κ_L) contributions, utilizing Wiedemann-Franz Law analysis. It was determined that κ_e contributed ~2-9% to κ_T.

contributed ~91-98% to κ_T. Notice that in **Figure 5.3.15b**, κ_e increased from 300-550 K, then decreased afterward. Recall that $\kappa_e = L\sigma T$: so, we can see the temperature effect on κ_e dominated the behavior at this range. From 550-800 K, the electrical conductivity contribution takes over, causing the decrease seen in κ_e in this regime. Recall that for **Figure 5.3.13a**, we saw that after the transition temperature (~425 K), σ decreased with increasing T. The overall temperature-

dependent behavior of κ_L in **Figure 5.3.15c** mirrored that of κ_T. According to Ashcroft & Mermin, at high-T, κ_L is given by the following power law:

$$\kappa_L \sim \frac{1}{T^x} \qquad \textbf{5.3-2,}$$

where x ranges from 1-2.[110] The precise value of x is dependent on the type of phonon scattering processes involved.[110] So, from **Equation 5.3-2**, we can see that with increasing T, the amount of phonon scattering increases, decreasing κ_L. Since κ_L is the dominant contribution to κ_T, this explains the temperature-dependent behavior of κ_T. In general, the high-symmetry cubic lattice also helps explain why κ_L and κ_T are relatively large, as the well-ordered crystal will propogate phonons better than lower symmetry polymorphs.

Finally, temperature-dependent the thermoelectric figure of merit (zT) is shown in **Figure 5.3.13d**. With increasing T, zT was found to increase from 0.005 at 300 K to 0.08 at 800 K. At some T > 800 K, the $Cu_2Zn_3Se_4$ zT should reach 0.1. Recall that zT is given by the equation $zT = (\sigma S^2/\kappa_T)T$: The large σ and moderate S are promising, but since κ_T is > 1 throughout the temperature range, the zT value is relatively low.

5.3.2 Conclusion & Future Work: $Cu_2Zn_3Se_4$ (x = 1.5):

$Cu_2Zn_3Se_4$ single crystals were grown via a high-T annealing method at 1080 °C. Amber yellow faceted crystals were created, with the largest of the crystal sizes being ~0.2 mm wide. Single-crystal XRD and structure refinement revealed a small cell and larger 3x3 supercell, both crystallizing in the cubic Fm-3m space group with lattice parameters of a = 5.6721 Å and 17.014 Å, respectively. $Cu_2Zn_3Se_4$ was isostructural with β-Cu_2Se, the high-T cubic Fm-3m phase. For SC, Zn1 and Cu1 shared the same site, having a 3/8 total vacancy. The 3x3 supercell was found to resolve the ordering of Cu and Zn in all tetrahedral sites. For LC, the vacancies at each site decreased overall. All metals for SC and LC were found in tetrahedral MSe_4 coordination. Distances between metal atoms were typically < 3 Å. For SC, M-Se distances were uniformly 2.4561 Å, while LC bond distances ranged from ~2.44-2.5 Å. Bond angles in the small cell were all 109.5°, while the large cell had some Se-M-Se bond angles that were ideal, others narrower than expected, and some wider than 109.5°.

$Cu_2Zn_3Se_4$ powder was synthesized, and PXRD revealed a phase match with both the SC and LC phases. PDXL phase matching identified a minor binary phase of Cu_2Se C2/c. DSC revealed a phase transition at 131.7 °C, followed by melting at 1148.4 °C. Upon cooling, multiple peaks were noticed-evidence of thermal instability. To probe the phase transition further, high-T PXRD was used, and revealed that above 131.7 °C, a peak at 12.92° disappears, further proof of the phase transition. Referencing the ASM Cu-Se binary phase diagram noted that the thermal events closely mirrored the Cu_2Se RT to HT phase transition, followed by melting. This is consistent with the fact that $Cu_2Zn_3Se_4$ was modeled after the Cu_2Se HT structure. XPS confirmed the expected oxidation states for each of the elements present.

Diffuse reflectance UV-Vis-NIR spectroscopy was implemented to analyze the optical properties of the sample, and the Kubelka-Munk function and Tauc plot analysis was applied to gather the direct optical bandgap, E_g. The analysis revealed that E_g = 2.24 eV, corresponding to a λ_{Max} of 554 nm. As such, $Cu_2Zn_3Se_4$ can absorb in the UV and a portion of the visible spectrum (violet, blue, cyan, and green). However, lower energy visible colors (yellow, orange, and red) will not be absorbed, as well as the whole NIR/IR portion of the solar spectrum. For reference, the binary Cu_2Se RT monoclinic phase has an indirect bandgap of 1-1.3 eV. So, the measured bandgap belongs to $Cu_2Zn_3Se_4$.

Thermoelectric properties of $Cu_2Zn_3Se_4$ were also measured. Electrical conductivity revealed a highly conductive material, with values ranging from 6672.3 S/m at T = 800 K to 13682 S/m at T = 425 K; at T = 300 K, σ = 11681 S/m. Between T = 300-425 K, typical semiconductor behavior was noticed. However, for T = 425-800 K, degenerate semiconductor was seen, with σ decreasing in a 1/T-like fashion. The Seebeck coefficient was moderate and positive (p-type material), generally increasing with increasing T in a degenerate semiconductor Mott equation-like behavior. S values ranged from +70.7 μV/K at T = 350 K, to +151.3 μV/K at T = 800 K. Power factor increased with increasing T, ranging from 0.634 μV/cm*K for T = 300 K to 1.53 μV/cm*K for T = 800 K. Arrhenius analysis on σ vs. T revealed that in the low-T extrinsic region, an activation energy E_a of 36.6 meV was revealed, consistent with Cu vacancy defect levels reported in $CuInSe_2$. For σ vs. T, the increasing behavior from T = 300 K-425 K was caused by the carrier population of the Cu vacancy acceptor level. Similarly, the carrier population caused a slight dip in S vs. T from T = 300 K-350 K. With increasing T, κ_T was found to decrease from ~4 W/mK at 300 K, to ~1.52 W/mK at 800 K. Wiedemann-Franz Law analysis revealed that κ_e

contributed ~2-9% to κ_T. Finally, thermoelectric figure of merit was calculated, and zT was found to increase from 0.005 at 300 K to 0.08 at 800 K.

In summation, $Cu_2Zn_3Se_4$ single crystals were grown and polycrystalline powder was synthesized, and the compound exhibited promising properties such as a direct optical bandgap of 2.24 eV, being a wide-bandgap semiconductor. Also, the Seebeck coefficient revealed p-type conduction, and a large electrical/ thermal conductivity. Based on λ_{Max}, $Cu_2Zn_3Se_4$ could be a promising detector material for UV, as well as the visible colors violet, blue, cyan, and green. Interestingly, λ_{Max} is quite close to the wavelength where the sun peaks in spectral irradiance. Perhaps, $Cu_2Zn_3Se_4$ could also be integrated in a multi-junction solar cell, where it could absorb the higher energy portion of the solar spectrum.

In the future, it may be worthwhile to probe the acceptor states in the compound further with photoluminescence measurements. Additionally, thin film ellipsometry measurements could be interesting, as this would reveal the index of refraction (n), extinction coefficient (k), and optical absorption coefficient (α) of $Cu_2Zn_3Se_4$. For the ellipsometry measurements, a $Cu_2Zn_3Se_4$ thin film would need to be grown; with collaboration of the Heron lab, pulsed-laser deposition (PLD) could be a possible route, following similar thin film conditions to Chen *et al.*'s work on Cu_4TiSe_4.[92] These optical properties could be useful for further understanding its viability as a potential UV-visible photodetector and wide-bandgap photovoltaic absorber material. Additionally, due to the relatively low DSC phase transition at 131.9 °C, a temperature-dependent single-crystal XRD and structure refinement study of $Cu_2Zn_3Se_4$ from 80-400 K could be interesting to carry out.

5.4 $Cu_2Zn_2Ti_{0.5}Se_4$ (x = 1) Single Crystal Synthesis ($Cu_{2.75}Zn_{0.625}TiSe_4$), Structural, and Optical Properties:

5.4.1 Results & Discussion: $Cu_2Zn_2Ti_{0.5}Se_4$ (x = 1):

5.4.1.1 Single Crystal Synthesis ($Cu_{2.75}Zn_{0.625}TiSe_4$)

In order to grow single crystals, $Cu_2Zn_2Ti_{0.5}Se_4$ powder was reacted via a melt & slow cool method, starting at 900 °C, then slowly cooling to 750 °C. Refer to **Section 5.2** for more details. Interestingly, single-crystal XRD analysis and structure refinement revealed the crystals formed were a different stoichiometry than the powder used. In fact, $Cu_{2.75}Zn_{0.625}TiSe_4$ single crystals were grown-slightly Cu-rich, Zn-poor, and Ti-rich when compared to the original powder formula. As such, $Cu_{2.75}Zn_{0.625}TiSe_4$ must be the more stable stoichiometry. In **Figure 5.4.1**, the left image depicts the original $Cu_2Zn_2Ti_{0.5}Se_4$ powder, appearing greyish in color. The right image shows a mounted $Cu_{2.75}Zn_{0.625}TiSe_4$ single crystal, appearing grey/black in color and irregular in shape.

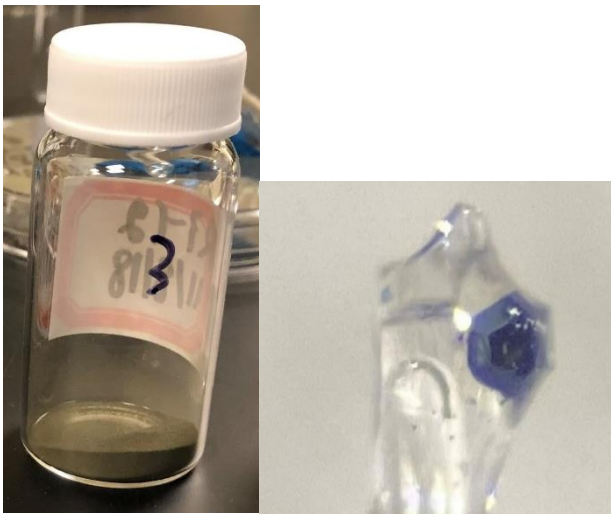

Figure 5.4.1: Left: $Cu_2Zn_2Ti_{0.5}Se_4$ powder after reaction and being ground. Photograph was taken using an Apple iPhone 11 Pro Max camera (12 MP). **Right:** $Cu_{2.75}Zn_{0.625}TiSe_4$ single crystal mounted on the tip of a glass fiber for single crystal XRD analysis. Image was recorded using a Leica S6E stereo microscope equipped with a Leica L2 light source at 4x zoom. Image was captured through the lenspiece with an Apple iPhone 11 Pro Max 2x telephoto optical zoom lens (12-megapixel), giving a total of ~8x magnification.

5.4.1.2 Structural Properties of $Cu_2Zn_2Ti_{0.5}Se_4$

In this work, $Cu_2Zn_2Ti_{0.5}Se_4$ powder was reacted to grow single crystals. Surprisingly, structure refinement revealed that the grown crystals were of a different stoichiometry: $Cu_{2.75}Zn_{0.625}TiSe_4$. $Cu_{2.75}Zn_{0.625}TiSe_4$ was found to crystallize in the F-43c space group (#219), with a lattice parameter of a = 11.2958 Å. **Table 5.4.1** lists selected crystal data for the compound.

Table 5.4.1: Selected crystallographic data for $Cu_{2.75}Zn_{0.625}TiSe_4$.

Formula	$Cu_{2.75}Zn_{0.625}TiSe_4$
Crystal system	Cubic
Space group	$F\bar{4}3c$ (#219)
a = b = c (Å)	11.2958(13)
$\alpha = \beta = \gamma$ (°)	90
V (Å^3)	1441.29(29)
Formula Mass (g/mol)	1158.66
ρ (g/cm^3)	5.33935
Z	4
Temperature (K)	300
R_{All}	0.037
R_{int}	0.0553
$R_1(F_o > 4\sigma(F_o))$	0.037
wR_2 (all)	0.1002
GooF	1.242

In **Table 5.4.2**, the atomic coordinates, isotropic displacement parameters, and site occupancies are listed. In this structure, Cu1, Zn1, and Ti1 all occupy separate sites in the crystal. The Cu1 site has a low amount of vacancies (~0.64/8), while the Zn1 site has a vacancy of ~3/8. Interestingly, the Ti1 position is fully occupied, with no vacancies. **Figure 5.4.2** shows the $Cu_{2.75}Zn_{0.625}TiSe_4$ crystal structure. Note that all metal positions are ordered and not shared.

Table 5.4.2: $Cu_{2.75}Zn_{0.625}TiSe_4$ atomic coordinates, equivalent isotropic displacement parameters $U_{eq.}$, and occupancies for all atoms.

Atom	Wyck.	S.O.F.	Vac.	x	y	z	$U_{eq.}$ ($Å^2$ x 10^{-4})
Se1	32e	1	-	0.12424(13)	0.12424(13)	0.12424(13)	284.4(7)
Cu1	24d	0.92	8%	0	0	0.25	75(7)
Zn1	8a	0.63	37%	0	0	0	126.8(20)
Ti1	8b	1	0%	0.25	0.25	0.25	157.3(17)

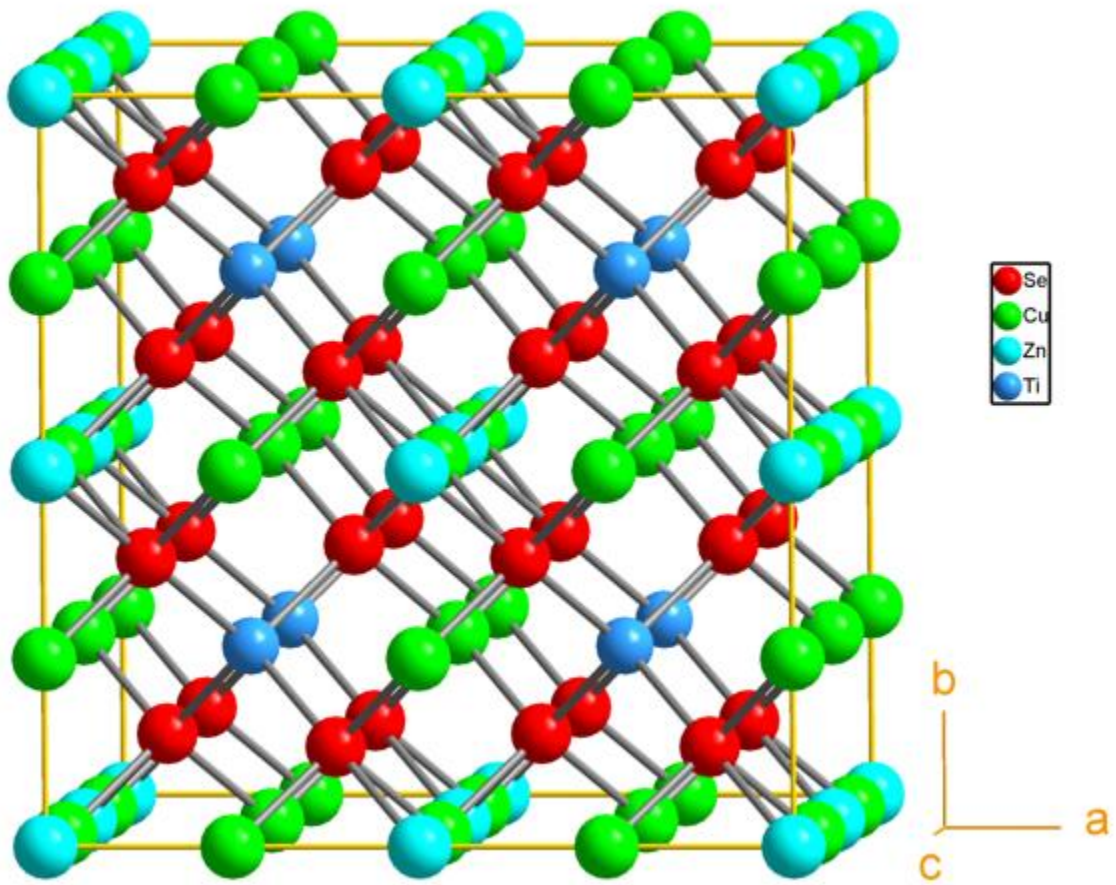

Figure 5.4.2: $Cu_{2.75}Zn_{0.625}TiSe_4$ crystal structure.

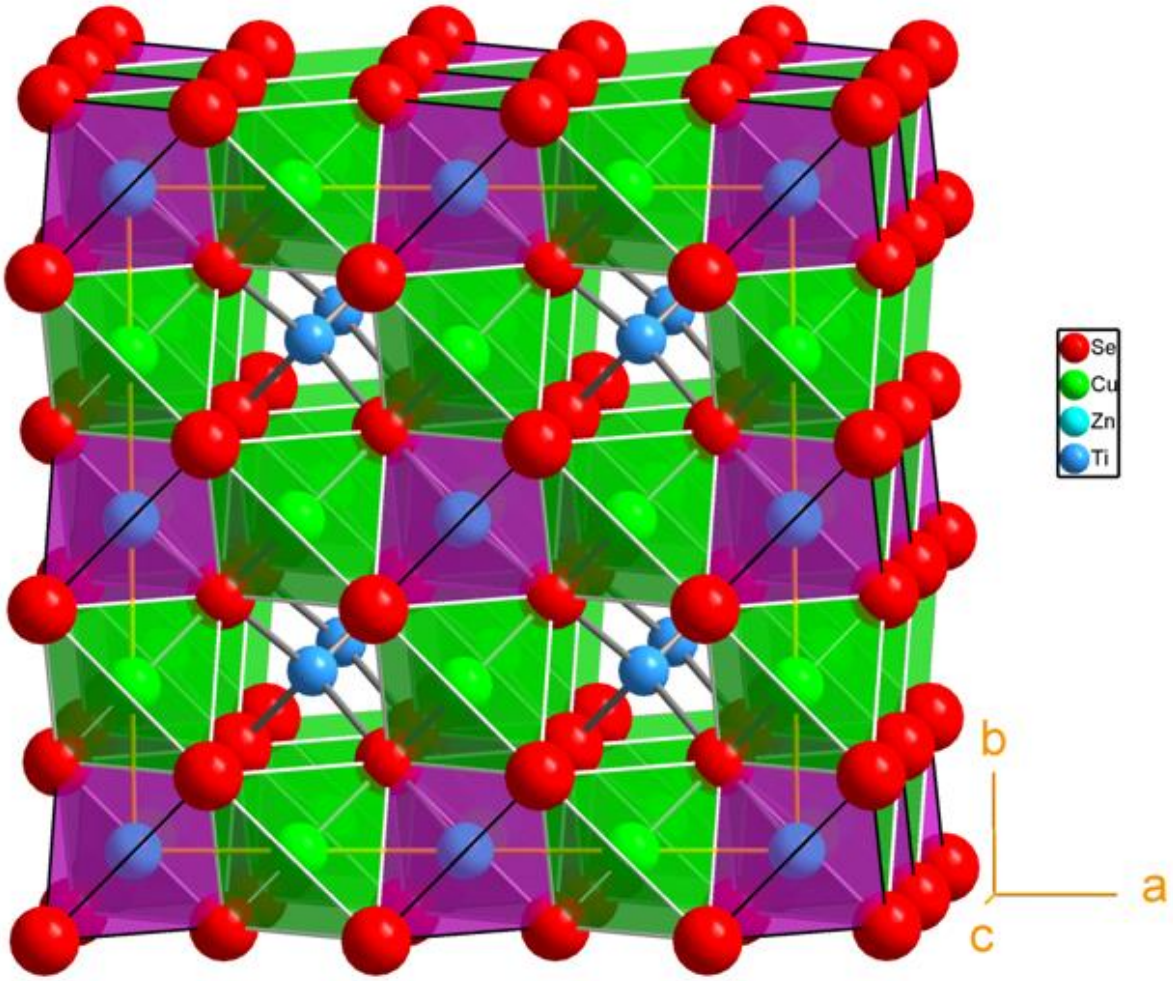

Figure 5.4.3: $Cu_{2.75}Zn_{0.625}TiSe_4$ crystal structure with tetrahedral polyhedra drawn.

In **Figure 5.4.3**, the tetrahedral polyhedra are depicted along with the crystal structure. **Figure 5.4.4** and **Figure 5.4.5** show the Ti and Zn connectivity in the lattice, respectively. There is corner-sharing between $ZnSe_4$ and $TiSe_4$ tetrahedra; edge-sharing between $ZnSe_4$ and $CuSe_4$ tetrahedra; corner-sharing between $CuSe_4$ tetrahedra. In **Table 5.4.3**, M-Se bond distances are reported. Within each metal, the interatomic distances are consistent. In general, values ranged between ~2.44-2.5 Å.

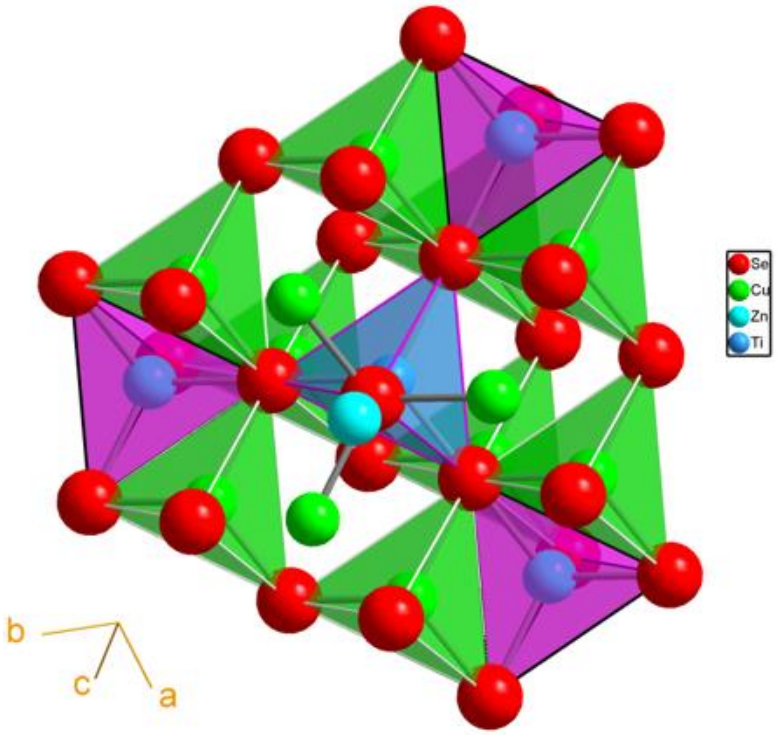

Figure 5.4.4: $Cu_{2.75}Zn_{0.625}TiSe_4$ Ti coordination connectivity.

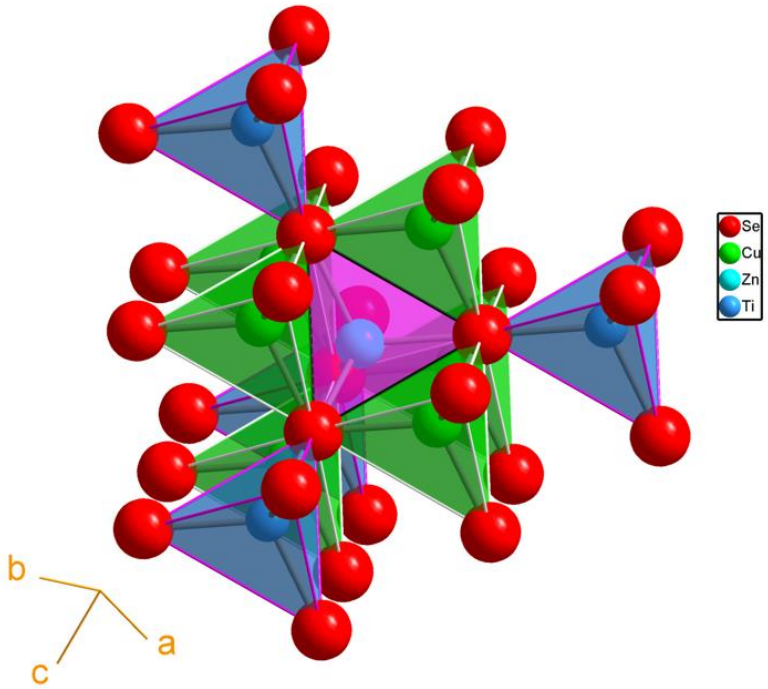

Figure 5.4.5: $Cu_{2.75}Zn_{0.625}TiSe_4$ Zn coordination connectivity.

Table 5.4.3: $Cu_{2.75}Zn_{0.625}TiSe_4$ selected inter-atomic bond distances (in Å). Operators for generating equivalent atoms: (i) y, z, x; (ii) z, x, y; (iii) -x, -y, z; (iv) -y, x, 0.5-z; (v) y, -x, 0.5-z; (vi) y, x, 0.5+z; (vii) x, -y, -z; (viii) -x, y, -z; (ix) y, -z, -x; (x) -z, -x, y; (xi) x, 0.5-y, 0.5-z; (xii) 0.5-x, 0.5-y, z; (xiii) 0.5-x, y, 0.5-z.

Atoms 1,2	**d 1,2 [Å]**
Cu1—Se1^{iii}	2.4407(9)
Cu1—Se1^{iv}	2.4407(9)
Cu1—Se1^{v}	2.4407(9)
Zn1—Se1^{vii}	2.431(2)
Zn1—Se1^{viii}	2.431(2)
Zn1—Se1^{iii}	2.431(2)
Ti1—Se1^{xi}	2.460(2)
Ti1—Se1^{xii}	2.460(2)
Ti1—Se1^{xiii}	2.460(2)

Anisotropic displacement parameters are reported in **Table D.1**, and Se-M-Se bond angles are found in **Table D.2**. For the case of M = Zn1 and Ti1, the bond angles were the ideal tetrahedral bond angle of 109.5°, while for the case of M = Cu1, the angle was either narrower or wider.

In order to verify the phase purity of the $Cu_2Zn_2Ti_{0.5}Se_4$ powder, PXRD was performed and compared to the $Cu_{2.75}Zn_{0.625}TiSe_4$ crystal reference pattern (**Figure 5.4.6**). The powder pattern matched extremely well, and PDXL phase matching did not identify any secondary phases present.

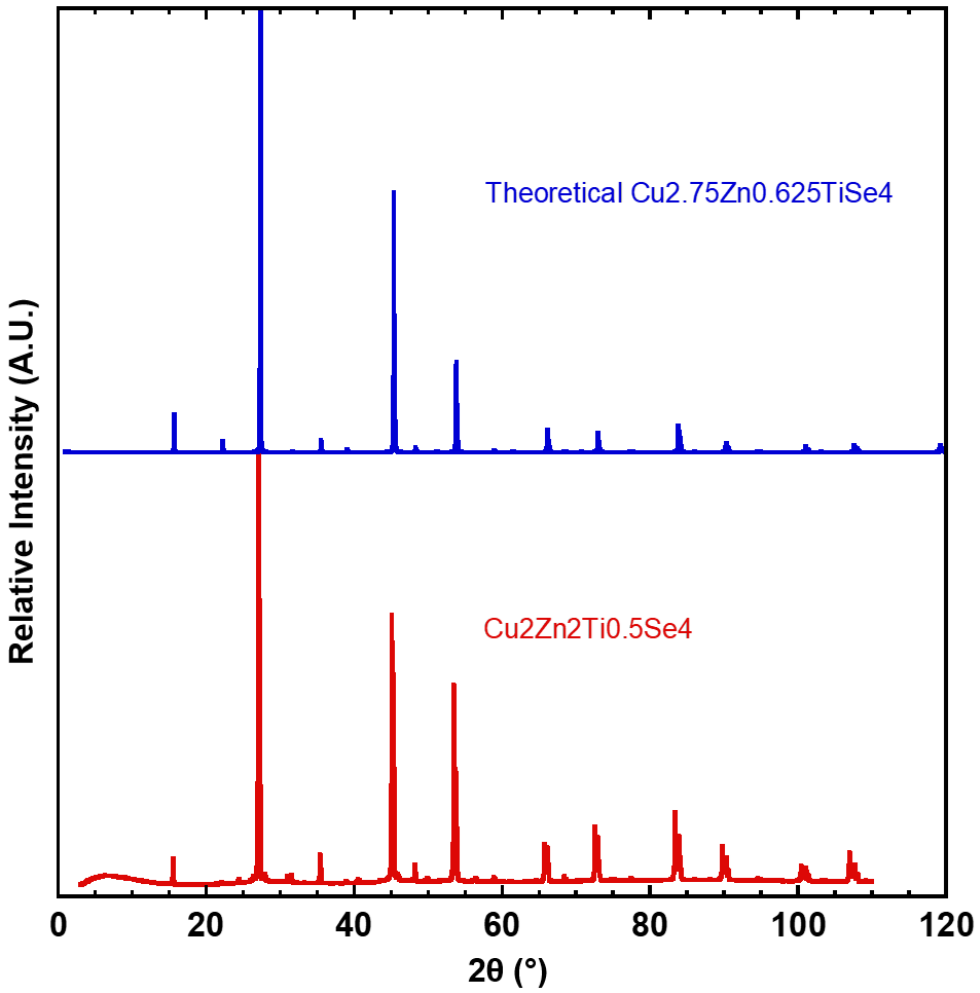

Figure 5.4.6: PXRD of $Cu_2Zn_2Ti_{0.5}Se_4$, plotted against the $Cu_{2.75}Zn_{0.625}TiSe_4$ single crystal pattern.

To test the thermal stability of $Cu_2Zn_2Ti_{0.5}Se_4$, DSC was implemented. The heating and cooling DSC is seen in **Figure 5.4.7**. Since XRD verified that $Cu_2Zn_2Ti_{0.5}Se_4$ is single phase, thermal events at 375.5 °C and 511 °C are likely phase transitions in the crystal. The melting point of the sample was 798.6 °C. Cooling DSC revealed multiple peaks present, meaning the melting point was not reversible. To probe the phase transitions further, high-T PXRD was taken at 425 °C and 600 °C, depicted in **Figure 5.4.8**. Interestingly, no changes in the XRD pattern was observed at elevated T.

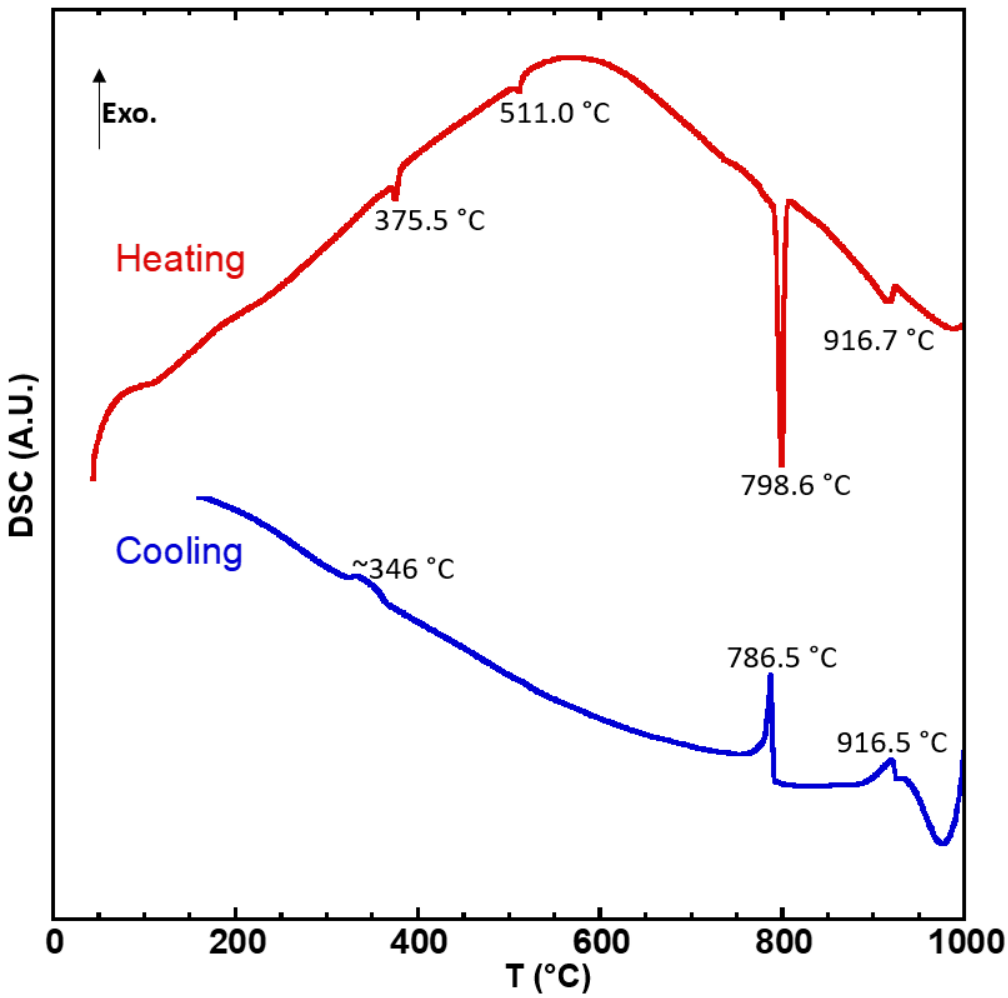

Figure 5.4.7: $Cu_2Zn_2Ti_{0.5}Se_4$ DSC vs. temperature for both heating and cooling. The thermal transitions were also noted.

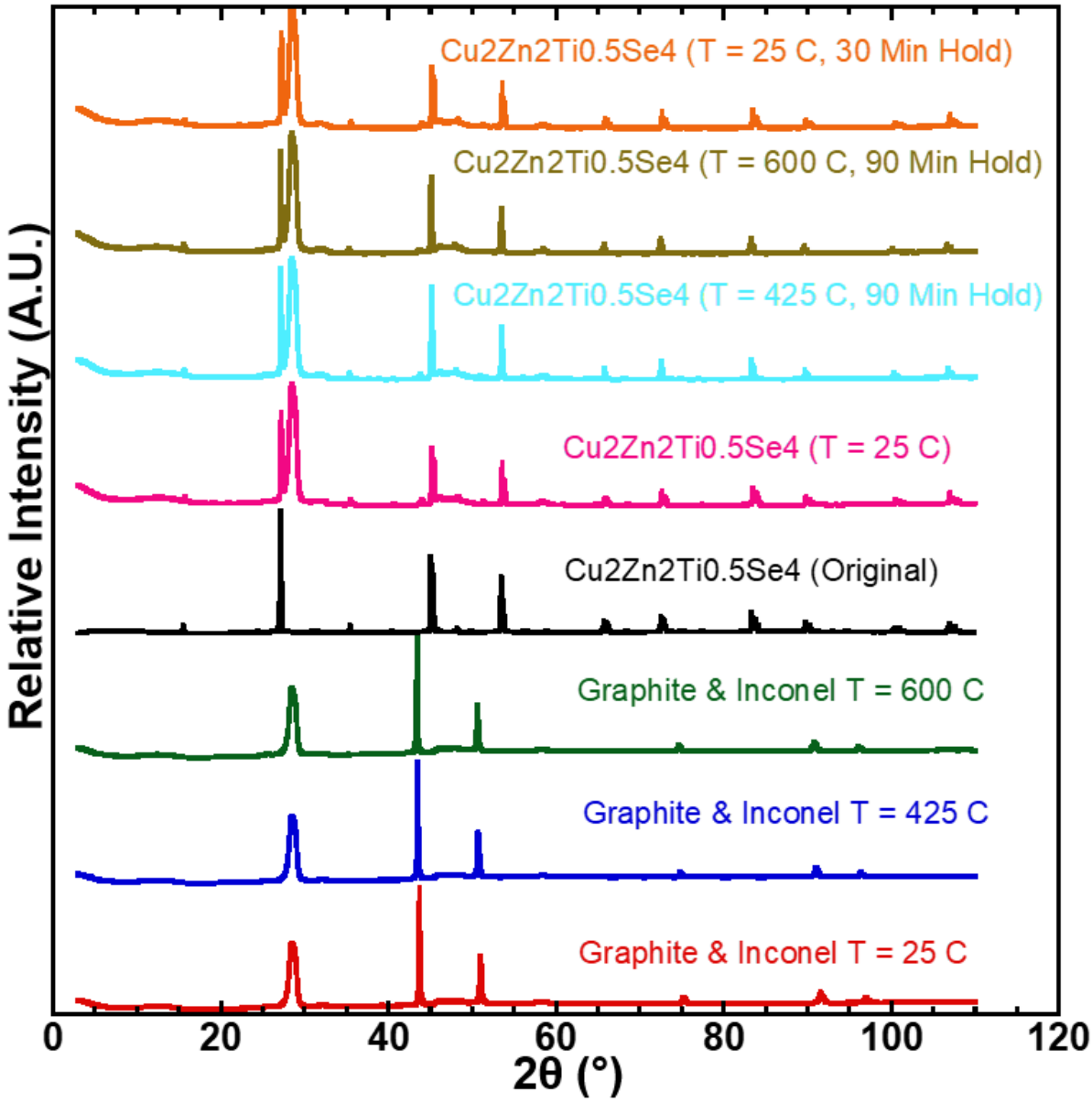

Figure 5.4.8: High-T PXRD of $Cu_2Zn_2Ti_{0.5}Se_4$. First, background scans were done on just the graphite dome and Inconel holder to help identify the peaks later. Next, the powder was scanned at various temperatures and dwell times.

5.4.1.3 Optical Properties of $Cu_2Zn_2Ti_{0.5}Se_4$

Diffuse reflectance UV-Vis-NIR spectroscopy was performed on $Cu_2Zn_2Ti_{0.5}Se_4$. Later, the Kubelka-Munk equation F(R)[33] was used to transform percent reflectance data to absorption, which was then plotted as a function of energy in electron volts, eV. The left image in **Figure 5.4.9** depicts F(R) vs. wavelength. On the right, we see a plot of $[F(R)*hv]^{1/r}$ vs. energy, where r = ½ corresponds to a direct bandgap E_g. To determine E_g, an absorption edge tangent line was extrapolated to the x-axis; the intercept with the x-axis corresponded to E_g. The direct bandgap was found to be 2.59 eV, corresponding to a maximum absorbed wavelength (λ_{Max}) of ~479 nm. As such, $Cu_2Zn_2Ti_{0.5}Se_4$ can absorb in the UV and a portion of the visible spectrum (violet, blue, and blue-cyan). However, visible colors such as cyan, green, yellow, orange, and red will not be absorbed. Additionally, the whole NIR/IR portion of the solar spectrum would be too low in energy as well. See **Figure 1.3.4** to reference the solar spectrum. No secondary phases were identified via PDXL in this case, so the recorded E_g value must be the true value for $Cu_2Zn_2Ti_{0.5}Se_4$.

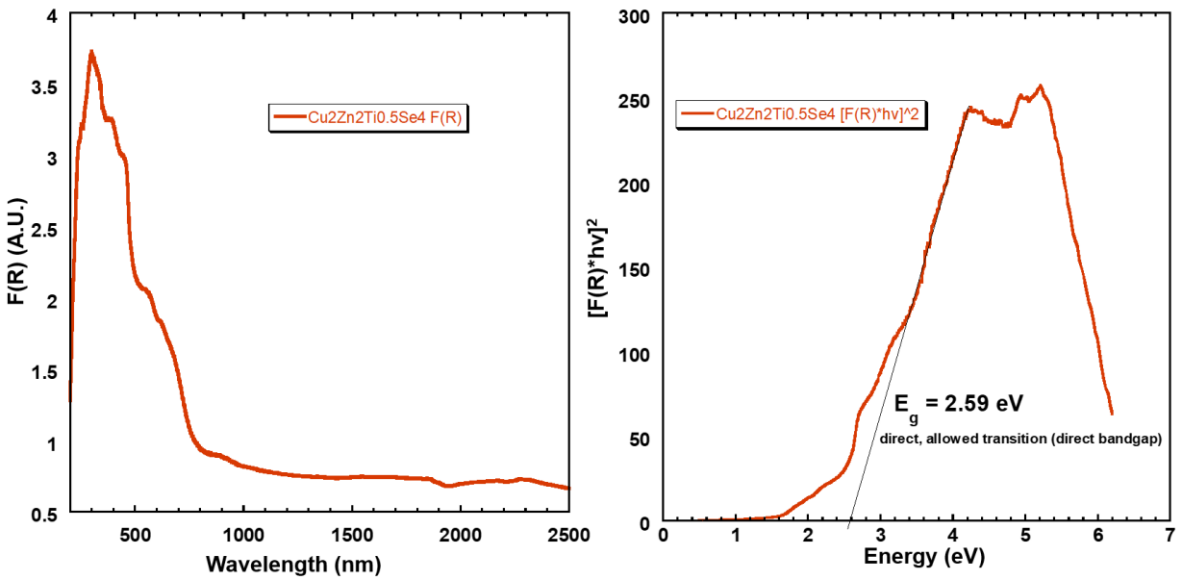

Figure 5.4.9: (Left): UV-Vis-NIR diffuse reflectance Tauc plot analysis. The Kubelka-Munk function F(R) was used to transform the reflectance data to absorbance. Plot of F(R) vs.

wavelength. **(Right):** Plot of $[F(R)*hv]^{1/r}$ vs. energy; r = ½ was chosen here to signify a direct, allowed transition (direct bandgap). To determine the direct optical bandgap (E_g), an absorption edge tangent line was extrapolated to the x-axis; the intercept with the x-axis corresponds to E_g.

5.4.2 Conclusion & Future Work: $Cu_2Zn_2Ti_{0.5}Se_4$ (x = 1):

In order to grow single crystals, $Cu_2Zn_2Ti_{0.5}Se_4$ powder was reacted via a melt & slow cool method, starting at 900 °C, then slowly cooling to 750 °C. Interestingly, single-crystal XRD analysis and structure refinement revealed that $Cu_{2.75}Zn_{0.625}TiSe_4$ single crystals were grown-slightly Cu-rich, Zn-poor, and Ti-rich when compared to the original powder formula. As such, $Cu_{2.75}Zn_{0.625}TiSe_4$ must be the more stable stoichiometry. The $Cu_{2.75}Zn_{0.625}TiSe_4$ single crystals were grey/black in color and irregular in shape. Structure refinement revealed that the sample crystallized in the cubic F-43c phase with a = 11.2958 Å. The Cu1 site had a low amount of vacancy at ~0.64/8, Zn1 had a vacancy of ~3/8, and Ti was fully occupied. All metal sites were ordered, with no mixed metal sharing. Every metal was found to be in tetrahedral coordination, with corner-sharing between $ZnSe_4$ and $TiSe_4$ tetrahedra; edge-sharing between $ZnSe_4$ and $CuSe_4$ tetrahedra; corner-sharing between $CuSe_4$ tetrahedra. M-Se distances were self-consistent, ranging from ~2.44-2.5 Å. For M = Zn1 and Ti1, the Se-M-Se bond angle was ideal at 109.5°, while for M = Cu1, the angle was either narrower or wider than expected.

PXRD revealed that although the $Cu_2Zn_2Ti_{0.5}Se_4$ powder formed a different single-crystal stoichiometry of $Cu_{2.75}Zn_{0.625}TiSe_4$, the peaks still matched quite well. PXDL phase analysis revealed no secondary phases. DSC revealed two phase transitions of 375.5 °C and 511 °C, followed by sample melting at 798.6 °C. Cooling revealed that the melting was not reversible. Surprisingly, high-T PXRD did not reveal any obvious phase transformations.

Diffuse reflectance UV-Vis-NIR spectroscopy was used to analyze the optical properties of the sample, and the Kubelka-Munk function and Tauc plot analysis was applied to gather the

direct optical bandgap, E_g. The analysis revealed that E_g = 2.59 eV, corresponding to a λ_{Max} of 479 nm; so, the material would absorb in the UV, and visible for violet, blue, and blue-cyan.

In the future, it would be interesting to measure the thermoelectric properties and XPS of $Cu_2Zn_2Ti_{0.5}Se_4$ and compare to $Cu_2Zn_3Se_4$. For this $Cu_2Zn_{2x}Ti_{(3-2x)/2}Se_4$ iteration, there is Ti present, so the effect of Ti on the properties would be intriguing. Further, it could be worthwhile to synthesize $Cu_{2.75}Zn_{0.625}TiSe_4$ powder using the same reaction profile and characterize via PXRD, DSC, and high-T PXRD to confirm similar behavior to $Cu_2Zn_2Ti_{0.5}Se_4$ powder.

5.5 $Cu_2ZnTiSe_4$ (x = 0.5) Single Crystal Synthesis ($Cu_2ZnTiSe_4$), Structural, and Optical Properties:

5.5.1 Results & Discussion: $Cu_2ZnTiSe_4$ (x = 0.5):

5.5.1.1 Single Crystal Synthesis ($Cu_2ZnTiSe_4$) (x = 0.5)

Single crystals were grown via a melt & slow cool method, starting at 900 °C, then slowly cooling to 750 °C. See **Section 5.2** for more details. The left image in **Figure 5.5.1** shows the $Cu_2ZnTiSe_4$ powder after reaction, appearing dark grey/black in color. The right image depicts a mounted $Cu_2ZnTiSe_4$ single crystal, appearing pink-red in color and irregular in shape.

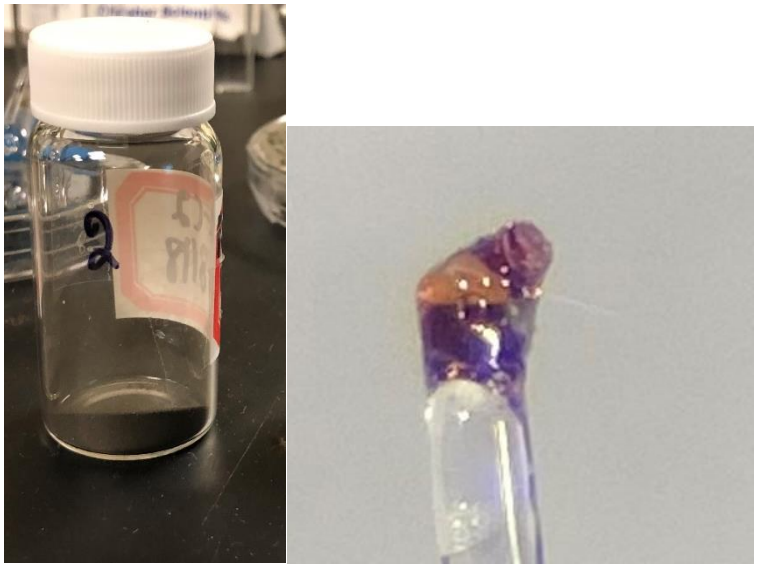

Figure 5.5.1: Left: $Cu_2ZnTiSe_4$ powder after reaction and being ground. Photograph was taken using an Apple iPhone 11 Pro Max camera (12 MP). **Right:** $Cu_2ZnTiSe_4$ single crystal mounted on the tip of a glass fiber for single crystal XRD analysis. Image was recorded using a Leica S6E stereo microscope equipped with a Leica L2 light source at 4x zoom. Image was captured through the lenspiece with an Apple iPhone 11 Pro Max 2x telephoto optical zoom lens (12-megapixel), giving a total of ~8x magnification.

5.5.1.2 Structural Properties of $Cu_2ZnTiSe_4$

$Cu_2ZnTiSe_4$ single crystals were grown and studied via single-crystal XRD and structure refinement. The results revealed a small cell, crystallizing in the cubic F-43m (#216) space group and possessing a lattice parameter of a = 5.6812 Å. Additionally, a larger 2x2x2 supercell (LC) was discovered, with space group Fd-3m (#227) and lattice parameter a = 11.3292 Å. The general crystal data is found in **Table 5.5.1**.

Table 5.5.1: Selected crystallographic data for $Cu_2ZnTiSe_4$.

Cell Type	Small Cell	Large Cell
Formula	$Cu_2ZnTiSe_4$	$Cu_2ZnTiSe_4$
Crystal system	Cubic	Cubic
Space group	$F\bar{4}3m$ (#216)	$Fd\bar{3}m$ (#227)
a = b = c (Å)	5.6812(7)	11.3292(13)
$\alpha = \beta = \gamma$ (°)	90	90
V ($Å^3$)	183.37(4)	1454.11(29)
Formula Mass (g/mol)	556.19	556.19
ρ (g/cm^3)	5.03647	5.08088
Z	1	8
Temperature (K)	300	300
R_{All}	0.021	0.0526
R_{int}	0.1832	0.1652
$R_1(F_o > 4\sigma(F_o))$	0.021	0.0409
wR_2 (all)	0.0533	0.1074
GooF	1.074	0.865

Table 5.5.2 and **Table 5.5.3** list the atomic coordinates, equivalent isotropic displacement parameters, and site occupancies for SC and LC. In SC, Cu1 and Zn1 share the same Wyckoff position 4c, with a total site vacancy of 2/8. On the other hand, Ti1 sits a the 4d position with a 6/8 vacancy. In the 2x2 supercell, Cu1 and Zn1 was found to share the 16d site, with a site vacancy of

~4.56/8. Similarly, Cu2 and Zn2 was found to share the 32e site, with a site vacancy of ~4.56/8. The 2x2x2 supercell resolved the Ti1 disorder, having 100% site occupancy.

Table 5.5.2: $Cu_2ZnTiSe_4$ Small Cell atomic coordinates, equivalent isotropic displacement parameters $U_{eq.}$, and occupancies for all atoms.

$Cu_2ZnTiSe_4$-small cell							
Atom	**Wyck.**	**S.O.F.**	**Vac.**	**x**	**y**	**z**	**$U_{eq.}$ ($Å^2$ x 10^{-4})**
Se1	4b	1	-	0.5	0.5	0.5	163.8(10)
Cu1	4c	0.5	50%	0.25	0.25	0.25	89.6(12)
Zn1	4c	0.25	75%	0.25	0.25	0.25	89.6(12)
Ti1	4d	0.25	75%	0.25	0.25	0.75	515.1(125)

Table 5.5.3: $Cu_2ZnTiSe_4$ Large Cell atomic coordinates, equivalent isotropic displacement parameters $U_{eq.}$, and occupancies for all atoms.

$Cu_2ZnTiSe_4$-large cell							
Atom	**Wyck.**	**S.O.F.**	**Vac.**	**x**	**y**	**z**	**$U_{eq.}$ ($Å^2$ x 10^{-4})**
Cu1	16d	0.29	71%	0.38	0.38	0.62	49.3(3)
Zn1	16d	0.14	86%	0.38	0.38	0.62	49.3(3)
Cu2	32e	0.29	71%	0.38	0.88	0.38	46.9(4)
Zn2	32e	0.14	86%	0.38	0.88	0.38	46.9(4)
Ti1	16d	1	0%	0.13	0.13	0.63	220.1(4)
Se1	48f	1	-	0.25	0.25	0.5	107.2(3)
Se2	48f	1	-	0.25	0	0.25	109.7(3)

Figure 5.5.2 and **Figure 5.5.3** depict the SC and LC along the a-direction. For both SC and LC, note the mixed metal site of Cu/Zn. For LC, the 2x2x2 supercell grid was drawn. In **Figure 5.5.4** and **Figure 5.5.5**, the MSe_4 tetrahedra were added, projected along the a-direction, rotated.

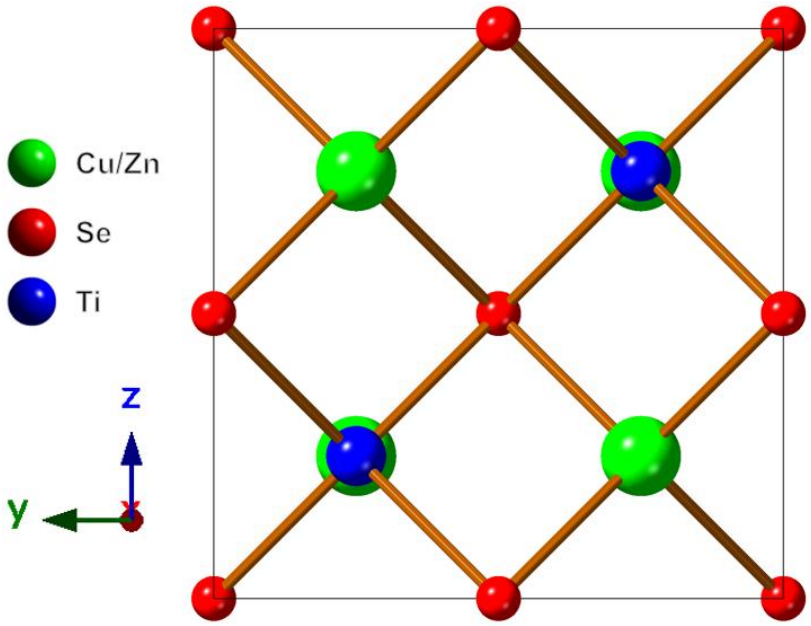

Figure 5.5.2: $Cu_2ZnTiSe_4$ Small Cell crystal projection along the a-direction.

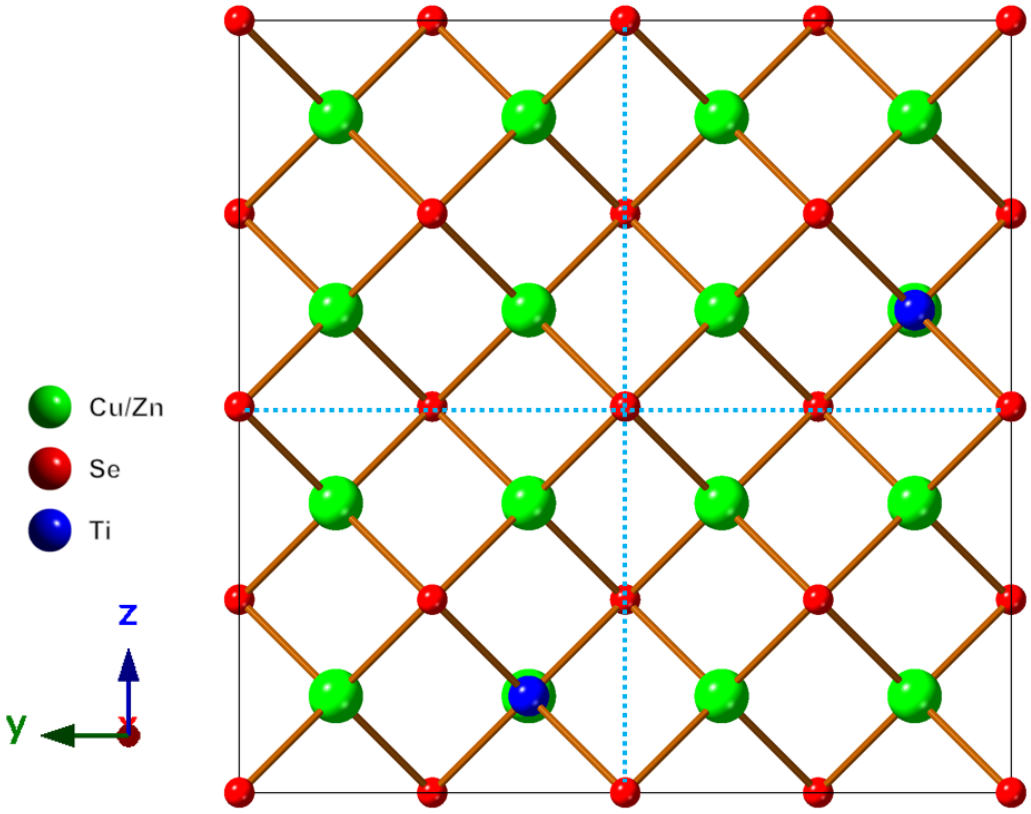

Figure 5.5.3: $Cu_2ZnTiSe_4$ Large Cell crystal projection along the a-direction. The blue dotted lines were overlayed to depict the 2x2 supercell. Each square represents the small cell.

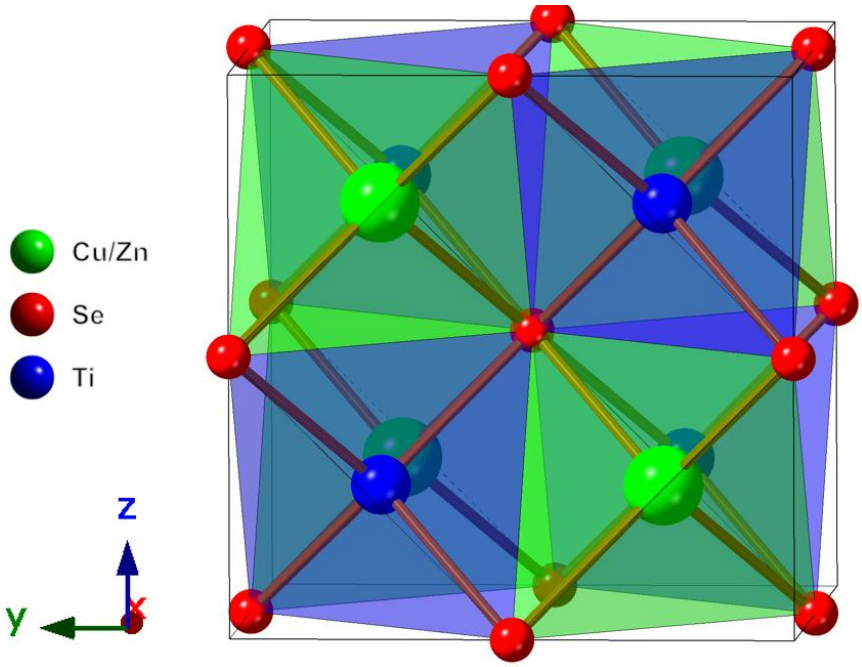

Figure 5.5.4: $Cu_2ZnTiSe_4$ Small Cell crystal projection along the a-direction, rotated, with all polyhedra.

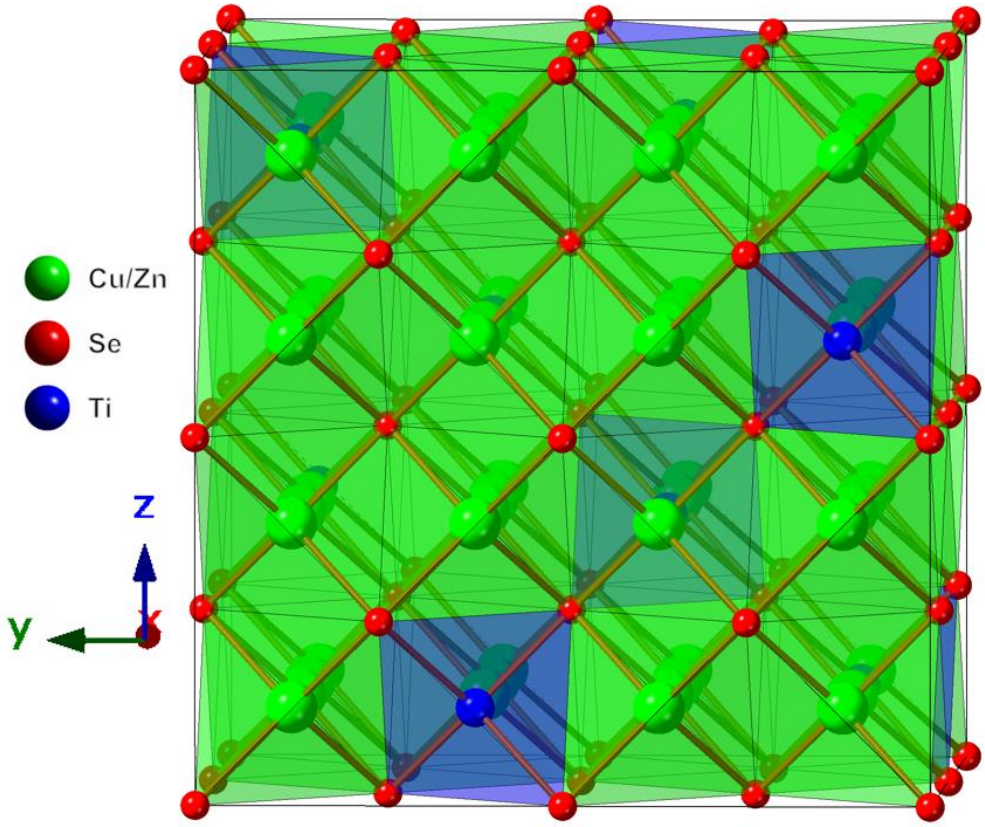

Figure 5.5.5: $Cu_2ZnTiSe_4$ Large Cell crystal projection along the a-direction, rotated, with all polyhedra.

To get a sense of the typical M-M distance in SC and LC, **Figure 5.5.6** and **Figure 5.5.7** was drawn. Distances between Cu/Zn-Cu/Zn and Cu/Zn-Ti were ~4 Å. For LC, the Ti-Ti distance was ~8 Å. This makes sense, as Ti^{4+}-Ti^{4+} has a large amount of electrostatic repulsion.

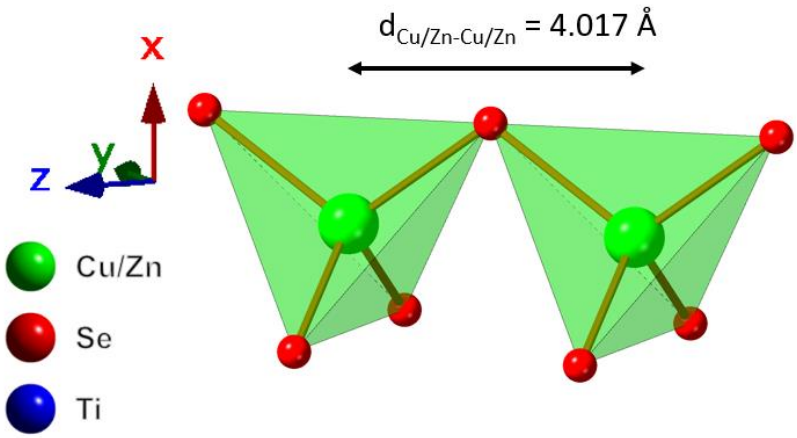

Figure 5.5.6: $Cu_2ZnTiSe_4$ small cell [011] direction rotated, Cu/Zn-Cu/Zn chain.

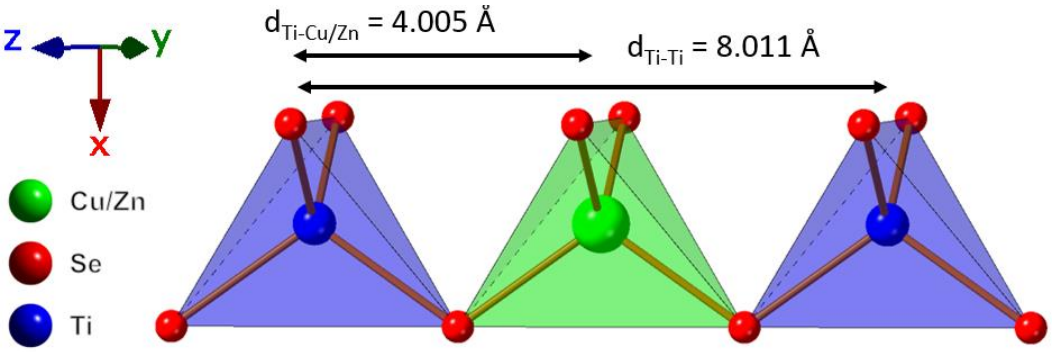

Figure 5.5.7: $Cu_2ZnTiSe_4$ large cell [011] direction rotated, Ti-Cu/Zn-Ti chain.

Table 5.5.4 and **Table 5.5.5** list the M-Se bond distances for SC and LC. For SC, all M-Se distances were 2.46 Å. For LC, all Ti-Se bond distances were 2.4518 Å, while the Cu/Zn-Se bond distances were slightly varied from 2.4527-2.4530 Å.

Table 5.5.4: $Cu_2ZnTiSe_4$ Small Cell selected inter-atomic bond distances (in Å). Small cell operators for generating equivalent atoms: i) 0.5+x, 0.5+y, z; (ii) x, 0.5+y, 0.5+z; (iii) 0.5+x, y, 0.5+z; (iv) x, 0.5+y, -0.5+z; (v) 0.5+x, y, -0.5+z; (vi) -0.5+x, -0.5+y, z; (vii) -0.5+x, y, -0.5+z; (viii) x, -0.5+y, -0.5+z; (ix) x, y, -1+z; (x) -0.5+x, y, 0.5+z; (xi) x, -0.5+y, 0.5+z; (xii) x, y, 1+z.

$Cu_2ZnTiSe_4$-small cell	
Atoms 1,2	**d 1,2 [Å]**
Cu1/Zn1—Se1^{vi}	2.4600(3)
Cu1/Zn1—Se1^{vii}	2.4600(3)
Cu1/Zn1—Se1^{viii}	2.4600(3)
Ti1—Se1^{vi}	2.4600(3)
Ti1—Se1^{x}	2.4600(3)
Ti1—Se1^{xi}	2.4600(3)

Table 5.5.5: $Cu_2ZnTiSe_4$ Large Cell selected inter-atomic bond distances (in Å). Large cell operators for generating equivalent atoms: (i) 0.25-z, 0.25-x, 0.25-y; (ii) 0.25-x, 0.25-y, 0.25-z; (iii) x, 0.5+y, 0.5+z; (iv) 0.75-x, 0.25+y, 1.75+z; (v) -0.5-z, -1-x, 1.5+y; (vi) 1.25-x, 1.75-z, 1.75-y; (vii) 1.25-x, 1.75+y, 1.75+z; (viii) 0.75-y, -0.75+x, 0.75+z; (ix) 0.25-z, 1.75+y, 0.75+x; (x) 0, 0, 0; (xi) x, 1+y, z; (xii) 0, 0, 0; (xiii) y, z, x; (xiv) 0, 0, 0; (xv) x, 0.5+y, -0.5+z; (xvi) -0.5+z, 0.5+x, y; (xvii) 0, 0, 0; (xviii) 0, 0, 0; (xix) y, 0.5-x, 1.5-z; (xx) 0.25-y, 0.25-z, 1.25-x; (xxi) 0, 0, 0; (xxii) -0.75-y, 0.75-x, 0.75-z; (xxiii) 0.5+x, -z, 1.5-y; (xxiv) 0.25+z, 0.25+x, 0.25-y; (xxv) 0, 0, 0; (xxvi) 0.5+z, 1-y, 0.5-x; (xxvii) x, -1+y, z; (xxviii) -y, -0.5-x, -0.5+z; (xxix) x, -0.5+y, -0.5+z; (xxx) -0.5+z, -0.5+x, y; (xxxi) 0, 0, 0.

$Cu_2ZnTiSe_4$-large cell	
Atoms 1,2	**d 1,2 [Å]**
Cu1/Zn1—Se1	2.4527(4)
Cu1/Zn1—Se1^{i}	2.4527(4)
Cu1/Zn1—Se2^{ii}	2.4530(4)
Cu1/Zn1—Se2^{iii}	2.4530(4)
Cu2/Zn2—Se2^{ix}	2.4528(3)
Cu2/Zn2—Se2^{x}	2.4528(3)
Cu2/Zn2—Se2^{i}	2.4528(3)
Cu2/Zn2—Se2^{xi}	2.4528(3)
Ti1—Se1^{xviii}	2.4528(3)
Ti1—Se1^{xix}	2.4528(3)
Ti1—Se1^{xx}	2.4528(3)
Ti1—Se1	2.4528(3)

Table E.1 and **Table E.2** lists the SC and LC anisotropic displacement parameters. The inter-atomic Se-M-Se bond angles for SC and LC are noted in **Table E.3** and **Table E.4**. For SC, all bond angles were the typical tetrahedral bond angle of 109.5°. For LC, most bond angles were also 109.5°, with tiny deviations noted for two Se-Cu/Zn-Se bonds.

To check the phase purity of the $Cu_2ZnTiSe_4$ powder, PXRD was implemented (**Figure 5.5.8**). The powder pattern was plotted against the SC and LC. Additionally, PDXL phase analysis identified a large secondary $TiSe_2$ P-3m1 phase. Surprisingly, there were two unidentified peaks

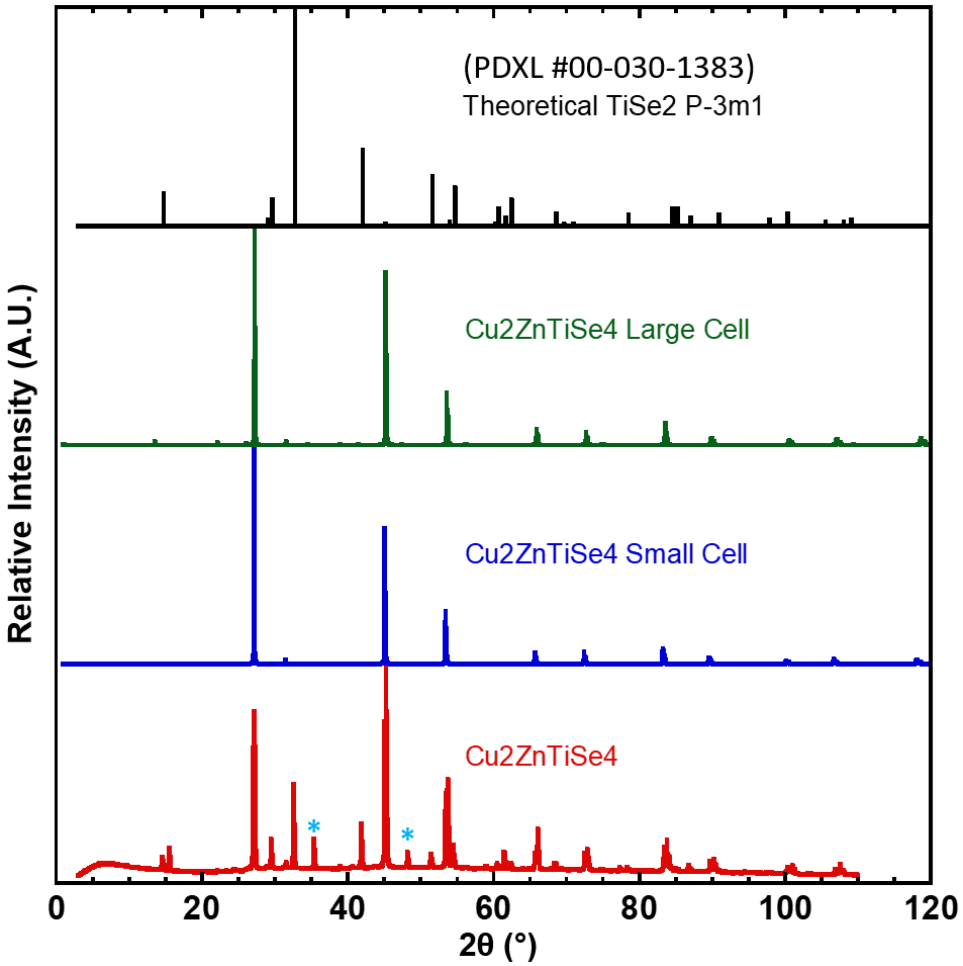

Figure 5.5.8: PXRD of $Cu_2ZnTiSe_4$, plotted against the small cell and large cell patterns, as well as a potential binary phase of $TiSe_2$ P-3m1 (PDXL #00-030-1383[111]). The two blue asterisks were unidentified peaks.

at 35.417° and 48.125°, noted by the blue asterisks.

To probe the thermal stability, heating and cooling DSC was measured (**Figure 5.5.9**). A single melting peak was observed at 795.7 °C, followed by decomposition. Upon cooling, multiple peaks were seen, so the melting was not reversible.

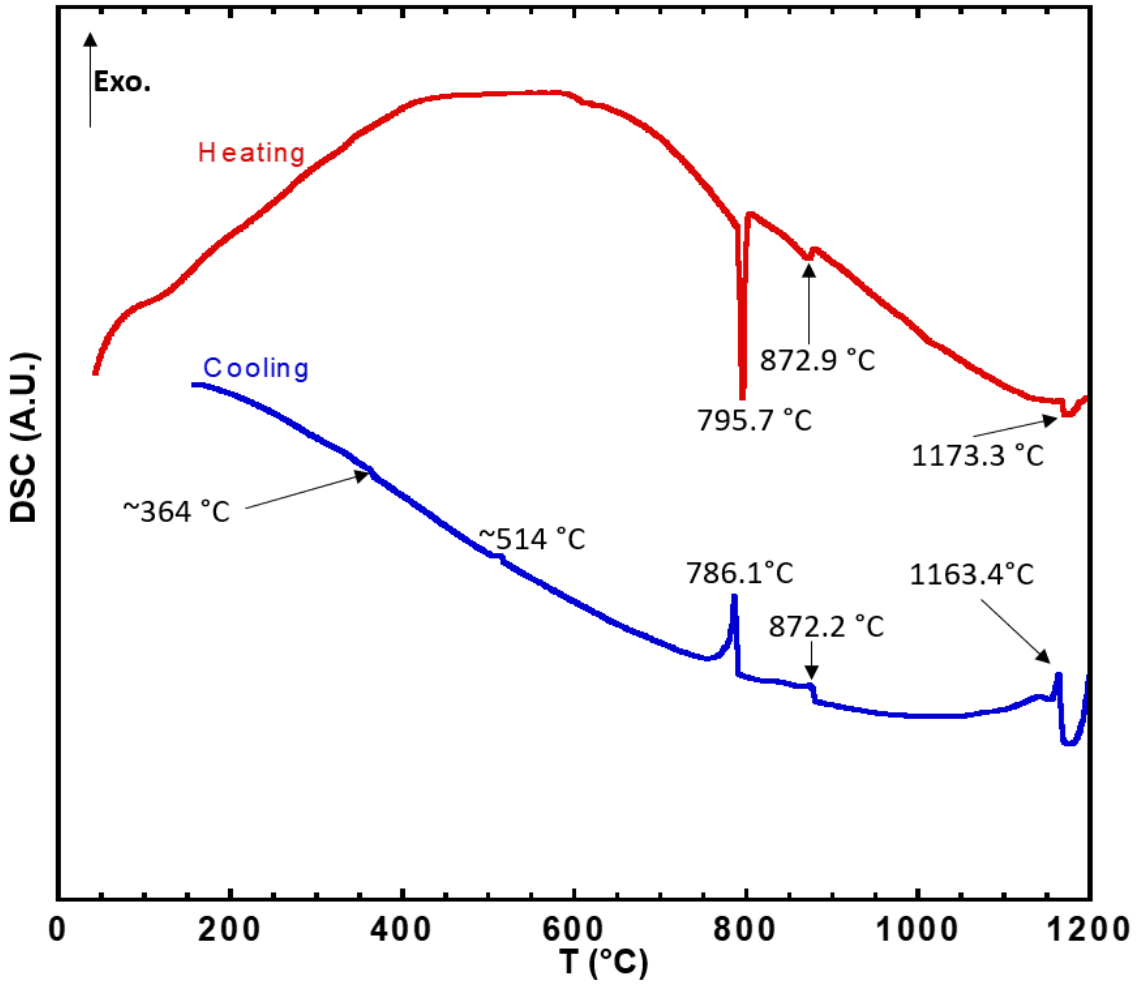

Figure 5.5.9: $Cu_2ZnTiSe_4$ DSC vs. temperature for both heating and cooling. The thermal transitions were also noted.

In order to analyze the PXRD and DSC results further, a Ti-Se binary phase diagram was referenced, as seen in **Figure E.1**. The DSC events upon melting were noted, as well as the $TiSe_2$ RT P-3m1 phase. Note that for $TiSe_2$, this corresponds to 33 at% Ti. Interestingly, near this composition range no $TiSe_2$ P-3m1 phase changes or melting were observed. To gain further

insight on the $TiSe_2$ binary, PXRD and DSC on $TiSe_2$ powder is depicted in **Figure E.2**. Surprisingly, only two minor heating peaks were observed that did not correlate to the $Cu_2ZnTiSe_4$ thermal events. Further, no melting was observed for the temperature range up to 1200 °C. As such, the $Cu_2ZnTiSe_4$ melting point seen in the heating DSC curve is indeed that of the main phase.

5.5.1.3 Optical Properties of $Cu_2ZnTiSe_4$

Diffuse reflectance UV-Vis-NIR spectroscopy was performed on $Cu_2ZnTiSe_4$. Later, the Kubelka-Munk equation F(R)[33] was used to transform percent reflectance data to absorption, which was then plotted as a function of energy in electron volts, eV. The left image in **Figure 5.5.10** depicts F(R) vs. wavelength. On the right, we see a plot of $[F(R)*h\nu]^{1/r}$ vs. energy, where r = ½ corresponds to a direct bandgap E_g. To determine E_g, an absorption edge tangent line was extrapolated to the x-axis; the intercept with the x-axis corresponded to E_g. The direct bandgap was found to be 2.61 eV, corresponding to a maximum absorbed wavelength (λ_{Max}) of ~475 nm. As such, $Cu_2ZnTiSe_4$ can absorb in the UV and a portion of the visible spectrum (violet, blue, and blue-cyan). However, visible colors such as cyan, green, yellow, orange, and red will not be absorbed. Additionally, the whole NIR/IR portion of the solar spectrum would be too low in energy as well. See **Figure 1.3.4** to reference the solar spectrum.

Now, in order to be complete in the optical analysis, one must consider the effect of the $TiSe_2$ P-3m1 secondary phase. According to Gaby *et al*., $TiSe_2$ is actually a semimetal with a band overlap of 0.2 eV.[112] As such, the recorded E_g value for $Cu_2ZnTiSe_4$ must be the true value.

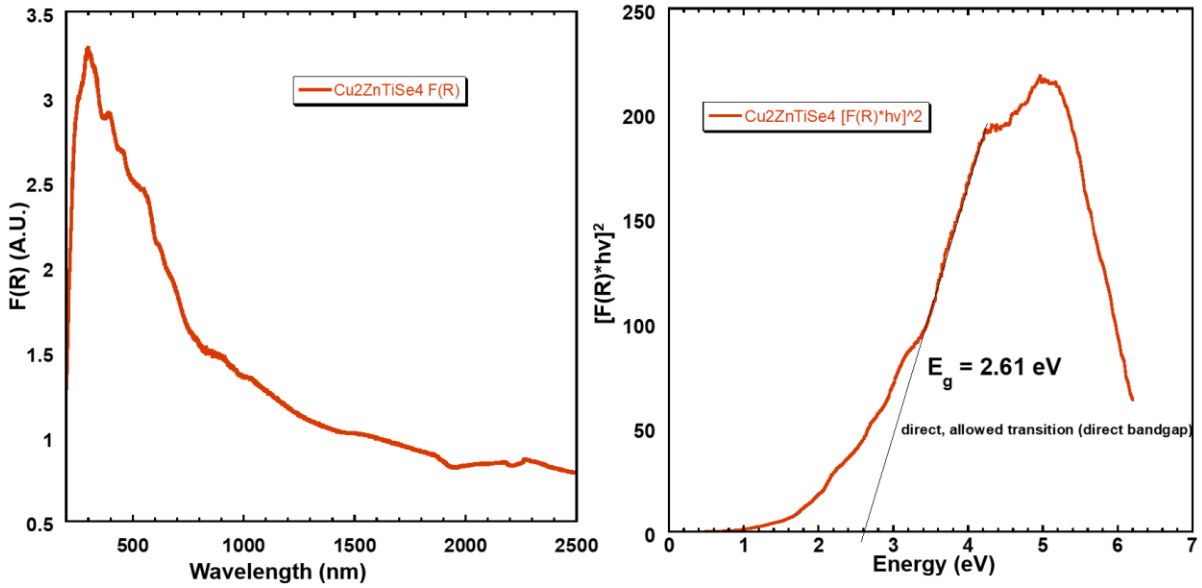

Figure 5.5.10: (Left): UV-Vis-NIR diffuse reflectance Tauc plot analysis. The Kubelka-Munk function F(R) was used to transform the reflectance data to absorbance. Plot of F(R) vs. wavelength. **(Right):** Plot of $[F(R)*hv]^{1/r}$ vs. energy; r = ½ was chosen here to signify a direct, allowed transition (direct bandgap). To determine the direct optical bandgap (E_g), an absorption edge tangent line was extrapolated to the x-axis; the intercept with the x-axis corresponds to E_g.

5.5.2 Conclusion & Future Work: $Cu_2ZnTiSe_4$ (x = 0.5):

Single crystals of $Cu_2ZnTiSe_4$ were grown via a melt & slow cool method, starting at 900 °C and then slowly cooling to 750 °C, appearing pink-red in color and irregular in shape. The single crystals were found to possess a small cell, crystallizing in the cubic F-43m (#216) space group and possessing a lattice parameter of a = 5.6812 Å. Additionally, a larger 2x2 supercell (LC) was discovered, with space group Fd-3m (#227) and lattice parameter a = 11.3292 Å. For SC, Cu1/Zn1 had a shared site vacancy of 2/8, while Ti1 had a 6/8 vacancy. In the 2x2 supercell, Cu1 and Zn1 was found to share the 16d site, with a site vacancy of ~4.56/8. Similarly, Cu2 and Zn2 was found to share the 32e site, with a site vacancy of ~4.56/8. The 2x2 supercell resolved the Ti1 disorder, having 100% site occupancy. In both cells, all metal sites had tetrahedral coordination. Typical M-M distances were ~4 Å; for SC, all M-Se distances were 2.46 Å. For LC, all Ti-Se bond distances were 2.4518 Å, while the Cu/Zn-Se bond distances were slightly varied from 2.4527-2.4530 Å. The SC Se-M-Se bond angles were all the ideal angle, while for LC had fluctuations in the Se-M-Se bond angle.

PXRD was used to check phase purity of the powders, and matched the SC and LC patterns. Additionally, PDXL phase matching identified a binary $TiSe_2$ P-3m1 phase. Upon inspection, the powder does indeed appear to be a mixture of the $Cu_2ZnTiSe_4$ SC/LC and the $TiSe_2$ P-3m1 phase. DSC analysis noted a single melting peak at 795.7 °C, with decomposition afterward. The cooling DSC revealed multiple peaks, suggesting thermal instability after melting. To analyze the melting peak and $TiSe_2$ P-3m1 phase further, a Ti-Se binary phase diagram was referenced. No thermal transitions at this temperature was noted in the phase diagram. Further, $TiSe_2$ powder DSC saw no melting up to 1200 °C. As such, the 795.7 °C melting did belong to $Cu_2ZnTiSe_4$.

Diffuse reflectance UV-Vis-NIR spectroscopy was used to analyze the optical properties of the sample, and the Kubelka-Munk function and Tauc plot analysis was applied to gather the direct optical bandgap, E_g. The analysis revealed that $E_g = 2.61$ eV, corresponding to a λ_{Max} of 475 nm; so, the material would absorb in the UV, and visible for violet, blue, and blu-cyan. For reference, the binary $TiSe_2$ P-3m1 phase is a semimetal with a band overlap of 0.2 eV. So, the measured bandgap belongs to $Cu_2ZnTiSe_4$.

In the future, since there was a large $TiSe_2$ P-3m1 phase found in the powder sample, the synthesis conditions of $Cu_2ZnTiSe_4$ need to be further optimized. One possible route is growing large amounts of $Cu_2ZnTiSe_4$ pink-red single crystals via the melt & slow-cool process and crushing that into powder for the various measurements. Alternatively, perhaps a Kesterite-like solid-state reaction profile from the literature could be implemented since there are similarities in the chemical formula. Once successfully synthesized, repeating the characterization sweep such as PXRD, DSC, optical bandgap, and thermoelectric measurements would be suggested.

5.6 $Cu_2Ti_{1.5}Se_4$ (x = 0) Single Crystal Synthesis ($Cu_3Ti_{1.25}Se_4$), Structural, and Optical Properties:

5.6.1 Results & Discussion: $Cu_2Ti_{1.5}Se_4$ (x = 0):

5.6.1.1 Single Crystal Synthesis ($Cu_3Ti_{1.25}Se_4$)

In order to grow single crystals, $Cu_2Ti_{1.5}Se_4$ powder was reacted via a dual-zone furnace method. The hot thermocouple was set to 720 °C, while the cold thermocouple was set to 520 °C. The sample powder end of the tube was aligned at the hot thermocouple side, with the temperature gradient causing crystals to form on the cold end of the tube via a temperature-assisted vapor transport mechanism. See **Section 5.2**, **Figure 5.2.1**, and **Figure 5.2.2** for more details. Interestingly, single-crystal XRD analysis and structure refinement revealed the crystals formed were a different stoichiometry than the powder used. In fact, $Cu_3Ti_{1.25}Se_4$ single crystals were grown-slightly Cu-rich and Ti-poor when compared to the powder formula. As such, $Cu_3Ti_{1.25}Se_4$ must be the more stable stoichiometry. The left image in **Figure 5.6.1** shows the reacted $Cu_2Ti_{1.5}Se_4$ powder, appearing black in color. The right image was a $Cu_3Ti_{1.25}Se_4$ single crystal, appearing black in color and faceted.

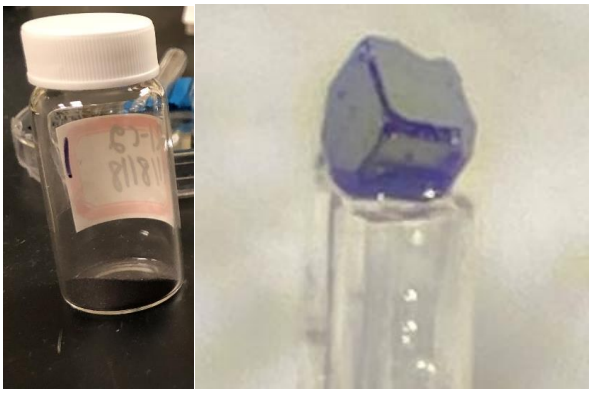

Figure 5.6.1: Left: $Cu_2Ti_{1.5}Se_4$ powder after reaction and being ground. Photograph was taken using an Apple iPhone 11 Pro Max camera (12 MP). **Right:** $Cu_3Ti_{1.25}Se_4$ single crystal mounted on the tip of a glass fiber for single crystal XRD analysis. Image was recorded using a Leica S6E stereo microscope equipped with a Leica L2 light source at 4x zoom. Image was captured through

the lenspiece with an Apple iPhone 11 Pro Max 2x telephoto optical zoom lens (12-megapixel), giving a total of ~8x magnification.

5.6.1.2 Structural Properties of $Cu_2Ti_{1.5}Se_4$

In this work, $Cu_2Ti_{1.5}Se_4$ powder was reacted to grow single crystals. Surprisingly, structure refinement revealed that the grown crystals were of a different stoichiometry: $Cu_3Ti_{1.25}Se_4$. $Cu_3Ti_{1.25}Se_4$ was found to crystallize in the cubic F-43m space group (#216), with a lattice parameter of a = 11.2954 Å. **Table 5.6.1** lists selected crystal data for the compound.

Table 5.6.1: Selected crystallographic data for $Cu_3Ti_{1.25}Se_4$.

Formula	$Cu_3Ti_{1.25}Se_4$
Crystal system	Cubic
Space group	$F\bar{4}3m$ (#216)
a = b = c (Å)	11.2954(11)
$\alpha = \beta = \gamma$ (°)	90
V (Å^3)	1441.14(24)
Formula Mass (g/mol)	1132.67
ρ (g/cm^3)	5.22014
Z	4
Temperature (K)	300
R_{All}	0.0485
R_{int}	0.0744
$R_1(F_o > 4\sigma(F_o))$	0.047
wR_2 (all)	0.1409
GooF	1.197

The atomic coordinates, equivalent isotropic displacement parameters, and site occpancies are found in **Table 5.6.2**. In the structure, Cu1 is highly ordered, having only ~1/8 total vacancy. Cu2/Ti2 actually share the same 4c site, with a total tetrahedral site vacancy of ~1/8. Ti1, Ti3, and Ti4 possess their own positions with varying vacancy levels: ~1/8, ~4/8, and ~2/8, respectively. **Figure 5.6.2** depicts the $Cu_3Ti_{1.25}Se_4$ crystal lattice, with tetrahedral polyhedra shown. In the figure, note the Cu/Ti shared site, corresponding to the Cu2/Ti2 atoms.

Table 5.6.2: $Cu_3Ti_{1.25}Se_4$ atomic coordinates, equivalent isotropic displacement parameters $U_{eq.}$, and occupancies for all atoms.

Atom	Wyck.	S.O.F.	Vac.	x	y	z	$U_{eq.}$ ($Å^2$ x 10^{-4})
Cu1	24g	0.89	11%	0.25	0.25	-0.00001(10)	164.1(4)
Cu2	4c	0.65	35%	0.25	0.25	0.25	125.4(10)
Ti2	4c	0.28	72%	0.25	0.25	0.25	125.4(10)
Ti1	4d	0.91	9%	0.25	0.25	-0.25	216.1(13)
Ti3	4b	0.52	48%	0	0.5	0	273.3(31)
Ti4	4a	0.79	21%	0.5	0.5	0	83.9(12)
Se1	16e	1	-	0.37425(6)	0.37425(6)	-0.12575(6)	202.7(7)
Se2	16e	1	-	0.12567(5)	0.37433(5)	0.12567(5)	124(5)

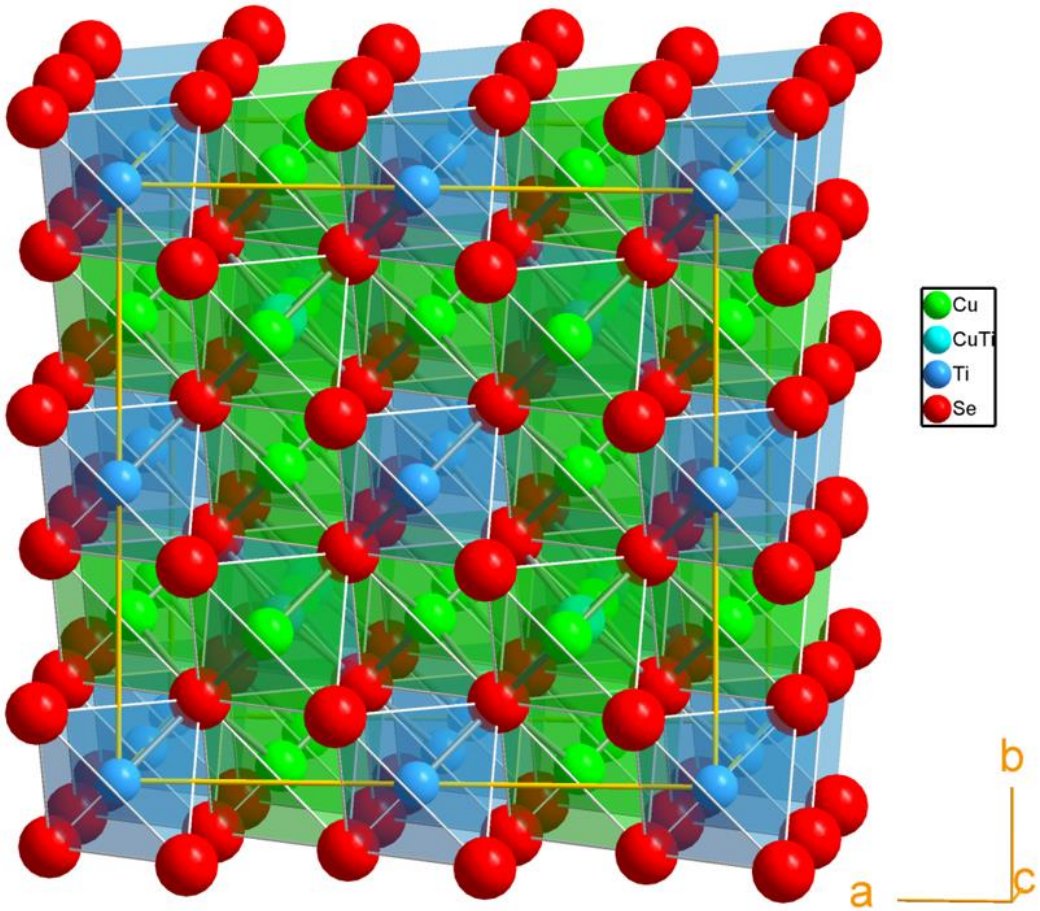

Figure 5.6.2: $Cu_3Ti_{1.25}Se_4$ crystal structure, with polyhedra drawn.

Figure 5.6.3 shows the Ti substructure in the $Cu_3Ti_{1.25}Se_4$ crystal lattice. In this case, $Cu(1)Se_4$ tetrahedra share corners and edges with $Ti(1)Se_4$ and $Ti(2)Se_4$ tetrahedra to form layers that intersect with each other at the $Ti(1)Se_4$ and $Ti(2)Se_4$ tetrahedra to form a three dimensional Cu-substructure that fills the empty channels of the Ti-sublattice. In **Figure 5.6.4**, the Cu substructure is depicted. Here, $Cu(1)Se_4$ tetrahedra share corners and edges with $Ti(1)Se_4$ and $Ti(2)Se_4$ tetrahedra to form layers that intersect with each other at the $Ti(1)Se_4$ and $Ti(2)Se_4$ tetrahedra to form a three-dimensional Cu-substructure that fills the empty channels of the Ti-sublattice.

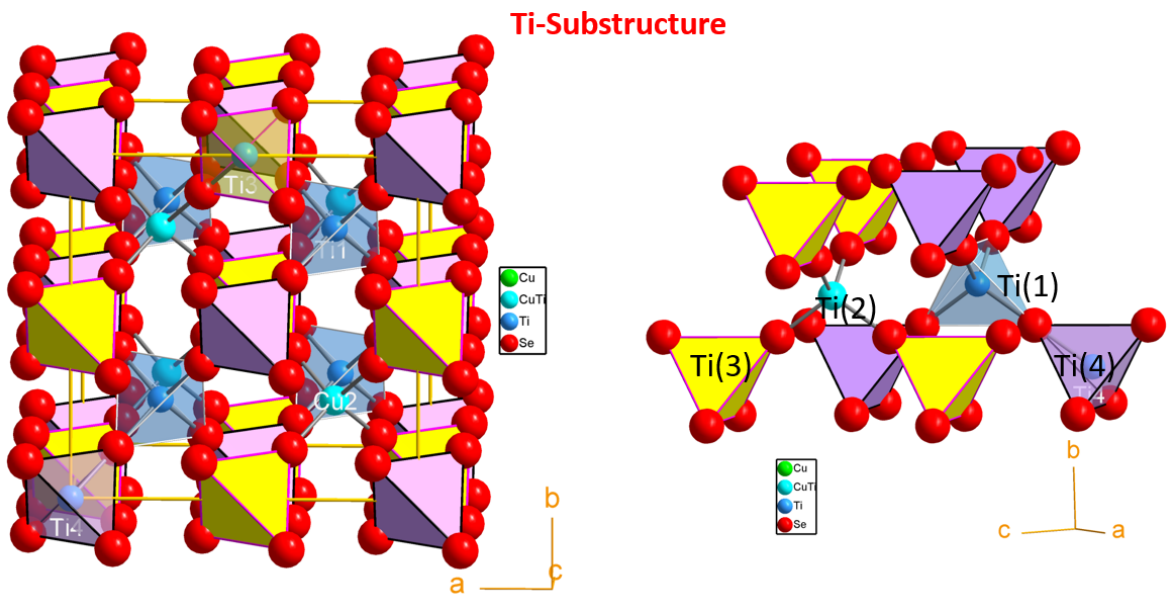

Figure 5.6.3: $Cu_3Ti_{1.25}Se_4$ Ti substructure.

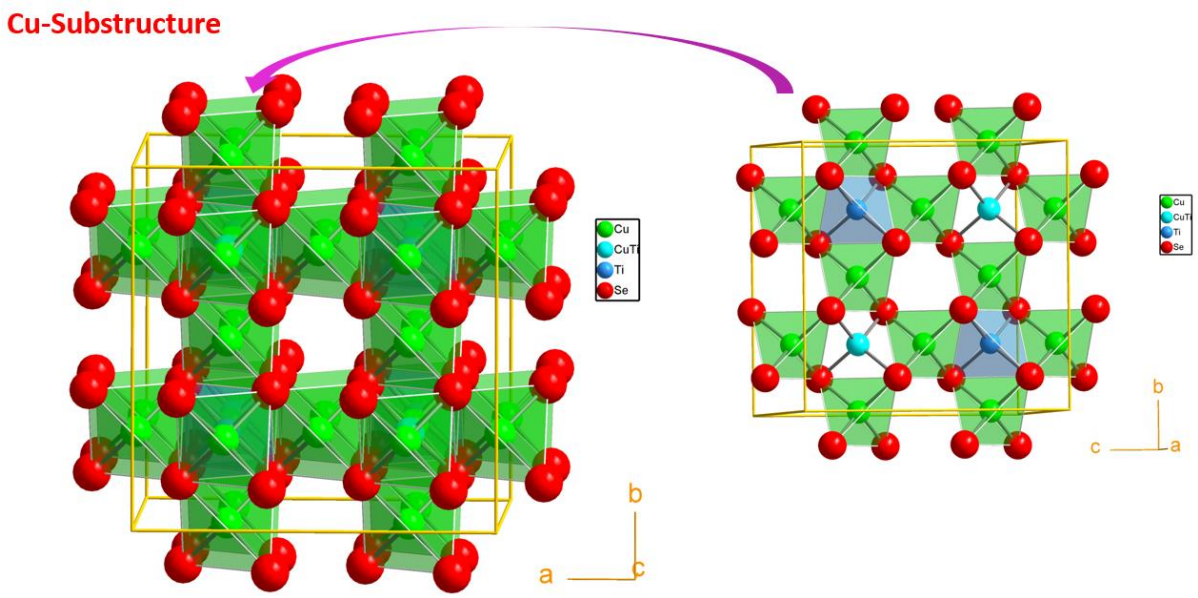

Figure 5.6.4: $Cu_3Ti_{1.25}Se_4$ Cu substructure.

Table 5.6.3: $Cu_3Ti_{1.25}Se_4$ selected inter-atomic bond distances (in Å). Operators for generating equivalent atoms: (i) 0.5-x, 0.5-y, z; (ii) 0.5-x, y, 0.5-z; (iii) x, 0.5-y, 0.5-z; (iv) z, x, y; (v) 0.5-z, 0.5-x, y; (vi) y, z, x; (vii) y, 0.5-z, 0.5-x; (viii) x, 0.5-y, -0.5-z; (ix) 0.5-x, y, -0.5-z; (x) 0.5+z, x, -0.5+y; (xi) -z, 0.5-x, -0.5+y; (xii) y, 0.5+z, -0.5+x; (xiii) y, -z, -x; (xiv) -x, y, -z; (xv) x, 1-y, -z; (xvi) -x, 1-y, z; (xvii) 1-x, 1-y, z; (xviii) 1-x, y, -z.

Atoms 1,2	**d 1,2 [Å]**	**Atoms 1,2**	**d 1,2 [Å]**
Cu1—Se1^{i}	2.4406(8)	Ti3—Se2^{xiv}	2.4586(10)
Cu1—Se1	2.4406(8)	Ti3—Se2	2.4586(10)
Cu1—Se2^{i}	2.4413(7)	Ti3—Se2^{xv}	2.4586(10)
Cu1—Se2	2.4413(7)	Ti3—Se2^{xvi}	2.4586(10)
Cu2|Ti2—Se2^{ii}	2.4324(10)	Ti4—Se1	2.4602(12)
Cu2|Ti2—Se2^{iii}	2.4324(10)	Ti4—Se1^{xv}	2.4602(12)
Cu2|Ti2—Se2^{i}	2.4324(10)	Ti4—Se1^{xvii}	2.4602(12)
Cu2|Ti2—Se2	2.4324(10)	Ti4—Se1^{xviii}	2.4602(12)
Ti1—Se1	2.4308(12)	-	-
Ti1—Se1^{viii}	2.4308(12)	-	-
Ti1—Se1^{ix}	2.4308(12)	-	-
Ti1—Se1^{i}	2.4308(12)	-	-

Additionally, the $Cu_3Ti_{1.25}Se_4$ selected interatomic bond distances are listed in **Table 5.6.3**. Cu1-Se had distances ranging from 2.406-2.4413 Å, while Cu2/Ti2-Se were consistently 2.4324 Å. Ti1-Se remained at 2.4308 Å, Ti3-Se bond distances were 2.4586 Å, and Ti4-Se were 2.4602 Å. **Table F.1** lists the anisotropic displacement parameters, and **Table F.2** shows the interatomic Se-M-Se bond angles. Interestingly, Se-Cu1-Se had some bond angles shorter than 109.5° while some were wider than expected. All other Se-M-Se bond angles (M = Cu2/Ti2, Ti1, Ti3, Ti4) were the ideal bond angle.

In order to probe the phase purity of the $Cu_2Ti_{1.5}Se_4$ powder, PXRD was implemented (**Figure 5.6.5**). The powder and pressed pellet was compared to the single crystal $Cu_3Ti_{1.25}Se_4$

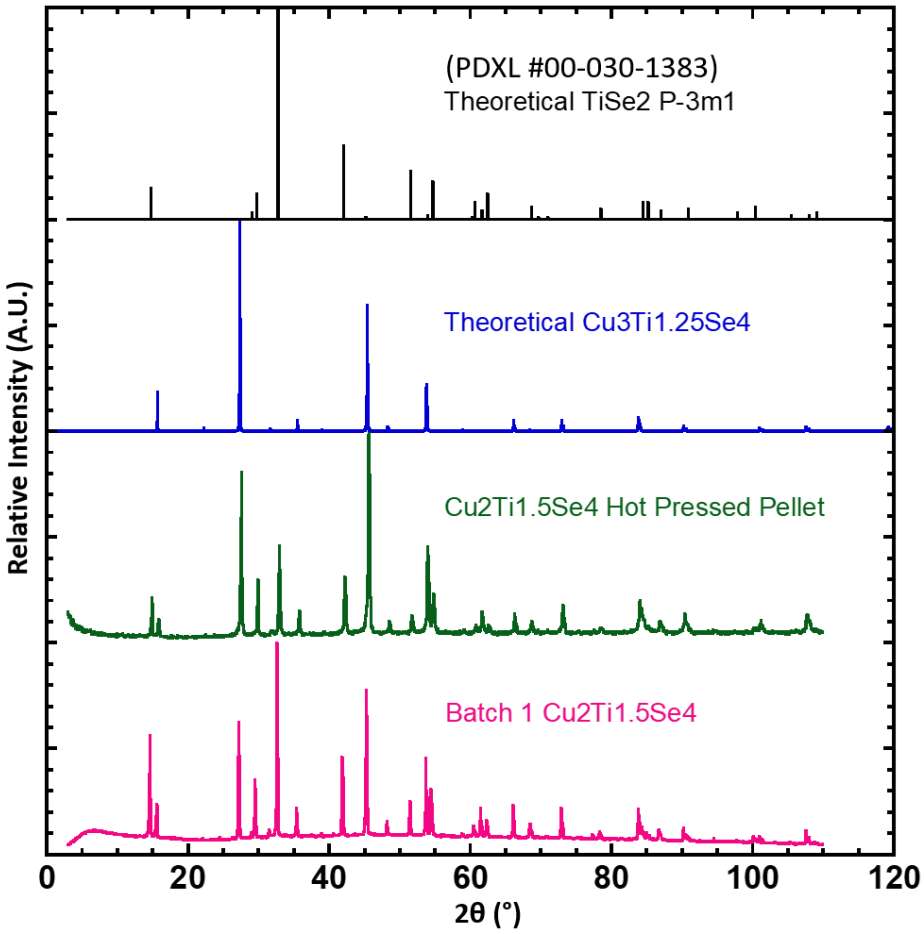

Figure 5.6.5: PXRD of $Cu_2Ti_{1.5}Se_4$, plotted against the $Cu_3Ti_{1.25}Se_4$ single crystal pattern, as well as a potential binary $TiSe_2$ P-3m1 phase (PDXL #00-030-1383[111]).

reference pattern. Also, PDXL phase analysis revealed a $TiSe_2$ P-3m1 secondary phase. So, it appears as though the $Cu_2Ti_{1.5}Se_4$ powder and pellet is a mixture of the $Cu_3Ti_{1.25}Se_4$ single crystal structure, as well as the $TiSe_2$ secondary phase. Next, DSC was implemented to analyze the thermal events in the powder, as well as the phase stability (**Figure 5.6.6**). Upon heating, a smaller event at 621.8 °C was observed, followed by the melting point at 814 °C. Upon cooling, recyrstallization was found at 806 °C, but multiple minor thermal events were also noted-i.e. the melting transition is not reversible.

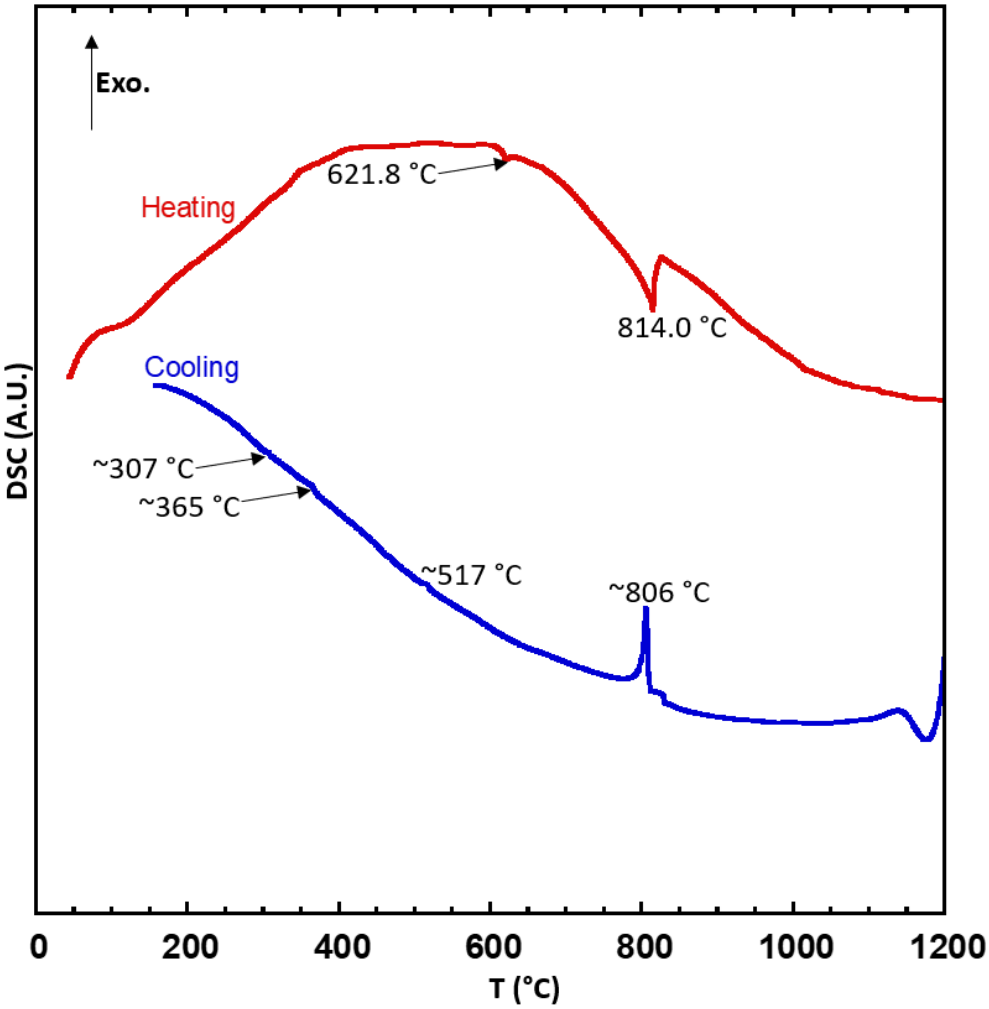

Figure 5.6.6: $Cu_2Ti_{1.5}Se_4$ DSC vs. temperature for both heating and cooling. The thermal transitions were also noted.

In order to probe the 621.8 °C thermal event further, high-T PXRD was implemented (**Figure 5.6.7**). First, the graphite dome and inconel holder was measured before powder was added. Next, a RT scan was recorded, followed by various high-T and hold time scans. Surprisingly, no changes were noted between the RT and HT scans. To analyze the $TiSe_2$ P-3m1 phase further, a Ti-Se binary phase diagram was referenced from the ASM alloy database, as seen

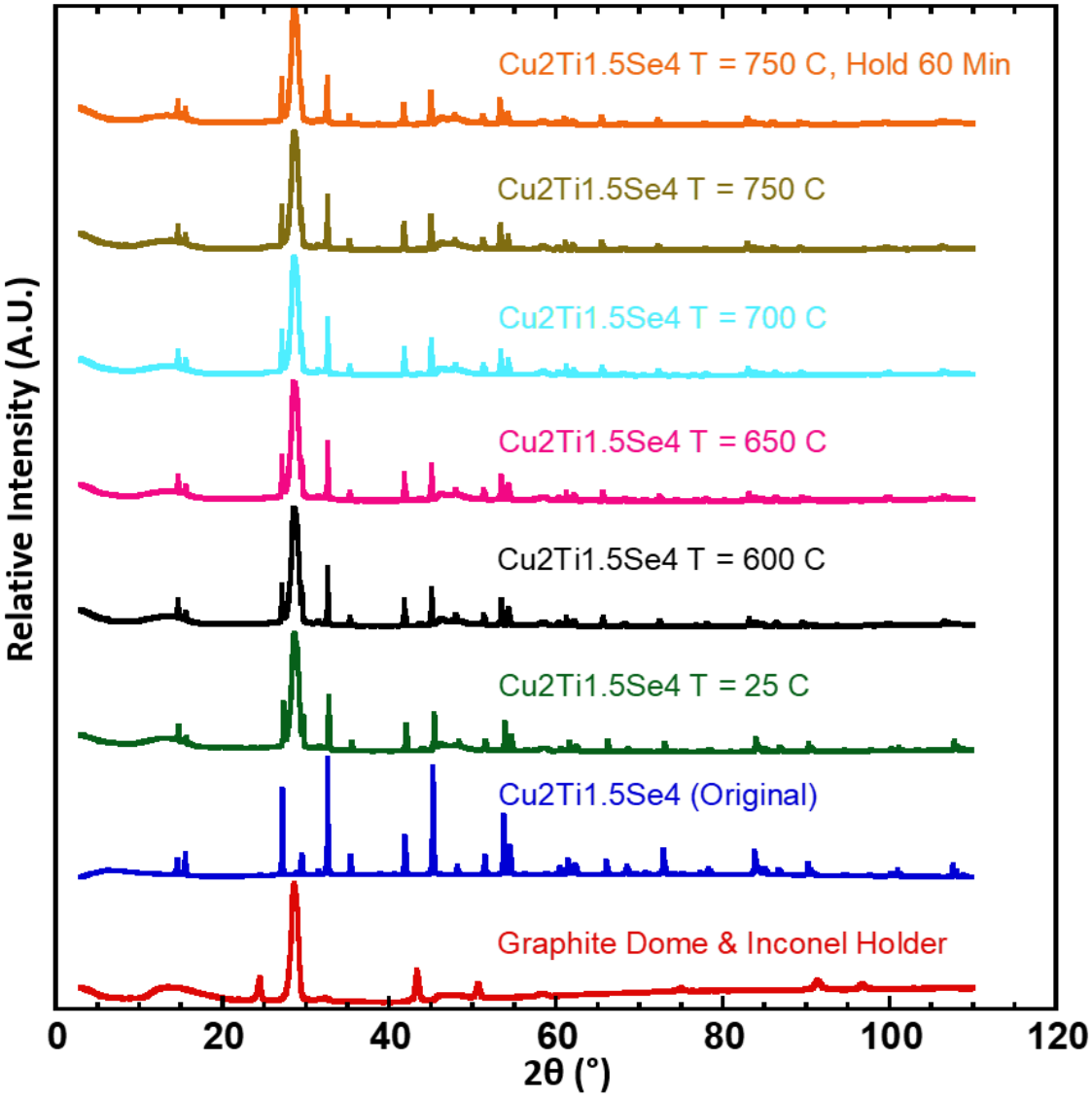

Figure 5.6.7: High-T PXRD of $Cu_2Ti_{1.5}Se_4$. First, background scans were done on just the graphite dome and Inconel holder to help identify the peaks later. Next, the powder was scanned at various temperatures and dwell times.

in **Figure F.1**. On the diagram, the two heating DSC peaks were noted, as well as the $TiSe_2$ RT P-3m1 phase. Recall that $TiSe_2$ corresponds to 33 at% Ti: toward the far-left portion of the diagram, the $TiSe_2$ phase does not appear to have any thermal events at or near the DSC peaks. Furthermore, PXRD and heating DSC plots on synthesized $TiSe_2$ powder are noted in **Figure F.2**. Up to 1200 °C, no melting peaks are noted, and no thermal events were seen at or near 621.8 °C or 814 °C. As such, the $Cu_2Ti_{15}Se_4$ heating DSC thermal events indeed belonged to the desired phase. So, the sample likely has a phase transition at 621.8 °C, followed by melting at 814 °C.

5.6.1.3 Optical Properties of $Cu_2Ti_{1.5}Se_4$

Diffuse reflectance UV-Vis-NIR spectroscopy was performed on $Cu_2Ti_{1.5}Se_4$. Later, the Kubelka-Munk equation F(R)[33] was used to transform percent reflectance data to absorption, which was then plotted as a function of energy in electron volts, eV. The left image in **Figure 5.6.8** depicts F(R) vs. wavelength. On the right, we see a plot of $[F(R)*hv]^{1/r}$ vs. energy, where r = ½ corresponds to a direct bandgap E_g. To determine E_g, an absorption edge tangent line was extrapolated to the x-axis; the intercept with the x-axis corresponded to E_g. The direct bandgap was found to be 2.75 eV, corresponding to a maximum absorbed wavelength (λ_{Max}) of ~451 nm. As such, $Cu_2Ti_{1.5}Se_4$ can absorb in the UV and a portion of the visible spectrum (violet and blue). However, visible colors such as blue-cyan, cyan, green, yellow, orange, and red will not be absorbed. Additionally, the whole NIR/IR portion of the solar spectrum would be too low in energy as well. See **Figure 1.3.4** to reference the solar spectrum.

Now, in order to be complete in the optical analysis, one must consider the effect of the $TiSe_2$ P-3m1 secondary phase. According to Gaby *et al*., $TiSe_2$ is actually a semimetal with a band overlap of 0.2 eV.[112] As such, the recorded E_g value for $Cu_2Ti_{1.5}Se_4$ must be the true value.

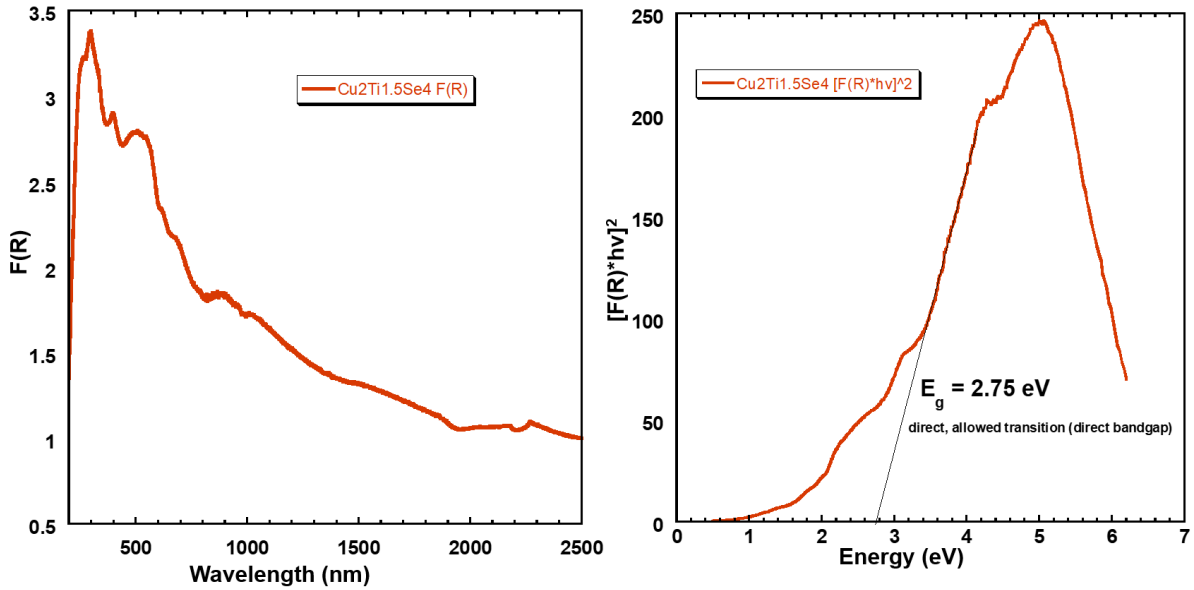

Figure 5.6.8: (Left): UV-Vis-NIR diffuse reflectance Tauc plot analysis. The Kubelka-Munk function F(R) was used to transform the reflectance data to absorbance. Plot of F(R) vs. wavelength. **(Right):** Plot of $[F(R)*h\nu]^{1/r}$ vs. energy; r = ½ was chosen here to signify a direct, allowed transition (direct bandgap). To determine the direct optical bandgap (E_g), an absorption edge tangent line was extrapolated to the x-axis; the intercept with the x-axis corresponds to E_g.

5.6.2 Conclusion & Future Work: $Cu_2Ti_{1.5}Se_4$ (x = 0):

In order to grow single crystals, $Cu_2Ti_{1.5}Se_4$ powder was reacted via a dual-zone furnace method, where T_{Hot} = 720 °C and T_{Cold} = 520 °C. Surprisingly, structure refinement revealed that $Cu_3Ti_{1.25}Se_4$ single crystals were grown-slightly Cu-rich and Ti-poor when compared to the powder formula. As such, $Cu_3Ti_{1.25}Se_4$ must be the more stable stoichiometry. The $Cu_3Ti_{1.25}Se_4$ single crystals appeared black in color and faceted. $Cu_3Ti_{1.25}Se_4$ was found to crystallize in the cubic F-43m space group (#216), with a lattice parameter of a = 11.2954 Å. In the structure, Cu1 is highly ordered, having only ~1/8 total vacancy. Cu2/Ti2 actually share the same 4c site, with a total tetrahedral site vacancy of ~1/8. Ti1, Ti3, and Ti4 possess their own positions with varying vacancy levels: ~1/8, ~4/8, and ~2/8, respectively. All metal positions coordinated in a tetrahedral coordination; further visual analysis of the crystal revealed substructures of Ti and Cu, where either sublattice filled the empty channels of the other. A mixture of edge and corner sharing was observed. Between the various MSe_4 tetrahedra. Cu1-Se had distances ranging from 2.406-2.4413 Å, while Cu2/Ti2-Se were consistently 2.4324 Å. Ti1-Se remained at 2.4308 Å, Ti3-Se bond distances were 2.4586 Å, and Ti4-Se were 2.4602 Å. Interestingly, Se-Cu1-Se had some bond angles shorter than 109.5° while some were wider than expected. All other Se-M-Se bond angles (M = Cu2/Ti2, Ti1, Ti3, Ti4) were the ideal bond angle.

To verify the phase purity of the $Cu_2Ti_{1.5}Se_4$ powder, PXRD was used, and the powder was plotted against the $Cu3Ti_{1.25}Se_4$ pattern. PDXL phase analysis revealed a significant binary phase of $TiSe_2$ P-3m1. Upon further investigation, the powder appeared to be a mix of the $Cu_3Ti_{1.25}Se_4$ and $TiSe_2$ P-3m1 phases. DSC revealed a small transition at 621.8 °C, followed by melting at 814 °C. Cooling DSC noted multiple peaks, signs of thermal instability after melting. High-T PXRD did not notice any changes between RT and HT scans. Consulting the Ti-Se binary phase diagram,

as well as the powder $TiSe_2$ DSC curves did not have any thermal transitions correlating to the $Cu_2Ti_{1.5}Se_4$ DSC. So, 621.8 °C and 814 °C must be a $Cu_2Ti_{1.5}Se_4$ phase transition and melting point, respectively.

Diffuse reflectance UV-Vis-NIR spectroscopy was used to analyze the optical properties of the sample, and the Kubelka-Munk function and Tauc plot analysis was applied to gather the direct optical bandgap, E_g. The analysis revealed that $E_g = 2.75$ eV, corresponding to a λ_{Max} of 451 nm; so, the material would absorb in the UV, and visible for violet and blue. For reference, the binary $TiSe_2$ P-3m1 phase is a semimetal with a band overlap of 0.2 eV. So, the measured bandgap indeed belongs to $Cu_2Ti_{1.5}Se_4$.

In the future, since there was a large $TiSe_2$ P-3m1 phase found in the powder sample, the synthesis conditions of $Cu_2Ti_{1.5}Se_4$ needs to be further optimized. One possible route is growing large amounts of $Cu_2Ti_{1.5}Se_4$ single crystals via the dual-zone process and crushing that into powder for the various measurements. Since the crystals were irregular in shape and dark, isolating some candidate $Cu_2Ti_{1.5}Se_4$ single crystals and analyzing the stoichiometry via EDX or XRF would be recommended, as this could aid in selecting the proper crystals. Once successfully synthesized, repeating the characterization sweep such as PXRD, DSC, optical bandgap, and thermoelectric measurements would be suggested.

5.7 $Cu_2Mn_3Se_4$ Single Crystal Synthesis ($Cu_2Mn_3Se_4$), Structural Properties, Optical Properties, and Predicted Magnetic Moment

5.7.1 Results & Discussion: $Cu_2Mn_3Se_4$:

5.7.1.1 Single Crystal Synthesis ($Cu_2Mn_3Se_4$)

In order to grow single crystals, $Cu_2Mn_3Se_4$ powder was reacted via a dual-zone furnace method. The hot thermocouple was set to 450 °C, while the cold thermocouple was set to 250 °C. The sample powder end of the tube was aligned at the hot thermocouple side, with the temperature gradient causing crystals to form on the cold end of the tube via a temperature-assisted vapor transport mechanism. See **Section 5.2**, **Figure 5.2.1**, and **Figure 5.2.2** for more details. The left image in **Figure 5.7.1** is the reacted $Cu_2Mn_3Se_4$ powder, appearing blue-grey in color. The right image depicts a $Cu_2Mn_3Se_4$ single crystal mounted on a glass fiber, appearing black in color and faceted.

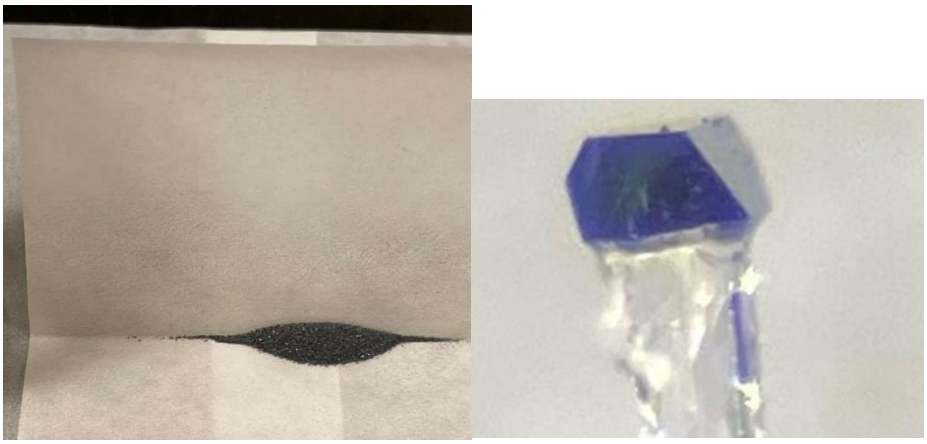

Figure 5.7.1: Left: $Cu_2Mn_3Se_4$ powder after reaction and being ground. Photograph was taken using an Apple iPhone 11 Pro Max camera (12 MP). **Right:** $Cu_2Mn_3Se_4$ single crystal mounted on the tip of a glass fiber for single crystal XRD analysis. Image was recorded using a Leica S6E stereo microscope equipped with a Leica L2 light source at 4x zoom. Image was captured through the lenspiece with an Apple iPhone 11 Pro Max 2x telephoto optical zoom lens (12-megapixel), giving a total of ~8x magnification.

5.7.1.2 Structural Properties of $Cu_2Mn_3Se_4$

The structure of $Cu_2Mn_3Se_4$ single crystals were analyzed using single-crystal XRD and structure refinement. It was revealed that the $Cu_2Mn_3Se_4$ crystals had both a small cell and a 2x2x2 supercell, i.e. large cell. The SC crystallizes in the cubic Fm-3m (#225) space group, with a lattice parameter of a = 5.7454 Å. As for LC, it possessed a cubic Fd-3m (#227) space group with a lattice parameter of a = 11.4932 Å. The selected crystal data is seen in **Table 5.7.1**.

Table 5.7.1: Selected crystallographic data for $Cu_2Mn_3Se_4$.

Cell Type	Small Cell	Large Cell
Formula	$Cu_2Mn_3Se_4$	$Cu_2Mn_3Se_4$
Crystal system	Cubic	Cubic
Space group	$Fm\bar{3}m$ (#225)	$Fd\bar{3}m$ (#227)
a = b = c (Å)	5.7454(7)	11.4932(13)
$\alpha = \beta = \gamma$ (°)	90	90
V (Å^3)	189.65(4)	1518.18(30)
Formula Mass (g/mol)	607.74	607.74
ρ (g/cm^3)	5.32084	5.31751
Z	1	8
Temperature (K)	300	300
R_{All}	0.0432	0.057
R_{int}	0.1799	0.1918
$R_1(F_o > 4\sigma(F_o))$	0.0411	0.0569
wR_2 (all)	0.0985	0.1137
GooF	1.395	1.461

The SC and LC atomic coordinates, isotropic displacement parameters and site occupancies are listed in **Table 5.7.2** and **Table 5.7.3**, respectively. For SC, Mn1 and Cu1 were found to share the 8c position, with a total site vacancy of 3/8. The 2x2x2 supercell was able to resolve the Cu and Mn, now occupying separate sites. In LC, with Cu3 sitting at the 16c site with 100% occupancy; Cu4 was found at the 16d site, also possessing 100% site occupancy; Mn5 had 50% occupancy,

corresponding to a 4/8 tetrahedral site vacancy. So, the 2x2x2 supercell ordered the crystal quite well.

Table 5.7.2: $Cu_2Mn_3Se_4$ Small Cell atomic coordinates, equivalent isotropic displacement parameters $U_{eq.}$, and occupancies for all atoms.

$Cu_2Mn_3Se_4$-small cell							
Atom	**Wyck.**	**S.O.F.**	**Vac.**	**x**	**y**	**z**	**$U_{eq.}$ ($Å^2$ x 10^{-4})**
Mn1	8c	0.38	62%	0.25	0.25	0.25	306.7(8)
Cu1	8c	0.25	25%	0.25	0.25	0.25	306.7(8)
Se2	4b	1	-	0.5	0	0	308.4(8)

Table 5.7.3: $Cu_2Mn_3Se_4$ Large Cell atomic coordinates, equivalent isotropic displacement parameters $U_{eq.}$, and occupancies for all atoms.

$Cu_2Mn_3Se_4$-large cell							
Atom	**Wyck.**	**S.O.F.**	**Vac.**	**x**	**y**	**z**	**$U_{eq.}$ ($Å^2$ x 10^{-4})**
Se1	8b	1	-	0	0.5	0	234.4(30)
Se2	8a	1	-	0.5	0.5	0	355.4(41)
Cu3	16c	1	0%	0.625	0.625	0.125	1880.4(378)
Cu4	16d	1	0%	0.125	0.625	0.125	894(216)
Mn5	96g	0.5	50%	0.88723(1)	0.625	0.125	*34.9(23)

SC and LC crystal projections along the a-direction are found in **Figure 5.7.2** and **Figure 5.7.3**. For SC, note the mixed Cu/Mn atomic site. In LC, the 2x2 grid was overlaid; also note that the Cu and Mn now occupy separate sites. In **Figure 5.7.4** and **Figure 5.7.5**, the tetrahedra were added for all metal sites for SC and LC, projecting each crystal along the a-direction rotated.

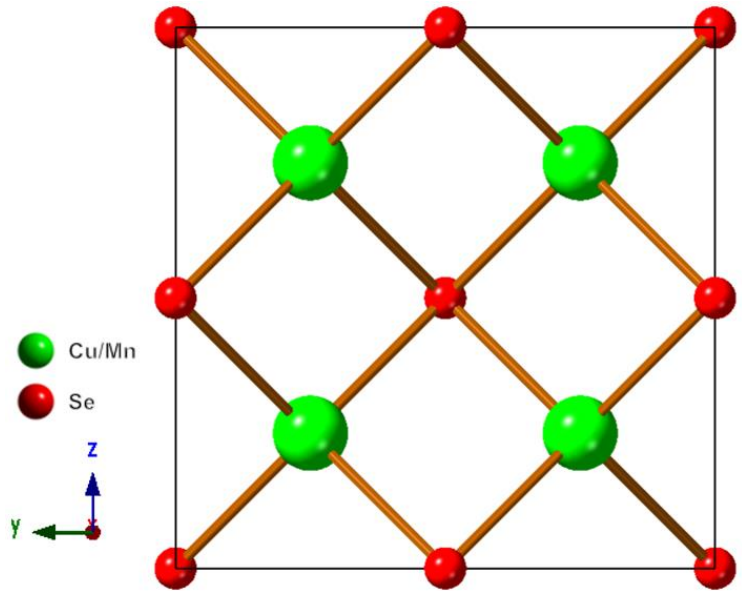

Figure 5.7.2: $Cu_2Mn_3Se_4$ Small Cell crystal projection along the a-direction.

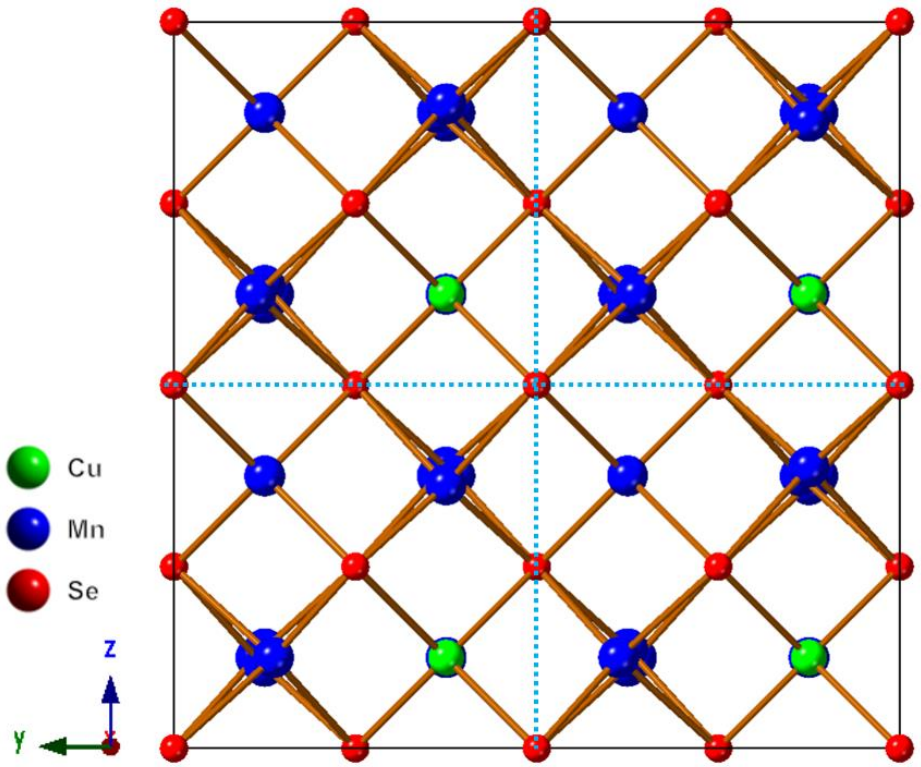

Figure 5.7.3: $Cu_2Mn_3Se_4$ Large Cell crystal projection along the a-direction. The blue dotted lines were overlayed to depict the 2x2 supercell. Each square represents the small cell.

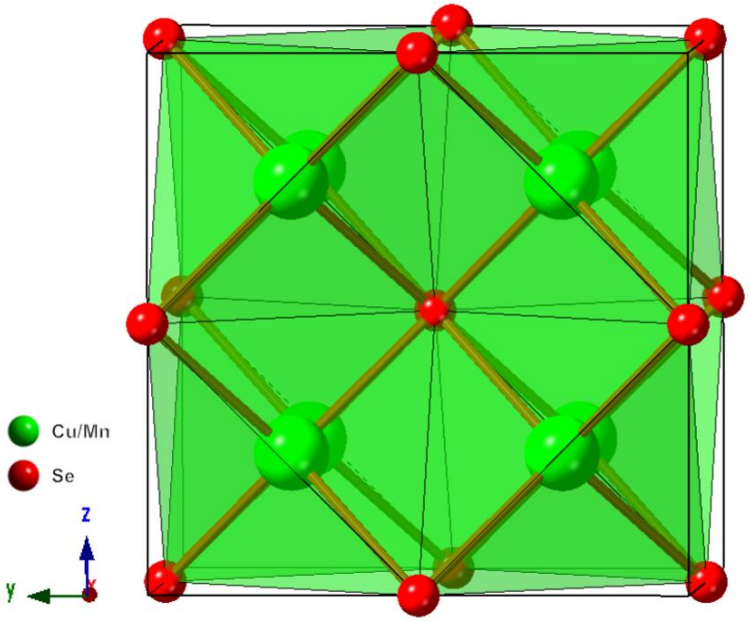

Figure 5.7.4: $Cu_2Mn_3Se_4$ Small Cell crystal projection along the a-direction, rotated, with all polyhedra.

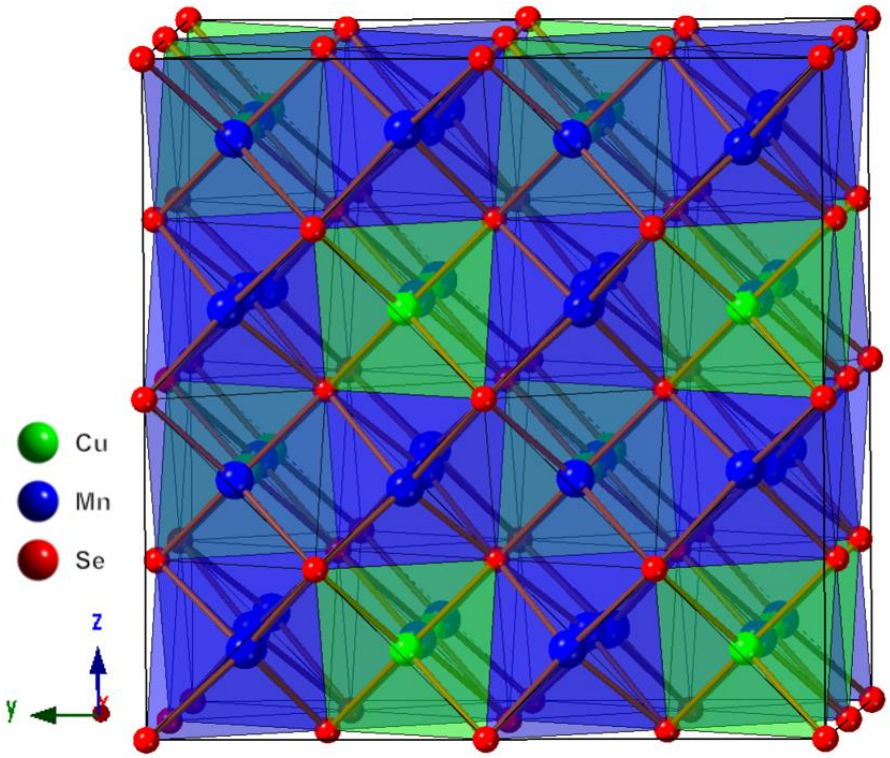

Figure 5.7.5: $Cu_2Mn_3Se_4$ Large Cell crystal projection along the a-direction, rotated, with all polyhedra.

To analyze the M-M distances, tetrahedral metal chains were drawn for SC and LC in **Figure 5.7.6** and **Figure 5.7.7**. For SC, the Cu/Mn-Cu-Mn distances were 2.873 Å. For LC, the Mn-Mn distance ranged from 3.865-4.262 Å.

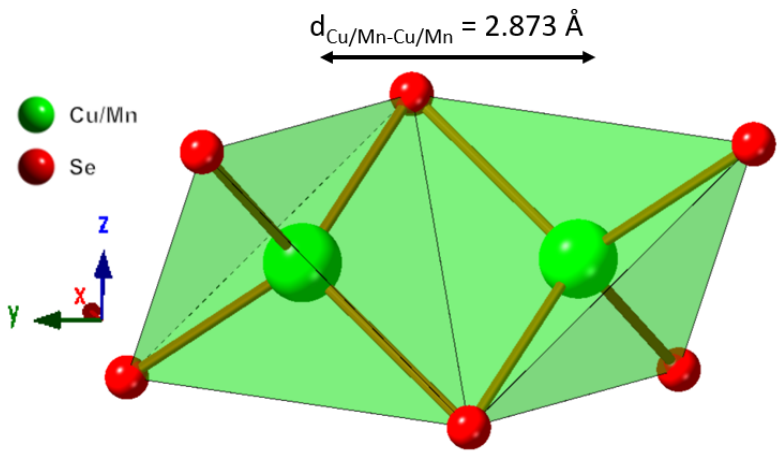

Figure 5.7.6: $Cu_2Mn_3Se_4$ Small Cell a-direction rotated, Mn-Mn chain with distances between metal ions noted.

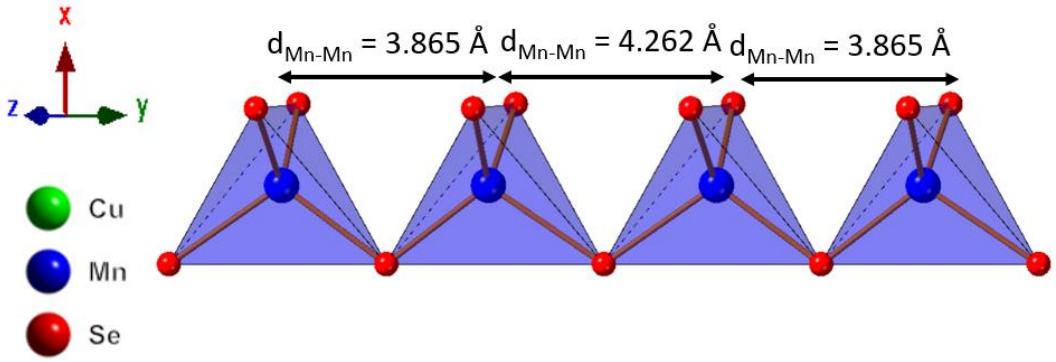

Figure 5.7.7: $Cu_2Mn_3Se_4$ Large Cell a-direction, rotated Mn-Mn chain, with distances between metal ions noted.

The M-Se bond distances for SC and LC are seen in **Table 5.7.4** and **Table 5.7.5**. For SC, the Mn1/Cu1-Se bond distance was uniformly 2.4878 Å. For LC, the Cu3-Se and Cu4-Se distance was 2.4884 Å. However, Mn5-Se1 had a shorter bond distance than Mn5-Se2-2.410 Å and 2.572 Å, respectively. The SC and LC anisotropic displacement parameters are listed in **Table G.1**

Table 5.7.4: $Cu_2Mn_3Se_4$ Small Cell selected inter-atomic bond distances (in Å). Small cell operators for generating equivalent atoms: (i) x, 0.5+y, 0.5+z; (ii) -0.5+x, 0.5+y, z; (iii) -0.5+x, y, 0.5+z; (iv) -x, 0.5-y, 0.5-z; (v) 0.5-x, 1-y, 0.5-z; (vi) 0.5-x, 0.5-y, -z; (vii) 0.5-x, 0.5-y, 1-z; (viii) 1-x, 0.5-y, 0.5-z; (ix) 0.5-x, -y, 0.5-z; (x) x, -0.5+y, -0.5+z; (xi) 0.5+x, -0.5+y, z; (xii) 1-x, -y, -z; (xiii) 0.5+x, y, -0.5+z.

$Cu_2Mn_3Se_4$-Small Cell	
Atoms 1,2	**d 1,2 [Å]**
Mn1/Cu1—Se2^{i}	2.4878(3)
Mn1/Cu1—Se2^{ii}	2.4878(3)
Mn1/Cu1—Se2^{iii}	2.4878(3)
Mn1/Cu1—Se2	2.4878(3)

Table 5.7.5: $Cu_2Mn_3Se_4$ Large Cell selected inter-atomic bond distances (in Å). Large cell operators for generating equivalent atoms: (i) 0, 0z, 0; (ii) -0.5+y, 0.5+z, -1+x; (iii) y, 1.5+z, 0.5+x; (iv) -1+x, y, z; (v) 1+y, 1-z, -x; (vi) z, -0.5+x, -0.5+y; (vii) y, 1-z, -x; (viii) 0, 0, 0; (ix) 1.25-y, 1.25+x, 0.25+z; (x) -0.5-y, -1-x, 0.5+z; (xi) x, 1.5+z, 0.5+y; (xii) 0, 0, 0; (xiii) 0, 0, 0; (xiv) 0.25+x, 1.25-z, 0.25+y; (xv) 1.25+z, 0.25+y, 0.25-x; (xvi) y, 0.5+z, -0.5+x; (xvii) 0.5+z, x, -0.5+y; (xviii) 0.25-y, 1.25+x, 0.25+z; (xix) 0.25+z, 0.25+y, 0.25-x; (xx) 0.75+z, 0.25+x, 1.75-y; (xxi) 0, 0, 0; (xxii) 1.25+x, 1.25-z, 0.25+y; (xxiii) 1+x, y, z; (xxiv) 0, 0, 0; (xxv) 1+y, 1.5+z, 0.5+x; (xxvi) 0.25-z, 1.25-y, -0.75-x; (xxvii) 1-y, -0.5+z, -0.5-x.

$Cu_2Mn_3Se_4$-large cell	
Atoms 1,2	**d 1,2 [Å]**
Cu3—Se2^{xiv}	2.4884(3)
Cu3—Se2^{xv}	2.4884(3)
Cu3—Se2^{ix}	2.4884(3)
Cu4—Se1^{xiv}	2.4884(3)
Cu4—Se1^{xviii}	2.4884(3)
Cu4—Se1^{xix}	2.4884(3)
Mn5—Se1^{xxii}	2.410(8)
Mn5—Se1^{xxiii}	2.410(8)
Mn5—Se2^{xv}	2.572(9)
Mn5—Se2^{ix}	2.572(9)

and **Table G.2**. The Se-M-Se bond angles for SC and LC are depicted in **Table G.3** and **Table G.4**. In the case of SC, all Se-Mn1/Cu1-Se bond angles are 109.5°. All LC Se-Cu3-Se and Se-Cu4-Se bond angles were also 109.5°. However, in the case of Se-Mn5-Se, there was much

tetrahedral bond angle variation. Se1-Mn5-Se2 bond angles were consistently 109.26°, close to the expected tetrahedral angle. However, Se1-Mn5-Se1 had a much larger than expected angle of 114.9°, while Se2-Mn5-Se2 had a narrow angle of 104.4°. **Figure 5.7.8** and **Figure 5.7.9** depict a single Cu1/Mn1 and Mn5 tetrahedron for SC and LC, respectively. The atomic labels, bond angles, and bond distances were noted.

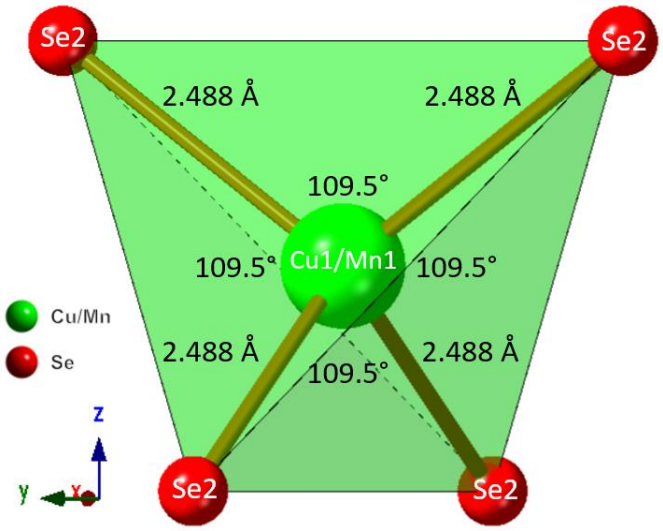

Figure 5.7.8: $Cu_2Mn_3Se_4$ Small Cell single Cu/Mn tetrahedron. Note that all bond angles are what is expected: 109.5°. Additionally, all Cu1/Mn1-Se bond distances are regular.

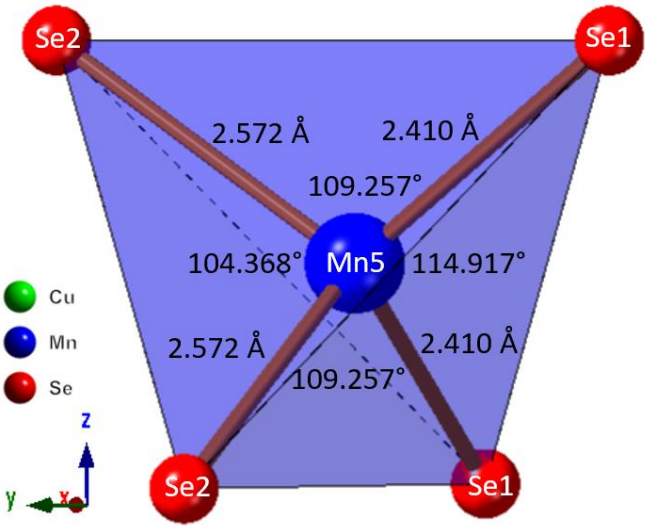

Figure 5.7.9: $Cu_2Mn_3Se_4$ Large Cell single Mn tetrahedron. Note that some bond angles are smaller than 109.5°, while other bond angles are larger than 109.5°. Also, all Mn5-Se1 bond distances are shorter at 2.410 Å, while the Mn5-Se2 bond distances are longer at 2.572 Å.

To analyze the phase purity of the powder $Cu_2Mn_3Se_4$, PXRD was utilized (**Figure 5.7.10**). The powder was plotted against both the SC and LC patterns. PDXL phase analysis identified two extra phases present: MnSe Fm-3m and Cu_3Se_2 P-421m. Upon inspection, MnSe Fm-3m does indeed appear to be the dominate phase, with the rest of the peaks beint either the $Cu_2Mn_3Se_4$ phase or Cu_3Se_2 P-421m. To probe the thermal events, DSC was applied upon heating and cooling,

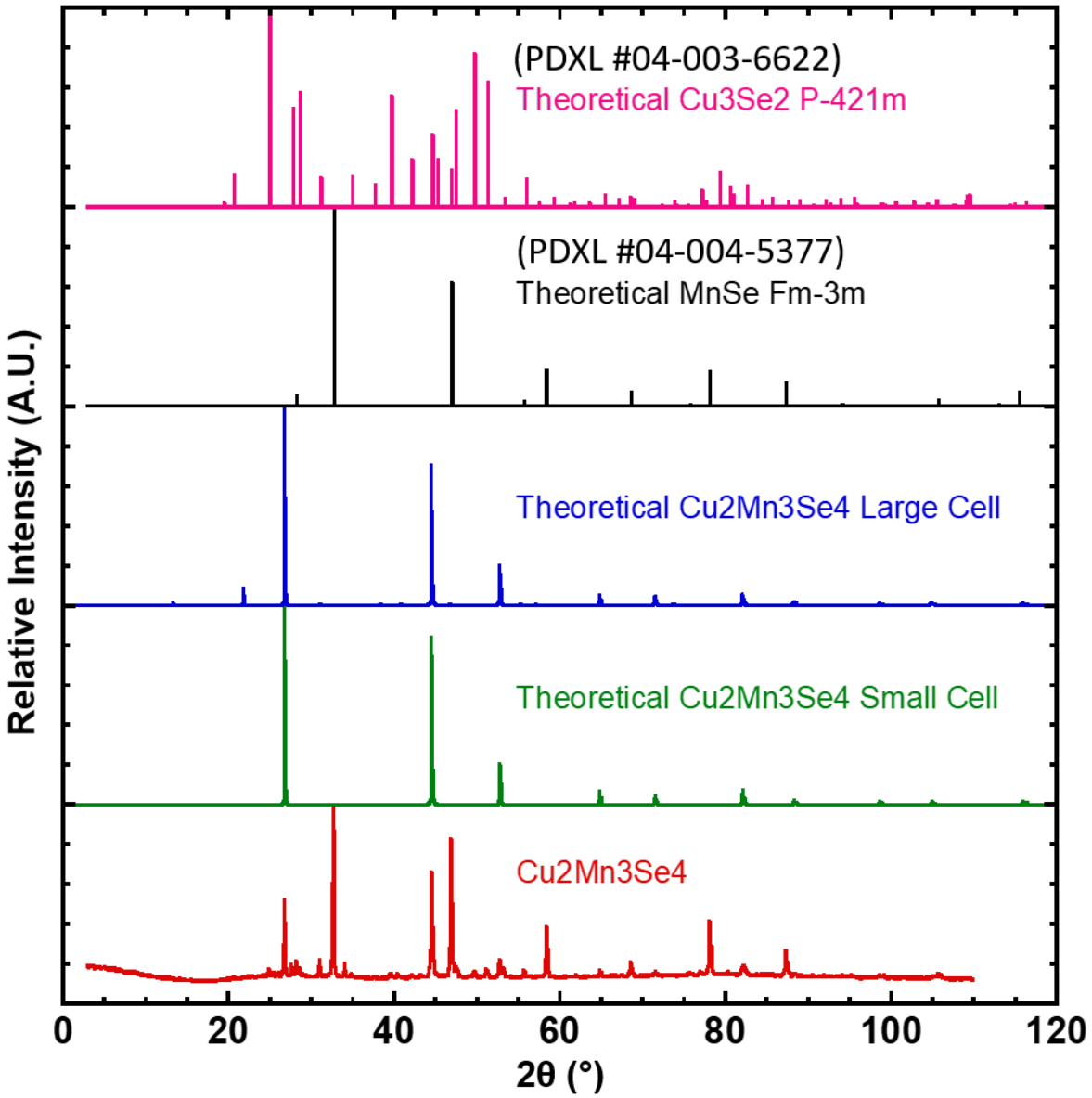

Figure 5.7.10: PXRD of $Cu_2Mn_3Se_4$, plotted against the small cell and large cell patterns, as well as a potential binary phases of MnSe Fm-3m (PDXL #04-004-5377[113]) and Cu_3Se_2 P-421m (PDXL #04-003-6622[114]).

as seen in **Figure 5.7.11**. Upon heating, a single melting peak was observed at 550.2 °C. Based on the cooling curve, the sample appeared to have decomposed after melting, as multiple thermal events are observed. To assist in the identification of the heating thermal event, Mn-Se and Cu-Se binary phase diagrams were referenced. For the Mn-Se diagram (**Figure G.1**), the 550.2 °C heating DSC peak was noted, as well as the MnSe Fm-3m phase. At T = 675 °C, MnSe Fm-3m is seen to decompose into a $MnSe_2$ RT Pa-3 phase, which then melts at that same temperature. Now,

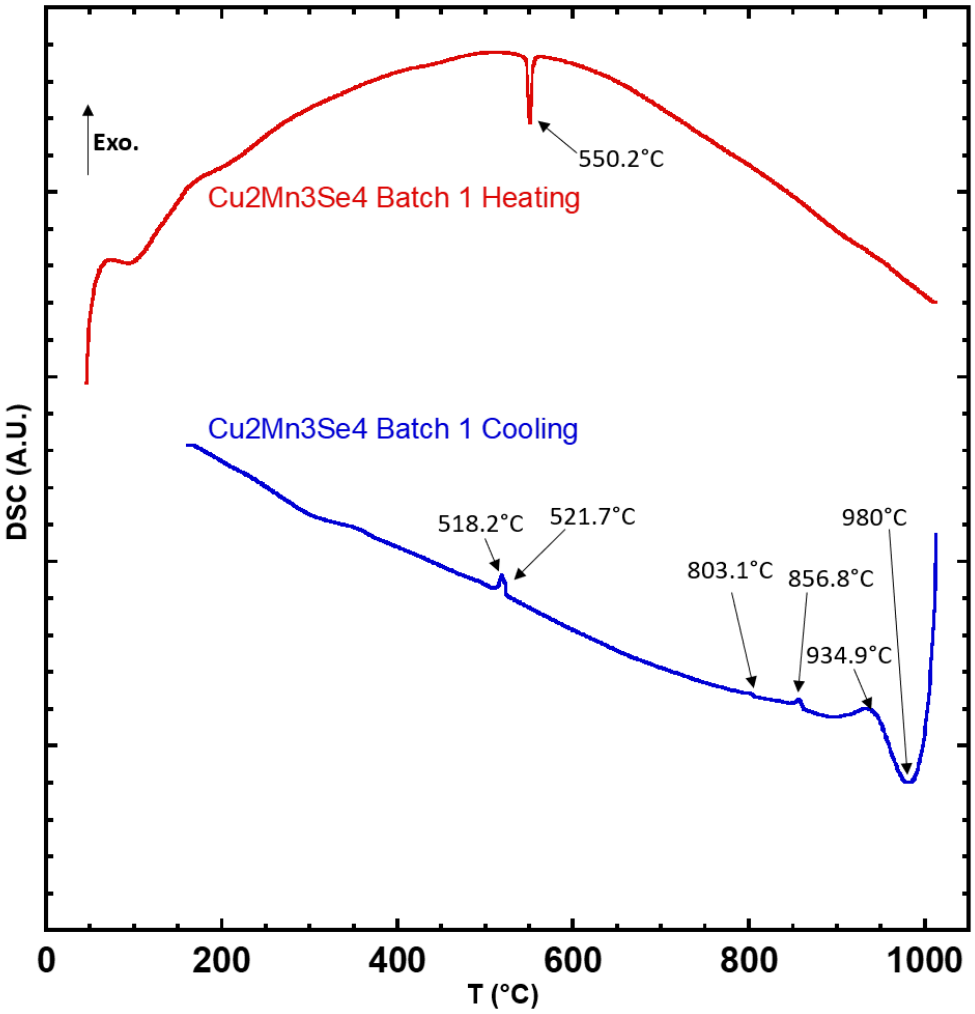

Figure 5.7.11: $Cu_2Mn_3Se_4$ DSC vs. temperature for both heating and cooling. The thermal transitions were also noted.

in the Cu-Se binary phase diagram (**Figure G.2**), the 550.2 °C heating DSC peak was noted, as well as the Cu_3Se_2 RT P-421m phase. For Cu_3Se_2, multiple low-T thermal events are observed-at 50 °C and 135 °C. Referring back to the DSC curve (**Figure 5.7.11**), upon heating only one peak was noted at 550.2 °C. So, Cu_3Se_2 cannot be the culprit. Thus, the 550.2 °C thermal event corresponds to MnSe decomposing to $MnSe_2$, which then melts at the same temperature.

5.7.1.3 Optical Properties of $Cu_2Mn_3Se_4$

Diffuse reflectance UV-Vis-NIR spectroscopy was performed on $Cu_2Mn_3Se_4$. Later, the Kubelka-Munk equation F(R)[33] was used to transform percent reflectance data to absorption, which was then plotted as a function of energy in electron volts, eV. The left image in **Figure 5.7.12** depicts F(R) vs. wavelength. On the right, we see a plot of $[F(R)*h\nu]^{1/r}$ vs. energy, where r = ½ corresponds to a direct bandgap E_g. To determine E_g, an absorption edge tangent line was extrapolated to the x-axis; the intercept with the x-axis corresponded to E_g. The direct bandgap was found to be 1.36 eV, corresponding to a maximum absorbed wavelength (λ_{Max}) of ~912 nm. As such, $Cu_2Mn_3Se_4$ can absorb in the UV, Visible, and a small portion of the NIR. However, most of the IR spectrum will be too low in energy to be absorbed. See **Figure 1.3.4** to reference the solar spectrum.

Now, in order to be complete in the optical analysis, one must consider both secondary phases identified via PDXL: MnSe Fm-3m and Cu_3Se_2 P-421m. For MnSe Fm-3m, Thanigaimani *et al*. reported the thin film direct bandgap to be ~1.12 eV.[115] Now, Cu_3Se_2 P-421m has a film direct bandgap of 1.91-2.01 eV.[116] Note that the $Cu_2Mn_3Se_4$ direct bandgap was found to be 1.36 eV, relatively close to the value reported for MnSe Fm-3m. Based on the PXRD shown in **Figure 5.7.10**, MnSe Fm-3m is indeed the dominant phase in the experimental pattern, with Cu_3Se_2 P-421m contributing a smaller amount to the pattern. So, most likely the calculated bandgap is a result of some fractional contribution from both MnSe Fm-3m and Cu_3Se_2 P-421m (to a lesser extent).

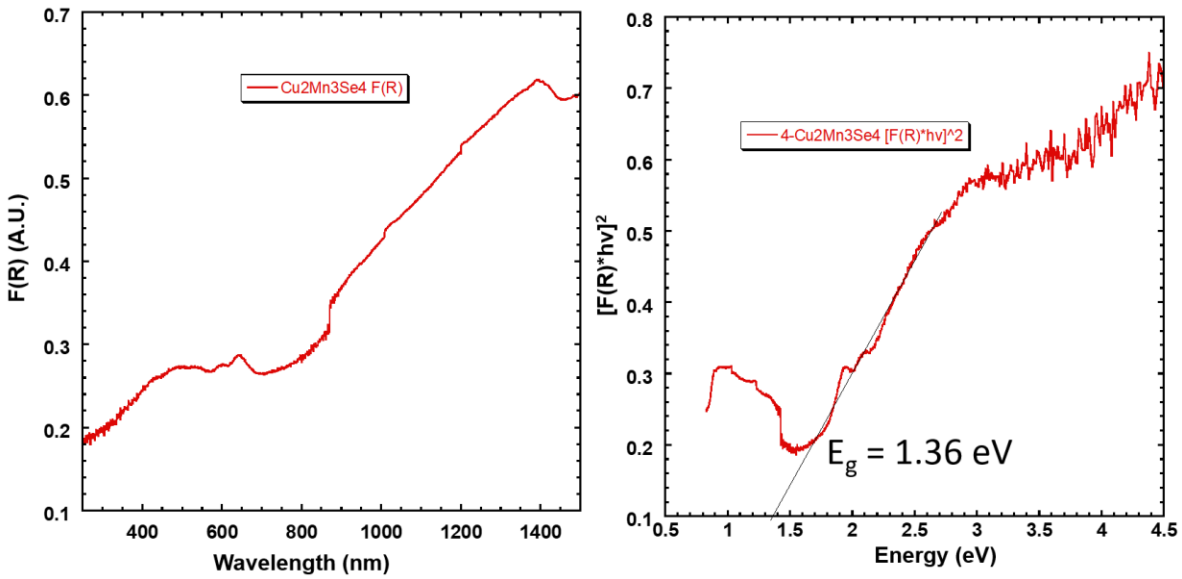

Figure 5.7.12: (Left): UV-Vis-NIR diffuse reflectance Tauc plot analysis. The Kubelka-Munk function F(R) was used to transform the reflectance data to absorbance. Plot of F(R) vs. wavelength. **(Right):** Plot of $[F(R)*h\nu]^{1/r}$ vs. energy; r = ½ was chosen here to signify a direct, allowed transition (direct bandgap). To determine the direct optical bandgap (E_g), an absorption edge tangent line was extrapolated to the x-axis; the intercept with the x-axis corresponds to E_g.

5.7.1.4 Predicted Magnetic Moment of $Cu_2Mn_3Se_4$

Due to the fact that Mn^{2+} [Ar]$3d^5$ is found in this $Cu_2M_3Se_4$ iteration, there is a possibility of generating antiferromagnetic ordering in the compound. From **Figure 5.7.6** and **Figure 5.7.7**, we can see that the Mn^{2+} forms $MnSe_4$ tetrahedra, where along certain directions the $Cu_2Mn_3Se_4$ large cell has Mn-Mn chains. As such, it is worthwhile to predict the magnetic moment of the compound. Based on crystal field theory, the tetrahedral Se^{2-} ligand geometry would split the degenerate Mn^{2+} 3d orbitals into a doublet and a higher energy triplet state, as seen in **Figure 5.7.13**. According to the spectrochemical series (**Figure 5.7.14**), Se^{2-} is a weak-field ligand (same column as S^{2-}), filling the Mn $3d^5$ electrons in a high-spin fashion. Based on quantum numbers and Hund's rules, the theoretical magnetic moment can be predicted (**Appendix H**). For Mn^{2+} high-spin in a tetrahedral arrangement, $\mu_{theo} = 5.92\mu_B$.

Furthermore, recall that **Figure 5.7.8** and **Figure 5.7.9** depict a single Cu1/Mn1 and Mn5 tetrahedron for SC and LC, respectively. In the SC case, Mn-Se bond distances are regular, and all bond angles are the ideal tetrahedral angle. However, in the LC case, both the bond distances and bond angles are irregular. The Mn5-Se1 bond distances are shorter than the Mn5-Se2 bond distances. The Se2-Mn5-Se1 bond angles were close to ideal: 109.257°. However, the Se2-Mn5-Se2 bond angle was much smaller, at 104.368°; the Se1-Mn5-Se1 bond angle was much larger than expected, at 114.917°. Distortions in the $Cu_2Mn_3Se_4$ large cell tetrahedral bond lengths and bond angles may cause additional intriguing magnetic phenomena. For example, due to the distortions, the experimental magnetic moment may deviate from the theoretical predictions.

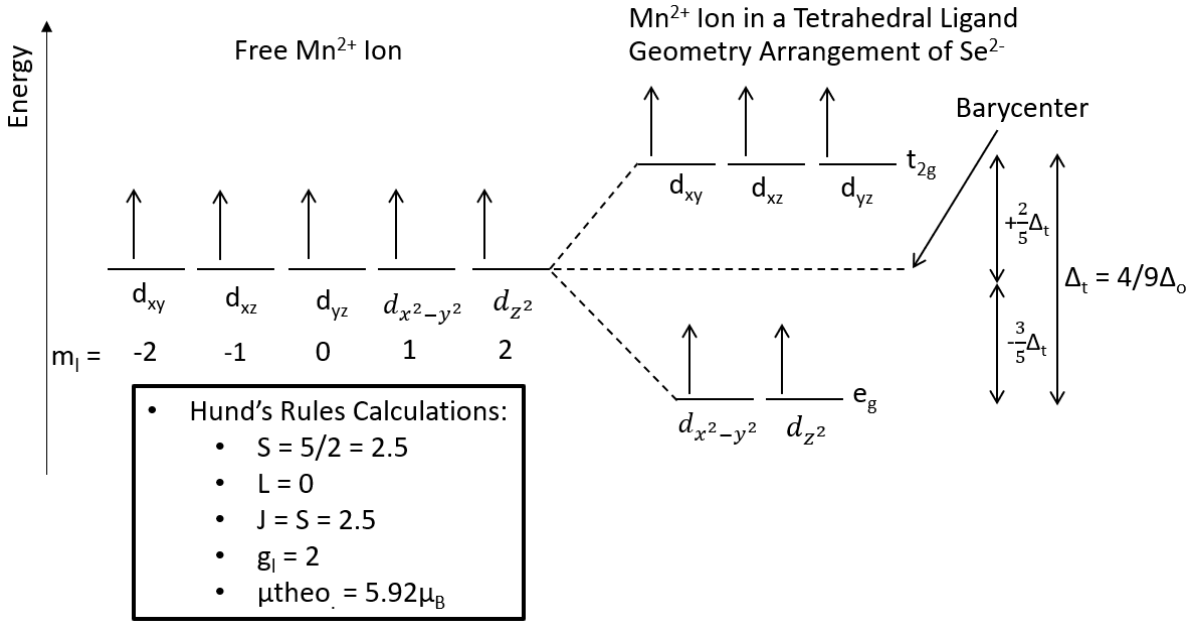

Figure 5.7.13: Predicting the Mn^{2+} [Ar]$3d^5$ theoretical magnetic moment in a tetrahedral Se^{2-} ligand geometry using Hund's rules and crystal-field theory.

$I^- < Br^- < S^{2-} < SCN^- < Cl^- < NO_3^- < N_3^- < F^- < OH^- < C_2O_4^{2-} < H_2O < NCS^- < CH_3CN < py < NH_3$

$< en < bipy < phen < NO_2^- < PPh_3 < CN^- < CO$

Figure 5.7.14: Spectrochemical series of ligands, listed from weaker to stronger ligands. A weak-field ligand would lead to a high-spin configuration, while a strong-field ligand would lead to a low-spin configuration. Based on work originally done by Tsuchida.[117]

5.7.2 Conclusion & Future Work: $Cu_2Mn_3Se_4$:

In order to grow single crystals, $Cu_2Mn_3Se_4$ powder was reacted via a dual-zone furnace method, where T_{Hot} = 450 °C and T_{Cold} = 250 °C. Crystals appeared black in color and faceted. Structure refinement revealed that the $Cu_2Mn_3Se_4$ crystals had both a small cell and a 2x2 supercell, i.e. large cell. The SC crystallized in the cubic Fm-3m (#225) space group, with a lattice parameter of a = 5.7454 Å. As for LC, it possessed a cubic Fd-3m (#227) space group with a lattice parameter of a = 11.4932 Å. For SC, Mn1 and Cu1 were found to share the 8c position, with a total site vacancy of 3/8. The 2x2 supercell was able to resolve the Cu and Mn, now occupying separate sites. In LC, with Cu3 sitting at the 16c site with 100% occupancy; Cu4 was found at the 16d site, also possessing 100% site occupancy; Mn5 had 50% occupancy, corresponding to a 4/8 tetrahedral site vacancy. So, the 2x2 supercell ordered the crystal quite well.

For both SC and LC, all metal positions were in tetrahedral coordination. For SC, the Cu/Mn-Cu-Mn distances were 2.873 Å. For LC, the Mn-Mn distance ranged from 3.865-4.262 Å. For SC, the Mn1/Cu1-Se bond distance was uniformly 2.4878 Å. For LC, the Cu3-Se and Cu4-Se distance was 2.4884 Å. However, Mn5-Se1 had a shorter bond distance than Mn5-Se2-2.410 Å and 2.572 Å, respectively. In the case of SC, all Se-Mn1/Cu1-Se bond angles are 109.5°. All LC Se-Cu3-Se and Se-Cu4-Se bond angles were also 109.5°. However, in the case of Se-Mn5-Se, there was much tetrahedral bond angle variation. Se1-Mn5-Se2 bond angles were consistently 109.26°, close to the expected tetrahedral angle. However, Se1-Mn5-Se1 had a much larger than expected angle of 114.9°, while Se2-Mn5-Se2 had a narrow angle of 104.4°.

PXRD was implemented to analyze the phase purity of the powder, and was plotted against both SC and LC patterns. PDXL phase analysis identified binary compounds of MnSe Fm-3m and Cu_3Se_2 P-421m. Upon inspection, the powder does indeed appear to be a mixture of $Cu_2Mn_3Se_4$

and the two binary compounds, with MnSe Fm-3m being the dominant phase. DSC revealed a single melting peak at 550.2 °C. Consulting both Mn-Se and Cu-Se binary phase diagrams revealed that the thermal transition corresponded to the decomposition of MnSe Fm-3m into a $MnSe_2$ RT Pa-3 phase, which then melted at the same temperature.

Diffuse reflectance UV-Vis-NIR spectroscopy was used to analyze the optical properties of the sample, and the Kubelka-Munk function and Tauc plot analysis was applied to gather the direct optical bandgap, E_g. The analysis revealed that E_g = 1.36 eV, corresponding to a λ_{Max} of 912 nm; so, the material would absorb in the UV, visible, and a small portion of the NIR. Now, MnSe Fm-3m was reported to have a film direct bandgap of 1.12 eV, while Cu_3Se_2 P-421m had a bandgap of 1.91-2.01 eV. Due to the fact that MnSe Fm-3m was a dominant phase in the PXRD, the $Cu_2Mn_3Se_4$ bandgap measured was likely a mixture of contributions of both binary phases.

In the $Cu_2Mn_3Se_4$ compound, Mn^{2+} [Ar]$3d^5$ is present in tetrahedral coordination of $MnSe_4$. As such, it is possible to generate AFM order in the compound. In the crystal structure, Mn-Mn tetrahedral chains exist in the large cell. Crystal field theory and Hund's rules predict a theoretical magnetic moment of $\mu_{theo} = 5.92\mu_B$. Interestingly, for the large cell the $MnSe_4$ tetrahedra are distorted, with some bond M-Se distances longer than others, and Se-M-Se bond angles were found to deviate widely from 109.5°. These bond distance and bond angle distortions may result in intriguing magnetic properties, such as a deviation between μ_{theo} and $\mu_{experimental}$.

In the future, since there was a large MnSe Fm-3m phase, as well as a smaller Cu_3Se_2 P-421m phase present, the synthesis conditions of $Cu_2Mn_3Se_4$ needs to be further optimized. In general, Mn^{2+} prefers octahedral coordination-partially due to the R_{cation}/R_{anion} ratio of 0.404, close to the limit of 0.414 for a tetrahedral compound. So, it is not that surprising that $Cu_2Mn_3Se_4$ seems difficult to synthesize. The most promising route is by growing large amounts of $Cu_2Mn_3Se_4$ single

crystals via the dual-zone process and crushing that into powder for the various measurements. Once successfully synthesized, a characterization sweep such as PXRD, DSC, optical bandgap, and thermoelectric measurements would be suggested. Additionally, low-T magnetic susceptibility measurements are encouraged to elucidate if there is indeed AFM ordering at certain temperatures. Further, if more $Cu_2Mn_3Se_4$ single crystals are grown, additional magnetic measurements to test for anisotropy along certain directions could also be interesting due to the distortions in the $MnSe_4$ tetrahedral Mn-Se bond distances and Se-Mn-Se bond angles.

Finally, since $Cu_2Mn_3Se_4$ should be optically active and possess AFM ordering, more exotic measurements could be carried out to see if there is any coupled magneto-optic behavior occurring in the compound. For example, Newnham discusses a magneto-optic Kerr effect (MOKE) where the plane of polarization of linearly polarized light is rotated by the magnetic film via reflection.[118] Three types of Kerr effects exists-polar, longitudinal, or transverse, depending on the magnetic film magnetization direction.[118] Magneto-optic media typically utilizes the polar Kerr effect in particular.[118] To probe the MOKE, a setup involving a laser and magnetic field would be needed, as found in Gadetsky *et al*.[119] The MOKE is more typically observed in ferromagnetic films, but it is possible to occur in AFM materials too. For example, Kang *et al*. observed the polar MOKE in AFM M_2As (M = Cr, Mn, Fe).[120] It is important to note that the MOKE setup uses magnetic thin films, so a $Cu_2Mn_3Se_4$ thin film would need to be grown; with collaboration of the Heron lab, pulsed-laser deposition (PLD) could be a possible route, following similar thin film conditions to Chen *et al*.'s work on Cu_4TiSe_4.[92] On a similar note, the magneto-optics of the sample could also be probed using X-ray magnetic circular dichroism (XMCD) or X-ray magnetic linear dichroism (XMLD).[118] XMCD or XMLD measurements could be performed at the Advanced Photon Source in Argonne National Laboratory.

CHAPTER 6: Conclusions and Future Work on $Cu_2Zn_{2x}Ti_{(3-2x)/2}Se_4$ (x = 1.5, 1, 0.5, 0) and $Cu_2Mn_3Se_4$

For $Cu_2Zn_{2x}Ti_{(3-2x)/2}Se_4$ (x = 1.5, 1, 0.5, 0), it was noted that by increasing the amount of Ti^{4+} in the compound, the number of tetrahedral vacancies increased. The higher Ti^{4+} content iterations also possessed a large $TiSe_2$ P-3m1 binary phase in addition to the desired $Cu_2Zn_{2x}Ti_{(3-2x)/2}Se_4$ powder. Likely, the powder synthesis difficulties arose from a combination of increased disorder in the lattice, as well as increased levels of electrostatic repulsion due to the rising amount of Ti^{4+} in the structure. Interestingly, decreasing the x value was observed to consistently increase E_g: 2.24 eV, 2.59 eV, 2.61 eV, and 2.75 eV for x = 1.5, 1, 0.5, and 0, respectively. **Table 6.1.1** portrays the optical bandgap, maximum absorbed wavelength, and absorbed regions of the solar spectrum. The increase in E_g with decreasing x value let to a decrease in λ_{Max}, cutting off longer wavelength portions of the visible spectrum.

Table 6.1.1: $Cu_2Zn_{2x}Ti_{(3-2x)/2}Se_4$ (x = 1.5, 1, 0.5, 0) E_g, λ_{Max}, and absorbed regions of the solar spectrum.

x Value	E_g for r = 1/2 (eV)	λ_{Max} (nm)	Absorbed Regions
1.5	2.24	~554	UV, Vis (violet→green)
1	2.59	~479	UV, Vis (violet→blue-cyan)
0.5	2.61	~475	UV, Vis (violet→blue-cyan)
0	2.75	~451	UV, Vis (violet and blue)

For both $Cu_2Zn_{2x}Ti_{(3-2x)/2}Se_4$ (x = 1.5, 1, 0.5, 0) and $Cu_2Mn_3Se_4$, aside from the conventional solid-state reaction from the elements or growing single crystals and grinding them, an "explosion" reaction method could also be implemented. Here, one would start from $CuSe_2$

precursor and mix in proper elemental stoichiometries to form the various x = 1.5, 1, 0.5, 0 or $Cu_2Mn_3Se_4$ iterations. Grind the powder with mortar and pestle, and cold press at RT and 100 MPa for 2 hours under vacuum using the graphite press to bring the precursor materials into closer contact. Place the pellet into a quartz tube and flame-seal under vacuum. According to the proper DSC melting peaks, choose a temperature ~100 °C below MP. Rapidly increase the temperature to MP – 100 °C over 4 hours, dwell for 1 or 2 hours, and quench in a bucket of water or liquid nitrogen (LN_2). Note: while initiating the programmable furnace steps, do not place the quartz tubes into mullite tubes because the rapid increase in temperature could cause thermal shock to the mullite. Ideally, the "explosion" reaction and quenching process should trap the cubic structure in place and avoid binary formation. It is essential to wear the proper heat-resistant attire while performing the "explosion" reaction for adequate protection. The ideal explosion reaction synthesis conditions likely still need to be optimized based on preliminary PXRD scans.

This same "explosion" reaction procedure could be implemented to create a substitution series of $Cu_2Zn_3Se_{4-4x}Te_{4x}$, where x = 0, 0.05, 0.1, 0.2, 0.5, 0.8, and 1. The x values correspond to the following compounds: $Cu_2Zn_3Se_4$, $Cu_2Zn_3Se_{3.8}Te_{0.2}$, $Cu_2Zn_3Se_{3.6}Te_{0.4}$, $Cu_2Zn_3Se_{3.2}Te_{0.8}$, $Cu_2Zn_3Se_2Te_2$, $Cu_2Zn_3Se_{0.8}Te_{3.2}$, and $Cu_2Zn_3Te_4$. Based on preliminary results, x = 0-0.4 appeared the most promising in terms of crystallizing as close to the $Cu_2Zn_3Se_4$ large cell structure as possible. Again, the synthesis conditions need to be optimized further. It is possible that annealing will be required to further purify the various $Cu_2Zn_3Se_{4-4x}Te_{4x}$ compositions. Most likely, substituting Se with Te could tune various physical properties such as the optical bandgap of the material, melting point, and thermoelectric properties.

APPENDICES

APPENDIX A: $Mn_{1-x}Zn_xSb_2Se_4$ (x = 0, 0.01, 0.04, 0.05, 0.06, 0.08, 0.1, 0.15)

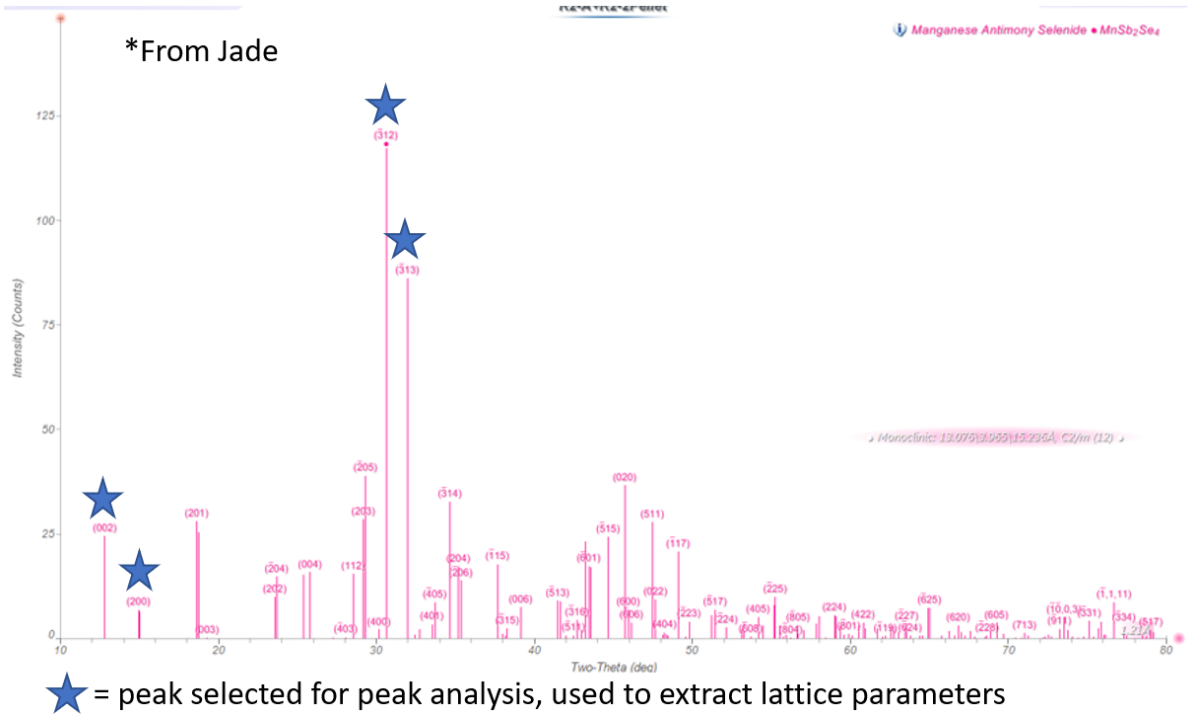

Figure A.1: $MnSb_2Se_4$ XRD peak analysis using Jade software. The Starred peaks were chosen to match the theoretical (hkl) values to the experimental 2θ values. Using Bragg's law and the monoclinic interplanar spacing equation, the lattice parameters a, b, c, and β were calculated.

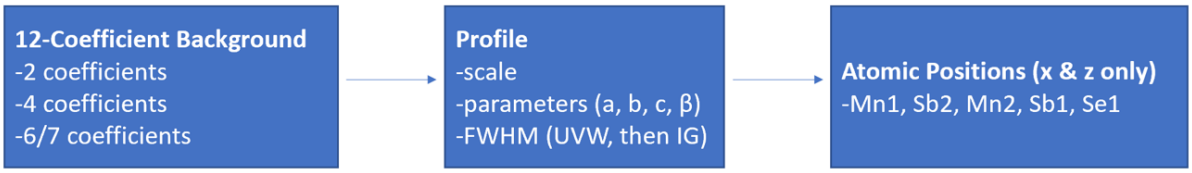

Figure A.2: Rietveld refinement procedure of the main phase using the FullProf software.

Table A.1: Extracted information from Rietveld refinement of the secondary phase, ZnSe. $\chi 2$ was noted before and after secondary phase refinement to depict the moderate improvement in the quality of fit upon secondary refinement. The lattice parameter of ZnSe for each composition was determined and compared to ICSD reference values. *ICSD Reference #77091[29] (ZnSe, F-43m).

Zn Content (x)	$\chi 2$ Value (Before Secondary Phase Refinement)	$\chi 2$ Value (After Secondary Phase Refinement)	aZnSe (Å)
ZnSe*	N/A	N/A	5.674
0.04	8.34	8.19	5.7014
0.05	0.824	0.776	5.690867
0.06	4.12	4.08	5.67654
0.08	14.9	14.6	5.708696
0.1	21.1	21	5.699156
0.15	13.5	12.8	5.701872

Table A.2: XPS energy values, cross-referenced with the corresponding elemental energy windows.

Zn Content (x)	Mn L_3 $2p_{3/2}$ (eV)	Zn L_3 $2p_{3/2}$ (eV)	Sb M_5 $3d_{5/2}$ (eV)	Se M_4 $3d_{3/2}$ (eV)	Se M_5 $3d_{5/2}$ (eV)
Reference	640.2[54]	1021.0[55]	529[56]	55.0[31]	53.7[31]
0.01	641.4	Unable to determine peak position	529.6	54.7	54.2
0.03	Unable to determine peak position	Unable to determine peak position	529.6	54.4	54.1
0.04	Unable to determine peak position	Unable to determine peak position	529.6	54.8	54.2
0.05	641.4	1024.7	529.5	54.7	54.2

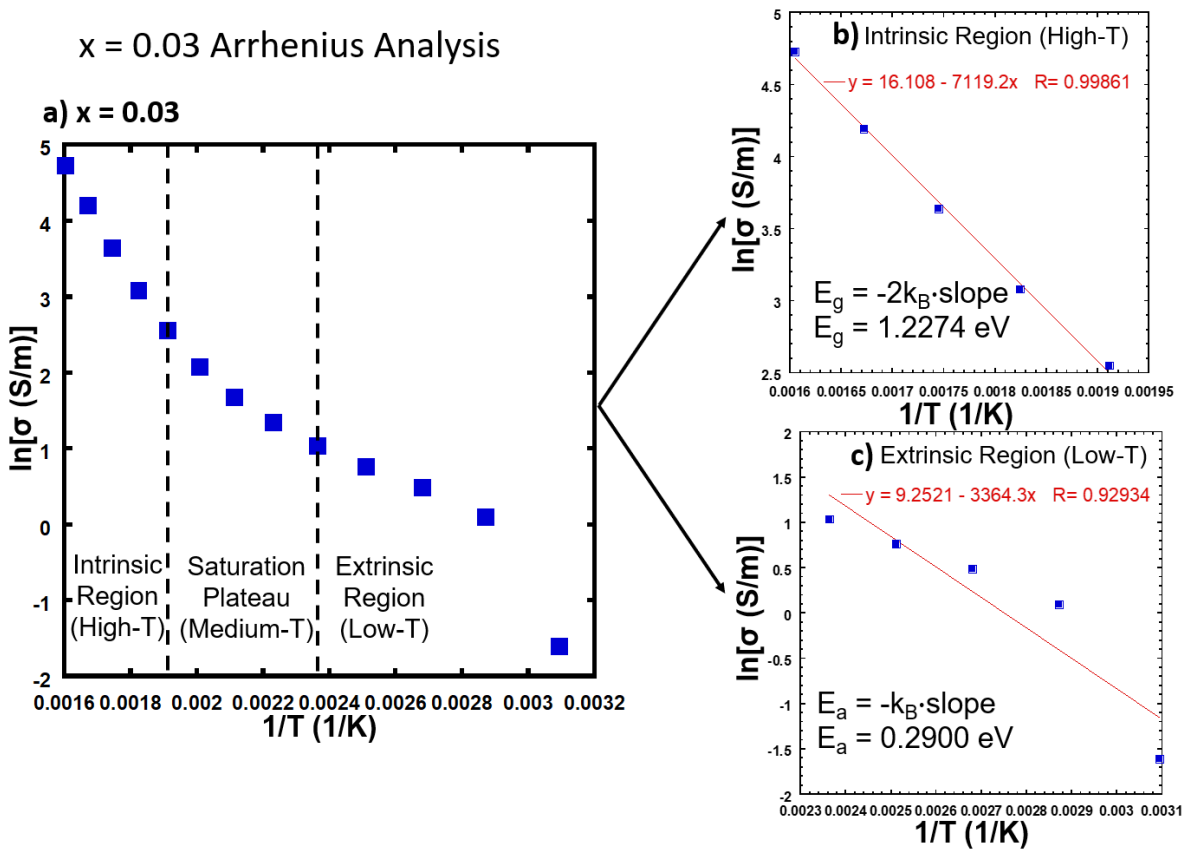

Figure A.3: (a) $Mn_{0.97}Zn_{0.03}Sb_2Se_4$ (x = 0.03) electrical conductivity Arrhenius plot. The figure was divided into the intrinsic region, saturation plateau, and extrinsic region depending on temperature; **(b)** Intrinsic region Arrhenius plot, utilized to extract electronic bandgap, E_g; **(c)** Extrinsic region Arrhenius plot, employed to obtain activation energy, E_a.

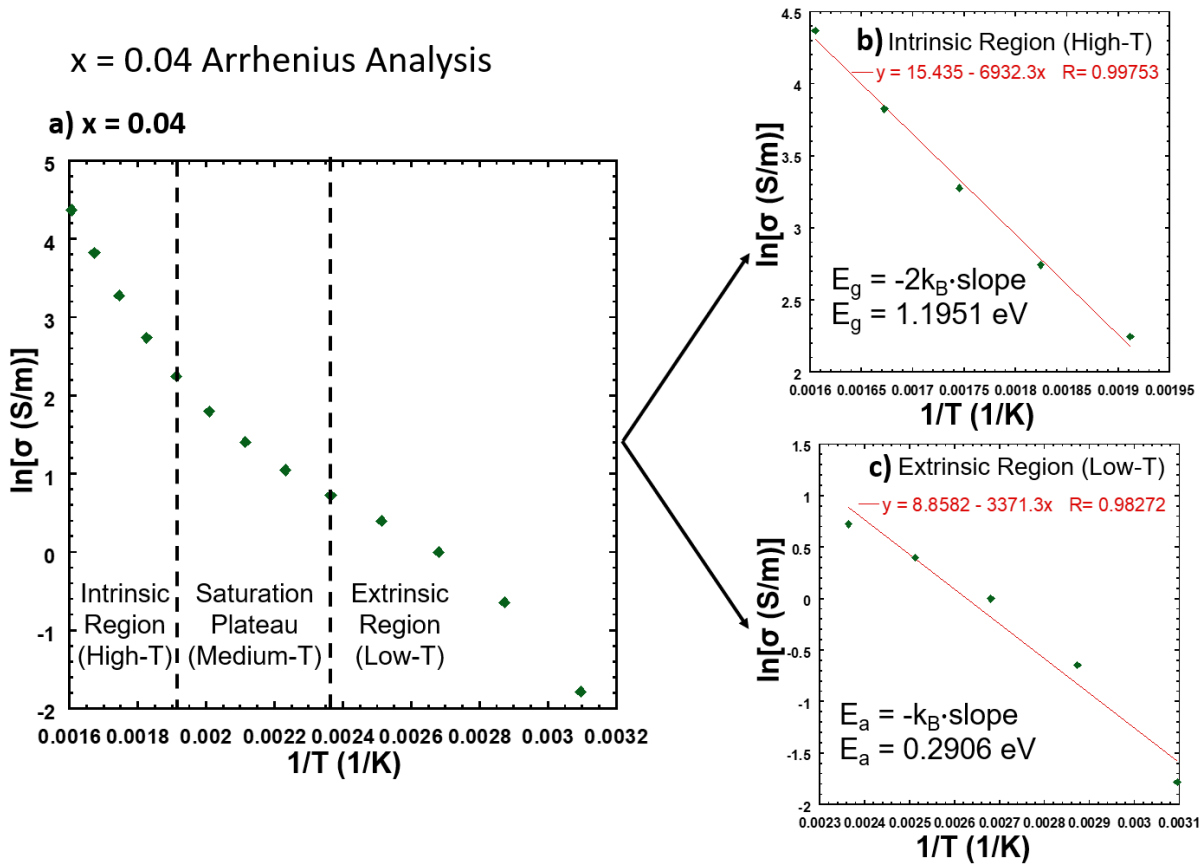

Figure A.4: (a) $Mn_{0.96}Zn_{0.04}Sb_2Se_4$ (x = 0.04) electrical conductivity Arrhenius plot. The figure was divided into the intrinsic region, saturation plateau, and extrinsic region depending on temperature; **(b)** Intrinsic region Arrhenius plot, utilized to extract electronic bandgap, E_g; **(c)** Extrinsic region Arrhenius plot, employed to obtain activation energy, E_a.

Table A.3: Electrical conductivity of typical insulators, semiconductors, and metals. As a reference, $Mn_{1-x}Zn_xSb_2Se_4$ $\sigma \sim 10^{-1}$-10^{2} S/m.[121]

Material	Electrical Conductivity (S/m)
Insulators	
Fused Silica	$< 10^{-18}$
Al_2O_3	$< 10^{-13}$
Soda-lime glass	10^{-10}-10^{-11}
Semiconductors	
GaAs (undoped)	3×10^{-7}
Si (undoped)	3.4×10^{-4}
Ge	2.2×10^{1}
Metals	
Al	3.8×10^{7}
Cu	6×10^{7}
Ag	6.8×10^{7}

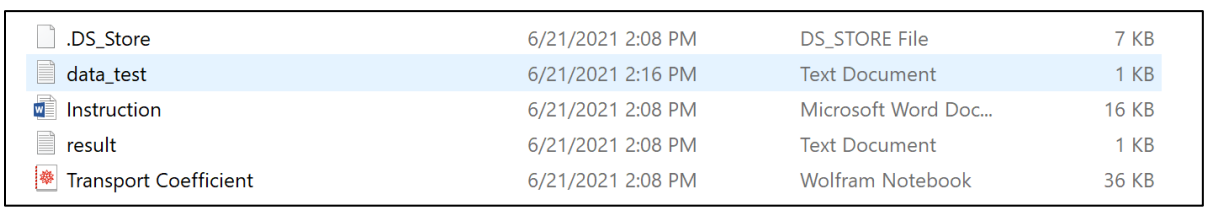

.DS_Store	6/21/2021 2:08 PM	DS_STORE File	7 KB
data_test	6/21/2021 2:16 PM	Text Document	1 KB
Instruction	6/21/2021 2:08 PM	Microsoft Word Doc...	16 KB
result	6/21/2021 2:08 PM	Text Document	1 KB
Transport Coefficient	6/21/2021 2:08 PM	Wolfram Notebook	36 KB

Figure A.5: Fermi-corrected Lorenz # file folder, displaying the relevant files.

data_test - Notepad

File Edit Format View Help

T	S
323.15	895.8
348.15	845.09
373.15	807.97
398.15	781.44
423.15	762.47
448.15	748.03
473.15	735.09
498.15	720.65
523.15	701.66
548.15	675.11
573.15	637.98
598.15	587.23
623.15	519.85

result - Notepad

File Edit Format View Help

"T"	"Fermi"	"Lorentz"
323.15	-8.395202874106108	1.4852138773501302
348.15	-7.806647897392976	1.4852474820048274
373.15	-7.375779095827821	1.4852881581302537
398.15	-7.067798701289149	1.4853300587926481
423.15	-6.847556343510603	1.485368996338374
448.15	-6.679890440540697	1.4854049455412828
473.15	-6.529626431774461	1.4854426984830253
498.15	-6.361924294681077	1.4854920929431448
523.15	-6.141342064217257	1.4855710236944335
548.15	-5.832854381005568	1.4857150292964383
573.15	-5.401190628389851	1.4860075415749856
598.15	-4.810454399465176	1.486677745041161
623.15	-4.0237205056951195	1.488463102498837

Figure A.6: (Left): Screenshot of the data_test file that loads in Seebeck coefficient data to the Fermi-corrected Lorenz # Mathematica script. **(Right):** Screenshot of the result file that is generated once the Mathematica script is ran.

```
(* ********************************************************************************************** *)
(* ********** Fermi Level, Effective Mass, Lorentz Number ********************************************** *)
(* ********** Version 0.2  ************************************************************************** *)
(* ********** Written by Hang Chi ******************************************************************** *)
(* ********** Last modified on April 13, 2012 ******************************************************** *)
(* ********** chihang@umich.edu ********************************************************************** *)
(* ********** The Uher Research Group **************************************************************** *)
(* ********** ALL RIGHTS RESERVED ******************************************************************** *)
(* ********************************************************************************************** *)



(* ********************************************************************************************** *)

(* Environmental Control Commands *)

In[50]:= SetDirectory[NotebookDirectory[]];

ResetDirectory[];

Exit[];

(* ********************************************************************************************** *)



(* ********************************************************************************************** *)

(* Physical Constants, Unit Conversions and Functions *)

In[51]:= kB = 1.3806504*^-23;
eC = 1.602176487*^-19;
hP = 6.62606957*^-34;
RA = 6.02214129*^23;
unitT = 1(* K to K *);
unitS = 1*^-6 (* μV/K to V/K *);
unitL = 1*^-8(* Watt-Ohm/K^2*);

F[n_, η_] := Integrate[ξ^n/(e^(ξ-η) + 1), {ξ, 0, ∞}] (* Fermi-Dirac Integral *)

S[r_, η_] := -kB/eC * (η - (r + 5/2)/(r + 3/2) * F[r + 3/2, η]/F[r + 1/2, η]) (* Seebeck for electron transport; τ=τ0E^r *)

L[r_, η_] := kB^2/eC^2 ((r + 3/2) (r + 7/2) F[r + 1/2, η] × F[r + 5/2, η] - (r + 5/2)^2 F[r + 3/2, η]^2)/((r + 3/2)^2 F[r + 1/2, η]^2) (* Lorentz number for  *)

LorentzNumber[{T0_, S0_}] := Module[{η, l, exprη},
  exprη = FindRoot[S[-1/2, η] == S0, {η, 0}]; (* r = -1/2, Acoustic Phonon; 3/2, Ionized Impurity *)
  l = L[-1/2, η] /. exprη; (* r = -1/2, Acoustic Phonon; 3/2, Ionized Impurity *)
  {T0, Re[η /. exprη], l/unitL}] (* returns {T0, η, l}, η=μ/(k_B T), l is the Lorentz Number *)

(* ********************************************************************************************** *)

(* ********************************************************************************************** *)
(* Working Interface *)
```

Figure A.7: Fermi-corrected Lorenz # Mathematica script, written by Hang Chi of the Uher group. It inputs Seebeck coefficient data and calculates accurate values for L.

```
(* test *)

In[62]:= data = Import["data_test.txt", "TSV", "HeaderLines" → 1];

In[63]:= resultOutput = {{"T", "Fermi", "Lorentz"}};
Print["Processing... "];
For[i = 1, i <= Length[data], i++,
  result = LorentzNumber[data[[i]] * {unitT, unitS}];
  Print[result];
  resultOutput = Append[resultOutput, result];
 ];
Export["result.txt", resultOutput, "TSV"]

Processing...
{323.15, -8.3952, 1.48521}
{348.15, -7.80665, 1.48525}
{373.15, -7.37578, 1.48529}
{398.15, -7.0678, 1.48533}
{423.15, -6.84756, 1.48537}
{448.15, -6.67989, 1.4854}
{473.15, -6.52963, 1.48544}
{498.15, -6.36192, 1.48549}
{523.15, -6.14134, 1.48557}
{548.15, -5.83285, 1.48572}
{573.15, -5.40119, 1.48601}
{598.15, -4.81045, 1.48668}
{623.15, -4.02372, 1.48846}

Out[66]= result.txt

(* END of test *)
```

Figure A.8: The bottom portion of the Fermi-corrected Lorenz # Mathematica script, written by Hang Chi of the Uher group.

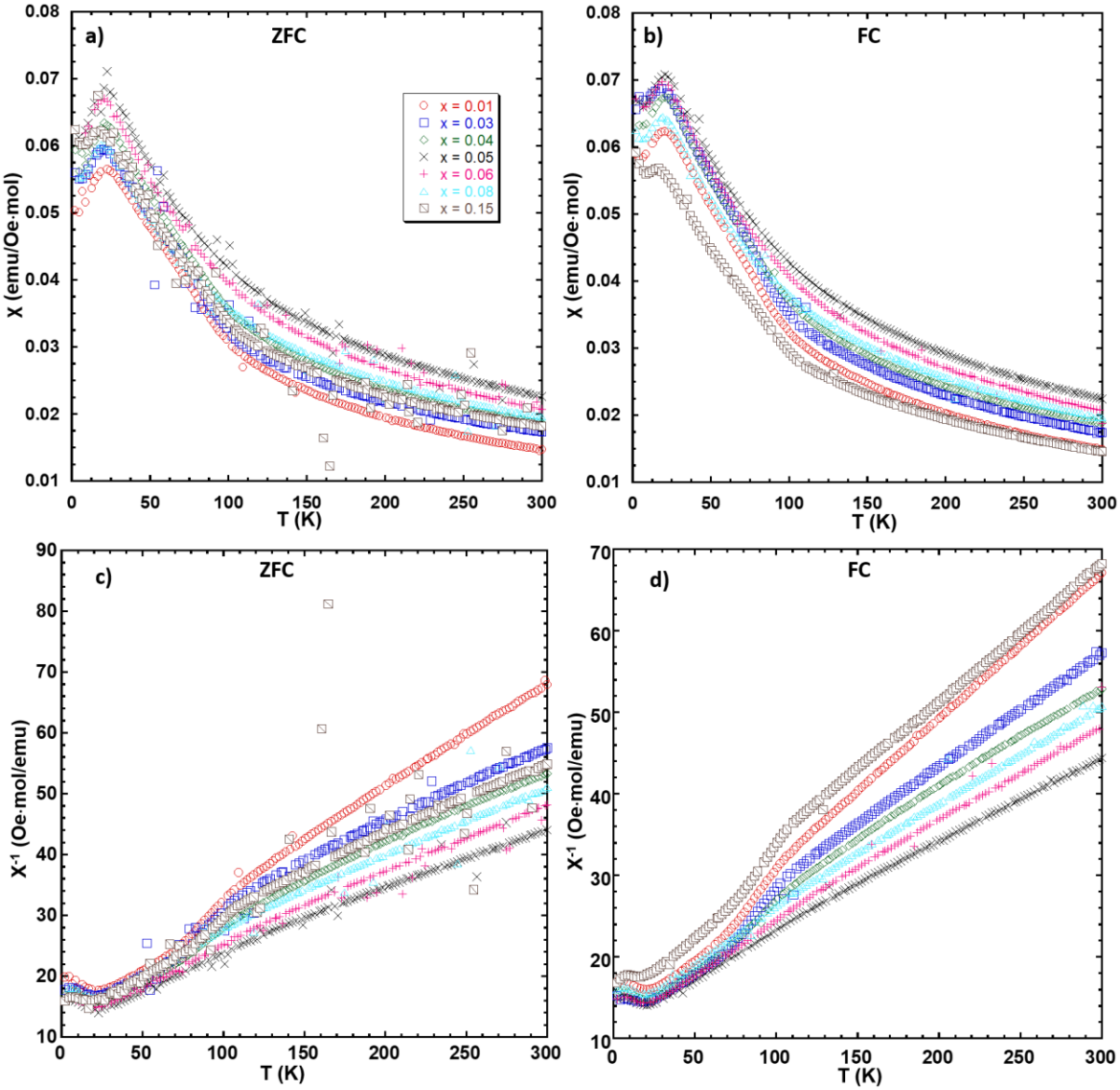

Figure A.9: (a, b) Temperature-dependent magnetic susceptibility in zero field-cooled (ZFC) and field-cooled (FC) configurations, respectively; **(c, d)** Temperature-dependent inverse magnetic susceptibility in ZFC and FC configurations.

APPENDIX B: $Sb_{2-x}Sn_xSe_3$ (x = 0, 0.01, 0.05, 0.1, 0.15, 0.2)

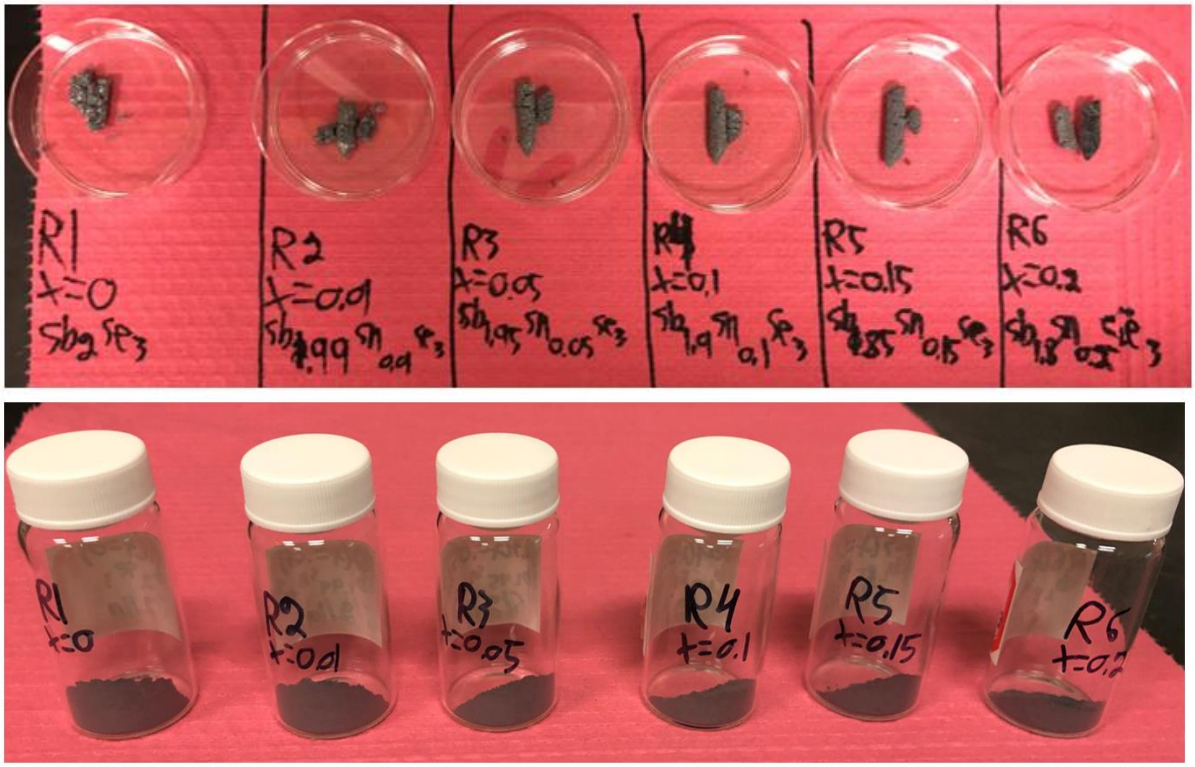

Figure B.1: (Top): $Sb_{2-x}Sn_xSe_3$ compound series ingots after the solid-state reaction. The ingots were dark grey and lustrous in appearance. No apparent color changes were seen. With increasing Sn content. **(Bottom):** After grinding the reacted ingots into powder-dark grey in appearance.

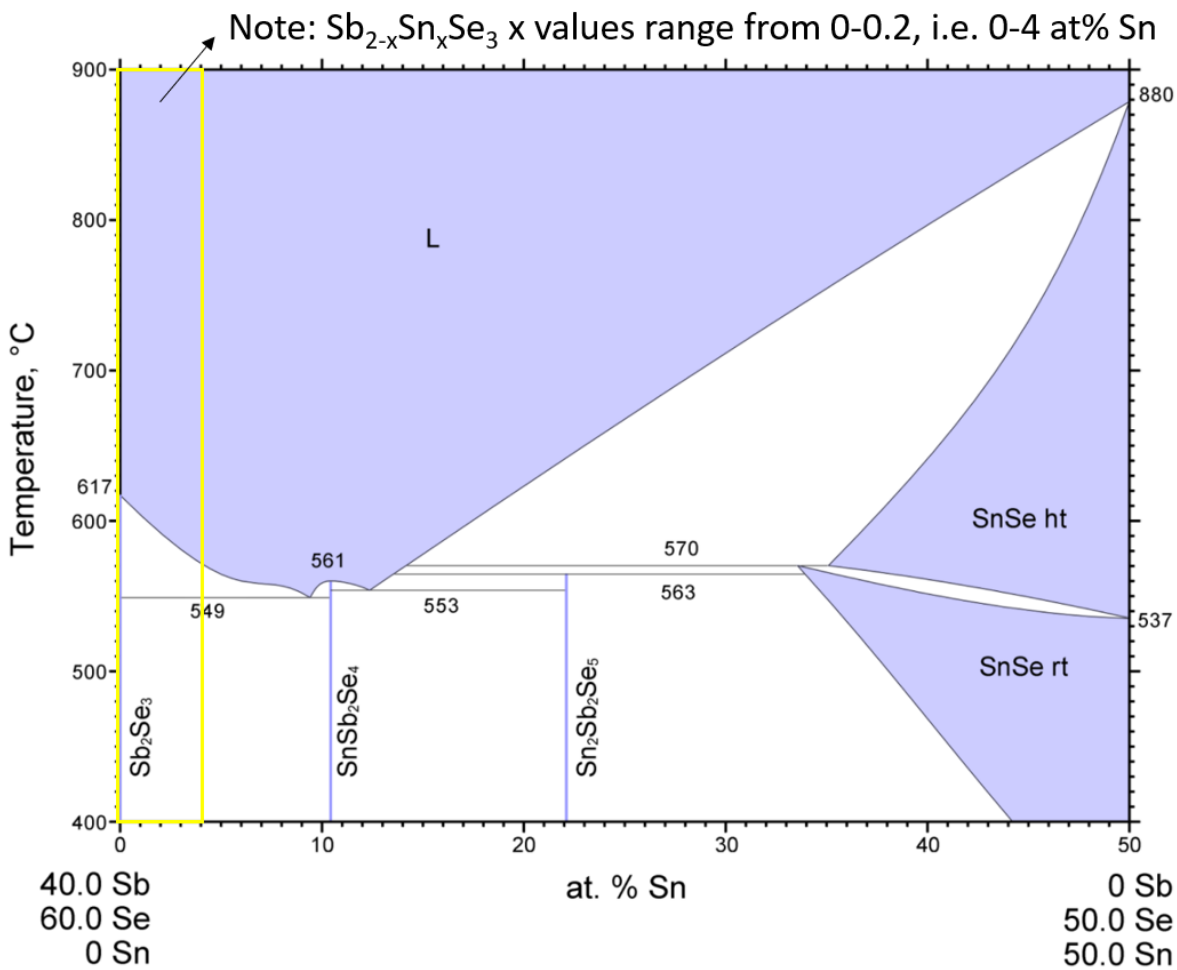

Figure B.2: Sb-Sn-Se pseudo-binary phase diagram (ASM #952732[82]). This diagram was gathered from a vertical section of the Sb-Sn-Se ternary phase diagram. For x = 0-0.2, this corresponded to 0-4 at% Sn. The proper window on the diagram was highlighted with a box in yellow. We see that as Sn increases, we go further into the 2-phase region on the phase diagram between the Sb_2Se_3 Pnma and $SnSb_2Se_4$ Pnnm phases. So, this is consistent with the heating DSC observation of a growing secondary peak from x = 0.1-0.2.

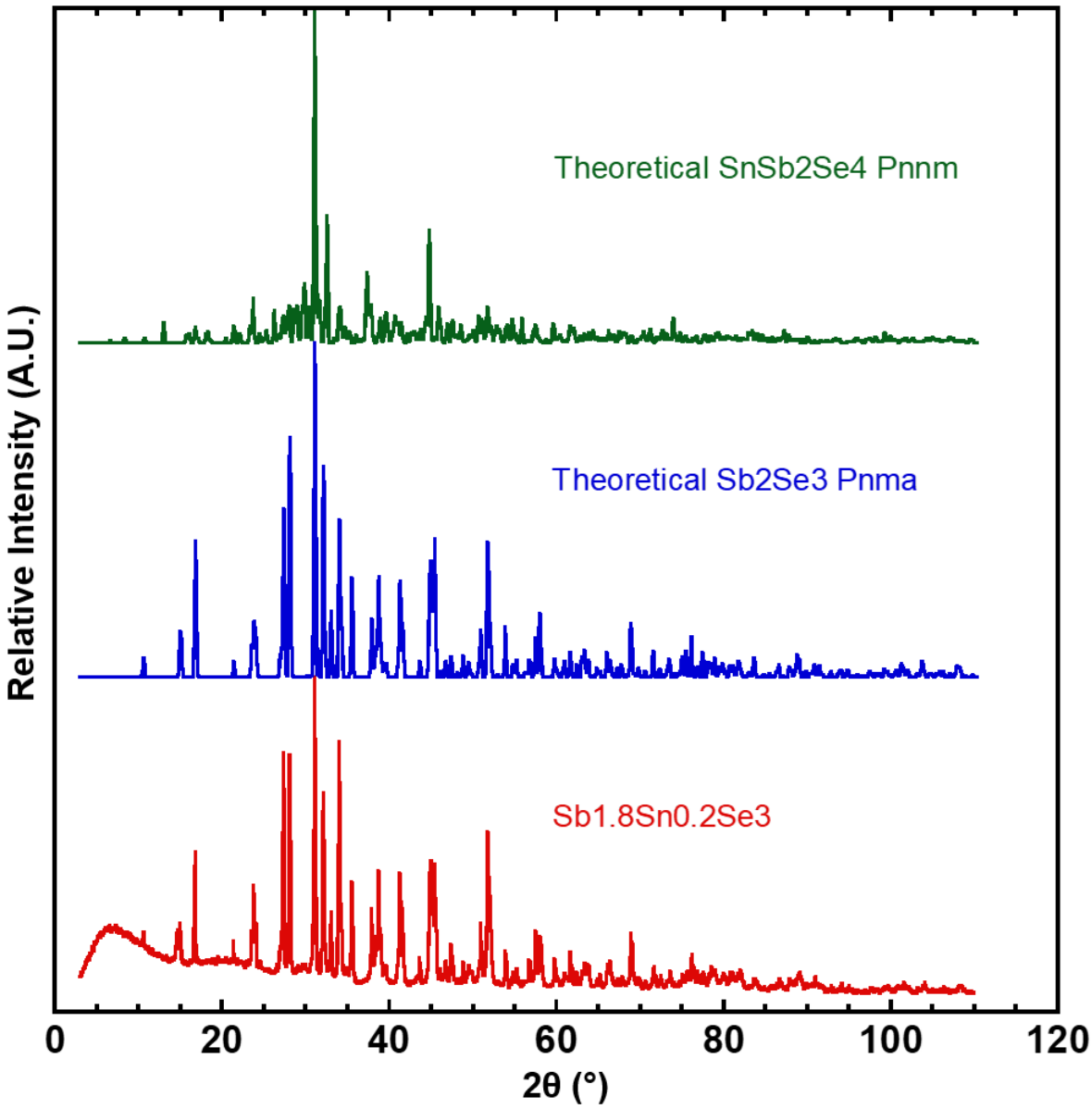

Figure B.3: Powder x-ray diffraction comparing $Sb_{1.8}Sn_{0.2}Se_3$ to both the Sb_2Se_3 Pnma (ICSD #30973[30]) and $SnSb_2Se_4$ Pnnm (ICSD #49723[122]) phases. At this zoom level, it is difficult to decipher if the $SnSb_2Se_4$ Pnnm phase is in fact present. See **Figure B.4** for a zoomed-in version of the curve.

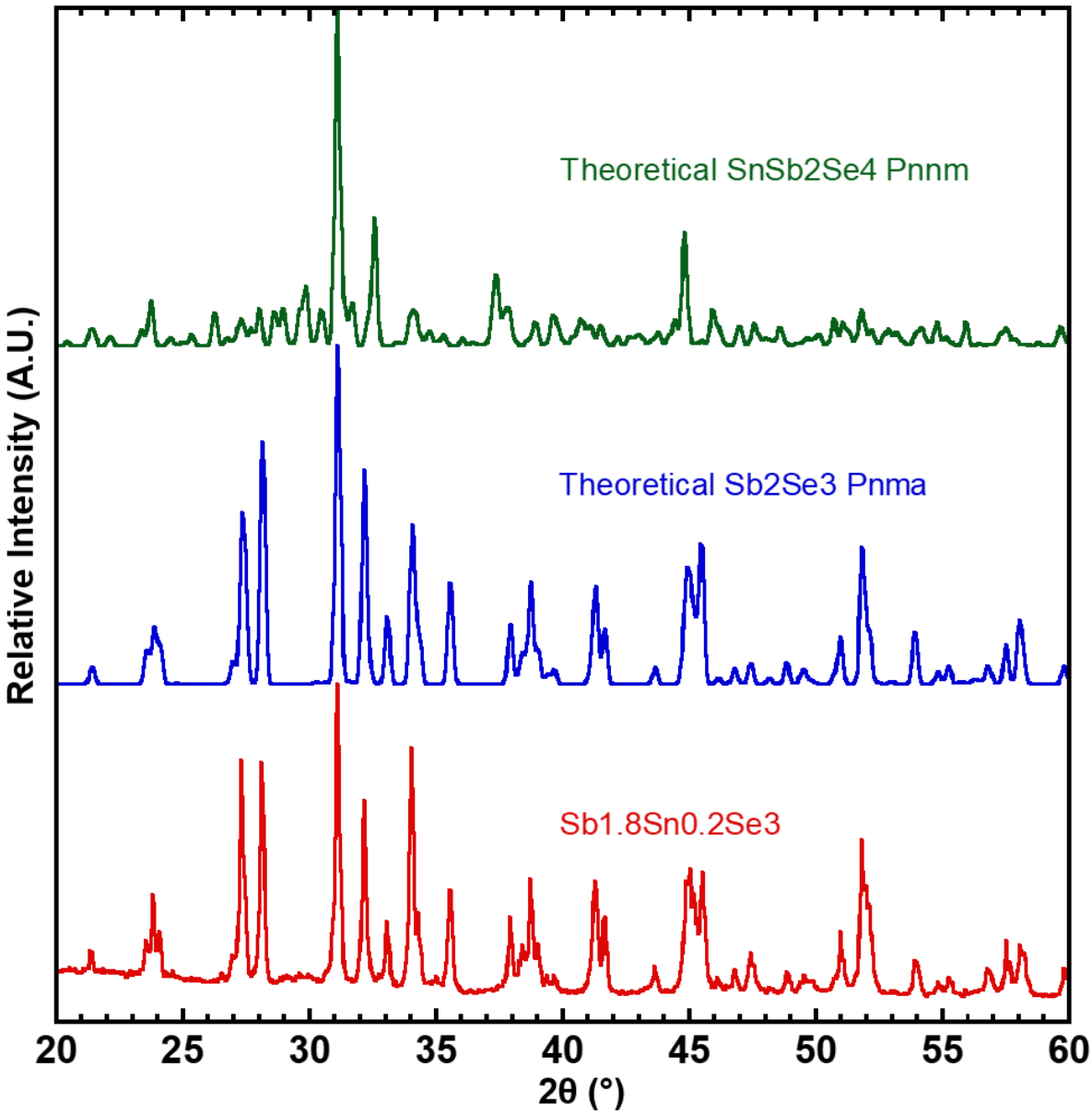

Figure B.4: Powder x-ray diffraction comparing $Sb_{1.8}Sn_{0.2}Se_3$ to both the Sb_2Se_3 Pnma (ICSD #30973[30]) and $SnSb_2Se_4$ Pnnm (ICSD #49723[122]) phases, zoomed-in from 20-60° to show the peaks more clearly. Upon close inspection, there are minor $SnSb_2Se_4$ Pnnm peaks present in the $Sb_{1.8}Sn_{0.2}Se_3$ in-between the Sb_2Se_3 Pnma peaks at various 2θ values.

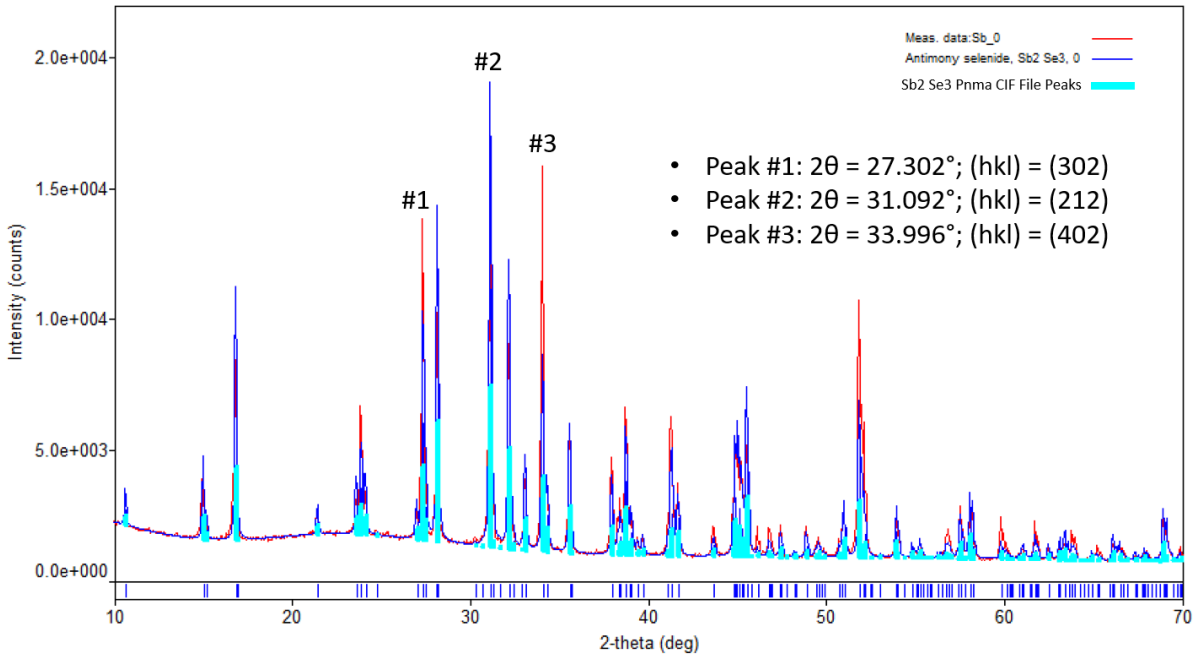

Figure B.5: Sb_2Se_3 (x = 0) lattice parameter analysis using PDXL software. The experimental data was compared to the Sb_2Se_3 Pnma (ICSD #30973[30]) phase with lattice parameters: a = 11.7938 Å; b = 3.9858 Å; c = 11.6478 Å; α = β = γ = 90°. Three sets of (hkl) values were correlated to the proper experimental 2θ values. Bragg's Law and the orthorhombic interplanar spacing equation were applied to manually extract more accurate lattice parameters. Corrected lattice parameters from manual peak analysis: a = 11.8126 Å; b = 3.98339 Å; c = 11.6672 Å; α = β = γ = 90°.

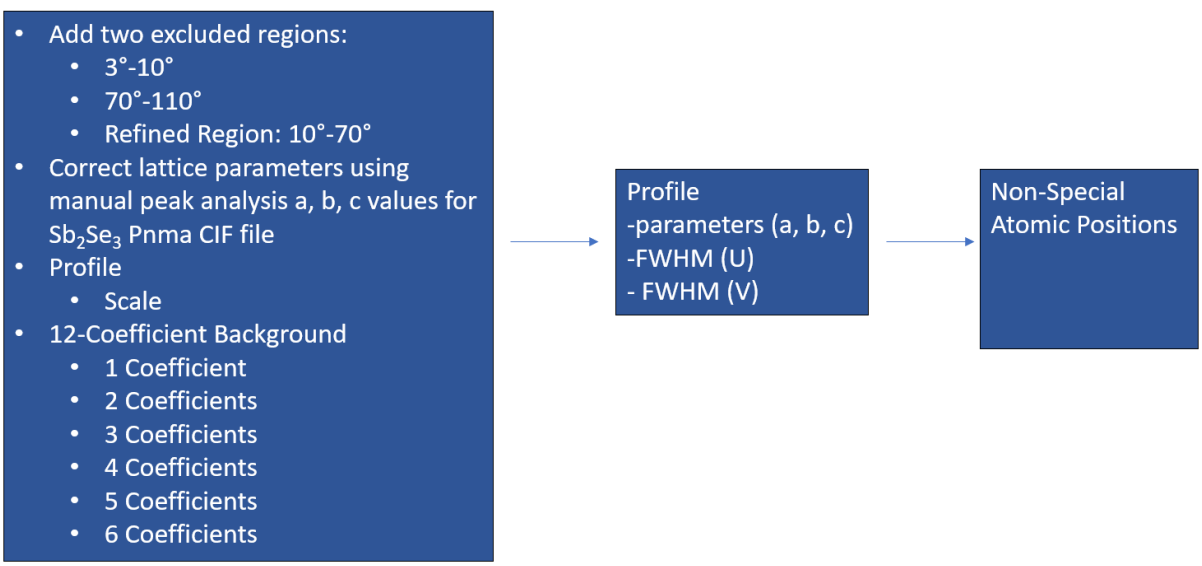

Figure B.6: FullProf Rietveld refinement procedure implemented to gather the lattice parameters a, b, c for the $Sb_{2-x}Sn_xSe_3$ compound series.

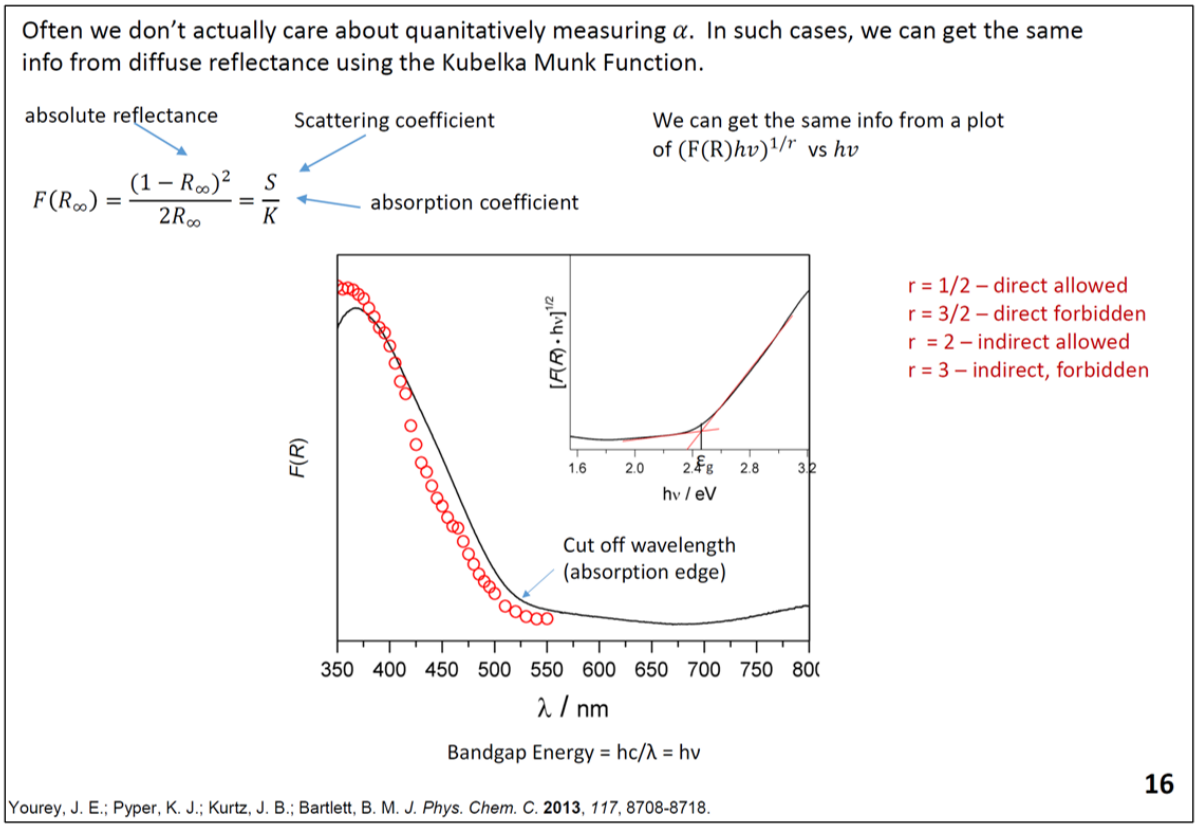

Figure B.7: Instructions on how to convert reflectance data into absorbance using the Kubelka-Munk function F(R). By plotting $[F(R)*h\nu]^{1/r}$ vs. energy, we can extract the proper optical transition. For the case of r = ½, this corresponds to a direct allowed transition, i.e., a direct optical bandgap (E_g). E_g is determined by extrapolating the absorption edge to the baseline; the intersection of the two tangent lines corresponds to E_g. In the case where there is not a clear baseline to extrapolate to, the intersection of the absorption edge tangent line with the x-axis corresponds to E_g. Note: this slide originated from course material in MSE 510: Materials Chemistry, instructed by Dr. McCrory at the University of Michigan.

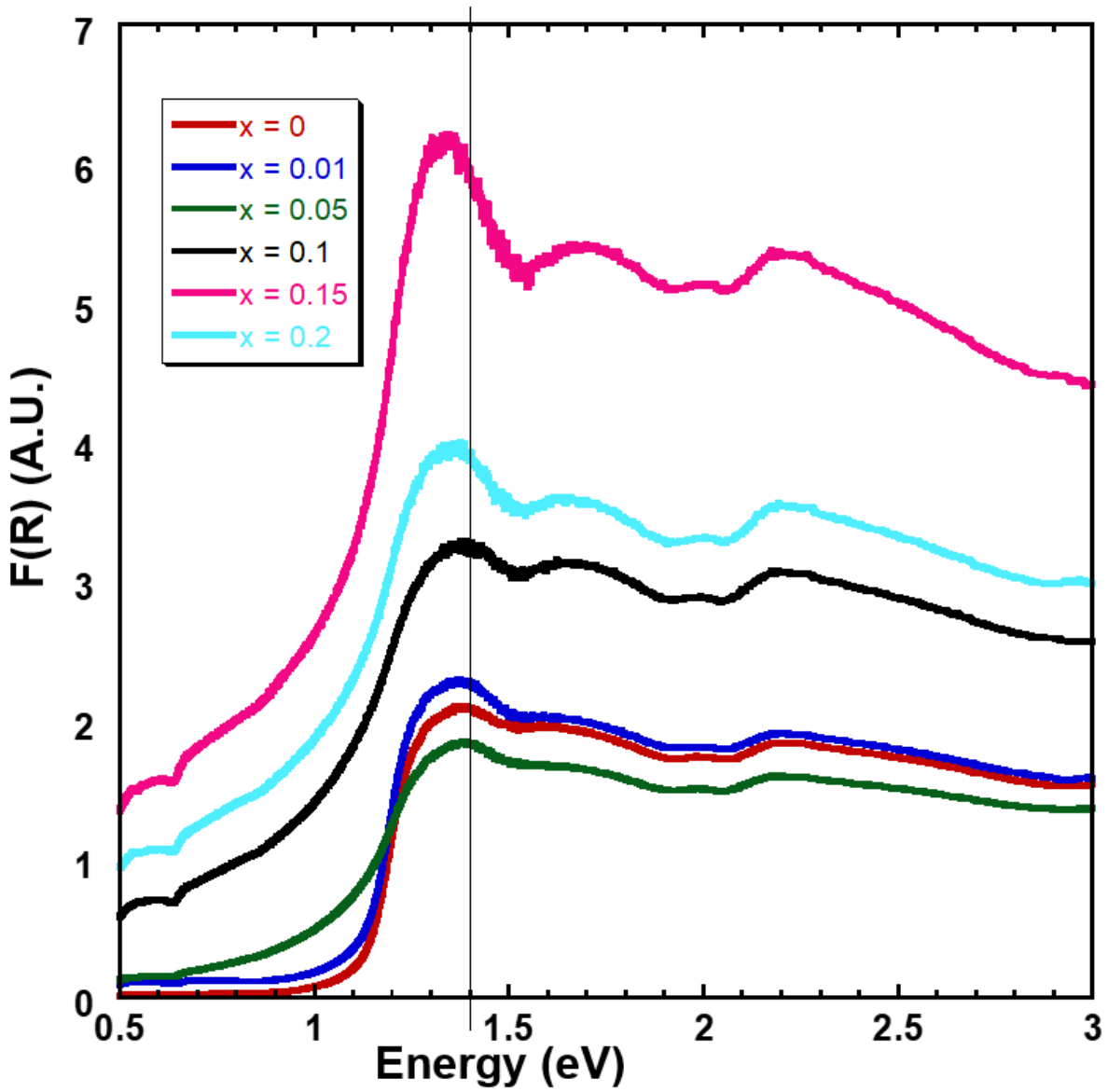

Figure B.8: Kubelka-Munk function F(R) vs. energy. Drawn on the plot is a vertical line at 1.4 eV, noting the onset of the absorption edge.

APPENDIX C: $Cu_2Zn_3Se_4$ (x = 1.5)

Table C.1: $Cu_2Zn_3Se_4$ small cell anisotropic displacement parameters, in units of $Å^2 \times 10^{-4}$.

$Cu_2Zn_3Se_4$-small cell						
Atom	**U_{11}**	**U_{22}**	**U_{33}**	**U_{12}**	**U_{13}**	**U_{23}**
Se1	349.4(7)	-	-	-	-	-
Zn1	420.7(9)	-	-	-	-	-
Cu1	420.7(9)	-	-	-	-	-

Table C.2: $Cu_2Zn_3Se_4$ large cell anisotropic displacement parameters in units of $Å^2 \times 10^{-4}$.

$Cu_2Zn_3Se_4$-large cell						
Atom	**U_{11}**	**U_{22}**	**U_{33}**	**U_{23}**	**U_{13}**	**U_{12}**
Se1	352.1(4)	352.1(4)	352.1(4)	0	0	0
Se2	287.3(2)	288.4(3)	287.3(2)	0	-0.6(2)	0
Se3	323.4(3)	323.4(3)	317.5(4)	0	0	0
Se4	256.4(2)	256.4(2)	256.4(2)	0.7(1)	0.7(1)	0.7(1)
Zn1	371.8(4)	371.8(4)	371.8(4)	3.8(3)	3.8(3)	-3.8(3)
Zn2	423.7(3)	423.7(3)	421.6(4)	1.5(3)	1.5(3)	5(3)
Cu1	273.2(5)	273.2(5)	273.2(5)	0	0	0
Cu2	218.6(3)	218.6(3)	218.6(3)	-2.7(2)	-2.7(2)	-2.7(2)
Cu3	273.5(3)	269(4)	273.5(3)	0	2.2(4)	0

Table C.3: $Cu_2Zn_3Se_4$ small cell selected inter-atomic bond angles (in °). Small cell operators for generating equivalent atoms: (i) x, y+1/2, z+1/2; (ii) x+1/2, y, z+1/2; (iii) x+1/2, y+1/2, z; (iv) x, y-1/2, z-1/2; (v) x-1/2, y, z-1/2; (vi) x-1/2, y-1/2, z; (vii) -x, -y+1, -z+1; (viii) -x, -y+3/2, -z+3/2; (ix) -x+1, -y+3/2, -z+3/2; (x) -x+1/2, -y+1, -z+3/2; (xi) -x+1/2, -y+2, -z+3/2; (xii) -x+1/2, -y+3/2, -z+1; (xiii) -x+1/2, -y+3/2, -z+2.

$Cu_2Zn_3Se_4$-small cell	
Atoms 1,2,3	**Angle 1,2,3 [°]**
$Se1^{i}$—Zn1/Cu1—$Se1^{ii}$	109.5
$Se1^{iii}$—Zn1/Cu1—$Se1^{ii}$	109.5
Se1—Zn1/Cu1—$Se1^{ii}$	109.5
$Se1^{iii}$—Zn1/Cu1—$Se1^{i}$	109.5
Se1—Zn1/Cu1—$Se1^{i}$	109.5
Se1—Zn1/Cu1—$Se1^{iii}$	109.5

Table C.4: $Cu_2Zn_3Se_4$ large cell selected inter-atomic bond angles (in °). Large cell operators for generating equivalent atoms: (i) -x, 1-y, 1-z; (ii) -x, y, z; (iii) -x, 1-y, z; (iv) x, y, 1-z; (v) -x, y, 1-z; (vi) x, 1-y, z; (vii) x, 1-y, 1-z; (viii) 1-x, y, z; (ix) 1-x, 1-y, z; (x) -0.5+z, -0.5+x, 1-y; (xi) -0.5+z, 1.5-x, 1-y; (xii) 0.5-x, 1-y, 1.5-z; (xiii) -1+x, y, z; (xiv) -1+x, 1-y, z; (xv) 1.5-y, -0.5+z, 1-x; (xvi) z, 0.5-x, 1.5-y; (xvii) 0.5+y, -0.5+z, x; (xviii) z, -0.5+x, 0.5+y; (xix) 1-z, 0.5-x, 1.5-y; (xx) 0.5-y, 1.5-z, 1-x; (xxi) x, y, 2-z; (xxii) 1-z, 1.5-x, 0.5+y; (xxiii) 0.5-y, 1.5-z, x; (xxiv) 0.5+y, 1-z, 0.5+x; (xxv) 1+x, y, z; (xxvi) 2-x, y, z; (xxvii) x, 0.5-y, 1.5-z; (xxviii) 1.5-x, 0.5-y, z; (xxix) 1.5-x, y, 1.5-z; (xxx) 0.5+x, -0.5+y, z; (xxxi) z, x, y; (xxxii) y, -0.5+z, 0.5+x; (xxxiii) -0.5+z, 0.5+x, y; (xxxiv) -0.5+y, z, 0.5+x; (xxxv) 0.5-y, z, 1.5-x; (xxxvi) -0.5+x, 1-y, 1.5-z; (xxxvii) -0.5+x, 0.5+y, z.

$Cu_2Zn_3Se_4$-large cell			
Atoms 1,2,3	**Angle 1,2,3 [°]**	**Atoms 1,2,3**	**Angle 1,2,3 [°]**
Se3—Zn1—Se3^{xix}	110.01(4)	Se4^{xxviii}—Cu1—Se4^{xxix}	109.5
Se3—Zn1—Se3^{xx}	110.01(4)	Se2^{xxxiii}—Cu2—Se2^{xxxiv}	109.95(3)
Se3^{xix}—Zn1—Se3^{xx}	110.01(4)	Se2^{xxxiii}—Cu2—Se2	109.95(3)
Se3—Zn1—Se4^{ix}	108.92(4)	Se2^{xxxiv}—Cu2—Se2	109.95(3)
Se3^{xix}—Zn1—Se4^{ix}	108.92(4)	Se2^{xxxiii}—Cu2—Se1	108.99(3)
Se3^{xx}—Zn1—Se4^{ix}	108.92(4)	Se2^{xxxiv}—Cu2—Se1	108.99(3)
Se2^{ix}—Zn2—Se2^{xxiv}	110.01(5)	Se2—Cu2—Se1	108.99(3)
Se2^{ix}—Zn2—Se4	109.51(3)	Se4^{xxxvi}—Cu3—Se4^{ix}	109.50(6)
Se2^{xxiv}—Zn2—Se4	109.51(3)	Se4^{xxxvi}—Cu3—Se2	109.469(7)
Se2^{ix}—Zn2—Se3^{xxv}	109.44(3)	Se4^{ix}—Cu3—Se2	109.469(7)
Se2^{xxiv}—Zn2—Se3^{xxv}	109.44(3)	Se4^{xxxvi}—Cu3—Se2^{xii}	109.469(7)
Se4—Zn2—Se3^{xxv}	108.91(5)	Se4^{ix}—Cu3—Se2^{xii}	109.469(7)
Se4—Cu1—Se4^{xxvii}	109.5	Se2—Cu3—Se2^{xii}	109.45(5)
Se4—Cu1—Se4^{xxviii}	109.5	-	-
Se4^{xxvii}—Cu1—Se4^{xxviii}	109.5	-	-
Se4—Cu1—Se4^{xxix}	109.5	-	-
Se4^{xxvii}—Cu1—Se4^{xxix}	109.5	-	-

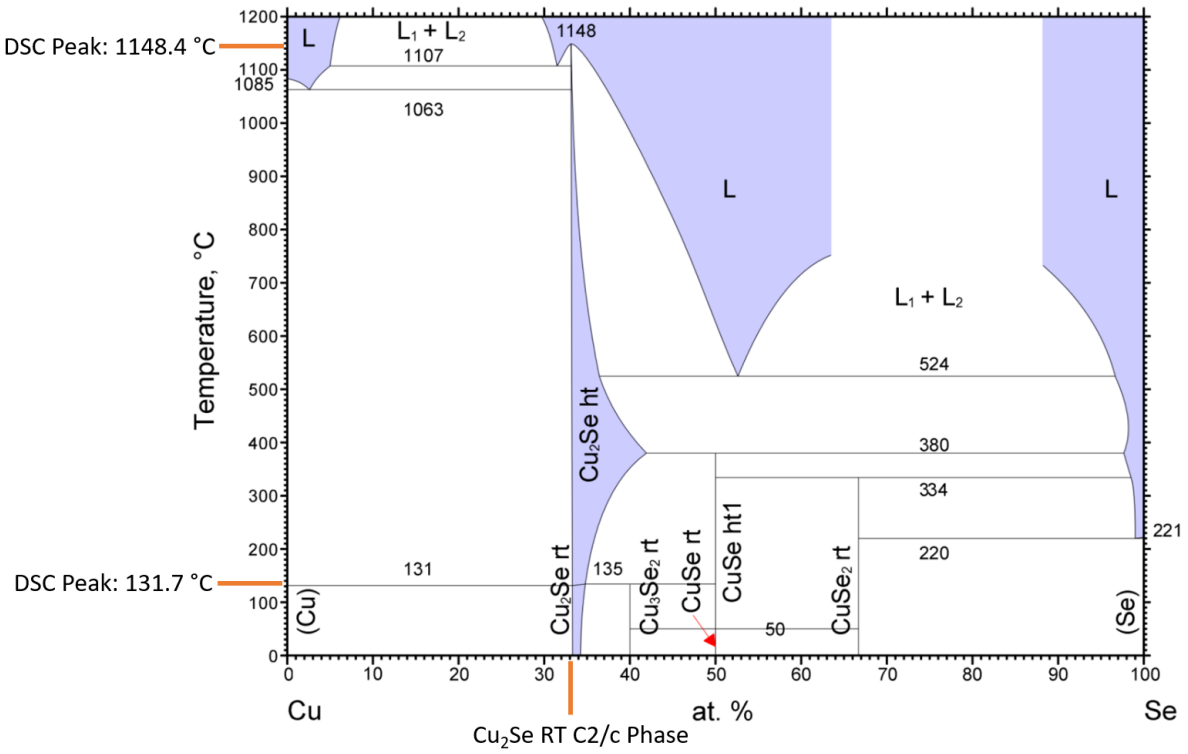

Figure C.1: Cu-Se binary phase diagram from ASM alloy phase diagram database (#101112[123]). The relevant $Cu_2Zn_3Se_4$ DSC peaks were noted with orange horizontal lines. The binary Cu_2Se RT C2/c phase was noted with an orange vertical line.

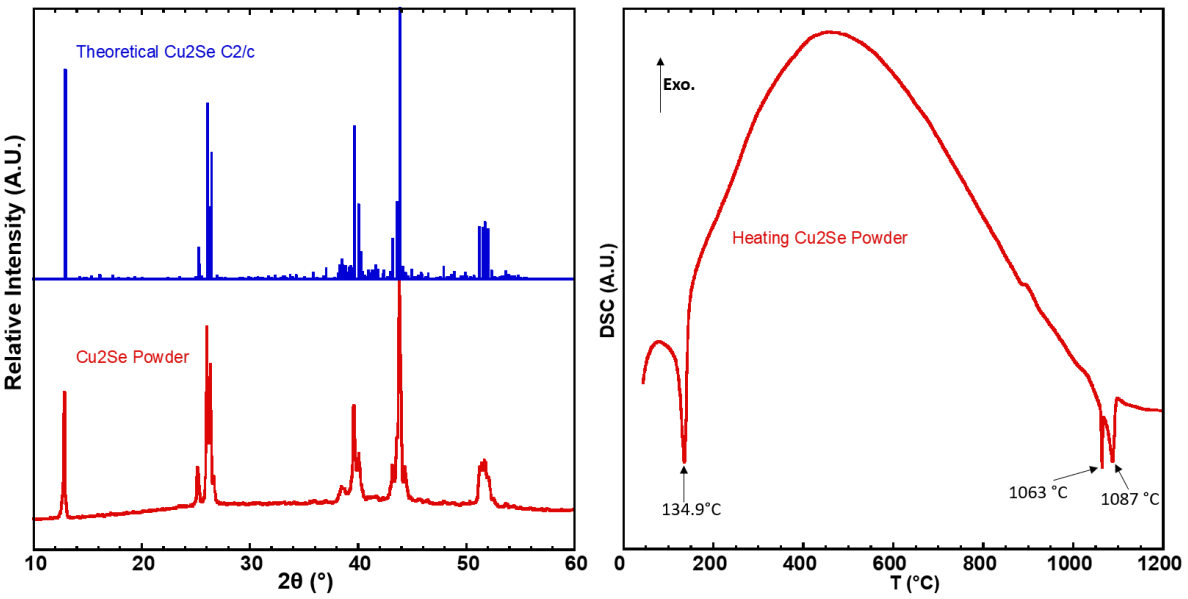

Figure C.2: Cu_2Se powder XRD, compared to the binary Cu_2Se C2/c phase. **(Right):** Heating DSC of Cu_2Se powder with the peaks noted.

Table C.5: XPS energy values, cross-referenced with the corresponding elemental energy windows.[31]

Cu XPS Information			
Element/Compound	**Cu $2p_{1/2}$ BE (eV)**	**Cu $2p_{3/2}$ BE (eV)**	**Cu Δ (eV)**
$Cu_2Zn_3Se_4$-Hot Pressed-#1	952.28	932.35	19.93
$Cu_2Zn_3Se_4$-Hot Pressed-#2	952.04	932.41	19.63
Cu Reference[31] (Cu_2Se, p. 203)	?	931.9	?
Cu Reference[31] (p. 86)	952.5	932.7	19.8
Zn XPS Information			
Element/Compound	**Zn $2p_{1/2}$ BE (eV)**	**Zn $2p_{3/2}$ BE (eV)**	**Zn Δ (eV)**
$Cu_2Zn_3Se_4$-Hot Pressed-#1	1044.59	1021.38	23.21
$Cu_2Zn_3Se_4$-Hot Pressed-#2	1044.96	1021.56	23.4
Zn Reference[31] (ZnS, p. 204)	?	1022	?
Zn Reference[31] (p. 88)	1044.77	1021.8	22.97
Se XPS Information			
Element/Compound	**Se $3d_{3/2}$ BE (eV)**	**Se $3d_{5/2}$ BE (eV)**	**Se Δ (eV)**
$Cu_2Zn_3Se_4$-Hot Pressed-#1	54.55	53.65	0.9
$Cu_2Zn_3Se_4$-Hot Pressed-#2	54.62	53.82	0.8
Se Reference[31] (SnSe, p. 237)	55	53.7	1.3
Se Reference[31] (p. 96)	56.46	55.6	0.86

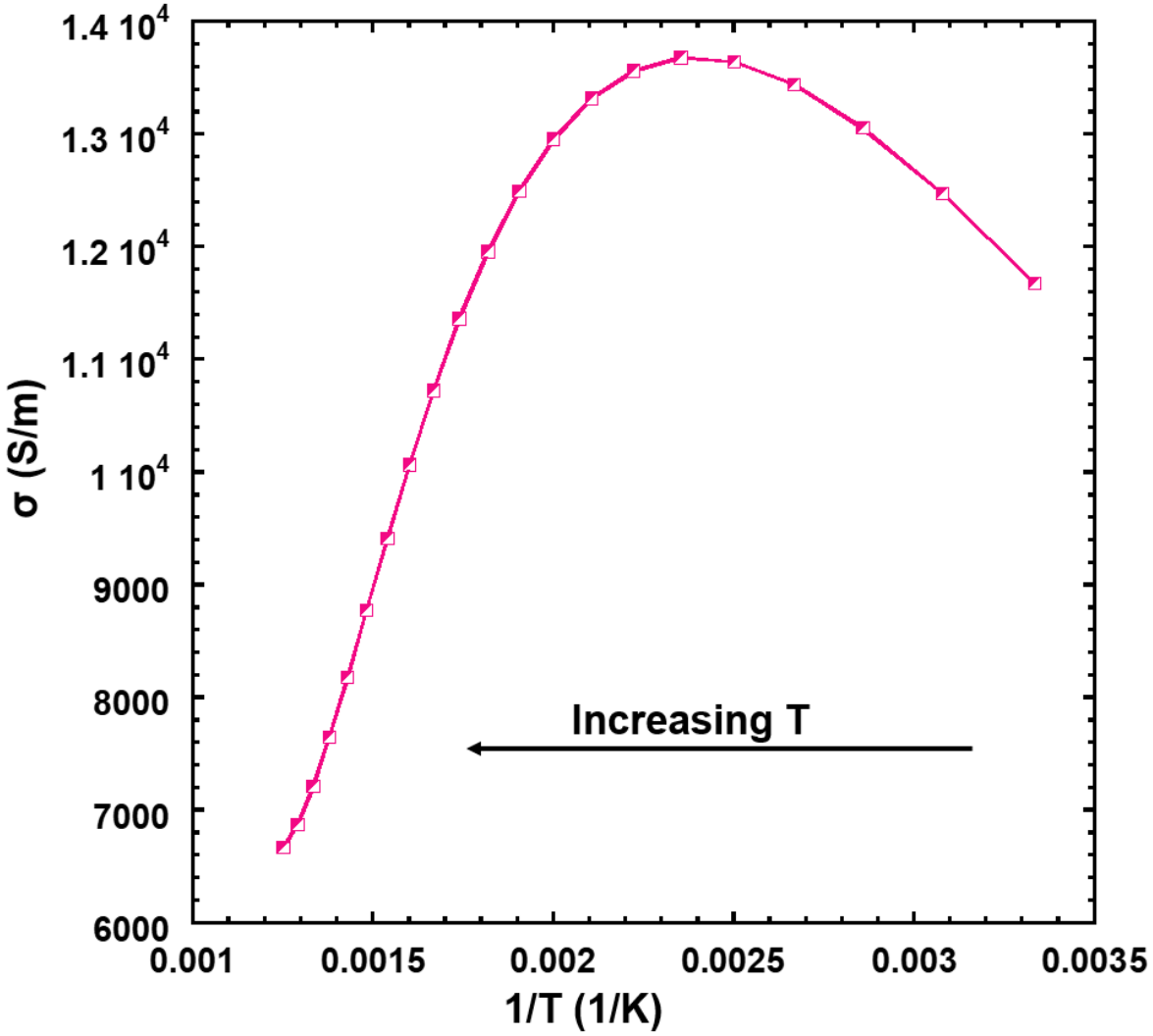

Figure C.3: $Cu_2Zn_3Se_4$ σ vs. 1/T plot. At high-T, we see the relationship become linear.

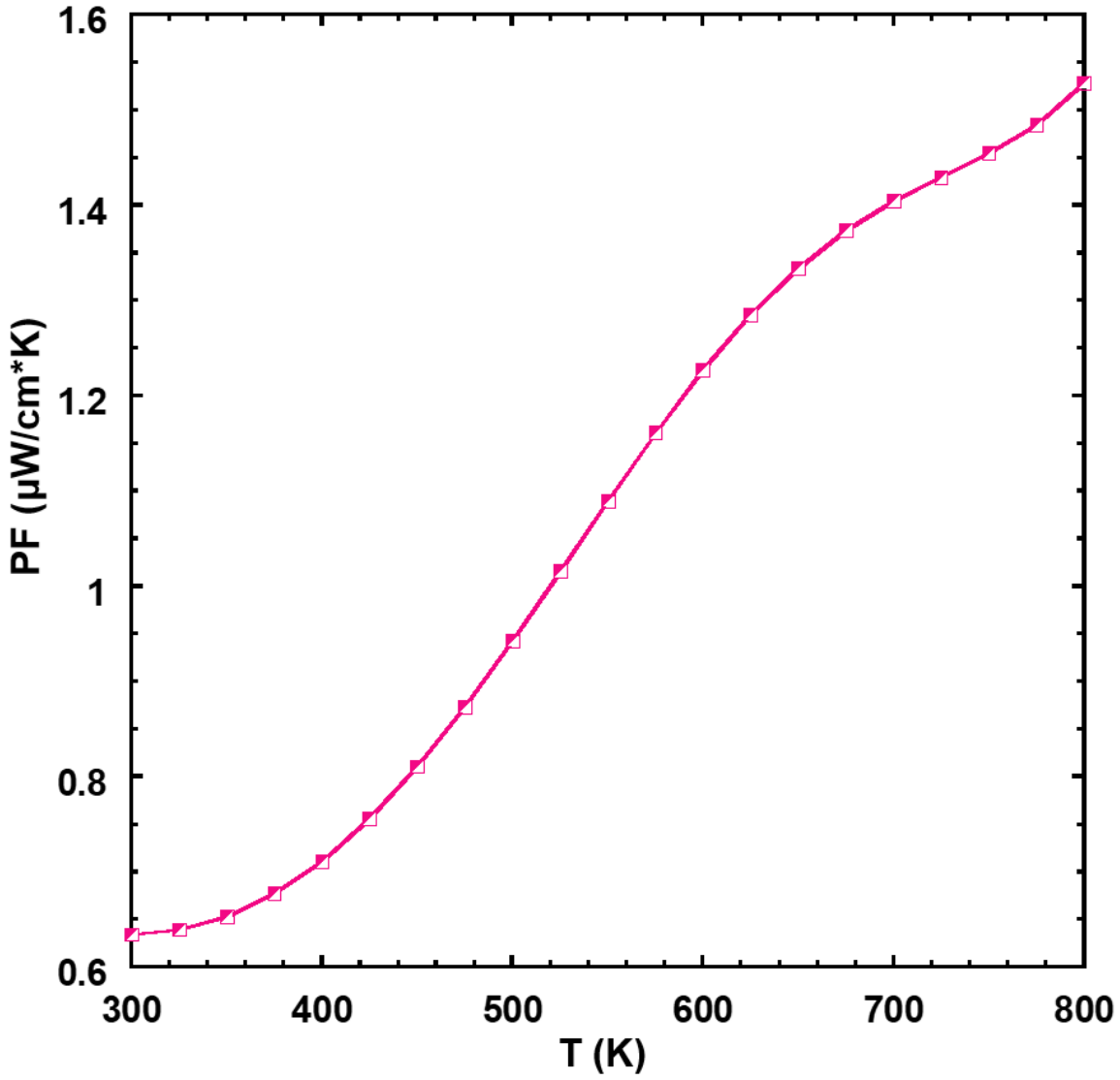

Figure C.4: Power Factor ($PF = \sigma S^2$) vs. temperature. With increasing T, PF also increased. Values ranged from 0.63-1.53 μW/cm*K.

APPENDIX D: $Cu_2Zn_2Ti_{0.5}Se_4$ (x = 1)

Table D.1: $Cu_{2.75}Zn_{0.625}TiSe_4$ anisotropic displacement parameters, in units of $Å^2 \times 10^{-4}$.

Atom	U_{11}	U_{22}	U_{33}	U_{23}	U_{13}	U_{12}
Se1	284.4(7)	284.4(7)	284.4(7)	25.9(30)	25.9(30)	25.9(30)
Cu1	93.4(8)	93.4(8)	38.1(12)	0	0	0
Zn1	126.8(20)	126.8(20)	126.8(20)	0	0	0
Ti1	157.3(17)	157.3(17)	157.3(17)	0	0	0

Table D.2: $Cu_{2.75}Zn_{0.625}TiSe_4$ selected inter-atomic bond angles (in °). Operators for generating equivalent atoms: (i) y, z, x; (ii) z, x, y; (iii) -x, -y, z; (iv) -y, x, 0.5-z; (v) y, -x, 0.5-z; (vi) y, x, 0.5+z; (vii) x, -y, -z; (viii) -x, y, -z; (ix) y, -z, -x; (x) -z, -x, y; (xi) x, 0.5-y, 0.5-z; (xii) 0.5-x, 0.5-y, z; (xiii) 0.5-x, y, 0.5-z.

Atoms 1,2,3	Angle 1,2,3 [°]	Atoms 1,2,3	Angle 1,2,3 [°]
$Se1^{iii}$—Cu1—Se1	108.81(11)	Se1—Ti1—$Se1^{xi}$	109.5
$Se1^{iii}$—Cu1—$Se1^{iv}$	109.80(5)	Se1—Ti1—$Se1^{xii}$	109.5
Se1—Cu1—$Se1^{iv}$	109.80(5)	$Se1^{xi}$—Ti1—$Se1^{xii}$	109.5
$Se1^{iii}$—Cu1—$Se1^{v}$	109.80(5)	Se1—Ti1—$Se1^{xiii}$	109.5
Se1—Cu1—$Se1^{v}$	109.80(5)	$Se1^{xi}$—Ti1—$Se1^{xiii}$	109.5
$Se1^{iv}$—Cu1—$Se1^{v}$	108.81(11)	$Se1^{xii}$—Ti1—$Se1^{xiii}$	109.5
Se1—Zn1—$Se1^{vii}$	109.5	-	-
Se1—Zn1—$Se1^{viii}$	109.5	-	-
$Se1^{vii}$—Zn1—$Se1^{viii}$	109.5	-	-
Se1—Zn1—$Se1^{iii}$	109.5	-	-
$Se1^{vii}$—Zn1—$Se1^{iii}$	109.5	-	-
$Se1^{viii}$—Zn1—$Se1^{iii}$	109.5	-	-

APPENDIX E: $Cu_2ZnTiSe_4$ (x = 0.5)

Table E.1: $Cu_2ZnTiSe_4$ small cell anisotropic displacement parameters, in units of $Å^2 \times 10^{-4}$.

$Cu_2ZnTiSe_4$-small cell						
Atom	**U_{11}**	**U_{22}**	**U_{33}**	**U_{12}**	**U_{13}**	**U_{23}**
Se1	163.8(10)	163.8(10)	163.8(10)	0	0	0
Cu1	89.6(12)	89.6(12)	89.6(12)	0	0	0
Zn1	89.6(12)	89.6(12)	89.6(12)	0	0	0
Ti1	515.1(125)	515.1(125)	515.1(125)	0	0	0

Table E.2: $Cu_2ZnTiSe_4$ large cell anisotropic displacement parameters, in units of $Å^2 \times 10^{-4}$.

$Cu_2ZnTiSe_4$-large cell						
Atom	**U_{11}**	**U_{22}**	**U_{33}**	**U_{23}**	**U_{13}**	**U_{12}**
Cu1	48(4)	48(4)	52.1(4)	0	0	-0.7(3)
Zn1	48(4)	48(4)	52.1(4)	0	0	-0.7(3)
Cu2	46.9(4)	46.9(4)	46.9(4)	0	0	0
Zn2	46.9(4)	46.9(4)	46.9(4)	0	0	0
Ti1	220.1(4)	220.1(4)	220.1(4)	0	0	0
Se1	107.2(3)	107.2(3)	107.2(3)	2.2(1)	2.2(1)	-2.2(1)
Se2	109.7(3)	109.7(3)	109.7(3)	-1.9(1)	1.9(1)	-1.9(1)

Table E.3: $Cu_2ZnTiSe_4$ small cell selected inter-atomic bond angles (in °). Small cell operators for generating equivalent atoms: i) 0.5+x, 0.5+y, z; (ii) x, 0.5+y, 0.5+z; (iii) 0.5+x, y, 0.5+z; (iv) x, 0.5+y, -0.5+z; (v) 0.5+x, y, -0.5+z; (vi) -0.5+x, -0.5+y, z; (vii) -0.5+x, y, -0.5+z; (viii) x, -0.5+y, -0.5+z; (ix) x, y, -1+z; (x) -0.5+x, y, 0.5+z; (xi) x, -0.5+y, 0.5+z; (xii) x, y, 1+z.

$Cu_2ZnTiSe_4$-small cell	
Atoms 1,2,3	**Angle 1,2,3 [°]**
Se1—Cu1/Zn1—Se1^{vi}	109.5
Se1—Cu1/Zn1—Se1^{vii}	109.5
Se1^{vi}—Cu1/Zn1—Se1^{vii}	109.5
Se1—Cu1/Zn1—Se1^{viii}	109.5
Se1^{vi}—Cu1/Zn1—Se1^{viii}	109.5
Se1^{vii}—Cu1/Zn1—Se1^{viii}	109.5
Se1^{vi}—Ti1—Se1	109.5
Se1^{vi}—Ti1—Se1^{x}	109.5
Se1—Ti1—Se1^{x}	109.5
Se1^{vi}—Ti1—Se1^{xi}	109.5
Se1—Ti1—Se1^{xi}	109.5
Se1^{x}—Ti1—Se1^{xi}	109.5

Table E.4: $Cu_2ZnTiSe_4$ large cell selected inter-atomic bond angles (in °). Large cell operators for generating equivalent atoms: (i) 0.25-z, 0.25-x, 0.25-y; (ii) 0.25-x, 0.25-y, 0.25-z; (iii) x, 0.5+y, 0.5+z; (iv) 0.75-x, 0.25+y, 1.75+z; (v) -0.5-z, -1-x, 1.5+y; (vi) 1.25-x, 1.75-z, 1.75-y; (vii) 1.25-x, 1.75+y, 1.75+z; (viii) 0.75-y, -0.75+x, 0.75+z; (ix) 0.25-z, 1.75+y, 0.75+x; (x) 0, 0, 0; (xi) x, 1+y, z; (xii) 0, 0, 0; (xiii) y, z, x; (xiv) 0, 0, 0; (xv) x, 0.5+y, -0.5+z; (xvi) -0.5+z, 0.5+x, y; (xvii) 0, 0, 0; (xviii) 0, 0, 0; (xix) y, 0.5-x, 1.5-z; (xx) 0.25-y, 0.25-z, 1.25-x; (xxi) 0, 0, 0; (xxii) -0.75-y, 0.75-x, 0.75-z; (xxiii) 0.5+x, -z, 1.5-y; (xxiv) 0.25+z, 0.25+x, 0.25-y; (xxv) 0, 0, 0; (xxvi) 0.5+z, 1-y, 0.5-x; (xxvii) x, -1+y, z; (xxviii) -y, -0.5-x, -0.5+z; (xxix) x, -0.5+y, -0.5+z; (xxx) -0.5+z, -0.5+x, y; (xxxi) 0, 0, 0.

$Cu_2ZnTiSe_4$-large cell			
Atoms 1,2,3	**Angle 1,2,3 [°]**	**Atoms 1,2,3**	**Angle 1,2,3 [°]**
Se1—Cu1|Zn1—Se1^{i}	109.484(19)	Se1^{xviii}—Ti1—Se1^{xix}	109.5
Se1—Cu1|Zn1—Se2^{ii}	109.5	Se1^{xviii}—Ti1—Se1^{xx}	109.5
Se1^{i}—Cu1|Zn1—Se2^{ii}	109.5	Se1^{xix}—Ti1—Se1^{xx}	109.5
Se1—Cu1|Zn1—Se2^{iii}	109.5	Se1^{xviii}—Ti1—Se1	109.5
Se1^{i}—Cu1|Zn1—Se2^{iii}	109.5	Se1^{xix}—Ti1—Se1	109.5
Se2^{ii}—Cu1|Zn1—Se2^{iii}	109.459(19)	Se1^{xx}—Ti1—Se1	109.5
Se2^{ix}—Cu2|Zn2—Se2^{x}	109.5	-	-
Se2^{ix}—Cu2|Zn2—Se2^{i}	109.5	-	-
Se2^{x}—Cu2|Zn2—Se2^{i}	109.5	-	-
Se2^{ix}—Cu2|Zn2—Se2^{xi}	109.5	-	-
Se2^{x}—Cu2|Zn2—Se2^{xi}	109.5	-	-
Se2^{i}—Cu2|Zn2—Se2^{xi}	109.5	-	-

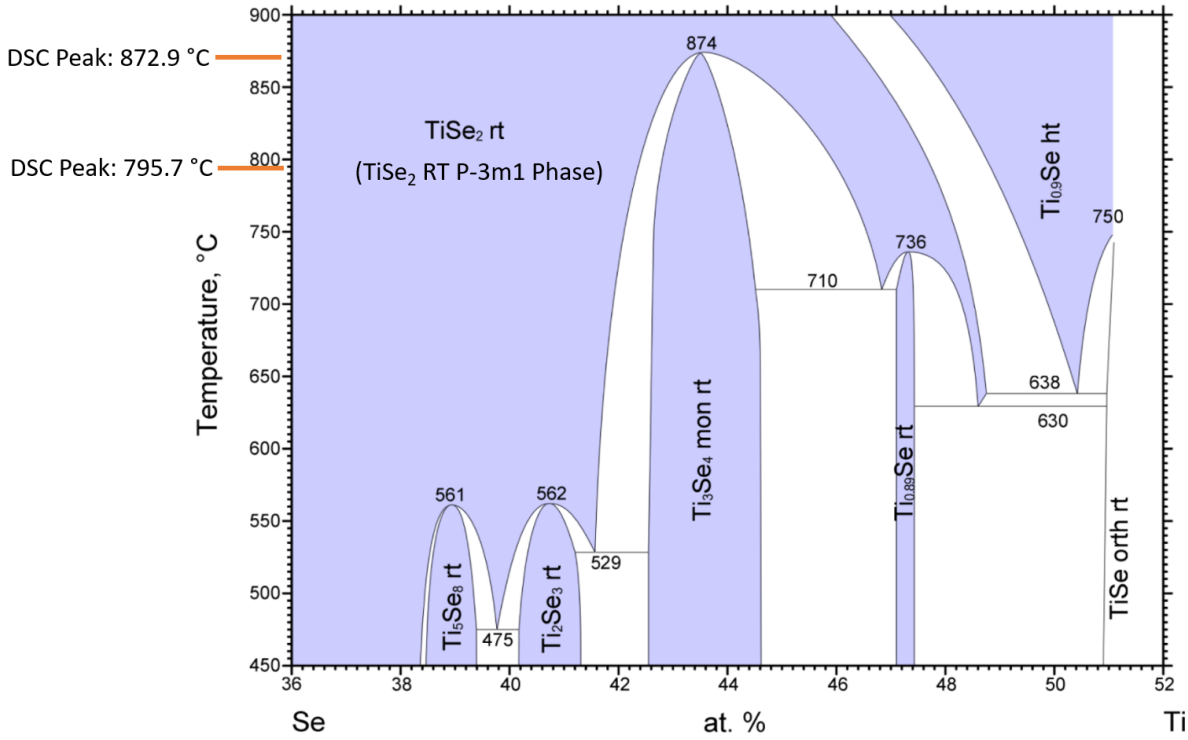

Figure E.1: Ti-Se binary phase diagram from ASM alloy phase diagram database (#903522[124]). The relevant $Cu_2ZnTiSe_4$ DSC peaks were noted with orange horizontal lines. The binary $TiSe_2$ RT P-3m1 phase was also noted. Note: this phase diagram displays a Ti At% range from 36-52 At% Ti. For the $TiSe_2$ RT P-3m1 phase, this corresponds to 33 At% Ti. So, this phase diagram does not display the optimal Ti At% range. Interestingly, this was the only Ti-Se binary phase diagram on the ASM database.

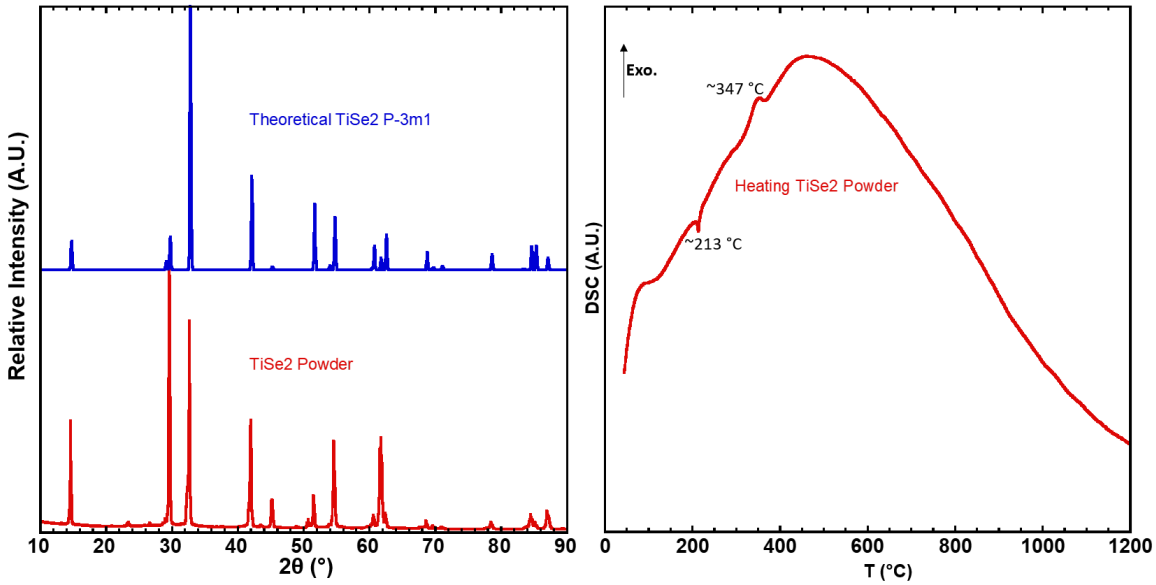

Figure E.2: (Left): $TiSe_2$ powder XRD, compared to the binary $TiSe_2$ phase. **(Right):** Heating DSC of $TiSe_2$ powder with the peaks noted. This data was used for comparison purposes with the $Cu_2ZnTiSe_4$ DSC peaks.

APPENDIX F: $Cu_2Ti_{1.5}Se_4$ (x = 0)

Table F.1: $Cu_3Ti_{1.25}Se_4$ anisotropic displacement parameters, in units of $Å^2 \times 10^{-4}$.

Atom	U_{11}	U_{22}	U_{33}	U_{23}	U_{13}	U_{12}
Cu1	177.1(5)	177.1(5)	138(6)	0	0	2.1(8)
Cu2	125.4(10)	125.4(10)	125.4(10)	0	0	0
Ti2	125.4(10)	125.4(10)	125.4(10)	0	0	0
Ti1	216.1(13)	216.1(13)	216.1(13)	0	0	0
Ti3	273.3(31)	273.3(31)	273.3(31)	0	0	0
Ti4	83.9(12)	83.9(12)	83.9(12)	0	0	0
Se1	202.7(7)	202.7(7)	202.7(7)	-7.9(5)	-7.9(5)	-7.9(5)
Se2	124(5)	124(5)	124(5)	9.5(4)	-9.5(4)	9.5(4)

Table F.2: $Cu_3Ti_{1.25}Se_4$ selected inter-atomic bond angles (in °). Operators for generating equivalent atoms: (i) 0.5-x, 0.5-y, z; (ii) 0.5-x, y, 0.5-z; (iii) x, 0.5-y, 0.5-z; (iv) z, x, y; (v) 0.5-z, 0.5-x, y; (vi) y, z, x; (vii) y, 0.5-z, 0.5-x; (viii) x, 0.5-y, -0.5-z; (ix) 0.5-x, y, -0.5-z; (x) 0.5+z, x, -0.5+y; (xi) -z, 0.5-x, -0.5+y; (xii) y, 0.5+z, -0.5+x; (xiii) y, -z, -x; (xiv) -x, y, -z; (xv) x, 1-y, -z; (xvi) -x, 1-y, z; (xvii) 1-x, 1-y, z; (xviii) 1-x, y, -z.

Atoms 1,2,3	Angle 1,2,3 [°]	Atoms 1,2,3	Angle 1,2,3 [°]
$Se1^{i}$—Cu1—Se1	108.83(7)	Se1—Ti1—$Se1^{i}$	109.5
$Se1^{i}$—Cu1—$Se2^{i}$	109.78(2)	$Se1^{viii}$—Ti1—$Se1^{i}$	109.5
Se1—Cu1—$Se2^{i}$	109.78(2)	$Se1^{ix}$—Ti1—$Se1^{i}$	109.5
$Se1^{i}$—Cu1—Se2	109.78(2)	$Se2^{xiv}$—Ti3—Se2	109.5
Se1—Cu1—Se2	109.78(2)	$Se2^{xiv}$—Ti3—$Se2^{xv}$	109.5
$Se2^{i}$—Cu1—Se2	108.89(7)	Se2—Ti3—$Se2^{xv}$	109.5
$Se2^{ii}$—Cu2|Ti2—$Se2^{iii}$	109.5	$Se2^{xiv}$—Ti3—$Se2^{xvi}$	109.5
$Se2^{ii}$—Cu2|Ti2—$Se2^{i}$	109.5	Se2—Ti3—$Se2^{xvi}$	109.5
$Se2^{iii}$—Cu2|Ti2—$Se2^{i}$	109.5	$Se2^{xv}$—Ti3—$Se2^{xvi}$	109.5
$Se2^{ii}$—Cu2|Ti2—Se2	109.5	Se1—Ti4—$Se1^{xv}$	109.5
$Se2^{iii}$—Cu2|Ti2—Se2	109.5	Se1—Ti4—$Se1^{xvii}$	109.5
$Se2^{i}$—Cu2|Ti2—Se2	109.5	$Se1^{xv}$—Ti4—$Se1^{xvii}$	109.5
Se1—Ti1—$Se1^{viii}$	109.5	Se1—Ti4—$Se1^{xviii}$	109.5
Se1—Ti1—$Se1^{ix}$	109.5	$Se1^{xv}$—Ti4—$Se1^{xviii}$	109.5
$Se1^{viii}$—Ti1—$Se1^{ix}$	109.5	$Se1^{xvii}$—Ti4—$Se1^{xviii}$	109.5

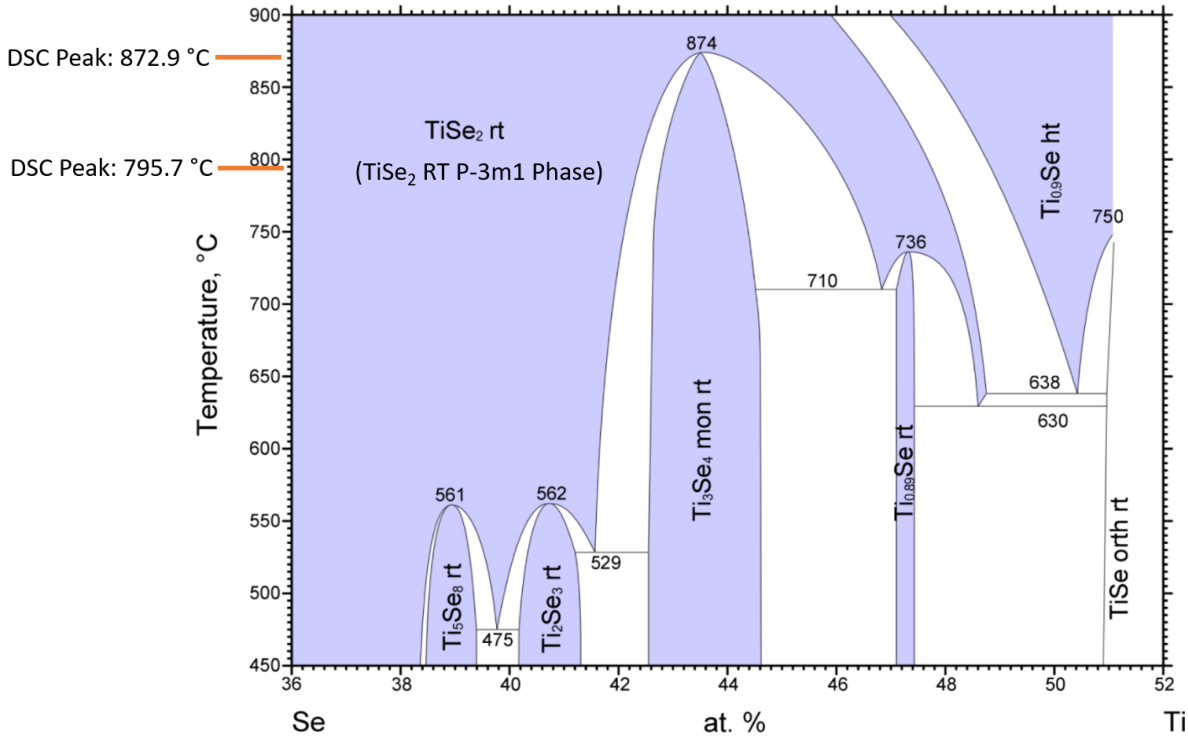

Figure F.1: Ti-Se binary phase diagram from ASM alloy phase diagram database (#903522[124]). The relevant $Cu_2Ti_{1.5}Se_4$ DSC peaks were noted with orange horizontal lines. The binary $TiSe_2$ RT P-3m1 phase was also noted. Note: this phase diagram displays a Ti At% range from 36-52 At% Ti. For the $TiSe_2$ RT P-3m1 phase, this corresponds to 33 At% Ti. So, this phase diagram does not display the optimal Ti At% range. Interestingly, this was the only Ti-Se binary phase diagram on the ASM database.

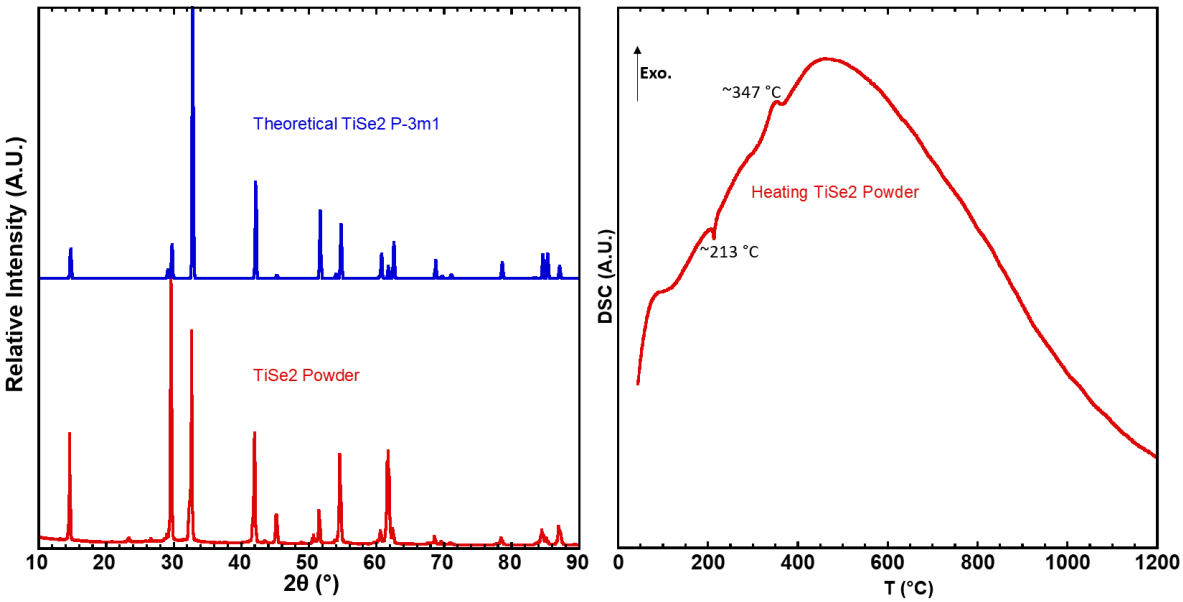

Figure F.2: $TiSe_2$ powder XRD, compared to the binary $TiSe_2$ phase. **(Right):** Heating DSC of $TiSe_2$ powder with the peaks noted. This data was used for comparison purposes with the $Cu_2Ti_{1.5}Se_4$ DSC peaks.

APPENDIX G: $Cu_2Mn_3Se_4$

Table G.1: $Cu_2Mn_3Se_4$ small cell anisotropic displacement parameters, in units of $Å^2 \times 10^{-4}$.

$Cu_2Mn_3Se_4$-small cell						
Atom	**U_{11}**	**U_{22}**	**U_{33}**	**U_{12}**	**U_{13}**	**U_{23}**
Mn1	306.7(8)	306.7(8)	306.7(8)	0	0	0
Cu1	306.7(8)	306.7(8)	306.7(8)	0	0	0
Se2	308.4(8)	308.4(8)	308.4(8)	0	0	0

Table G.2: $Cu_2Mn_3Se_4$ large cell anisotropic displacement parameters, in units of $Å^2 \times 10^{-4}$.

$Cu_2Mn_3Se_4$-large cell						
Atom	**U_{11}**	**U_{22}**	**U_{33}**	**U_{23}**	**U_{13}**	**U_{12}**
Se1	234.4(30)	234.4(30)	234.4(30)	-94.4(61)	-94.4(61)	-94.4(61)
Se2	355.4(41)	355.4(41)	355.4(41)	-39.9(84)	-39.9(84)	-39.9(84)
Cu3	1880.4(378)	1880.4(378)	1880.4(378)	-	-	-
Cu4	894(216)	894(216)	894(216)	-	-	-
Mn5	34.9(23)	-	-	-	-	-

Table G.3: $Cu_2Mn_3Se_4$ small cell selected inter-atomic bond angles (in °). Small cell operators for generating equivalent atoms: (i) x, 0.5+y, 0.5+z; (ii) -0.5+x, 0.5+y, z; (iii) -0.5+x, y, 0.5+z; (iv) -x, 0.5-y, 0.5-z; (v) 0.5-x, 1-y, 0.5-z; (vi) 0.5-x, 0.5-y, -z; (vii) 0.5-x, 0.5-y, 1-z; (viii) 1-x, 0.5-y, 0.5-z; (ix) 0.5-x, -y, 0.5-z; (x) x, -0.5+y, -0.5+z; (xi) 0.5+x, -0.5+y, z; (xii) 1-x, -y, -z; (xiii) 0.5+x, y, -0.5+z.

$Cu_2Mn_3Se_4$-small cell	
Atoms 1,2,3	**Angle 1,2,3 [°]**
$Se2^{i}$—Mn1/Cu1—$Se2^{ii}$	109.5
$Se2^{i}$—Mn1/Cu1—$Se2^{iii}$	109.5
$Se2^{ii}$—Mn1/Cu1—$Se2^{iii}$	109.5
$Se2^{i}$—Mn1/Cu1—Se2	109.5
$Se2^{ii}$—Mn1/Cu1—Se2	109.5
$Se2^{iii}$—Mn1/Cu1—Se2	109.5

Table G.4: $Cu_2Mn_3Se_4$ large cell selected inter-atomic bond angles (in °). Large cell operators for generating equivalent atoms: (i) 0, 0z, 0; (ii) -0.5+y, 0.5+z, -1+x; (iii) y, 1.5+z, 0.5+x; (iv) -1+x, y, z; (v) 1+y, 1-z, -x; (vi) z, -0.5+x, -0.5+y; (vii) y, 1-z, -x; (viii) 0, 0, 0; (ix) 1.25-y, 1.25+x, 0.25+z; (x) -0.5-y, -1-x, 0.5+z; (xi) x, 1.5+z, 0.5+y; (xii) 0, 0, 0; (xiii) 0, 0, 0; (xiv) 0.25+x, 1.25-z, 0.25+y; (xv) 1.25+z, 0.25+y, 0.25-x; (xvi) y, 0.5+z, -0.5+x; (xvii) 0.5+z, x, -0.5+y; (xviii) 0.25-y, 1.25+x, 0.25+z; (xix) 0.25+z, 0.25+y, 0.25-x; (xx) 0.75+z, 0.25+x, 1.75-y; (xxi) 0, 0, 0; (xxii) 1.25+x, 1.25-z, 0.25+y; (xxiii) 1+x, y, z; (xxiv) 0, 0, 0; (xxv) 1+y, 1.5+z, 0.5+x; (xxvi) 0.25-z, 1.25-y, -0.75-x; (xxvii) 1-y, -0.5+z, -0.5-x.

$Cu_2Mn_3Se_4$-large cell			
Atoms 1,2,3	**Angle 1,2,3 [°]**	**Atoms 1,2,3**	**Angle 1,2,3 [°]**
Se2—Cu3—Se2^{xiv}	109.5	Se1^{xxii}—Mn5—Se1^{xxiii}	114.9(6)
Se2—Cu3—Se2^{xv}	109.5	Se1^{xxii}—Mn5—Se2^{xv}	109.26(4)
Se2^{xiv}—Cu3—Se2^{xv}	109.5	Se1^{xxiii}—Mn5—Se2^{xv}	109.26(4)
Se2—Cu3—Se2^{ix}	109.5	Se1^{xxii}—Mn5—Se2^{ix}	109.26(4)
Se2^{xiv}—Cu3—Se2^{ix}	109.5	Se1^{xxiii}—Mn5—Se2^{ix}	109.26(4)
Se2^{xv}—Cu3—Se2^{ix}	109.5	Se2^{xv}—Mn5—Se2^{ix}	104.4(5)
Se1—Cu4—Se1^{xiv}	109.5	-	-
Se1—Cu4—Se1^{xviii}	109.5	-	-
Se1^{xiv}—Cu4—Se1^{xviii}	109.5	-	-
Se1—Cu4—Se1^{xix}	109.5	-	-
Se1^{xiv}—Cu4—Se1^{xix}	109.5	-	-
Se1^{xviii}—Cu4—Se1^{xix}	109.5	-	-

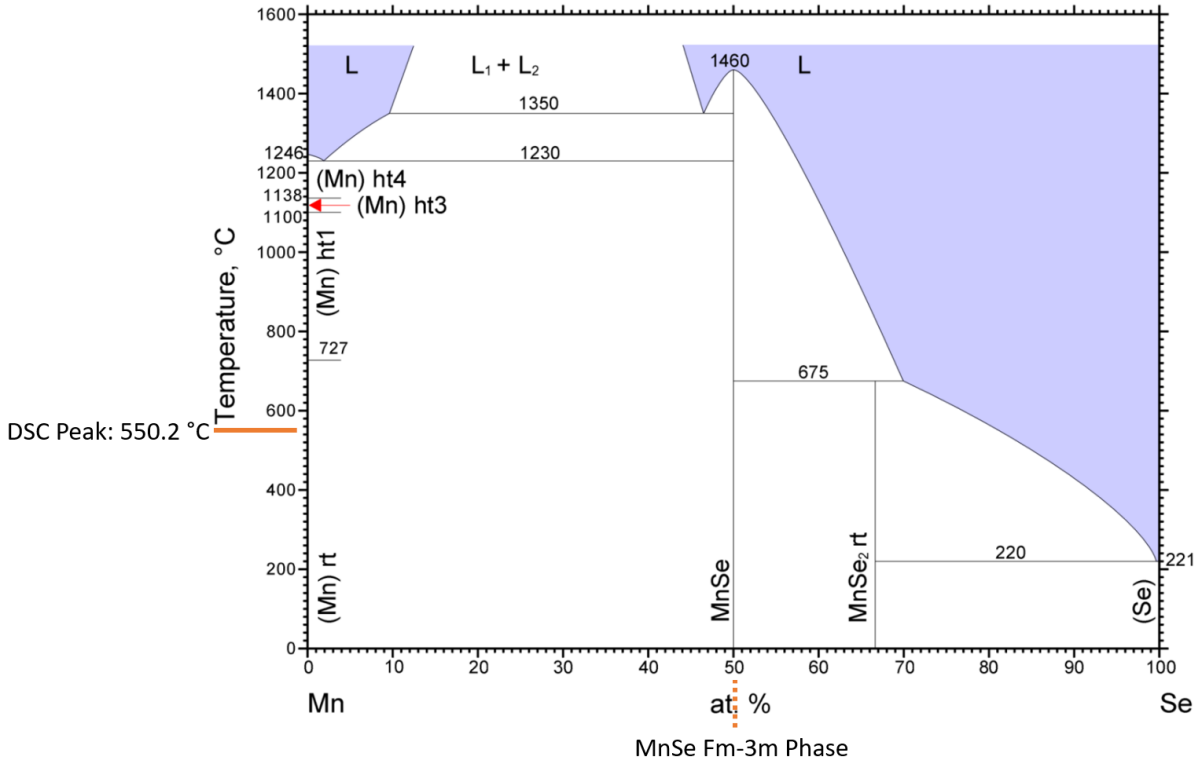

Figure G.1: Mn-Se binary phase diagram from ASM alloy phase diagram database (#901613[125]). The relevant $Cu_2Mn_3Se_4$ DSC peak was noted with an orange horizontal line. The binary MnSe Fm-3m phase was noted with an orange vertical line.

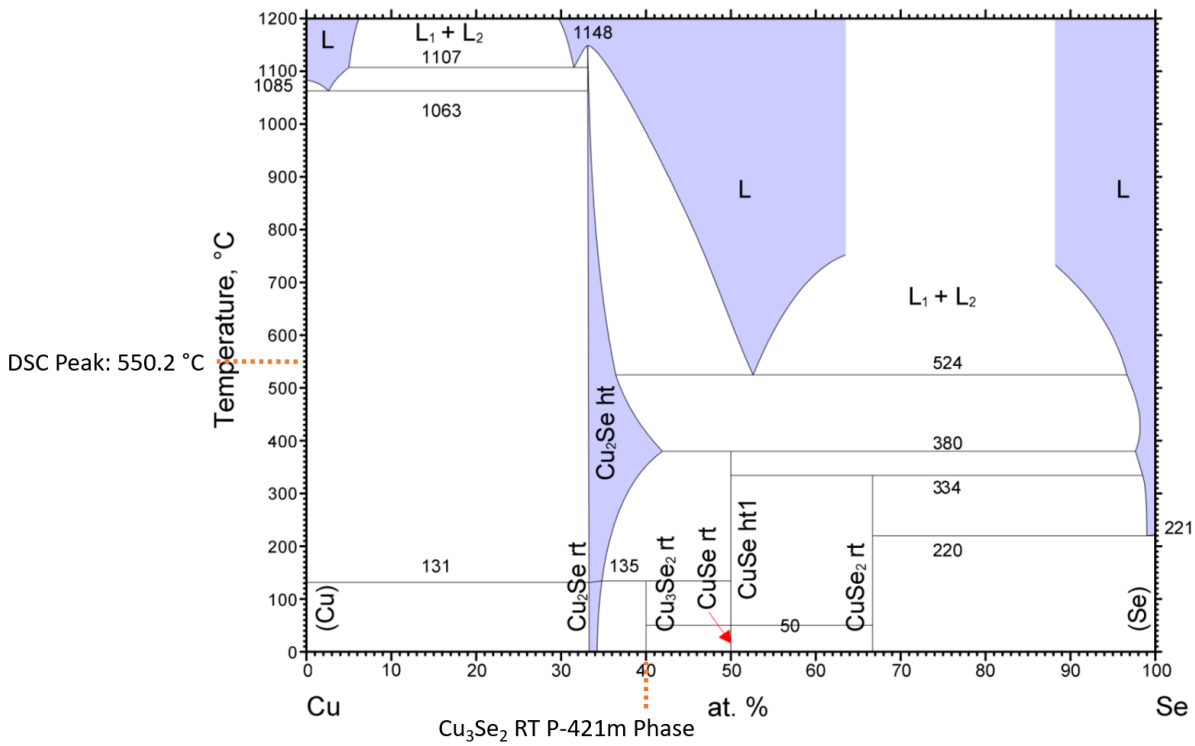

Figure G.2: Cu-Se binary phase diagram from ASM alloy phase diagram database (#101112[123]). The relevant DSC peak was noted with an orange horizontal line. The binary Cu_3Se_2 RT P-421m phase was noted with an orange vertical line.

APPENDIX H: Magnetic Property Equations

To predict the magnetic moment of a compound, we must first review quantum numbers. The principal quantum number (n), orbital angular momentum quantum number (l), magnetic quantum number (m_l), and spin quantum number (m_s) are given by:

$$n = 1, 2, 3, \ldots \quad \textbf{H-1}$$

$$l = 0, 1, 2, \ldots, n - 1 \quad \textbf{H-2}$$

$$m_l = -l, -l+1, \ldots, +l \quad \textbf{H-3}$$

$$m_s = \pm 1/2 \quad \textbf{H-4.}$$

Now that the four quantum numbers have been reviewed, we can utilize Hund's rules, as they provide us with the predictive power to calculate the expected magnetic moment. The first of Hund's rules states that the total spin angular momentum (S) is given as the summation of the individual spin quantum number values. Hund's second rule lists the total orbital angular momentum (L) as the summation of the magnetic quantum number values. The third Hund's rule states that the total angular momentum of a less-than half-filled orbital should be calculated by the difference between J and S; for a more than half-full orbital, J and S are additive. The equations for Hund's rules are as follows:

$$S = \sum m_s \quad \textbf{H-5}$$

$$L = \sum m_l \quad \textbf{H-6}$$

$$J = |L - S| \ (less\ than\ half - full\ orbital) \quad \textbf{H-7}$$

$$J = |L + S| \ (more\ than\ half - full\ orbital) \quad \textbf{H-8.}$$

With S, L, and J defined, the Landé g-factor (g_l) and theoretical magnetic moment can then be calculated:

$$g_l = 1 + \frac{J(J+1)+S(S+1)-L(L+1)}{2J(J+1)} \qquad \textbf{H-9}$$

$$\mu_{theo} = g_l\sqrt{J(J+1)}\mu_B \qquad \textbf{H-10,}$$

where μ_B = Bohr magneton = 9.274 x 10^{-24} J/T.

To compare the effective magnetic moment (μ_{eff}) to μ_{theo}, one must first define the Curie-Weiss law of paramagnetism. This equation is given by:

$$\chi = \frac{C}{T - \theta} \qquad \textbf{H-11,}$$

where χ is magnetic susceptibility, C is the Curie constant, T is temperature, and θ is the Weiss constant. When θ = -, this corresponds to antiferromagnetic ordering; when θ = +, this means ferromagnetic ordering. Now, taking the inverse magnetic susceptibility:

$$\chi^{-1} = \frac{1}{C}T - \frac{\theta}{C}, \qquad \textbf{H-12,}$$

we can plot χ^{-1} vs. T and fit a linear trendline. From this fitting, we can calculate C and θ.

With the known value of the Curie constant, the Langevin theory of paramagnetism can be applied to calculate μ_{eff}.

$$\mu_{eff} = \sqrt{\frac{3k_B}{N_A}C} \qquad \textbf{H-13,}$$

where k_B is the Boltzmann constant and N_A is Avogadro's number.

APPENDIX I: Thermoelectric Equations

Thermoelectric figure of merit (zT):

$$zT = \frac{\sigma S^2}{\kappa_T} T \qquad \textbf{I-1.}$$

Electrical conductivity of a semiconductor in the low-T extrinsic region:

$$\sigma = \sigma_o e^{-E_a/k_B T} \qquad \textbf{I-2.}$$

Electrical conductivity of a semiconductor in the high-T intrinsic region:

$$\sigma = \sigma_o e^{-E_g/2k_B T} \qquad \textbf{I-3.}$$

Arrhenius relation of a semiconductor in the low-T extrinsic region:

$$\ln(\sigma) = -\frac{E_a}{k_B} T + \ln(\sigma_o) \qquad \textbf{I-4.}$$

When ln(σ) vs. 1/T is plotted, we get a linear relationship y = mx + b. Similarly, for the Arrhenius relation of a semiconductor in the high-T intrinsic region:

$$\ln(\sigma) = -\frac{E_g}{2k_B} T + \ln(\sigma_o) \qquad \textbf{I-5.}$$

Seebeck coefficient:

$$S = -\frac{\Delta V}{\Delta T} \qquad \textbf{I-6.}$$

Seebeck coefficient for a p-type semiconductor according to the single parabolic band model:

$$S = \frac{8\pi^{8/3} k_B^{\,2}}{3^{5/3} h^2} m^* p^{-2/3} T \qquad \textbf{I-7.}$$

Effective mass and band structure curvature:[93]

$$m^* = \hbar^2 \left(\frac{d^2E}{dk^2}\right)^{-1} \qquad \textbf{I-8.}$$

Hole carrier concentration is defined by the following four equations:[110]

$$p_v(x) = P_v(T)e^{-(\mu - E_v)/k_B T} \quad \textbf{I-9}$$

$$P_v(T) = \int_{-\infty}^{E_v} g_v(E)e^{-(E_v - E)/k_B T} dE \quad \textbf{I-10}$$

$$g_v(E) = \int_{S_v(E)}^{0} \frac{1}{4\pi^3} \frac{1}{|\nabla E_v(k)|} dS \quad \textbf{I-11}$$

$$\mu = \mu_i \approx E_v + \frac{1}{2}E_g + \frac{3}{4}k_B T \ln\left(\frac{m_v}{m_c}\right) \quad \textbf{I-12.}$$

Note: these four equations only hold when the following condition is satisfied: [110]

$$\mu - E_v \gg k_B T \quad \textbf{I-13.}$$

Relationship between hole carrier concentration and electrical conductivity:

$$\sigma = pe\mu_h = pe\frac{e\tau_h}{m_h} = p\frac{e^2\tau_h}{m_h} \quad \textbf{I-14.}$$

Power Factor:

$$PF = \sigma S^2 \quad \textbf{I-15.}$$

Total thermal conductivity (density, C_p, D):

$$\kappa_T = \rho C_P D \quad \textbf{I-16.}$$

Dulong-Petit Law for c_p:

$$C_p = \frac{N3R}{FM} \quad \textbf{I-17,}$$

where N = number of atoms in the unit cell, R is the ideal gas constant, and FM is the formula mass.

Thermal diffusivity:

$$D = D_o e^{-Q_d/RT} \quad \textbf{I-18.}$$

Total thermal conductivity:

$$\kappa_T = \kappa_L + \kappa_e \quad \textbf{I-19.}$$

Lattice thermal conductivity:

$$\kappa_L = \kappa_T - \kappa_e \quad \textbf{I-20.}$$

Wiedemann-Franz Law:

$$\kappa_e = L\sigma T \quad \textbf{I-21.}$$

Lorenz number for a metal:

$$L = 2.44 \times 10^{-8}\ W\Omega/K^2 \quad \textbf{I-22.}$$

Fermi-corrected Lorenz number for a semiconductor with low electrical conductivity. It utilizes the sample's temperature-dependent Seebeck coefficient for the calculation. The equations listed below were gathered from Lu *et al*.'s work on $Cu_2Se/CuFeSe_2$ composites.[57]

$$L = \left(\frac{k_B}{e}\right)^2 \left[\frac{\left(r+\frac{7}{2}\right)\left(r+\frac{3}{2}\right)F_{r+1/2}F_{r+5/2}(\xi) - \left(r+\frac{5}{2}\right)^2 F_{r+3/2}{}^2(\xi)}{\left(r+\frac{3}{2}\right)^2 F_{r+1/2}{}^2(\xi)}\right] \quad \textbf{I-23}$$

$$F_n(\xi) = \int_0^\infty \frac{x^n}{1+e^{x-\xi}}\,dx \quad \textbf{I-24}$$

$$\xi = \frac{E_F}{k_B T} \quad \textbf{I-25}$$

$$|S| = \frac{k_B}{e}\left[\frac{\left(r+\frac{5}{2}\right)F_{r+3/2}(\xi)}{\left(r+\frac{3}{2}\right)F_{r+1/2}(\xi)} - \xi\right] \quad \textbf{I-26,}$$

where k_B, e, ξ, and F_n are the Boltzmann constant, elementary charge, reduced Fermi energy, and Fermi integral, respectively.[57] Additionally, r is the scattering parameter: -1/2 for acoustic phonon scattering and +3/2 for ionized impurity scattering; S is the Seebeck coefficient.[57]

APPENDIX J: Structural Equations

Bragg's Law:

$$2d\sin\left(\frac{2\theta}{2}\right) = \lambda \qquad \textbf{J-1.}$$

Rearranging Bragg's Law for $1/d^2$:

$$\frac{1}{d^2} = \left[\frac{2}{\lambda}\sin\left(\frac{2\theta}{2}\right)\right]^2 \qquad \textbf{J-2.}$$

Monoclinic interplanar spacing:

$$\frac{1}{d^2} = \frac{1}{\sin^2\beta}\left(\frac{h^2}{a^2} + \frac{k^2\sin^2\beta}{b^2} + \frac{l^2}{c^2} - \frac{2hl\cos\beta}{ac}\right) \qquad \textbf{J-3.}$$

The equation for a monoclinic cell volume V_{Cell} is as follows:

$$V_{Cell} = abc \times \sin\beta. \qquad \textbf{J-4.}$$

Equating the rearranged Bragg's Law to the monoclinic interplanar spacing:

$$\left[\frac{2}{\lambda}\sin\left(\frac{2\theta}{2}\right)\right]^2 = \frac{1}{\sin^2\beta}\left(\frac{h^2}{a^2} + \frac{k^2\sin^2\beta}{b^2} + \frac{l^2}{c^2} - \frac{2hl\cos\beta}{ac}\right) \qquad \textbf{J-5.}$$

$Zn_{1-y}Mn_ySe$ Vegard's Law equation:

$$a_{Zn_{1-y}Mn_ySe} = ya_{MnSe} + (1-y)a_{ZnSe} \qquad \textbf{J-6.}$$

Solving this $Zn_{1-y}Mn_ySe$ Vegard's Law equation for y:

$$y = \frac{a_{Zn_{1-y}Mn_ySe} - a_{ZnSe}}{a_{MnSe} - a_{ZnSe}}. \qquad \textbf{J-7.}$$

FullProf determined the weight percent of each phase by the equation:

$$ATZ = \frac{ZM_w f^2}{t} \qquad \textbf{J-8,}$$

where Z is the number of formula units per cell, M_w is the molecular weight, f is the site multiplicity, and t is the Brindley coefficient for microabsorption.

Orthorhombic interplanar spacing:

$$\frac{1}{d^2} = \frac{h^2}{a^2} + \frac{k^2}{b^2} + \frac{l^2}{c^2} \qquad \textbf{J-9.}$$

Equating the rearranged Bragg's Law to the orthorhombic interplanar spacing:

$$\left[\frac{2}{\lambda}\sin\left(\frac{2\theta}{2}\right)\right]^2 = \frac{h^2}{a^2} + \frac{k^2}{b^2} + \frac{l^2}{c^2} \qquad \textbf{J-10.}$$

APPENDIX K: Optical Equations

Bandgap and photon energy:

$$E = h\nu = \frac{hc}{\lambda} \geq E_g \qquad \textbf{K-1.}$$

Bandgap and photon energy with more typical units:

$$E\ (\text{in eV}) = \frac{hc}{\lambda e} \geq E_g(\text{in eV}) \qquad \textbf{K-2.}$$

Bandgap and photon wavelength:

$$\lambda\ (\text{in nm}) \leq \frac{hc}{E_g(\text{in eV}) \times e} \times 10^9 \qquad \textbf{K-3.}$$

Optical absorption coefficient:[126]

$$\alpha = \frac{4\pi k}{\lambda}, \qquad \textbf{K-4,}$$

where α is in units of m^{-1}. As such, a higher α will more efficiently absorb incident photons, allowing for a thinner film of absorber material to absorb the same amount of light.

Kubelka-Munk Function F(R):[33]

$$F(R) = \frac{(1-R)^2}{2R} = \frac{K}{S} \qquad \textbf{K-5.}$$

Extracting optical bandgap using F(R):[33]

$$[F(R) \times h\nu]^{1/r} \text{ vs. } h\nu \qquad \textbf{K-6.}$$

r = ½-direct, allowed transition (direct bandgap)
r = 3/2-direct, forbidden transition
r = 2-indirect, allowed transition (indirect bandgap)
r = 3-indirect, forbidden transition

REFERENCES

1. Moore, G. E., Progress in digital integrated electronics [Technical literaiture, Copyright 1975 IEEE. Reprinted, with permission. Technical Digest. International Electron Devices Meeting, IEEE, 1975, pp. 11-13.]. *IEEE Solid-State Circuits Society Newsletter* **2006,** *11* (3), 36-37.
2. Moore, G. E., Cramming more components onto integrated circuits, Reprinted from Electronics, volume 38, number 8, April 19, 1965, pp.114 ff. *IEEE Solid-State Circuits Society Newsletter* **2006,** *11* (3), 33-35.
3. Mitchell, M., More than Moore. *Nature* **2016,** *530*, 144-147.
4. Shalf, J., The future of computing beyond Moore's Law. *Philosophical Transactions of the Royal Society A: Mathematical, Physical and Engineering Sciences* **2020,** *378* (2166), 20190061.
5. Baibich, M. N.; Broto, J. M.; Fert, A.; Vandau, F. N.; Petroff, F.; Eitenne, P.; Creuzet, G.; Friederich, A.; Chazelas, J., Giant Magnetoresistance of (001)Fe/(001) Cr Magnetic Superlattices. *Phys Rev Lett* **1988,** *61* (21), 2472-2475.
6. Chappert, C.; Fert, A.; Van Dau, F. N., The emergence of spin electronics in data storage. *Nat Mater* **2007,** *6* (11), 813-823.
7. Dieny, B.; Speriosu, V. S.; Parkin, S. S. P.; Gurney, B. A.; Wilhoit, D. R.; Mauri, D., Giant Magnetoresistance in Soft Ferromagnetic Multilayers. *Phys Rev B* **1991,** *43* (1), 1297-1300.
8. Goda, K.; Kitsuregawa, M., The History of Storage Systems. *P Ieee* **2012,** *100*, 1433-1440.
9. Moodera, J. S.; Kinder, L. R.; Wong, T. M.; Meservey, R., Large Magnetoresistance at Room-Temperature in Ferromagnetic Thin-Film Tunnel-Junctions. *Phys Rev Lett* **1995,** *74* (16), 3273-3276.
10. Tanaka, M.; Sugahara, S., MOS-Based Spin Devices for Reconfigurable Logic. *Ieee T Electron Dev* **2007,** *54* (5), 961-976.
11. Marti, X.; Fina, I.; Jungwirth, T., Prospect for Antiferromagnetic Spintronics. *Ieee T Magn* **2015,** *51* (4).
12. Ohno, H., Making Nonmagnetic Semiconductors Ferromagnetic. *Science* **1998,** *281* (5379), 951-956.
13. Spaldin, N. A., *Magnetic Materials: Fundamentals and Applications*. 2nd ed.; Cambridge University Press: Cambridge, 2011.
14. Wang, H.; Chen, L.; Zhao, J., Enhancement of the Curie temperature of ferromagnetic semiconductor (Ga,Mn)As. *Science China Physics, Mechanics and Astronomy* **2013,** *56* (1), 99-110.
15. Lifshitz, M., Anomalies of Electron Characteristics of a Metal in the High Pressure Region. *Journal of Experimental and Theoretical Physics* **1960,** *11* (5), 1130-1135.
16. Beaulieu, S.; Dong, S.; Tancogne-Dejean, N.; Dendzik, M.; Pincelli, T.; Maklar, J.; R; Michael; Wolf, M.; Rubio, A.; Rettig, L.; Ernstorfer, R., Ultrafast Dynamical Lifshitz Transition. *arXiv pre-print server* **2021**.
17. Zhang, Y.; Wang, C.; Liu, G.; Liang, A.; Zhao, L.; Huang, J.; Gao, Q.; Shen, B.; Liu, J.; Hu, C.; Zhao, W.; Chen, G.; Jia, X.; Yu, L.; Zhao, L.; He, S.; Zhang, F.; Zhang, S.; Yang, F.; Wang, Z.; Peng, Q.; Xu, Z.; Chen, C.; Zhou, X., Temperature-induced Lifshitz transition in topological insulator candidate HfTe 5. *Science Bulletin* **2017,** *62* (13), 950-956.
18. Wu, Y.; Jo, N. H.; Ochi, M.; Huang, L.; Mou, D.; Bud'Ko, S. L.; Canfield, P. C.; Trivedi, N.; Arita, R.; Kaminski, A., Temperature-Induced Lifshitz Transition inWTe2. *Phys Rev Lett* **2015,** *115* (16).
19. Jian, Y.; Wu, Q.; Yang, M.; Feng, Q.; Duan, J.; Chen, D.; Wang, Q.; Xiao, W.; Shi, Y.; Yazyev, O. V.; Yao, Y., Transport signatures of temperature-induced chemical potential shift

and Lifshitz transition in layered type-II Weyl semimetal TaIrTe4. *2D Materials* **2020,** *8* (1), 015020.
20. Back, S. Y.; Kim, Y.-K.; Cho, H.; Han, M.-K.; Kim, S.-J.; Rhyee, J. S., Temperature-Induced Lifshitz Transition and Charge Density Wave in InTe1−δ Thermoelectric Materials. *ACS Applied Energy Materials* **2020,** *3* (4), 3628-3636.
21. Schellnhuber, H. J., Global warming: Stop worrying, start panicking? *Proceedings of the National Academy of Sciences* **2008,** *105* (38), 14239-14240.
22. Hansen, J.; Sato, M.; Hearty, P.; Ruedy, R.; Kelley, M.; Masson-Delmotte, V.; Russell, G.; Tselioudis, G.; Cao, J.; Rignot, E.; Velicogna, I.; Tormey, B.; Donovan, B.; Kandiano, E.; Karina; Kharecha, P.; Legrande, A. N.; Bauer, M.; Lo, K.-W., Ice melt, sea level rise and superstorms: evidence from paleoclimate data, climate modeling, and modern observations that 2 °C global warming could be dangerous. *Atmospheric Chemistry and Physics* **2016,** *16* (6), 3761-3812.
23. Johnson, G. C.; Lyman, J. M., Warming trends increasingly dominate global ocean. *Nature Climate Change* **2020,** *10* (8), 757-761.
24. Hashim, J. H.; Hashim, Z., Climate Change, Extreme Weather Events, and Human Health Implications in the Asia Pacific Region. *Asia Pacific Journal of Public Health* **2016,** *28* (2_suppl), 8S-14S.
25. Schleussner, C.-F.; Lissner, T. K.; Fischer, E. M.; Wohland, J.; Perrette, M.; Golly, A.; Rogelj, J.; Childers, K.; Schewe, J.; Frieler, K.; Mengel, M.; Hare, W.; Schaeffer, M., Differential climate impacts for policy-relevant limits to global warming: the case of 1.5 °C and 2 °C. *Earth System Dynamics* **2016,** *7* (2), 327-351.
26. Andreae, M. O.; Jones, C. D.; Cox, P. M., Strong present-day aerosol cooling implies a hot future. *Nature* **2005,** *435* (7046), 1187-1190.
27. Cleveland, C. J.; Morris, C., Handbook of Energy Volume I: Diagrams, Charts, and Tables. Elsevier: England, 2013; Vol. 1, pp 405-450.
28. Djieutedjeu, H.; Makongo, J. P. A.; Rotaru, A.; Palasyuk, A.; Takas, N. J.; Zhou, X. Y.; Ranmohotti, K. G. S.; Spinu, L.; Uher, C.; Poudeu, P. F. P., Crystal Structure, Charge Transport, and Magnetic Properties of MnSb2Se4. *Eur J Inorg Chem* **2011,** (26), 3969-3977.
29. Rabadanov, M. K.; Loshmanov, A.; Shaldin, Y. V., Anharmonic thermal vibrations of atoms in crystals with sphalerite structure-GaP, ZnS, ZnSe, and ZnTe: High-temperature x-ray structure studies. *Crystallogr Rep+* **1997,** *42* (4), 592-602.
30. Voutsas, G. P.; Papazoglou, A. G.; Rentzeperis, P. J.; Siapkas, D., The crystal structure of antimony selenide, Sb2Se3. *Zeitschrift für Kristallographie - Crystalline Materials* **1985,** *171* (1-4), 261-268.
31. Moulder, J. F.; Stickle, W. F.; Sobol, P. E.; Bomben, K. D., *Handbook of X-ray Photoelectron Spectroscopy*. Perkins-Elmer Coorporation: Eden Prairie, Minnesota, 1992.
32. Lopez, J.; Djieutedru, H.; Buchanan, B.; Ranmohotti, K. G. S.; Page, A.; Uher, C.; Poudeu, P. F. P., Engineering Magnetic Transitions in Fe1-xSnxBi2Se4 n-Type Ferromagnetic Semiconductors through Chemical Manipulation of Spatial Separation between Magnetic Centers. *Chem Mater* **2019,** *31* (9), 3507-3518.
33. Kubelka, P.; Munk, F., Ein Beitrag Zur Optik Der Farbanstriche. *Zeitschrift für Technische Physik* **1931,** *12*, 593-601.
34. Milosevic, M.; Berets, S. L., A Review of FT-IR Diffuse Reflection Sampling Considerations. *Applied Spectroscopy Reviews* **2002,** *37* (4), 347-364.

35. Sheldrick, G. *SHELXTL, DOS Windows/NT*, version 6.12; Bruker analytical X-ray instruments Inc.: Madison, WI, USA, 2000.
36. Sheldrick, G. M., Crystal structure refinement with SHELXL. *Acta Crystallogr C* **2015,** *71* (1), 3-8.
37. Brandenburg, K.; Putz, H. *DIAMOND*, Version 3.0 c; Crystal Impact GbR: Bonn, Germany, 2005.
38. Djieutedjeu, H.; Lopez, J. S.; Lu, R. M.; Buchanan, B.; Zhou, X. Y.; Chi, H.; Ranmohotti, K. G. S.; Uher, C.; Poudeu, P. F. P., Charge Disproportionation Triggers Bipolar Doping in FeSb2-xSnxSe4 Ferromagnetic Semiconductors, Enabling a Temperature-Induced Lifshitz Transition. *J Am Chem Soc* **2019,** *141* (23), 9249-9261.
39. Djieutedjeu, H.; Olvera, A.; Page, A.; Uher, C.; Poudeu, P. F. P., High-T-c Ferromagnetism and Electron Transport in p-Type Fe1-xSnxSb2Se4 Semiconductors. *Inorg Chem* **2015,** *54* (21), 10371-10379.
40. Djieutedjeu, H.; Poudeu, P. F. P.; Takas, N. J.; Makongo, J. P. A.; Rotaru, A.; Ranmohotti, K. G. S.; Anglin, C. J.; Spinu, L.; Wiley, J. B., Structural-Distortion-Driven Cooperative Magnetic and Semiconductor-to-Insulator Transitions in Ferromagnetic FeSb2Se4. *Angew Chem Int Edit* **2010,** *49* (51), 9977-9981.
41. Djieutedjeu, H.; Zhou, X. Y.; Chi, H.; Haldolaarachchige, N.; Ranmohotti, K. G. S.; Uher, C.; Young, D.; Poudeu, P. F. P., Donor and acceptor impurity-driven switching of magnetic ordering in MnSb2-xSnxSe4. *J Mater Chem C* **2014,** *2* (30), 6199-6210.
42. Moroz, N. A.; Lopez, J. S.; Djieutedjeu, H.; Ranmohotti, K. G. S.; Olvera, A.; Ren, P.; Page, A.; Takas, N. J.; Uher, C.; Poudeu, P. F. P., Indium Preferential Distribution Enables Electronic Engineering of Magnetism in FeSb2-xInxSe4 p-Type High-Tc Ferromagnetic Semiconductors. *Chem Mater* **2016,** *28* (23), 8570-8579.
43. Nowka, C.; Gellesch, M.; Borrero, J. E. H.; Partzsch, S.; Wuttke, C.; Steckel, F.; Hess, C.; Wolter, A. U. B.; Bohorquez, L. T. C.; Buchner, B.; Hampel, S., Chemical vapor transport and characterization of MnBi2Se4. *J Cryst Growth* **2017,** *459*, 81-86.
44. Ranmohotti, K. G. S.; Djieutedjeu, H.; Lopez, J.; Page, A.; Haldolaarachchige, N.; Chi, H.; Sahoo, P.; Uher, C.; Young, D.; Poudeu, P. F. P., Coexistence of High-T-c Ferromagnetism and n-Type Electrical Conductivity in FeBi2Se4. *J Am Chem Soc* **2015,** *137* (2), 691-698.
45. Ranmohotti, K. G. S.; Djieutedjeu, H.; Poudeu, P. F. P., Chemical Manipulation of Magnetic Ordering in Mn1-xSnxBi2Se4 Solid-Solutions. *J Am Chem Soc* **2012,** *134* (34), 14033-14042.
46. Hirahara, T.; Eremeev, S. V.; Shirasawa, T.; Okuyama, Y.; Kubo, T.; Nakanishi, R.; Akiyama, R.; Takayama, A.; Hajiri, T.; Ideta, S.; Matsunami, M.; Sumida, K.; Miyamoto, K.; Takagi, Y.; Tanaka, K.; Okuda, T.; Yokoyama, T.; Kimura, S.; Hasegawa, S.; Chulkov, E. V., Large-Gap Magnetic Topological Heterostructure Formed by Subsurface Incorporation of a Ferromagnetic Layer. *Nano Lett* **2017,** *17* (6), 3493-3500.
47. Hou, Y. S.; Kim, J. W.; Wu, R. Q., Axion insulator state in ferromagnetically ordered CrI3/Bi2Se3/MnBi2Se4 heterostructures. *Phys Rev B* **2020,** *101* (12).
48. Hou, Y. S.; Wu, R. Q., Axion Insulator State in a Ferromagnet/Topological Insulator/Antiferromagnet Heterostructure. *Nano Lett* **2019,** *19* (4), 2472-2477.
49. Okuyama, Y.; Ishikawa, R.; Kuroda, S.; Hirahara, T., Role of hybridization and magnetic effects in massive Dirac cones: Magnetic topological heterostructures with controlled film thickness. *Appl Phys Lett* **2019,** *114* (5).
50. Li, S. M.; Zhao, H. Z.; Zhang, H.; Ren, G. K.; Liu, N.; Li, D. D.; Yang, C. S.; Jin, S. F.; Shang, D. S.; Wang, W. H.; Lin, Y. H.; Gu, L.; Chen, X. L., Enhancement of the

thermoelectric properties of MnSb2Se4 through Cu resonant doping. *Rsc Adv* **2015,** *5* (120), 99065-99073.
51. Cao, B. L.; Jian, J. K.; Ge, B. H.; Li, S. M.; Wang, H.; Liu, J.; Zhao, H. Z., Improved thermoelectric performance in p-type Bi0.48Sb1.52Te3 bulk material by adding MnSb2Se4. *Chinese Phys B* **2017,** *26* (1).
52. Tideswell, N. W.; Kruse, F. H.; McCullough, J. D., The crystal structure of antimony selenide, Sb2Se3. *Acta Crystallographica* **1957,** *10* (2), 99-102.
53. Baroni, D. A., Sul polimorfismo di MnSe. *Zeitschrift für Kristallographie - Crystalline Materials* **1938,** *99* (1-6), 336-339.
54. Franzen, H.; Sterner, C., X-Ray Photoelectron-Spectra of Mns, Mnse, and Mnte. *J Solid State Chem* **1978,** *25* (3), 227-230.
55. Shenasa, M.; Sainkar, S.; Lichtman, D., Xps Study of Some Selected Selenium-Compounds. *J Electron Spectrosc* **1986,** *40* (4), 329-337.
56. Wang, D. B.; Yu, D. B.; Mo, M. S.; Liu, X. M.; Qian, Y. T., Preparation and characterization of wire-like Sb2Se3 and flake-like Bi2Se3 nanocrystals. *J Cryst Growth* **2003,** *253* (1-4), 445-451.
57. Lu, R.; Bailey, T. P.; Uher, C.; Poudeu, P. F. P., Ultrafine Interwoven Dendritic Cu2Se/CuFeSe2 Composites with Enhanced Thermoelectric Performance. *ACS Applied Energy Materials* **2020,** *3* (9), 9133-9142.
58. Mavlonov, A.; Razykov, T.; Raziq, F.; Gan, J.; Chantana, J.; Kawano, Y.; Nishimura, T.; Wei, H.; Zakutayev, A.; Minemoto, T.; Zu, X.; Li, S.; Qiao, L., A review of Sb2Se3 photovoltaic absorber materials and thin-film solar cells. *Solar Energy* **2020,** *201*, 227-246.
59. Ma, Z.; Chai, S.; Feng, Q.; Li, L.; Li, X.; Huang, L.; Liu, D.; Sun, J.; Jiang, R.; Zhai, T.; Xu, H., Chemical Vapor Deposition Growth of High Crystallinity Sb2 Se3 Nanowire with Strong Anisotropy for Near-Infrared Photodetectors. *Small* **2019,** *15* (9), 1805307.
60. Wang, J.; Deng, Z.; Li, Y., Synthesis and characterization of Sb2Se3 nanorods. *Materials Research Bulletin* **2002,** *37* (3), 495-502.
61. Luo, X.; Chen, S.; Liu, L.; Lv, J.; Qadir, A.; Shehzad, K.; Qiao, X.; Xu, Y.; Kienle, L.; Lotnyk, A.; Zhang, X.; Qian, G.; Fan, X., Micron-Scale Photodetectors Based on One-Dimensional Single-Crystalline Sb2–xSnxSe3 Microrods: Simultaneously Improving Responsivity and Extending Spectral Response Region. *The Journal of Physical Chemistry C* **2019,** *123* (1), 810-816.
62. Wang, D.; Yu, D.; Mo, M.; Liu, X.; Qian, Y., Preparation and characterization of wire-like Sb2Se3 and flake-like Bi2Se3 nanocrystals. *J Cryst Growth* **2003,** *253* (1-4), 445-451.
63. Chen, S.; Shehzad, K.; Qiao, X.; Luo, X.; Liu, X.; Zhang, Y.; Zhang, X.; Xu, Y.; Fan, X., A high performance broadband photodetector based on (SnxSb1−x)2Se3 nanorods with enhanced electrical conductivity. *J Mater Chem C* **2018,** *6* (41), 11078-11085.
64. Hernandez, J. A.; Fonseca, L. F.; Pettes, M. T.; Jose-Yacaman, M., Thermoelectric properties of antimony selenide hexagonal nanotubes. *Nanotechnology* **2021,** *32* (9), 095705.
65. Li, Z.; Liang, X.; Li, G.; Liu, H.; Zhang, H.; Guo, J.; Chen, J.; Shen, K.; San, X.; Yu, W.; Schropp, R. E. I.; Mai, Y., 9.2%-efficient core-shell structured antimony selenide nanorod array solar cells. *Nature Communications* **2019,** *10* (1).
66. Yang, B.; Xue, D.-J.; Leng, M.; Zhong, J.; Wang, L.; Song, H.; Zhou, Y.; Tang, J., Hydrazine solution processed Sb2S3, Sb2Se3 and Sb2(S1−xSex)3 film: molecular precursor identification, film fabrication and band gap tuning. *Scientific Reports* **2015,** *5* (1), 10978.

67. Stoliaroff, A.; Lecomte, A.; Rubel, O.; Jobic, S.; Zhang, X.; Latouche, C.; Rocquefelte, X., Deciphering the Role of Key Defects in Sb2Se3, a Promising Candidate for Chalcogenide-Based Solar Cells. *ACS Applied Energy Materials* **2020,** *3* (3), 2496-2509.
68. Liu, X.; Xiao, X.; Yang, Y.; Xue, D.-J.; Li, D.-B.; Chen, C.; Lu, S.; Gao, L.; He, Y.; Beard, M. C.; Wang, G.; Chen, S.; Tang, J., Enhanced Sb2Se3solar cell performance through theory-guided defect control. *Progress in Photovoltaics: Research and Applications* **2017,** *25* (10), 861-870.
69. Chen, C.; Bobela, D. C.; Yang, Y.; Lu, S.; Zeng, K.; Ge, C.; Yang, B.; Gao, L.; Zhao, Y.; Beard, M. C.; Tang, J., Characterization of basic physical properties of Sb2Se3 and its relevance for photovoltaics. *Frontiers of Optoelectronics* **2017,** *10* (1), 18-30.
70. Liang, G.; Chen, X.; Ren, D.; Jiang, X.; Tang, R.; Zheng, Z.; Su, Z.; Fan, P.; Zhang, X.; Zhang, Y.; Chen, S., Ion doping simultaneously increased the carrier density and modified the conduction type of Sb2Se3 thin films towards quasi-homojunction solar cell. *Journal of Materiomics* **2021**.
71. Baig, F.; Khattak, Y. H.; Shuja, A.; Riaz, K.; Soucase, B. M., Performance investigation of Sb2Se3 based solar cell by device optimization, band offset engineering and Hole Transport Layer in SCAPS-1D. *Current Applied Physics* **2020,** *20* (8), 973-981.
72. Li, Y.; Wang, K.; Huang, D.; Li, L.; Tao, J.; Ghany, N. A. A.; Jiang, F., CdxZn1-xS/Sb2Se3 thin film photocathode for efficient solar water splitting. *Applied Catalysis B: Environmental* **2021,** *286*, 119872.
73. Farzaneh, S. M.; Rakheja, S., Intrinsic spin Hall effect in topological insulators: A first-principles study. *Physical Review Materials* **2020,** *4* (11).
74. Kong, P. P.; Sun, F.; Xing, L. Y.; Zhu, J.; Zhang, S. J.; Li, W. M.; Liu, Q. Q.; Wang, X. C.; Feng, S. M.; Yu, X. H.; Zhu, J. L.; Yu, R. C.; Yang, W. G.; Shen, G. Y.; Zhao, Y. S.; Ahuja, R.; Mao, H. K.; Jin, C. Q., Superconductivity in Strong Spin Orbital Coupling Compound Sb2Se3. *Scientific Reports* **2015,** *4* (1), 6679.
75. Iovu, M. S.; E. P. Colomeico, E. P.; Vasiliev, I. A., Photoconductivity of Amorphous Sb2Se3 and Sb2Se3:Sn
Thin Films. *Chalcogenide Letters* **2007,** *4* (9), 109-113.
76. Kumar, P.; Thangaraj, R., Effect of Sn addition on the photoconductivity of narrow-gap Sb2Se3films. *Philosophical Magazine Letters* **2009,** *89* (4), 241-249.
77. Iovu, M. S.; Vasiliev, I. A.; Colomeico, E. P. In *Negative Photoconductivity of Amorphous Sb2Se3 and Sb2Se3: Sn Films*, International Semiconductor Conference, 2007; IEEE: 2007; pp 219-222.
78. Kumar, P.; Sathiaraj, T. S.; Thangaraj, R., Optical properties of amorphous Sb2Se3:Sn films. *Philosophical Magazine Letters* **2010,** *90* (3), 183-192.
79. Iovu, M. S.; Harea, D. V.; Colomeico, E. P.; Cojocaru, I. A., Photoinduced effects and holographic recording in amorphous As100-xSex, As2Se3:Sn and Sb2Se3:Sn films. *Journal of Optoelectronics and Advanced Materials* **2008,** *10* (12), 3469-3476.
80. Iovu, M. S.; Harea, D. V.; Colomeico, E. P., Some optical properties of thermally deposited Sb2Se3 : Sn thin films. *Journal of Optoelectronics and Advanced Materials* **2008,** *10* (4), 862-866.
81. Chen, S.; Qiao, X.; Zheng, Z.; Cathelinaud, M.; Ma, H.; Fan, X.; Zhang, X., Enhanced electrical conductivity and photoconductive properties of Sn-doped Sb2Se3 crystals. *J Mater Chem C* **2018,** *6* (24), 6465-6470.

82. G.G., G.; I.N., O.; A.V., N., Reaction of SnSe with Sb2Se3. *Inorganic Materials* **1975,** *11*, 1033-1035.
83. Shannon, R. D., Revised effective ionic radii and systematic studies of interatomic distances in halides and chalcogenides. *Acta Crystallographica Section A* **1976,** *32* (5), 751-767.
84. Madelung, O., *Vx-VIy Compounds*. 3 ed.; 2004.
85. Miller, O. D.; Yablonovitch, E.; Kurtz, S. R., Strong Internal and External Luminescence as Solar Cells Approach the Shockley–Queisser Limit. *IEEE Journal of Photovoltaics* **2012,** *2* (3), 303-311.
86. Shi, W.; Gao, M.; Wei, J.; Gao, J.; Fan, C.; Ashalley, E.; Li, H.; Wang, Z., Tin Selenide (SnSe): Growth, Properties, and Applications. *Advanced Science* **2018,** *5* (4), 1700602.
87. Yoshikawa, K.; Kawasaki, H.; Yoshida, W.; Irie, T.; Konishi, K.; Nakano, K.; Uto, T.; Adachi, D.; Kanematsu, M.; Uzu, H.; Yamamoto, K., Silicon heterojunction solar cell with interdigitated back contacts for a photoconversion efficiency over 26%. *Nature Energy* **2017,** *2* (5), 17032.
88. Ramanathan, K.; Noufi, R.; Granata, J.; Webb, J.; Keane, J., Prospects for in situ junction formation in CuInSe2 based solar cells. *Solar Energy Materials and Solar Cells* **1998,** *55* (1-2), 15-22.
89. Hirai, Y.; Kurokawa, Y.; Yamada, A., Numerical study of Cu(In,Ga)Se2solar cell performance toward 23% conversion efficiency. *Japanese Journal of Applied Physics* **2014,** *53* (1), 012301.
90. Wang, W.; Winkler, M. T.; Gunawan, O.; Gokmen, T.; Todorov, T. K.; Zhu, Y.; Mitzi, D. B., Device Characteristics of CZTSSe Thin-Film Solar Cells with 12.6% Efficiency. *Advanced Energy Materials* **2014,** *4* (7), 1301465.
91. Fiducia, T. A. M.; Mendis, B. G.; Li, K.; Grovenor, C. R. M.; Munshi, A. H.; Barth, K.; Sampath, W. S.; Wright, L. D.; Abbas, A.; Bowers, J. W.; Walls, J. M., Understanding the role of selenium in defect passivation for highly efficient selenium-alloyed cadmium telluride solar cells. *Nature Energy* **2019,** *4* (6), 504-511.
92. Chen, E. M.; Williams, L.; Olvera, A.; Zhang, C.; Zhang, M.; Shi, G.; Heron, J. T.; Qi, L.; Guo, L. J.; Kioupakis, E.; Poudeu, P. F. P., Sustainable p-type copper selenide solar material with ultra-large absorption coefficient. *Chemical Science* **2018,** *9* (24), 5405-5414.
93. Kittel, C., *Introduction to Solid State Physics*. 8th ed.; Wiley: 2004.
94. Rios, L. E. V. Structural trends in off-stoichiometric kesterite type compound Cu2ZnSnSe4 semiconductor. University of Berlin, Berlin, 2016.
95. Rockett, A.; Birkmire, R. W., CuInSe2 for photovoltaic applications. *Journal of Applied Physics* **1991,** *70* (7), R81-R97.
96. Khoshsirat, N.; Yunus, N. A. M., Copper-Indium-Gallium-diSelenide (CIGS) Nanocrystalline Bulk Semiconductor as the Absorber Layer and Its Current Technological Trend and Optimization. InTech: 2016.
97. Fleischer, M., The abundance and distribution of the chemical elements in the earth's crust. *Journal of Chemical Education* **1954,** *31* (9), 446.
98. Survey, U. S. G., Mineral Commodity summaries 2010: U.S. Geological Survey. 2010; p 193.
99. Das, S.; Mandal, K. C.; Bhattacharya, R. N., Earth-Abundant Cu2ZnSn(S,Se)4 (CZTSSe) Solar Cells. Springer International Publishing: 2016; pp 25-74.
100. Knight, K. S., The crystal structures of CuInSe2 and CuInTe2. *Materials Research Bulletin* **1992,** *27* (2), 161-167.

101. Gao, F.; Yamazoe, S.; Maeda, T.; Wada, T., Structural Study of Cu-Deficient Cu2(1-x)ZnSnSe4 Solar Cell Materials by X-ray Diffraction and X-ray Absorption Fine Structure. *Japanese Journal of Applied Physics* **2012,** *51*, 10NC28.
102. Nateprov, A.; Kravtsov, V. C.; Gurieva, G.; Schorr, S., Single crystal X-ray structure investigation of Cu2ZnSnSe4. *Электронная обработка материалов* **2013,** (5).
103. Yamamoto, K.; Kashida, S., X-ray study of the average structures of Cu2Se and Cu1.8S in the room temperature and the high temperature phases. *J Solid State Chem* **1991,** *93* (1), 202-211.
104. White, S. L.; Banerjee, P.; Jain, P. K., Liquid-like cationic sub-lattice in copper selenide clusters. *Nature Communications* **2017,** *8* (1), 14514.
105. Sun, S.; Li, Y.; Chen, Y.; Xu, X.; Kang, L.; Zhou, J.; Xia, W.; Liu, S.; Wang, M.; Jiang, J.; Liang, A.; Pei, D.; Zhao, K.; Qiu, P.; Shi, X.; Chen, L.; Guo, Y.; Wang, Z.; Zhang, Y.; Liu, Z.; Yang, L.; Chen, Y., Electronic origin of the enhanced thermoelectric efficiency of Cu2Se. *Science Bulletin* **2020,** *65* (22), 1888-1893.
106. L., G.; M., D.; O., S.; A., P., Crystal structure of Cu2Se. *Chemistry of Metals and Alloys* **2011,** *4*, 200-205.
107. Choi, J.-H.; Han, Y.-K., Structural, electronic, and optical properties of bulk Cu2Se. *Current Applied Physics* **2015,** *15* (11), 1417-1420.
108. Nicolaou, M. C. Thermoelectric Figure of Merit of Degenerate and Nondegenerate Semiconductors. Northeastern University, Boston, MA, 2008.
109. Zhang, S. B.; Wei, S.-H.; Zunger, A.; Katayama-Yoshida, H., Defect physics of theCuInSe2chalcopyrite semiconductor. *Phys Rev B* **1998,** *57* (16), 9642-9656.
110. Ashcroft, N. W.; Mermin, N. D., *Solid state physics*. Saunders College Publishing: New York, 1976.
111. Calvert, L.; Canada, N. R. C. o., ICDD: Ottawa, Canada, 1978.
112. Gaby, J. H.; Delong, B.; Brown, F. C.; Kirby, R.; Lévy, F., Origin of the structural transition in TiSe2. *Solid State Communications* **1981,** *39* (11), 1167-1170.
113. Johnston, W. D.; Heikes, R. R., A Study of the System LixMn(1 - x)Se. *J Am Chem Soc* **1958,** *80* (22), 5904-5907.
114. Morimoto, N.; Koto, K., Crystal Structure of Umangite Cu3Se2. *Science* **1966,** *152* (3720), 345.
115. Thanigaimani, V.; Angadi, M. A., Optical properties of MnSe thin films. *Thin Solid Films* **1994,** *245* (1-2), 146-151.
116. Monjezi, F.; Jamali-Sheini, F.; Yousefi, R., Optoelectronic properties of Zn-doped Cu3Se2 nanosheets for photovoltaic application. *Ceramics International* **2020,** *46* (14), 21978-21988.
117. Tsuchida, R., Absorption Spectra of Co-ordination Compounds. I. *Bulletin of the Chemical Society of Japan* **1938,** *13* (5), 388-400.
118. Newnham, R. E., *Properties of materials: anisotropy, symmetry, structure*. Oxford University Press on Demand: 2005.
119. Gadetsky, S.; Syrgabaev, I.; Erwin, J. K.; Mansuripur, M.; Suzuki, T.; Ruane, M., Measurements of the magneto-optic Kerr effect and the extraordinary Hall effect on grooved glass substrates coated with amorphous TbFeCo. *J. Opt. Soc. Am. A* **1996,** *13* (2), 314-319.
120. Kang, K.; Yang, K.; Puthalath, K.; David; Schleife, A. e., Polar magneto-optical Kerr effect in antiferromagnetic M2As (M=Cr, Mn, Fe) under an external magnetic field. *arXiv pre-print server* **2020**.

121. Callister, W. D.; Rethwisch, D. G., *Materials Science and Engineering: an Introduction*. 9th ed.; Wiley: 2012.
122. Smith, P. P. K.; Parise, J. B., Structure determination of SnSb2S4 and SnSb2Se4 by high-resolution electron microscopy. *Acta Crystallographica Section B Structural Science* **1985,** *41* (2), 84-87.
123. Cohen, K.; Rivet, J.; Dugue, J., Description of the Cu-as-Se Ternary-System. *J Alloy Compd* **1995,** *224* (2), 316-329.
124. T., H.; Y., U.; K., K., Phase diagram of the TiSex system ($0.95 \leq x \leq 2.00$). *Materials Research Bulletin* **1988,** *23*, 1641-1650.
125. M., L., Mn-Se (Manganese-Selenium). In *Binary Alloy Phase Diagrams*, 2 ed.; Massalski, T. B., Ed. 1990; Vol. 3, pp 2598-2602.
126. Nelson, J., *The Physics of Solar Cells*. Imperial College Press: 2003.